Delft University of Technology

Mud dynamics in the Belgian coastal zone and siltation in the harbor of Zeebrugge

Vanlede, J.D.S.M.

DOI
10.4233/uuid:69e5aa74-9dd9-4915-8882-03b70506030a

Publication date
2022

Document Version
Final published version

Citation (APA)
Vanlede, J. D. S. M. (2022). *Mud dynamics in the Belgian coastal zone and siltation in the harbor of Zeebrugge*. https://doi.org/10.4233/uuid:69e5aa74-9dd9-4915-8882-03b70506030a

Important note
To cite this publication, please use the final published version (if applicable).
Please check the document version above.

Copyright
Other than for strictly personal use, it is not permitted to download, forward or distribute the text or part of it, without the consent of the author(s) and/or copyright holder(s), unless the work is under an open content license such as Creative Commons.

Takedown policy
Please contact us and provide details if you believe this document breaches copyrights.
We will remove access to the work immediately and investigate your claim.

This work is downloaded from Delft University of Technology.
For technical reasons the number of authors shown on this cover page is limited to a maximum of 10.

Mud dynamics in the Belgian coastal zone and siltation in the harbor of Zeebrugge

Mud dynamics in the Belgian coastal zone and siltation in the harbor of Zeebrugge

Proefschrift

ter verkrijging van de graad van doctor
aan de Technische Universiteit Delft,
op gezag van de Rector Magnificus, prof.dr.ir. T.H.J.J. van der Hagen,
voorzitter van het College voor Promoties,
in het openbaar te verdedigen op maandag 14 maart 2022 om 15:00 uur

door

Joris VANLEDE

Burgerlijk Mijnbouwkundig Ingenieur, Katholieke Universiteit Leuven, België
geboren te Sint-Niklaas, België.

Dit proefschrift is goedgekeurd door de

promotor: prof. dr. ir. J.C. Winterwerp

Samenstelling promotiecommissie:

Rector Magnificus	voorzitter
Prof. dr. ir. J.C. Winterwerp	Technische Universiteit Delft, promotor

Onafhankelijke leden:

Prof. dr. A.J. Mehta	University of Florida
Prof. dr. ir. T. De Mulder	Universiteit Gent
Prof. dr. J. Pietrzak	Technische Universiteit Delft
Prof. dr. ir. D. Roelvink	IHE Delft
Prof. dr. ir. E. Toorman	Katholieke Universiteit Leuven
Dr. ir. T. van Kessel	Deltares

TUDelft Delft University of Technology

Waterbouwkundig Laboratorium

Vlaanderen is wetenschap

Printed by: Print Service Ede, the Netherlands

Copyright © 2022 by J. Vanlede

ISBN 978-94-6366-521-6

An electronic version of this dissertation is available at
http://repository.tudelft.nl/.

Dedicated in loving memory of Annelies Decuypere

(1977-2009)

Contents

Summary

Ports are important drivers for economic activity. For the Port of Zeebrugge, important sectors include cars, containers and liquefied natural gas (LNG). Due to significant siltation, frequent maintenance dredging is necessary in order to ensure the nautical accessibility. For Zeebrugge, that responsibility falls on the Flemish department of mobility and public works, at a yearly cost of about 70 millions euro. This thesis aims to contribute to the body of knowledge on the mud dynamics in the Belgian Coastal Zone, on the mechanisms behind the siltation of the harbor, and on the effects of the disposal of dredged material at sea.

The cohesive sediment dynamics in the Belgian Coastal Zone (BCZ) are characterized by residual transport directed towards the northeast, and by the presence of a coastal turbidity maximum (CTM) that extends between Ostend and Zeebrugge. The resulting mud deposits are a persistent feature in the BCZ, at least since the beginning of the 20th century. Baroclinic effects, tidal asymmetry and local gradients in the residual current all play a role in trapping sediment in the CTM. In this thesis, the sediment dynamics are studied using a combination of data analysis and numerical modeling. First, a dataset is analysed that consists of 51 tripod deployments over nine years (2005-2013) at locations MOW1 and Blankenberge, kindly provided by the Royal Belgian Institute of Natural Sciences (RBINS). Tidal ensembles are derived of velocity and near-bed suspended sediment concentration (SSC). These ensembles are used to study the vertical gradient of SSC, the influence of waves, and the seasonal variation. Subsequently, a 1DV model is set up that computes the transient vertical distribution of a single fraction of SSC, and the mud content in the bed. This model is used to study the intratidal variation of the near-bed SSC observed at Blankenberge. It is shown that a two-fraction (coarse and fine) sediment model is necessary to model both the the ebb and the flood peak of SSC. Subsequently a 3D sediment transport model is set up. The settling velocity of the coarse and fine fraction are taken over from the 1DV model, as is the zero order resuspension constant. The set of measurements that is available for model calibration and validation is maximized by using both the comparable tide method and tidal ensembles.

The model confirms that local hydrodynamic conditions trap sediment in the CTM, and it is used to study the role of salinity-driven baroclinic currents. A sediment balance is derived to better understand the sediment dynamics in the BCZ as an open system with some closed characteristics: even though the residual sediment transport through the Dover Strait is an important sediment supply to the BCZ, the relative importance of local erosion and deposition gives it some characteristics of a closed system, like a different clay mineralogical composition than English Channel mud.

The mud dynamics in the harbor of Zeebrugge are studied with data analysis.

Three important timescales are established: intratidal, spring-neap and seasonal. On the intratidal timescale, most of the sediment exchange occurs from two hours before high water to high water. No evidence is found that daily siltation rates in the harbor correlate significantly with wave or wind conditions in the North Sea, or fresh water inflow into the harbor. The sediment influx per tide is three times higher during spring tide than during neap tide. Because there is no spring-neap modulation in dredging works, the level of the mud-water interface in Albert II dock typically rises 15 cm/day during spring tide conditions and falls 5 to 10 cm/day during neap and average tide conditions. The mud volume within the harbor basin is also larger in winter, with a lower density. Present regulations at Zeebrugge stipulate that for safe maritime access to the harbor, the ship should have a positive Under Keel Clearance (UKC) of at least 10% (relative to its draft) above the nautical bottom (defined as the density level of 1200 kg/m^3) and no more than 7% negative UKC below the mud-water interface. This research therefore highlights potential (and unwanted) spring-neap and seasonal variations in nautical accessibility, that need to be mitigated with maintenance dredging works.

The material that is dredged in the harbor and the access channels is disposed in the North Sea. The international framework for the disposal at sea of dredged material is formed by the regional OSPAR Convention (1992) and the worldwide London Convention (1972). Disposal at sea can have important ecological effects, e.g. through the influence on the underwater light climate, or the burial of benthic communities. In situ tracer experiments in the 90's had already indicated that recirculation could occur, although it could not be quantified due to uncertainties in the interpretation of the experiments. In 2013-2014, a field trial was setup in which the disposal location Zeebrugge Oost was changed for one month to location Zeebrugge West, which is located further offshore. The field campaign could not show unambiguously however that the relocation resulted in either a decrease in the suspended sediment concentration (SSC), or a reduction of the siltation inside the harbor. Therefore the field trial was replicated in the 3D model. The results show that even though there is a clear effect on the return flow, there is only a very limited effect on the SSC. The expected effects on near-bed SSC are so small, that even with a longer field experiment it would have been near-impossible to distinguish the effect on SSC from the natural variation during the field experiment. This case study is therefore an example of how a calibrated model can be a useful tool for predictions of a variable such as return flow that is difficult to measure directly.

Samenvatting

De vier Belgische zeehavens spelen een belangrijke logistieke rol, en zijn cruciaal voor Vlaanderen als bron van inkomsten en werkgelegenheid. Specifiek voor de haven van Zeebrugge gaat het om containertrafiek, de LNG-terminal in de voorhaven, en de roll-on-roll-off trafiek van nieuwe wagens. Regelmatige onderhoudsbaggerwerken zijn noodzakelijk om de nautische toegankelijkheid te garanderen. Voor Zeebrugge valt de verantwoordelijkheid daarvoor bij de afdeling maritieme toegang van het departement mobiliteit en openbare werken van de Vlaamse overheid, tegen een jaarlijkse kost van ongeveer 70 miljoen euro. Deze thesis wil bijdragen aan de kennis rond de slibdynamiek in het Belgische deel van de Noordzee, de aanslibbing van de haven van Zeebrugge, en het effect van het storten van baggerspecie in de Noordzee.

De slibdynamiek in de Belgische kustzone wordt gekenmerkt door een kustgebonden turbiditeitsmaximum (CTM) dat zich uitstrekt tussen Oostende en Zeebrugge. Het lokaal slibgehalte in de bodem is er hoger, en dat al zeker sinds het begin van de 20^{e} eeuw. Barocliene effecten, getij-asymmetrie en lokale gradiënten in de residuele stroming spelen elk een rol in het vangen van sediment in het turbiditeitsmaximum. De slibdynamiek wordt verder bestudeerd met een combinatie van data-analyse en numerieke modellering. Een dataset van het Koninklijk Belgisch Instituut van Natuurwetenschappen (KBIN) van 51 frame metingen over negen jaar (2005-2013) op twee locaties in de Noordzee (MOW1 en Blankenberge) wordt geanalyseerd. Aan de hand van getij-ensembles van sedimentconcentratie (SSC) wordt de invloed van golven en seizoenen onderzocht, alsook de verticale gradiënt van SSC. Vervolgens wordt een 1DV puntmodel opgesteld waarmee de SSC te Blankenberge wordt geanalyseerd. Hieruit blijkt dat twee sedimentfracties (grof en fijn) noodzakelijk zijn om zowel de eb- als de vloedpiek in SSC te verklaren. Tenslotte wordt ook een 3D model opgesteld, waarbij de valsnelheid van de grove en fijne fractie, en de erosieconstante worden overgenomen van het 1DV model. De hoeveelheid beschikbare metingen voor calibratie en validatie wordt gemaximaliseerd door het zoeken naar vergelijkbare getijden, en door het gebruik van getij-ensembles.

Het 3D model bevestigt dat lokale hydrodynamische condities sediment vangen in het turbiditeitsmaximum. Tevens wordt de rol van de saliniteitsgedreven barocliene stroming nader onderzocht. Een sedimentbalans uit het model wordt gebruikt om de sedimentdynamiek in de Belgische kustzone te begrijpen als een open systeem, met gesloten eigenschappen: hoewel de sedimentimport vanuit de straat van Dover een belangrijke bron van slib is, zorgt het relatief grote belang van lokale erosie en depositie ervoor dat de Belgische kustzone een aparte kleimineralogische samenstelling heeft.

De slibdynamiek in de haven van Zeebrugge wordt bestudeerd aan de hand

van data-analyse. Drie belangrijke tijdschalen worden onderscheiden: het getij, de springtij-doodtij cyclus en de seizoenen. Binnen één getij gebeurt de meeste sedimentuitwisseling tussen 2 uur vóór hoogwater en hoogwater. De aanslibbing in de haven wordt niet significant beïnvloed door meteo-condities (wind en golven op de Noordzee) of door zoetwaterlozingen in de haven. De sedimentimport is drie keer hoger tijdens springtij dan tijdens doodtij. Omdat de intensiteit van de baggerwerken geen springtij-doodtij variatie kent, stijgt de ligging van top-slib in het Albert II dok met 15 cm/dag tijdens springtij, en daalt het met 5 à 10 cm/dag tijdens dood- en gemiddeld tij. Het volume slib in de haven is ook groter in de winter, met een lagere densiteit. Voor een veilige toegang tot de haven moet een schip minstens 10% van zijn diepgang boven het niveau van de nautische bodem blijven (gedefinieerd als 1200 kg/m^3 in Zeebrugge), en mag het met maximaal 7% van zijn diepgang in het slib varen, waarbij de bovenkant van het slib overeenkomt met de 210 kHz reflector. Deze resultaten wijzen op de mogelijke (en ongewenste) variatie van de nautische toegankelijkheid op de seizoenale en springtij-doodtij tijdschalen, te mitigeren met onderhoudsbaggerwerk.

De onderhoudsbaggerspecie wordt gestort in de Noordzee, wat geregeld is volgens het OSPAR verdrag. Terugstorten op zee kan belangrijke ecologische gevolgen hebben, zoals een verminderde lichtindringing in de waterkolom, of het begraven van benthisch leven. Tracerexperimenten in de jaren ’90 hadden al aangetoond dat recirculatie van gestort materiaal kan plaatsvinden, al kon dat toen niet gekwantificeerd worden. In 2013-2014 werd daarom een veldexperiment opgezet, waarbij de stortlocatie Zeebrugge Oost gedurende één maand werd vervangen door de locatie Zeebrugge West, die verder van de kust is verwijderd. De analyse van dit experiment kon echter niet eenduidig aantonen dat deze relocatie tot een significante daling van de sedimentconcentraties leidde, of tot een vermindering van de retourstroming. Daarom werd dit veldexperiment nagebootst in het numeriek model. De resultaten geven aan dat er wel degelijk een verlaging is van de retourstroming, maar dat het verwachte effect op de sedimentconcentraties zo beperkt is dat het tijdens de meetcampagne niet van de natuurlijke variatie was te onderscheiden. Dit praktijkvoorbeeld toont aan hoe een gecalibreerd model een nuttig instrument kan zijn om een variabele als retourstroom te kwantificeren, die anders moeilijk rechtstreeks te meten is.

Prologue

”What a useful thing a pocket-map is!” I remarked.
”That’s another thing we’ve learned from your Nation,” said Mein Herr, ”map-making. But we’ve carried it much further than you. What do you consider the largest map that would be really useful?”
”About six inches to the mile.”
”Only six inches!” exclaimed Mein Herr. ”We very soon got to six yards to the mile. Then we tried a hundred yards to the mile. And then came the grandest idea of all! We actually made a map of the country, on the scale of a mile to the mile!”
”Have you used it much?” I enquired.
”It has never been spread out, yet,” said Mein Herr, ”the farmers objected: they said it would cover the whole country, and shut out the sunlight! So we now use the country itself, as its own map, and I assure you it does nearly as well.”

Lewis Carroll, *Sylvie and Bruno Concluded*, 1895

1

Introduction

1.1. Socio-economic relevance of fine-grained sediment dynamics

Ports are an important driver for economic activity. For the Port of Zeebrugge, important sectors include the transshipment of liquefied natural gas (LNG), cars and containers. Recently (February 2021), the cities of Bruges and Antwerp have reached a final agreement on the merger between the Port of Antwerp and the Port of Zeebrugge. Upon completion of the merger, the ports will operate under the name Port of Antwerp-Bruges.

Due to significant siltation, frequent maintenance dredging is necessary to ensure the nautical accessibility. For Zeebrugge, that responsibility falls on the maritime access department of the Flemish department of mobility and public works. Over the period 2011-2016, a yearly cost of 71.7 millions of euros was budgeted for the maintenance dredging of the harbors and the access channels of Zeebrugge and Oostende (Rekenhof, 2016). The maintenance dredging for Zeebrugge constitutes about 95% of this total (Lauwaert et al., 2016).

The turbidity can increase significantly in the water column due to the disposal of cohesive sediments. This in turn determines the underwater light climate and the primary production. A high sediment concentration can also influence the functioning of benthic communities (e.g. filter-feeding organisms) (Fettweis et al., 2011).

1.2. Research objective, approach and outline

The first objective of this thesis is to gain a better understanding of the cohesive sediment dynamics in the Belgian part of the North Sea. The physical system is described in chapter 2. Tidal ensembles are derived of frame measurements of velocity and near-bed suspended sediment concentration (SSC), that are later used for model validation. A 1DV point model is set up in chapter 5 that computes the transient vertical distribution of a single fraction of SSC, and the mud content in the bed. This model is used to study the intratidal variation of the near-bed SSC observed at Blankenberge. This analysis shows that a two-fraction (coarse and fine) sediment model is necessary to model both the the ebb and the flood peak of SSC.

Subsequently a 3D sediment transport model is set up. The settling velocity of the coarse and fine fraction are taken over from the 1DV model, as is the zero order resuspension constant. The set of measurements that is available for model calibration and validation is maximized by using both the comparable tide method (introduced in appendix C) and tidal ensembles. The calibration of the model is done using a dimensionless cost function (defined in appendix A) that synthesizes model skill against measured time series, maps and tidal ensembles.

The 3D model is used to study the role of salinity-driven baroclinic effects on the formation of the Coastal Turbidity Maximum (CTM). More in general, the model confirms that the local hydrodynamic conditions trap sediment in the CTM. A sediment balance derived from the model is used to better understand the recent results of Adriaens et al. (2018), in particular why the recent mud deposits in the Belgian Coastal Zone (BCZ) have a different clay mineralogical composition than the English Channel mud sources, even though the residual sediment transport through the Dover Strait is an important sediment supply to the BCZ.

The second objective is to study the mud dynamics in the harbor of Zeebrugge. Chapter 3 introduces a geometric decomposition of water and sediment exchange across a harbor entrance into three main components: the cross-sectional average and the horizontal and vertical exchange flow. The application of this method to measurements at the entrance of the harbor of Zeebrugge shows the relative importance of horizontal exchange.

Chapter 4 describes the mud dynamics in the harbor of Zeebrugge based on data analysis. It establishes three important timescales: the intratidal, spring-neap and seasonal timescale. No evidence is found that daily siltation rates in the harbor correlate significantly with wave or wind conditions in the North Sea, or fresh water inflow into the harbor. On the intratidal timescale, most of the sediment exchange occurs from two hours before high water to high water.

The material that is dredged in the harbor is disposed in the North Sea. In situ tracer experiments in the 90's had indicated that recirculation could occur, although it could not be quantified, due to uncertainties in the interpretation of the experiments. In 2013-2014, a field trial was setup in which the disposal location Zeebrugge Oost was changed for one month to location Zeebrugge West. The field campaign could not show unambiguously however, that the relocation resulted in either a decrease in the suspended sediment concentration (SSC), or a reduction of the siltation inside the harbor (Fettweis et al., 2016). Therefore a numerical experiment is setup in chapter 6 to quantify the return flow from both locations ZBO and ZBW.

References

Adriaens, R., Zeelmaekers, E., Fettweis, M., Vanlierde, E., Vanlede, J., Stassen, P., Elsen, J., Środoń, J., and Vandenberghe, N. (2018). Quantitative clay mineralogy as provenance indicator for recent muds in the southern North Sea. *Marine Geology*, 398:48–58.

Fettweis, M., Baeye, M., Cardoso, C., Dujardin, A., Lauwaert, B., Van den Eynde, D., Van Hoestenberghe, T., Vanlede, J., Van Poucke, L., Velez, C., and Martens, C. (2016). The impact of disposal of fine-grained sediments from maintenance dredging works on SPM concentration and fluid mud in and outside the harbor of Zeebrugge. *Ocean Dynamics*, 66(11).

Fettweis, M., Baeye, M., Francken, F., Lauwaert, B., Van den Eynde, D., Van Lancker, V., Martens, C., and Michielsen, T. (2011). Monitoring the effects of disposal of fine sediments from maintenance dredging on suspended particulate matter concentration in the Belgian nearshore area (southern North Sea). *Marine Pollution Bulletin*, 62(2):258–269.

Lauwaert, B., De Witte, B., Devriese, L., Fettweis, M., Martens, C., Timmermans, S., Van Hoey, G., and Vanlede, J. (2016). Synthesis report on the effects of dredged material dumping on the marine environment (licensing period 2012-2016). Technical report, RBINS-OD Nature/ILVO/aMT/aKust/WL, Brussels.

Rekenhof (2016). Baggerwerken in Vlaanderen. Technical report, Rekenhof, Brussels, Belgium.

2

Description of the physical system

The combination of strong tidal currents and waves on very heterogeneous sediments [...] make the problem of sediment dynamics in this area particularly challenging. In 1928, H. Kaufmann wrote about this problem ”Anyone who embarks on this investigation will soon discover that he has arrived in a strange world. Cause and effect are dancing around frantically; understanding the phenomena seems an elusive goal. Even the lights of science - such trustworthy beacons - can flicker unexpectedly. If we hope to emerge from this enchanting castle with a clear head, we must tread carefully and stay close to the observations.”

H.Kaufmann (1928) in Bastin (1974), translation by the author

2.1. Introduction

This chapter consists of two main parts. Sections 2.2 to 2.10 are a literature review covering the hydrodynamics (tides and waves) and the sediment properties, sources and transporting agents, and the resulting sediment distribution.

The second part consists of original data analyses, first of nine years of dredging and disposal data in section 2.11, and then of nine years of field observations of near-bed velocity and suspended sediment concentration (SSC) in section 2.12. Inevitably, there is some overlap between both parts.

2.2. The North Sea

The North Sea can be classified as a ”marginal sea”, that is, intermediate between the Mediterranean sea with a circulation that is mainly determined by internal dynamics and coastal regions of open oceans. In contrast to marginal seas with a mean depth over 1000 m, the North Sea has a relatively small depth, which largely determines its properties. More or less similar conditions can be found in the East China Sea, the northern part of the Adriatic Sea or the Gulf of Maine (Otto et al., 1990).

Large parts of the Southern Bight are shallow (water depth <30 m), so that material on the bed can be picked up by large waves and swell. Turbidity therefore increases during stormy periods and is generally higher during the winter and early spring (Eisma and Kalf, 1979). The effect of storms on suspended particulate matter (SPM) is described in section 2.9.

2.3. Tides in the North Sea

The dominant feature in the horizontal dynamics of the North Sea is tidal motion (Otto et al., 1990). As an illustration the M2 co-tidal chart of Proudman and Doodson (1924) is given in figure 2.1. This chart shows three amphidromic points: one at the southern tip of Norway, one at 56°, and one in the Southern Bight. The theoretical explanation of this pattern is given by Taylor (1922) for a channel in a rotating frame of reference which is open at one end and in which Kelvin waves propagate without friction (Pugh, 1987).

The residual circulation through the strait of Dover is of particular interest for the zone of interest. It is composed of three components: a tidal residual flow, a flow due to the long-term difference in mean sea level between the English Channel and the North Sea, and a wind- driven residual flow (Visser et al., 1991). Prandle et al. (1996) calculated a mean residual discharge of 94.000 $m^3\,s^{-1}$, about half of which of which is due to wind effects. This residual current drives net sediment transport through the strait of Dover, which is discussed in section 2.7.1.

The mean amplitude of a spring (neap) tide at Oostende is 4.6 m (3.0 m). The high tidal amplitudes and tidal velocities (maximum $>$ 1.0 m/s) result in generally well mixed waters (Fettweis et al., 2006). The tidal current ellipses are more elongated in the coastal zone (e.g. at Blankenberge in figure 2.19), and are more elliptical further offshore (e.g. at MOW1 in figure 2.20).

2.4. Wave climate

The Belgian coastal zone is a relatively sheltered area in the southern part of the North Sea. The overall wind climate is dominated by Southwesterly winds, followed by winds from the NE sector. Even though maximum wind speeds occur in the southwesterly sector, the highest waves are generated under northwesterly winds (Baeye, 2012).

Waves become important in resuspension of bed sediments when significant wave heights exceed 1.5 m, corresponding to a wave orbital velocity U_w of 0.3 m/s in a water depth of 10 m and with the JONSWAP spectrum of waves (Fettweis and Nechad, 2011; Baeye, 2012).

Water particles generally move in elliptical paths in very shallow water or water of intermediate depth, and in circular paths in deep water (see figure 2.2). For

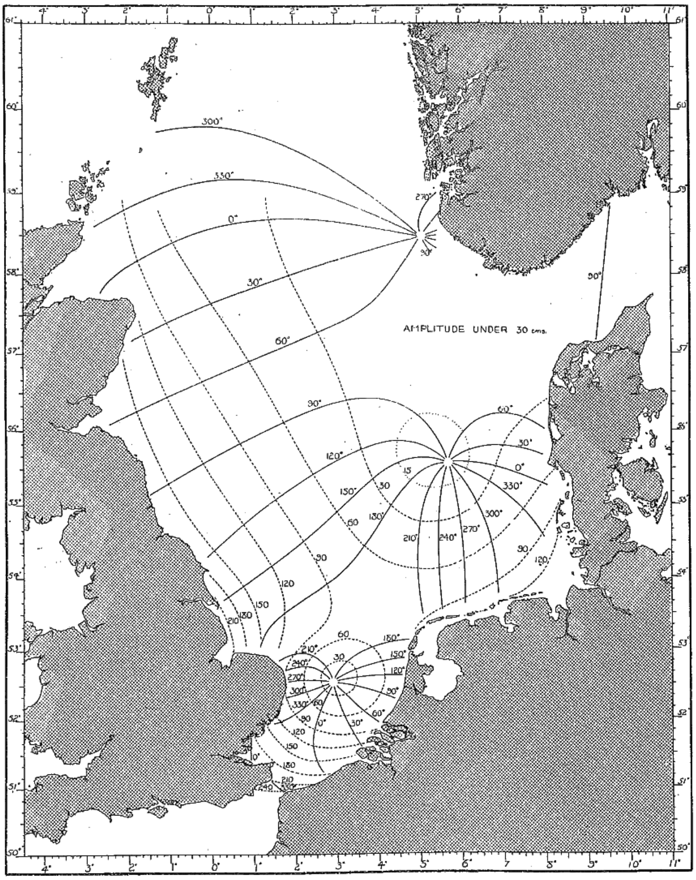

Figure 2.1: Co-tidal lines (degrees) and co-range lines (amplitudes in cm) of the M2 tide in the North Sea (Proudman and Doodson, 1924).

shallow regions, horizontal orbital velocities near the bottom can be large, and can play an important role in sediment resuspension.

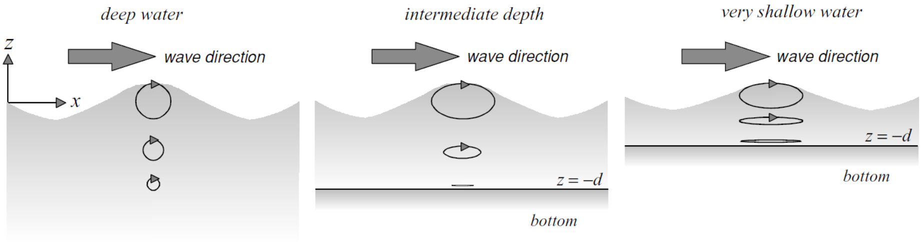

Figure 2.2: The orbital motion in deep water, intermediate-depth water and very shallow water (Holthuijsen, 2007).

Waves are classified as deep water, transitional water and shallow waver waves depending on the value of h/L (CERC, 1984):

- Deep water: $h/L > 1/2$
- Water of intermediate depth : $1/25 < h/L < 1/2$
- Shallow water: $h/L < 1/25$

with h the water depth, and L the wave length, which can be determined from the (implicit) dispersion relationship 2.1:

$$L = \frac{g\,T_p^2}{2\pi} tanh\left(\frac{2\pi h}{L}\right) \tag{2.1}$$

A typical wave climate in the North Sea, with a wave period T_p of 5 s, in water depth of 10 m, corresponds to a wave length of 37 m. The zone of interest can be classified as water of intermediate depth ($h/L = 0.28$), which means waves have a significant influence on the bed shear stress, and hence on sediment resuspension. This is confirmed in the data analysis of wave influence on near-bed SSC in section 2.12.2.

2.5. Salinity

The strong tidal currents and the low freshwater discharge of the Scheldt (yearly average is typically in the range 50 - 150 m³/s) result in a well-mixed water column in the Belgian coastal zone, with very small salinity and temperature stratification (Fettweis and Nechad, 2011).

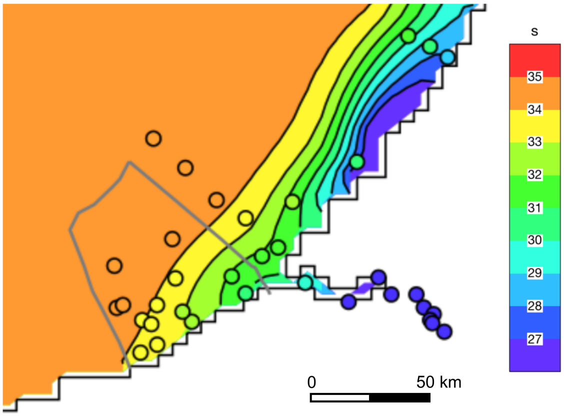

Figure 2.3: Surface salinity averaged over 1993-2002 from model results (background) and measurements (colored dots). The Belgian Exclusive Economic Zone is delimited by the solid line (Lacroix et al., 2004).

Figure 2.3 shows the salinity in the Belgian-Dutch coastal zone. There is a band of fresher water close to the coast, which is a mixture of water from the English

Channel and the North Sea with the outflow of the Scheldt and the Rhine/Meuse. The observations clearly show a horizontal salinity gradient perpendicular to the Belgian coast. Simulation results have shown that the freshwater, which induces this horizontal salinity gradient in the Belgian Coastal Zone (BCZ), originates primarily from the Rhine/Meuse outflow, with a smaller influence from the Scheldt estuary (Lacroix et al., 2004).

The buoyancy effect due to lateral density gradients results in an important onshore contribution to the residual flow near the bottom (Van Der Giessen and De Ruijter WPM, 1990). This is discussed further in section 2.8.2. The strength of this circulation is related to the horizontal density gradient so that it is generally stronger in winter than in summer (Visser et al., 1991).

2.6. Measurements of sediment properties

2.6.1. Critical shear stress for erosion

Erodibility measurements were performed in 2007-2008 on a total of 35 sediment samples in the nearshore zone in the framework of the Quest4D project. The sampling methodology consisted of box cores, which were carefully subsampled with cylindrical tubes (diameter 13.5 cm) in order to retrieve relatively undisturbed samples of the first 40 cm of the sea bed. The samples were analyzed for erodibility at the University of Stuttgart using the SETEG-flume (Witt and Westrich, 2003).

Figure 2.5 shows the measured depth profile of bulk density ρ_b and the critical shear stress for erosion ($\tau_{cr,e}$) of two selected cores: one with Holocene mud (core III/C4 from February 2008), and one with freshly deposited mud (core II/C1 from October 2007). Their locations are indicated in figure 2.4.

The profiles show the high variability of $\tau_{cr,e}$. Core III/C4 is characterized by a 5 cm thick surface layer of freshly deposited mud above soft to medium-consolidated mud. The Holocene mud deposits underneath are characterized by intercalations of thin sandy and shell layers. The Holocene mud layers show a higher resistance to erosion, with a $\tau_{cr,e}$ up to 13 Pa. The intermediate sandy layers on the other hand, exhibit a much lower $\tau_{cr,e}$ ($\sim$ 1 Pa) and a higher bulk density. This layered structure is typical for alternations of storm and calm weather periods and/or spring-neap tidal cycles. Core II/C1 is believed to consist of freshly deposited mud. The upper 45cm have a $\tau_{cr,e}$ of 1 to 4 Pa (Fettweis et al., 2010).

2.6.2. Settling velocity

Measurements to determine the in situ settling velocity were performed in spring tide conditions during three consecutive days in November 2006, using the INSSEV measurement system inside the harbor (see figure 2.6 for the locations). The sampling height was 65cm above the bed.

INSSEV measurements provide data on floc size, settling velocity and effective density of the sediment near the bed by observing size and settling velocity with a video-based technique that can observe individual macroflocs and microflocs. In addition, near-bed turbulence is measured with an acoustic doppler velocimeter and the turbidity is monitored by an array of optical backscatter sensors. An ADCP pro-

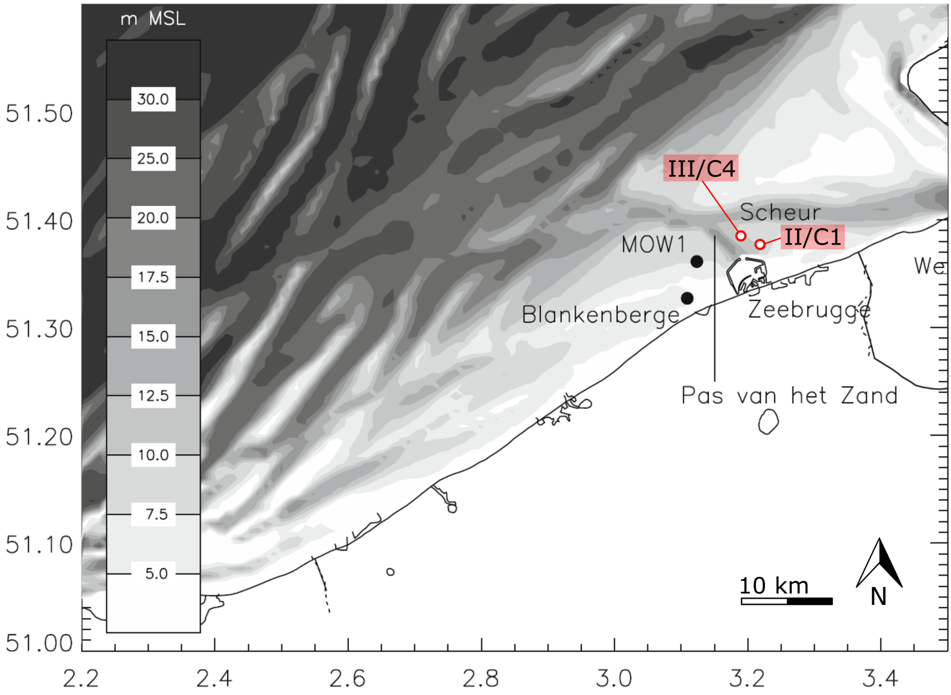

Figure 2.4: Location of two box-core samples for erosion behavior measurements (red dots). Redrawn from Fettweis et al. (2010).

vides additional velocity data. For more information on the measurement setup, the reader is referred to Manning and Dyer (2007) and IMDC (2007). Based on similar measurements in the Tamar (UK), Gironde (France) and Dollard (the Netherlands) estuaries, Manning and Dyer (2007) have formulated an empirical relationship between the settling velocity for macroflocs w_s^{macro}, turbulent shear stress and suspended sediment concentration. The results of this model are shown in dashed lines in figure 2.7. More recently, McAnally et al. (2021) analyzed a similar INSSEV dataset from the Tamar estuary (UK), and attributed part of the variation of settling velocity to hysteresis in the relation between turbulent shear and settling velocity in a tidal environment, with different relations during erosional and depositional phases.

The settling velocity for macroflocs ($> 160\mu m$) in the harbor is presented in figure 2.7. Macroflocs tend to have the most influence on the mass settling flux, as they have the highest settling velocity. Macroflocs represented on average 94.5% of the mass concentration and 99.5% of the mass settling flux during this measurement campaign. Their average excess density was 131 kg/m³. The floc observations in figure 2.7 illustrate the wide range in settling velocities w_s^{macro} (1 to 10 mm/s) measured inside the harbor during spring tide conditions. The survey also identified how rapidly the settling and floc mass distributions changed, particularly

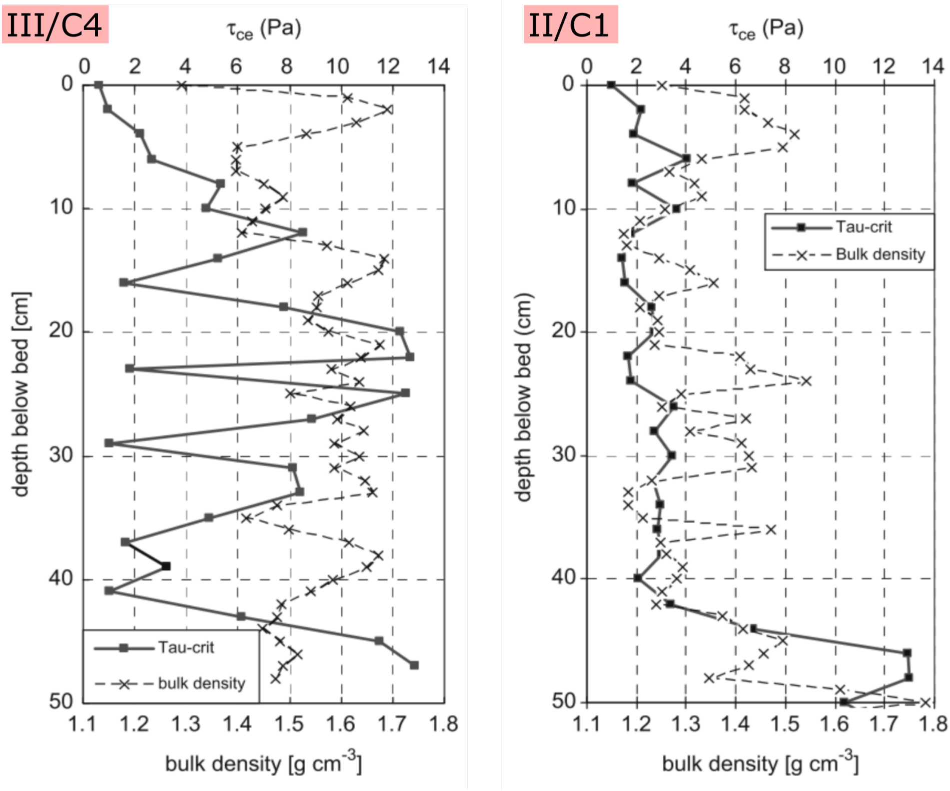

Figure 2.5: Depth profile of critical erosion shear stress $\tau_{cr,e}$ (full line) and bulk density ρ_b (dashed line) of two box cores. Left panel: 7 cm of soft mud above 40 cm of medium-consolidated mud (Holocene) with intercalations of sand, muddy sand and shell layers. Right panel: 40 cm of soft mud on top of medium- consolidated Holocene mud (Fettweis et al., 2010).

in response to rising shear stress and decreasing concentration.

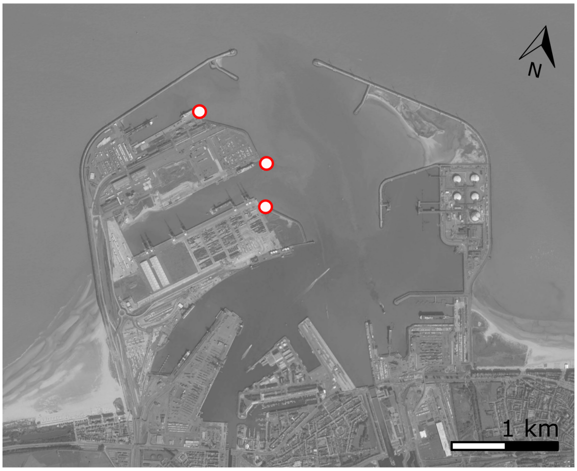

Figure 2.6: INSSEV Flocculation Survey Locations – November 2006.

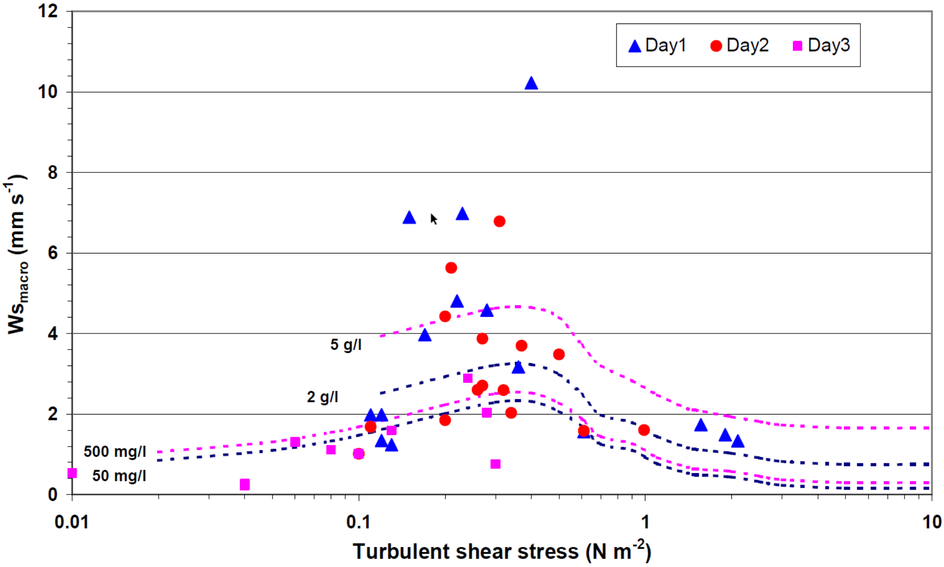

Figure 2.7: w_s^{macro} for each survey day against the corresponding shear stress (IMDC, 2007). The dashed lines indicate w_s^{macro} from the empirical model of Manning and Dyer (2007).

2.7. Sources of sediment

There are multiple ways in which suspended sediment can enter the French-Belgian-Dutch nearshore area. The main sources include net transport over the seaward boundary, sea floor erosion and sediment supply from rivers. The literature review in the following section cites the different estimates of each source in MTDM/yr (Million Tonnes of Dry Matter per year). It also shows that the processes driving both the coastal turbidity maximum (CTM) and the cohesive mud deposits are still under debate.

2.7.1. Residual sediment transport through the Dover Strait

Extensive scientific literature on the residual SPM transport through the Dover Strait exists. The values cited below for the yearly average supply of SPM from the Channel vary in the range [11.5 - 44] MTDM/yr. These big differences partially reflect the high temporal and spatial variability of the influx, but also have their origin in the way the SSC measurements were carried out, in the small number of SSC measurements on which the calculations were based, as well as in the differences in the way the residual SPM transport was calculated (Fettweis et al., 2007). A selection of reported estimates is listed below to illustrate the range. The reader is referred to Fettweis and Van den Eynde (1999) for a more complete list of references.

Eisma and Kalf (1979) estimate the yearly average suspended matter influx through the Dover strait to be in between 11.5 and 15 MTDM/yr. van Alphen (1990) estimates the total transport through Dover strait to be 17 MTDM/year. McManus and Prandle (1997) estimate the supply through Dover strait at 44 MTDM/yr by combining model results and measurement data from the North Sea Project (1987-1992). Concentrations across the strait of Dover have a seasonal variability, with winter concentrations both in coastal and offshore waters higher than in summer (Visser et al., 1991).

Following Eisma (1981), van Alphen (1990) estimates the long term year-averaged suspended matter transport from Dover strait to Belgian-Dutch waters as half of the total transport through Dover strait, or 8.5 MTDM/year. The mud balance by van Alphen (1990) (see figure 2.8) shows the supply through Dover strait as the dominant factor in the mud transport through the Belgian and Dutch coastal zone. This mud balance does not contain the maintenance dredging of Zeebrugge harbor.

More recently, Fettweis et al. (2007) estimated the yearly average SPM transport through the Dover Strait using a combination of satellite images (SeaWiFS), in situ measurements and a 2D hydrodynamic numerical model as 32 MTDM/yr from which about 40% flows through the English and 60% through the French part of the Strait. This corresponds to a The northeastward residual sediment flux of 19.2 MTDM/yr in the Belgian coastal zone, which is used as a calibration target for the numerical model in section 5.12.1.

2.7.2. Sea floor erosion

By comparing successive depth charts of the area, Gossé (1977) estimates the mud input from the Flemish banks to be between 0 and 2.4 MTDM/year. Because

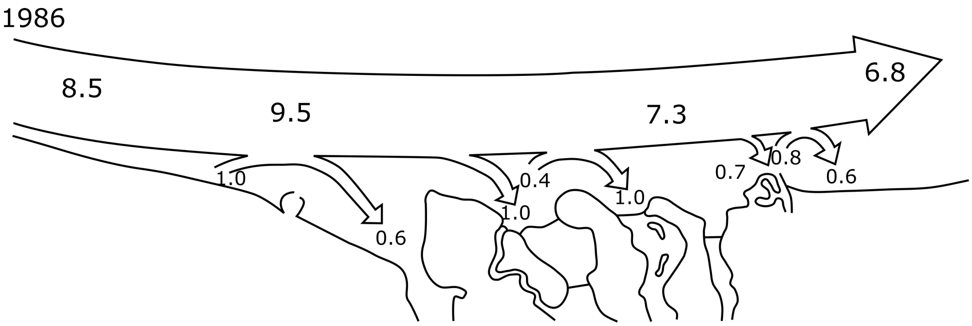

Figure 2.8: Mud balance for 1986 in MTDM per year (redrawn from van Alphen, 1990). The width of the arrows is proportional to the amount of mud transport.

they consist mainly of sandy material however, Fettweis and Van den Eynde (1999) dismiss them as a significant source for mud.

Some studies have considered the local erosion of Quaternary (Holocene to Pleistocene) (Baeteman, 1999; Bastin, 1974) or Tertiary clays (Gullentops et al., 1977). These layers are not easily erodible however, as argued in section 2.6.1: erosion measurements show a higher resistance to erosion for the Holocene layers, with a $\tau_{cr,e}$ up to 13 Pa.

Harbor extension works have been carried out in the period 1979 to 1986. Subsequently, the access channels Scheur West, Scheur East and Pas van het Zand have been deepened in the period 1986-2000, as shown in the right panel of figure 2.9. The left panel of figure 2.9 shows the bathymetric evolution of the sea bed over 42 years (1970-2011). Most of the erosion east and west of the access channel "Pas van het Zand" (indicated in the black polygons next to the access channel) has occurred in the period 1983-1997.

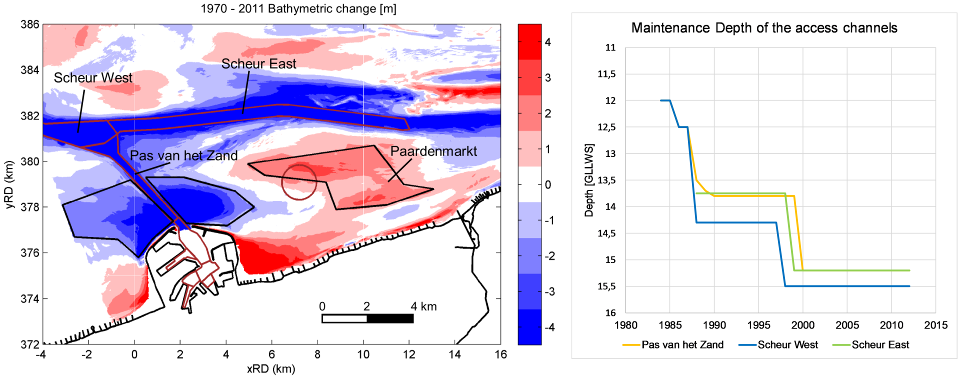

Figure 2.9: Left panel: bathymetric evolution (erosion/fairway deepening in blue) between 1970 and 2011 (De Maerschalck et al., 2017). Right panel: evolution of maintenance depth of the access channels between 1984 and 2012 (Vroom and Schrijvershof, 2015).

Human interventions in the 80's and 90's (harbor extension works of Zeebrugge and channel deepening) have triggered an important morphological response, with reworking of sediment. Over the area where box-cores show the presence of medium-consolidated (Holocene) mud, the erosion flux is estimated at maximally 2.3 MTDM/yr (Vroom et al., 2016). This is an upper estimate, since it is known that the Holocene mud deposits are not pure mud, but are intercalated with sand and shell fragments (see section 2.6.1). Since the area in front of the harbor has become morphologically more stable after 2000, the importance of this source term has diminished over time however.

Recently Adriaens et al. (2018) used the quantitative clay mineral composition ($<2\mu m$) as a provenance indicator for mud in the southern North Sea. They found that the clay mineralogical composition of weakly- and medium consolidated mud from the Belgian Coastal Zone (BCZ) is similar to the composition of the suspended matter in the BCZ and the Dutch nearshore. This is consistent with a residual sediment transport towards the northeast (see also section 2.8.1).

English Channel sources have a distinct clay composition, with 10–30% less smectite than what is found in the BCZ. This means that, even though the net sediment influx through the Dover strait is an important sediment input in the Southern North Sea (as discussed in section 2.7.1), it is not the dominant sediment supply for SPM in the BCZ.

The strong connection between the location of the mud deposits and that of the coastal turbidity maximum can be explained in terms of sediment exchange between the bed and the water column. On the one hand, local hydrodynamic conditions trap SPM in the Belgian coastal zone (see section 2.8.1), which leads to a higher mud content in the bed through deposition. On the other hand, erosion and resuspension increase the local suspended sediment concentration. The importance of local deposition and resuspension on the mud balance in the BCZ is further discussed based on model results in section 5.12.1.

The presence of mud deposits in the BCZ was already indicated on the maps of Van Mierlo (1899) in a similar location, which shows the persistence of the mud fields, and the fact that they are not caused by the (significant) human interventions in the area.

2.7.3. Sediment supply from rivers

Eisma (1981) estimate the total river supply to the North Sea at 4.5 MTDM/yr. For the rivers that enter the southern bight, Eisma and Kalf (1979) estimates a sediment load of 2 MTDM/yr. Only a negligible amount of the mud supplied by the river Scheldt escapes to the sea, and a net deposition of marine mud of 0.6 MTDM/yr is assumed in the Western Scheldt according to van Alphen (1990) (see figure 2.8).

2.7.4. Other sources

Eisma and Kalf (1979) estimates the supply from primary production at less than 1 MTDM/yr. The atmospheric supply is estimated at 1.6 MTDM/yr (Eisma, 1981). McCave (1973) estimates the input from coastal erosion at 0.7 MTDM/yr.

2.8. Transporting agents of sediment

2.8.1. Tidal currents

Asymmetries in tidal velocity directly control net sediment transport patterns. This section discusses both tidal current asymmetry (peak flow and slack duration asymmetry) and the residual current, and their effect on suspended sediment transport in the Belgian coastal zone.

Tidal current asymmetry

For fine suspended sediment in starved bed conditions, slack duration asymmetry induces residual transport. If the duration of slack water after flood (or high water slack) exceeds the duration of slack water after ebb (or low water slack), a residual sediment transport in flood direction occurs because there is more time for sediment to settle out after flood (Groen, 1967; Dronkers, 1986; Wang et al., 1999). This effect is also known as temporal settling lag, since it relies on a time lag in the relationship between stress and concentration. Since the timescale for erosion and sedimentation is longer for finer sediment, it is more sensitive to slack duration asymmetry than coarse sediment. (Friedrichs, 2011; Burchard et al., 2018).

An asymmetry in the maximum flow (or peak flow asymmetry) can also induce residual transport of sediment for any relationship in which the sediment transport rate is proportional to a power of the velocity (Friedrichs and Aubrey, 1988). For capacity, or near-capacity conditions the sediment transport is proportional to U^4, since it can be shown that the capacity (or saturation) concentration is proportional to U^3 (Winterwerp, 2001).

This means that for fine-grained sediments, both peak flow and slack duration asymmetry may be important, depending on the sedimentological status (i.e. starved bed or capacity conditions) of a system (Winterwerp, 2003).

Assuming a channel with a depth-averaged velocity that is composed of a semi-diurnal component and its first overtide (equation 2.2)

$$U = U_2 \cos(\omega t - \phi_2) + U_4 \cos(2\omega t - \phi_4) \tag{2.2}$$

where U_2 and U_4 are the velocity amplitude, and ϕ_2 and ϕ_4 the phase angles of the M_2 and M_4 tide, and ω is the frequency of the M_2 tide, then the phase lag between the M_2 and M_4 component of the velocity is expressed as:

$$\theta_U = 2\phi_2 - \phi_4 \tag{2.3}$$

The duration of high water slack exceeds that of low water slack when $0^\circ < \theta_U < 180^\circ$, which corresponds to a residual sediment transport in the flood direction due to temporal settling lag.

The peak flood velocity exceeds the peak ebb velocity when $-90^\circ < \theta_U < +90^\circ$, corresponding to residual sediment transport in the flood direction due to asymmetry in the magnitude of maximum flow.

Vroom et al. (2016) apply this conceptual framework to the 2D hydraulic simulations of Verduin (2009) to study tidal asymmetry in the Wielingen and Scheur channel in front of the harbor of Zeebrugge (indicated with crosses in the top panel of figure 2.10). In order to analyze tidal asymmetry, the depth-averaged velocity is decomposed into an along channel component and a component perpendicular to the channel. The along-channel component is then harmonically analyzed.

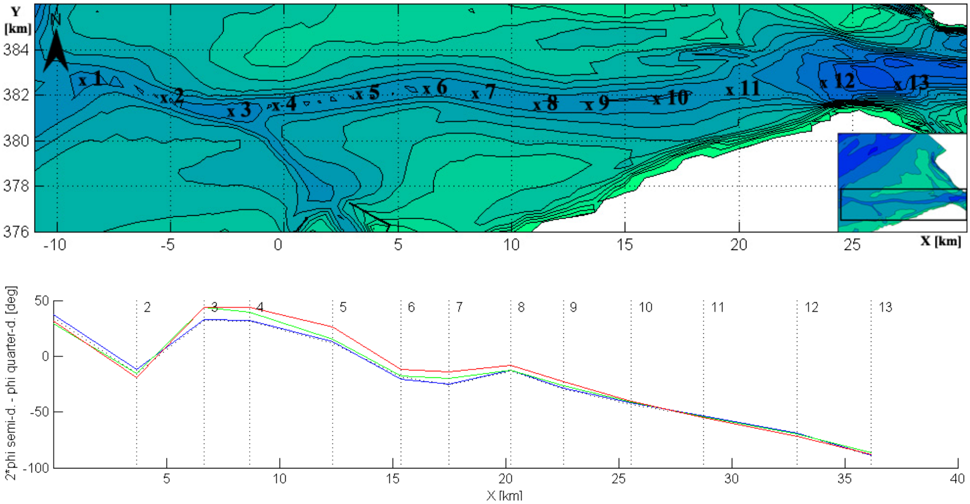

Figure 2.10: Location of the output stations (top panel), relative phase of the along-channel velocity magnitude (bottom panel). Simulation results for 1970 in blue, for 1983 in green and for 2002 in red (Verduin, 2009).

The results in the bottom panel of figure 2.10 show that the tidal asymmetry of the horizontal tide has not been impacted significantly by the human interventions in the 80's and 90's (harbor extension works of Zeebrugge and channel deepening, see also section 2.7.2).

Along the Scheur en Wielingen channel, the peak flow asymmetry is flood dominant, since $-90^\circ < \theta_U < +50^\circ$ for points 1-13. The slack tide asymmetry changes sign in the vicinity of the harbor. It is flood dominant west of Zeebrugge ($\theta_U > 0^\circ$ for points 1,3,4,5) and ebb dominant east of it. This leads to the convergence of fine sediments in front of the harbor. As noted before, slack tide asymmetry relies on the time lag between stress (or velocity) and concentration. At station Blankenberge this time lag is small however (see section 2.12.2), so the slack tide asymmetry might well be overshadowed by the peak flow asymmetry.

It is also important to note that flow in a coastal zone typically follows a tidal ellipse. Vroom et al. (2016) analyze only the along-channel component of the velocity. To the best of our knowledge, there is no accepted theory that extends the harmonic decomposition of equation 2.2 and the subsequent analysis of tidal asymmetry to tidal ellipses.

Residual current

The residual flow in the Belgian coastal zone is directed to the northeast near the coastline. The Eulerian residual water transport $\overrightarrow{u_{res}}$ is calculated as:

$$\overrightarrow{u_{res}} = \frac{\int_0^{kT} h\vec{u}}{\int_0^{kT} h} \tag{2.4}$$

where $\vec{u}$ and h are the instantaneous flow velocity and water depth, respectively. T is the tidal period, and k stands for the number of tides over which the residual flow is calculated.

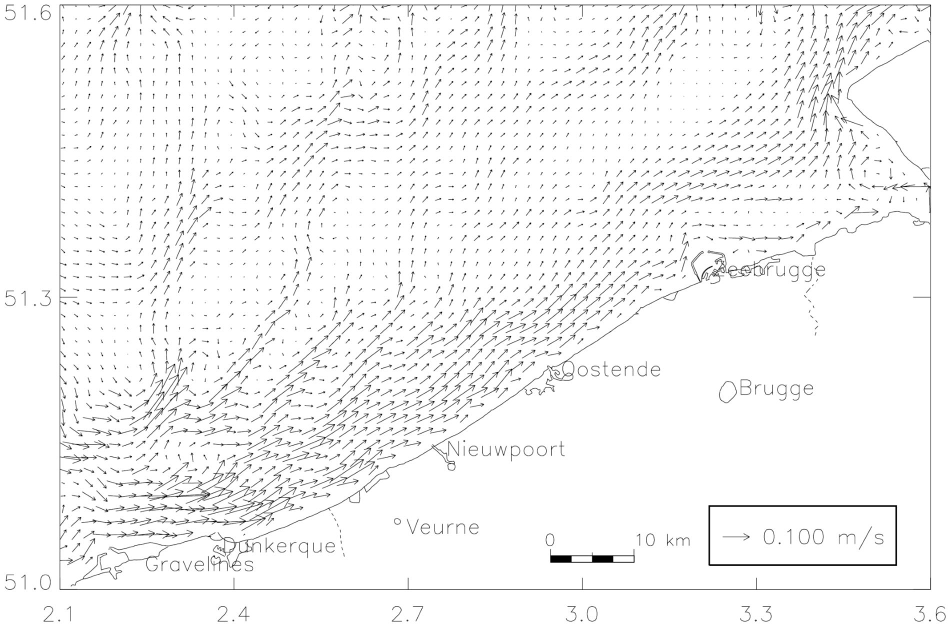

Figure 2.11: Residual (water) transport as computed with the Mu-BCZ model (Van den Eynde, 1999).

Figure 2.11 shows the simulated residual transport, computed over one month, without wind influence (Van den Eynde, 1999). Closer to the coast, the residual transport is larger than further offshore. Fettweis and Van den Eynde (2003) mention the decreasing residual water transport vectors between Oostende and Zeebrugge as a contributing factor to the presence of the CTM.

Nihoul and Ronday (1975) simulated the residual flow directly by solving the 2D continuity and momentum equations, averaged over multiple tidal cycles. They introduce a tidal stress term that is estimated from another, transient circulation model. Their residual flow model shows a clockwise residual circulation pattern in the Belgian coastal zone (BCZ). The residual gyre was subsequently used to explain the higher suspended sediment concentrations in the BCZ through entrainment of turbid Scheldt water and increased residence times (Nihoul, 1975; Gullentops et al., 1977; Eisma and Kalf, 1979). More recent models with a higher resolution (see e.g. figure 2.11) do not show such a large gyre in the residual water transport pattern (Fettweis and Van den Eynde, 2003; Vroom et al., 2016). Also in the numerical model that was developed in the framework of this study (see chapter 5), such a residual gyre was not found.

2.8.2. Density currents

Salinity-driven baroclinic effects on the flow are known to have an influence on the distribution of sediments. Horizontal salinity gradients generate salinity-driven currents near the bottom that point towards the fresher water.

In the Belgian coastal zone, there is a clear horizontal salinity gradient with fresher water near the coast (see section 2.5). The resulting residual current near the seabed is directed towards the coast. Since higher SSC occurs close to the bottom, this baroclinic current leads to increased turbidity in the near-shore area. Recent numerical work confirms this effect (see section 5.10.3 and van Maren et al. (2020)).

In comparison, sediment-induced density currents only have a limited impact on the residual current, and the sediment distribution in the Belgian coastal zone (van Maren et al., 2020).

2.8.3. Wind driven residual flow

Van den Eynde (1999) showed the impact of wind on the residual current patterns in the BCZ. Wind towards the north enhanced the computed residual transport, while wind towards the south decreased the residual transport vectors.

Baeye et al. (2011) studied the influence of wind on residual current and SSC using long-term observations at location Blankenberge (see figure 2.17 for the location). They found that wind-driven alongshore advection has a significant influence on SSC. Winds coming from the southwest decrease the SSC. This is related to the advection of less turbid English Channel water to the measuring location. North-easterly winds induce a subtidal (residual) flow towards the southwest, which leads to an increase in near-bed SSC, and to the formation of high concentration benthic suspensions (HCBS) layers around slack tide at station Blankenberge.

De Maerschalck et al. (2020) extended the analysis of Baeye et al. (2011) on the impact of wind on subtidal flow, and found that the impact of wind on subtidal flow is non-linear, with a stronger effect for stronger winds (see figure 2.12). Furthermore, of the three locations (MOW1, Blankenberge and WZ Buoy), the relation was most pronounced at Blankenberge, which might be due to the fact that Blankenberge is the shallowest measurement location of the three.

2.9. Effect of storms

Suijlen and Duin (2002) present an atlas of near-surface suspended matter concentrations based on the DONAR dataset from 1975 to 1983. They show that wave height is an important factor for SSC in the Dutch Coastal Zone, with high con-

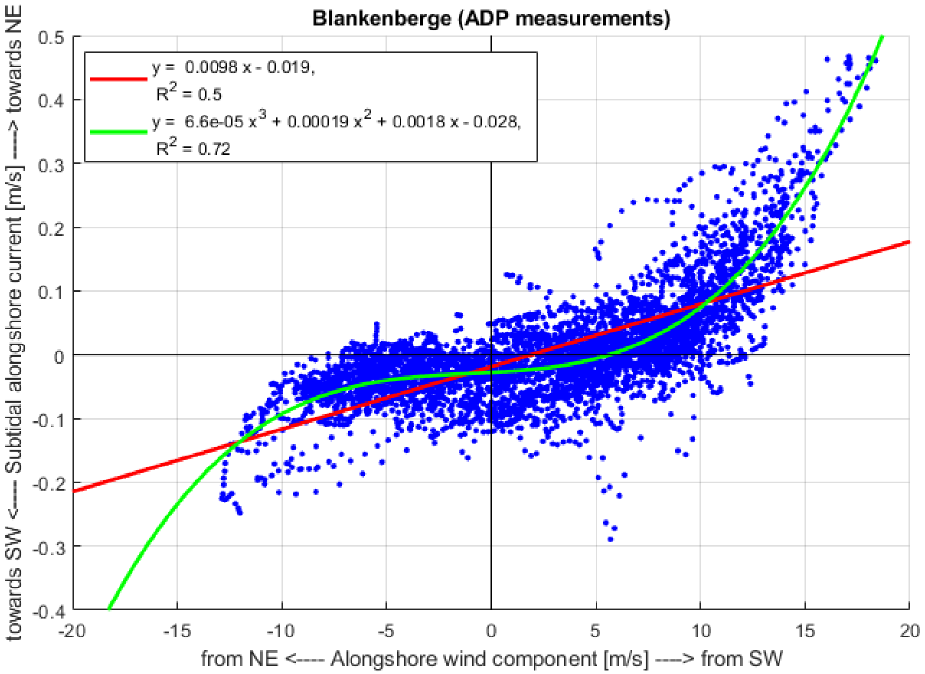

Figure 2.12: Relation between subtidal alongshore flow and alongshore wind at Blankenberge (De Maerschalck et al., 2020).

centrations during the stormy winter periods and low concentrations during calm summer periods. This is illustrated in figure 2.13, which in the left panel shows the average surface concentration 1-3 days after a storm. The right panel shows the average surface SSC during calm summer conditions.

Figure 2.14 shows measurements at Blankenberge during a northwestern storm with significant wave heights up to 2.7 m. Suspended sediment concentrations increase close to the bottom, but *decrease* higher in the water column. Vertical mixing is clearly suppressed here, which is probably a consequence of turbulence damping by vertical gradients in sediment concentration (Winterwerp and Van Kessel, 2003). These data suggest that fluid mud layers can occur near the seabed in the CTM of the Belgian–Dutch nearshore zone during and after a storm in locations were significant amounts of fine-grained sediments can be resuspended (e.g. navigation channels and disposal grounds of dredged material).

Liquefaction of soft mud layers could form fluid mud in a short time interval (in the order of minutes). Winterwerp et al. (2012) however tested a series of samples with bulk densities ranging from 1320-1790 kg m^{-3}, and found no evidence of liquefaction in cyclical triaxial tests. This would leave only the softest mud layers corresponding to freshly deposited mud possibly subjected to liquefaction under storm conditions. A more plausible explanation for the formation of fluid mud would

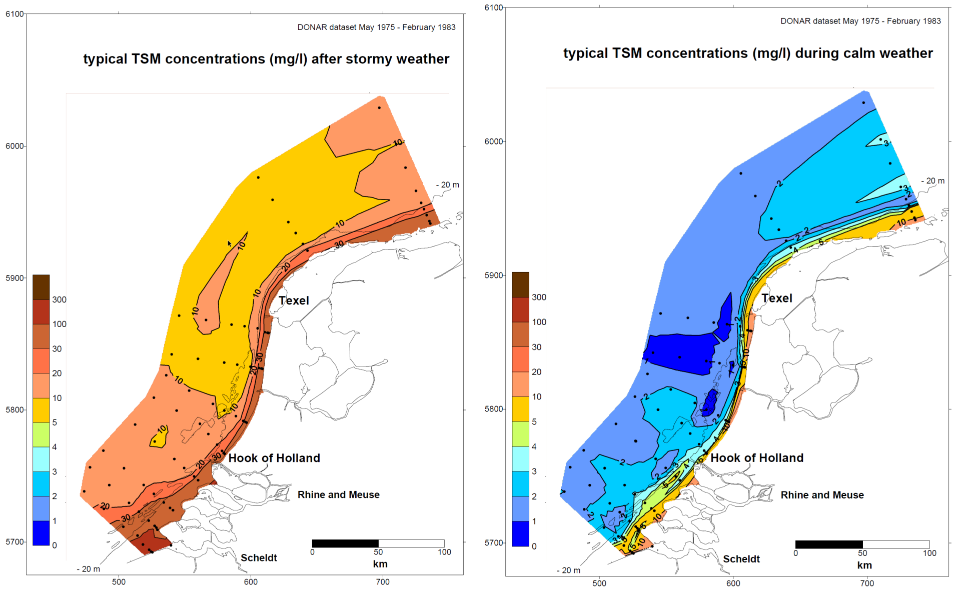

Figure 2.13: Map of the Dutch coastal zone, showing observed SSC after stormy weather (left) and during calm summer weather (right) (Suijlen and Duin, 2002).

be through deposition of mud that was eroded during the storm (Winterwerp et al., 2012; Li and Mehta, 2000).

Erosion of more consolidated muds in stormy conditions could occur by mass failure (Li and Mehta, 2000). In that mode of failure, bed material clasts are dislodged and the bed becomes pitted. Mud pebbles are an indication of this type of erosion, and have been observed in the BCZ (Fettweis et al., 2009).

2.10. Sediment distribution

2.10.1. Bed composition and mud content

Van Lancker et al. (2007) published a map of the distribution of the silt/clay percentage in the Belgian coastal zone (see figure 2.15). Grain-size data were derived from the sedisurf@ database, which is hosted by the Renard Centre of Marine Geology at Ghent University (Verfaillie et al., 2006). Note the occurrence of patches of high mud content (50-100%) close to the coast, to the east of Oostende. The presence of mud deposits in the BCZ was already indicated on the maps of Van Mierlo (1899) in a similar location. They are also present in the reconstruction of the nearshore sedimentary environment in the period 1900-1910, based on the historical Gilson collection (Houziaux et al., 2011).

The cohesive sediments in the BCZ consist of three types with variable thickness (Fettweis et al., 2009): fluid mud, periodically forming the uppermost layer with a density of 1100 kg m^{-3} to 1200 kg m^{-3}, weakly-consolidated, soft butter-like

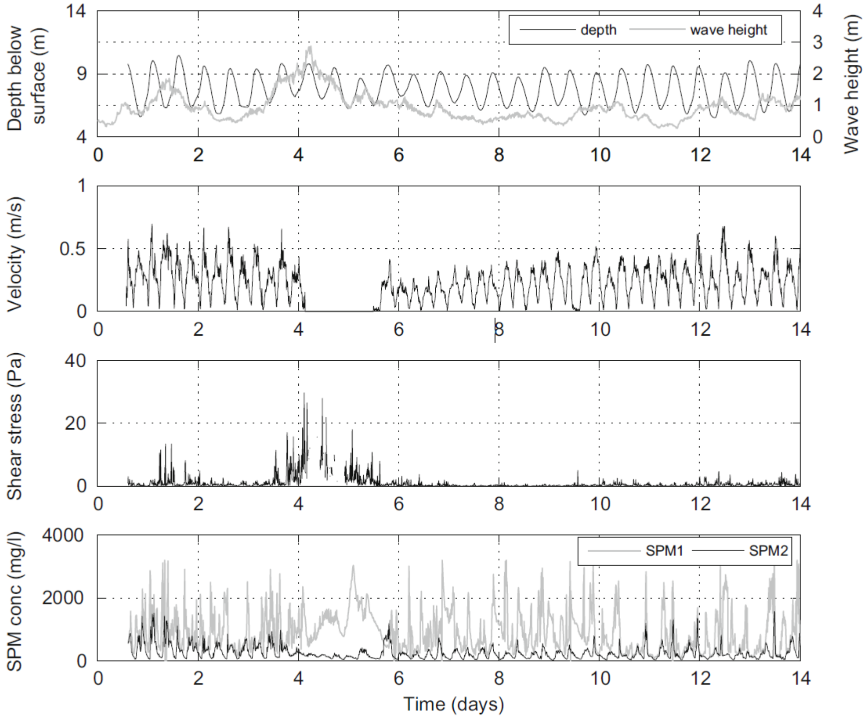

Figure 2.14: Tripod measurements at Blankenberge 7–20 November 2006. From up to down: depth below water surface (m) and significant wave heights; ADV current velocity (m/s); shear stress (Pa) derived from the ADV; and SSC at 0.3 mab (SPM1) and 2.3 mab (SPM2) (Fettweis et al., 2010).

muds with a bulk density of 1300 kg m^{-3} to 1500 kg m^{-3} and medium-consolidated, stiffer muds sometimes intercalated with more sandy layers with a bulk density of 1500 kg m^{-3} to 1800 kg m^{-3}.

The map of bed composition of figure 2.15 is used as a calibration target for the sediment transport model in section 5.11.

2.10.2. SeaWifs satellite images

Because the waters in the Belgian coastal zone are generally well-mixed throughout the year (Lacroix et al., 2004; Fettweis et al., 2006; Pietrzak et al., 2011), the distribution of suspended sediment can be studied through observations of surface SSC. The satellite data are used to establish seasonal patterns in SSC in section 4.4.5, and as a calibration target in section 5.11.

Because the satellite images are taken by sun-synchronous satellites, there is no uniform sampling over the spring-neap cycle. Spring tide conditions are over-represented in the hours before high water, for example. Furthermore, there is good-weather bias, because data can only be collected on cloud-free days, which generally correspond to days with relatively little wind and small significant wave

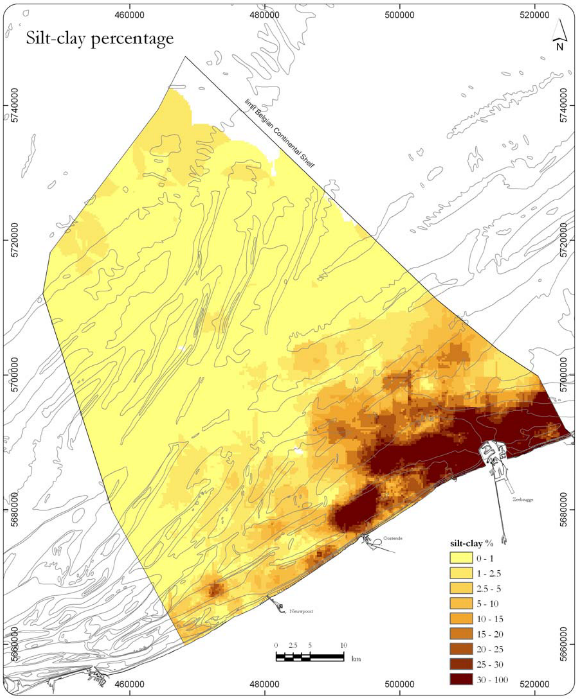

Figure 2.15: Spatial distribution of the silt-clay percentage (Van Lancker et al., 2007).

height (Fettweis and Nechad, 2011; Baeye, 2012). Despite these limitations, surface SSC derived from satellite imagery (e.g. SeaWiFS, MODIS, MERIS) is routinely used in research on SPM dynamics in the North Sea (Van den Eynde et al., 2007; Fettweis et al., 2007; Eleveld et al., 2008; Nechad et al., 2010; Pietrzak et al., 2011).

2.11. Dredging and disposal

Five disposal sites have been designated in the Belgian part of the North Sea: S1, S2, Zeebrugge Oost (ZBO), Oostende and Nieuwpoort (Lauwaert et al., 2016), of which the first three are located within the study area. Figure 2.16 shows the five dredging areas within the study area.

A database on dredging and disposal has kindly been provided by Maritime Access Division. The database contains quantities of maintenance and capital dredging in tonnes of dry matter (TDM). Only data on maintenance dredging are considered here. The database contains total sediment amounts (sand + mud). In order to separate the mud fraction from the total amount of maintenance dredging, the mud fraction reported by BMM and AWZ (1993) is used for all dredging sites except for the location CDNB, for which more recent data in Pieters et al. (2001) are used.

Table 2.1 shows the mud fraction per dredging location, the yearly averaged dredging amount (only the mud fraction) in million tonnes of dry matter (MTDM)

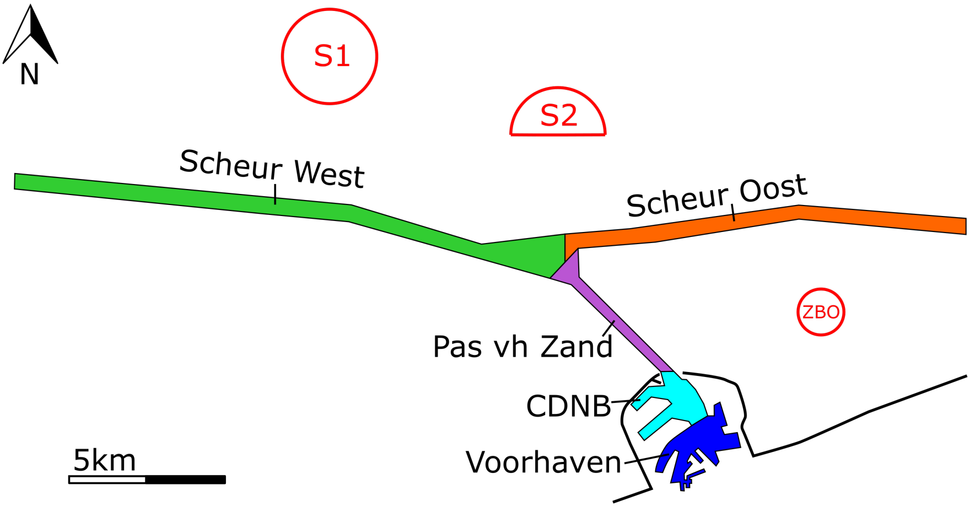

Figure 2.16: Dredging areas (colored) and disposal sites (outlined in red).

and the distribution of the dredged material over the three disposal locations, as derived from the dredging logs (2005 to 2013). Monitoring of the dumping sites shows that most of the fine-grained sediments are washed out, leaving only the sand fraction (Van den Eynde, 2004; Du Four and Van Lancker, 2008).

		Mud fraction	Dredging Mud [MTDM/yr]	Disposal ZBO	S1	S2
Harbor	Voorhaven	60%	1.2	72%	14%	14%
	CDNB	94%	3.1	50%	35%	15%
Channels	Pas vh Zand	66%	1.4		70%	30%
	Scheur West	49%	0.7		85%	15%
	Scheur Oost	18%	0.2		81%	19%

Table 2.1: Mud fraction per dredging location (Pieters et al., 2001; BMM and AWZ, 1993), yearly averaged dredging amount (only the mud fraction of the maintenance dredging) in million tonnes of dry matter and the distribution of the dredged material over the disposal sites (2005-2013).

Averaged over nine years, 4.3 (2.6 to 5.0) MTDM/yr of mud was dredged from Zeebrugge harbor and 2.3 (1.5 to 3.0) MTDM/yr from the access channels, with the range over the period 2005 to 2013 indicated in brackets.

The comparison between the total amount of mud involved in the maintenance dredging of Zeebrugge and its access channels (4 to 8 MTDM/yr), and the residual long-shore mud transport in the Belgian coastal zone (8 to 20 MTDM/yr, see section 2.7.1) shows that an important part of SPM is involved in the dredging/disposal cycle (Fettweis et al., 2009).

An additional indication of the importance of dredging in the local sediment dynamics is the occurrence of clay and mud pebbles, which occur more frequently now than in the historic dataset of sediment samples of Gilson (1900). The higher frequency of occurrence of clay and mud pebbles in the vicinity of the disposal grounds is most probably linked to the disposal of sediments from capital dredging works (Du Four and Van Lancker, 2008). Due to the deepening works, Holocene mud deposits outcrop more frequently today than at the beginning of the 20th century and as a result, erosion of these layers (e.g. during storms, see section 2.9) is more prominent today (Fettweis et al., 2009).

2.12. Field observations and data analysis

Data of 51 tripod deployments were gathered over nearly 9 years (2005-2013) at locations MOW1 (45 deployments) and Blankenberge (6 deployments). The measurement locations are indicated in figure 2.17. The data were gathered within the framework of the MOMO project (see e.g. Fettweis et al. (2014)) and were kindly provided by RBINS - OD Nature. A typical deployment lasts 2 weeks to 1 month. The observations of velocity and SSC were re-analyzed, and the results are discussed below.

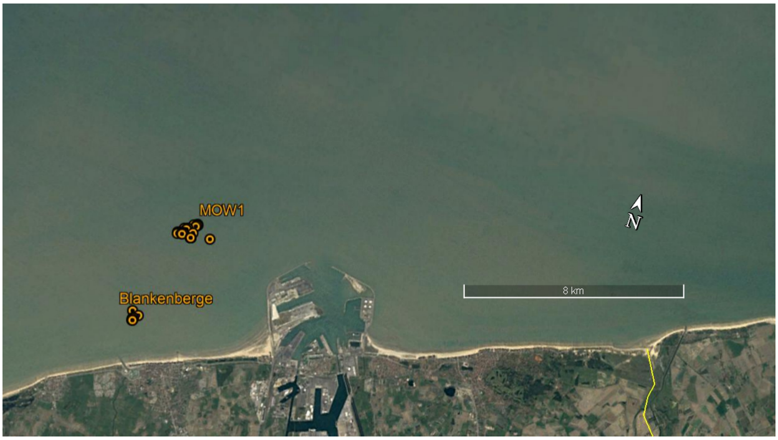

Figure 2.17: Location of the OD Nature tripod deployments at MOW1 and Blankenberge (orange dots).

2.12.1. Field observations of velocity

Velocity was measured using a SonTek 3 MHz Acoustic Doppler Profiler (ADP), mounted near the top of the tripod looking downwards. The ADP velocity in the highest bin, positioned at 1.9 meter above the bed (mab) is shown here in order to study its relation to the sediment concentration at 2.3 mab (discussed in the next section 2.12.2).

Figure 2.18 shows the phase-averaged velocity magnitude at locations MOW1 and Blankenberge for neap, normal and spring tide. The boundaries between the three tidal classes are set at the 33rd and 66th percentile of the tidal range at Vlissingen, determined over a 10-year period (2004-2013). The moments of high

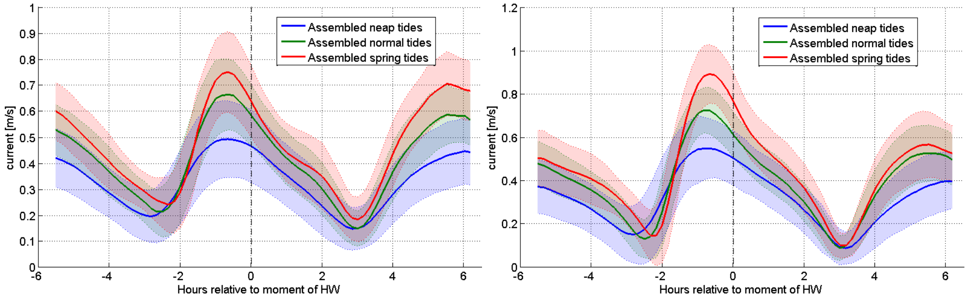

Figure 2.18: Mean and standard deviation over a tidal cycle of the velocity [m/s] at location MOW1 (left panel) and Blankenberge (right panel) at 1.9 mab. Blue curve: neap tide, green: normal tide, red: spring tide (De Maerschalck et al., 2020).

water are determined with the local pressure signal. The error bands around the velocity magnitude represent the standard deviation.

Tidal asymmetry, expressed as the flood-to-ebb ratio of maximum velocity, is lower at MOW1 (1.0 to 1.1 for neap and spring tide conditions, respectively) than at Blankenberge (1.3 to 1.5 for neap and spring tide conditions, respectively). The more pronounced velocity asymmetry at Blankenberge can be related to the fact that during ebb flow, the measurement site is located in the wake of the protruding breakwaters. The spring-to-neap ratio in peak velocities is more pronounced for peak flood flow (1.8 for Blankenberge and 1.7 for MOW1) than for peak ebb flow (1.4 for Blankenberge and 1.5 for MOW1).

Maximum flood occurs 45 minutes before high water, which corresponds to a phase lead of the horizontal tide to the vertical tide of 22°, illustrating the mixed nature (between progressive and standing wave) of the tidal wave, which propagates as a Kelvin wave along the Belgian coast. Maximum ebb flow occurs 6 hours after HW at neap tide, and 5 hours after HW for spring tide. Note that in general, the phase relationship between vertical and horizontal tide is complex. Not only friction but also (partial) reflections of the tidal wave introduce phase differences between velocity and elevation (Bosboom and Stive, 2021).

The tidal current ellipses are more elongated at Blankenberge (see figure 2.19), which is closer to the coast than MOW1 (see figure 2.20).

2.12.2. Field observations of SSC

SSC is measured using two OBS sensors mounted on a measurement frame at about 0.3 and 2.3 mab. The OBS signal is first processed to turbidity levels [FTU] with a calibration based on laboratory tests. The turbidity levels are then converted to sediment concentration [mg/l] with a correlation based on in situ water samples taken with a Niskin Carousel. Data collection, calibration and conversion to mg/l was performed at RBINS - OD Nature. The data analysis was performed at Flanders Hydraulics Research (FHR).

Blankenberge

The left panel in figure 2.19 shows the phase-averaged SSC at 2.3 mab for neap, average and spring tides at station Blankenberge. Note the phase shift of maximum ebb SSC over the spring-neap cycle that was also observed for velocity in figure 2.18.The levels of peak SSC rise monotonically with the levels of peak velocity. The pronounced tidal asymmetry for velocities is therefore also present in the SSC values, with a flood/ebb ratio of 1.25 during average and neap tides, and 1.5 during spring tides.

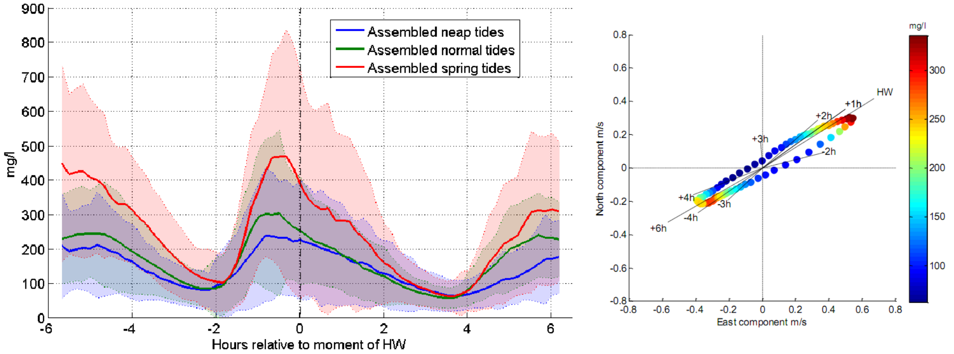

Figure 2.19: Intratidal variation of SSC [mg/l] at 2.3 mab at Blankenberge. Ensemble average showing the median, and P10 and P90 percentile of SSC for neap, normal and spring tide (left panel) and a tidal ellipse with SSC for an average tide (right panel) (De Maerschalck et al., 2020).

The tidal ellipse in the right panel of figure 2.19 combines the velocity at 1.1 mab and SSC at 2.3 mab for an average tide at Blankenberge. The elongated shape of the tidal ellipse is related to the fact that the measurement location is situated relatively near the coast at 1.5 km. The peak in SSC coincides with maximum flood, and lags one hour after maximum ebb. The small time lag between SSC and velocity suggests the importance of local erosion and sedimentation, and a large availability of mud in the bed. This is explored further with a 1DV sediment model in section 5.11.1.

MOW1

The left panel in figure 2.20 shows the phase-averaged SSC at 2.3 mab for neap, average and spring tides at station MOW1. Even though the two stations are close to each other, the SSC signal at MOW1 looks quite different from that at Blankenberge. The peak in SSC during flood occurs later in the tidal cycle at MOW1 than at Blankenberge. The ebb peak in SSC is stronger than the flood peak, with flood-to-ebb ratios varying from 0.7 during neap tide to 0.5 during spring tide. The spring-neap variation is also stronger during ebb (ratio of 2.9) than during flood (ratio of 2.1). Note that the peak ebb velocity at MOW1 is actually lower than the peak flood velocity (see figure 2.18), which suggests that the ebb peak in SSC is not due to local resuspension, but is being advected with the ebb flow. This would put the sediment source eastward of the measurement location. One potential candidate is the freshly deposited sediment in the access channel ”Pas van het Zand”, which is located east of the measurement station.

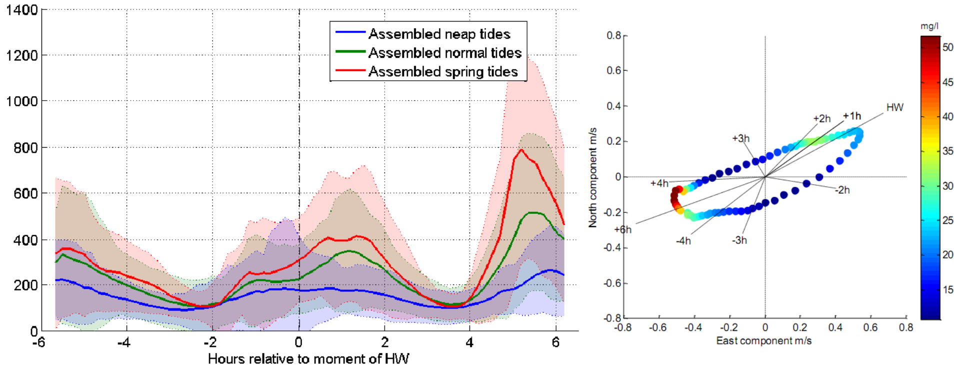

Figure 2.20: Intratidal variation of SSC [mg/l] at 2.3 mab at location MOW1. Ensemble average showing the median, and P10 and P90 percentile of SSC for neap, normal and spring tide (left panel) and a tidal ellipse with SSC for an average tide (right panel) (De Maerschalck et al., 2020).

The right panel of figure 2.20 shows the tidal ellipse for an average tide. The ebb peak in SSC occurs from one hour before to the moment of peak ebb flow. The flood peak in SSC however, occurs one to two hours after maximum flood flow. The hysteresis between local flow velocity and local SSC during flood tide is more pronounced for station MOW1 when compared with station Blankenberge.

For both locations MOW1 and Blankenberge, the median concentration during slack water drops to a background value around 100 mg/l, regardless of tidal amplitude. This indicates the existence of a finer fraction that hardly settles.

Vertical gradient of SSC

In steady flow, and assuming a constant settling velocity and a parabolic form of momentum diffusivity, the vertical suspended concentration profile can be described by the Rouse equation (Rouse, 1951):

$$\begin{aligned} c_z &= c_a \left(\frac{h-z}{z} \frac{a}{h-a} \right)^{\mathrm{Ro}} \\ \mathrm{Ro} &= \frac{w_s \sigma_T}{\kappa u_*} \end{aligned} \tag{2.5}$$

with c_z the suspended sediment concentration at height z above the bed, c_a the concentration at the reference height a above the bed, and h the water depth. The exponent Ro is the Rouse number, which is the ratio between settling and turbulence strength. w_s is the settling velocity, σ_T is the turbulent Prandtl-Schmidt number. κ is the von Kármán constant (typically taken as 0.41 for clear water) and u_* is the shear velocity.

Equation 2.5 can be re-arranged to determine the exponent $\widetilde{\text{Ro}}$ from simultaneously measured suspended sediment concentrations at two different heights.

$$\widetilde{\text{Ro}} = \frac{ln\frac{c_{z1}}{c_{z2}}}{ln\left(\frac{h-z_1}{h-z_2}.\frac{z_2}{z_1}\right)} \tag{2.6}$$

Note that equation 2.6 uses the notation $\widetilde{\text{Ro}}$, in order to differentiate from Ro in equation 2.5, which is only valid under a set of conditions that is not strictly met in non-stationary, tidal flow. In what follows, $\widetilde{\text{Ro}}$ is calculated from the sediment concentrations at two different heights in order to quantify the vertical gradient in a dimensionless number. A higher value of $\widetilde{\text{Ro}}$ means a sharper vertical concentration gradient. The water column is perfectly mixed when $\widetilde{\text{Ro}}$ approaches zero.

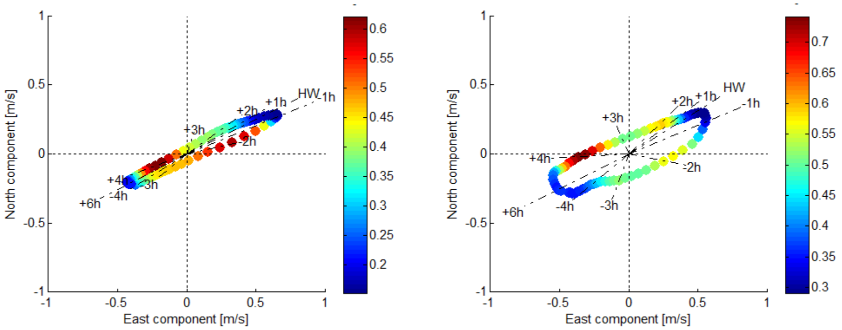

Figure 2.21: Tidal ellipse with the color scale indicating $\widetilde{\text{Ro}}$ for Blankenberge (left panel) and MOW1 (right) (De Maerschalck et al., 2020).

The tidal variation of the vertical gradient strength $\widetilde{\text{Ro}}$ is similar for neap, normal and spring tides. Figure 2.21 shows the tidal variation of $\widetilde{\text{Ro}}$ for average tidal conditions. At both locations, the vertical gradient strength is strongest around 4 hours after high water and two hours before high water, which is slightly after slack water conditions. This time lag corresponds to the time needed for sediment to settle. At station MOW1, the vertical gradient strength is comparatively weaker for the slack period before HW than at Blankenberge.

Wave influence on near-bed SSC

Figure 2.22 shows a clear influence of the wave climate on the near-bed SSC. As established in section 2.4, waves become important for the resuspension of sediments when the significant wave height exceeds 1.5 m (Fettweis and Nechad, 2011; Baeye, 2012). For these high waves, the near-bed SSC is consistently higher (see figure 2.22). Also, because the timing of individual waves is randomly distributed within a tidal cycle, the intratidal variation of SSC at high waves is less pronounced than at low waves, with a larger spread around the median (here visualized as the distance between the P10 and P90 percentile).

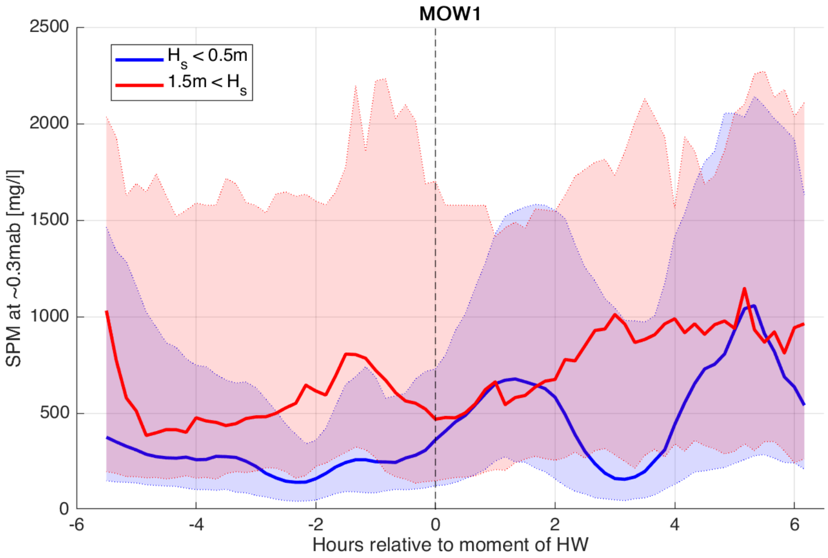

Figure 2.22: Median SSC over a tidal cycle at 0.3 mab at station MOW1 in low wave (blue) and high wave (red) conditions. Colored bands indicate P10 and P90 percentiles.

Seasonal variation of SSC

The frame-mounted OBS data at station MOW1 show a clear seasonal signal for the higher sensor at 2.3 mab (figure 2.23, top panel). The median SSC over a tidal cycle is consistently higher during fall/winter, than during spring/summer. This seasonal variation is less pronounced however at 0.3 mab (bottom panel). The spread around the median is also higher in fall/winter, which might be related to the higher wave activity in winter (see previous paragraph). This seasonal variation is consistent with the seasonal variation of SSC that is observed in the harbor (see section 4.4.5) and with the seasonality in SSC that is observed in the Belgian nearshore area (Fettweis et al., 2007; Fettweis and Baeye, 2015).

This seasonal variation is also apparent in the tidal ensembles of the vertical gradient strength $\widetilde{\mathrm{Ro}}$ in figure 2.24, with a sharper vertical gradient in SSC in spring/summer than during fall/winter. This suggests that the vertical balance between turbulent mixing of SSC and the settling velocity of the particles varies seasonally. This is consistent with the results of Fettweis and Baeye (2015) who attribute this effect to larger floc size and higher settling velocity in summer, caused by biological effects on marine flocs.

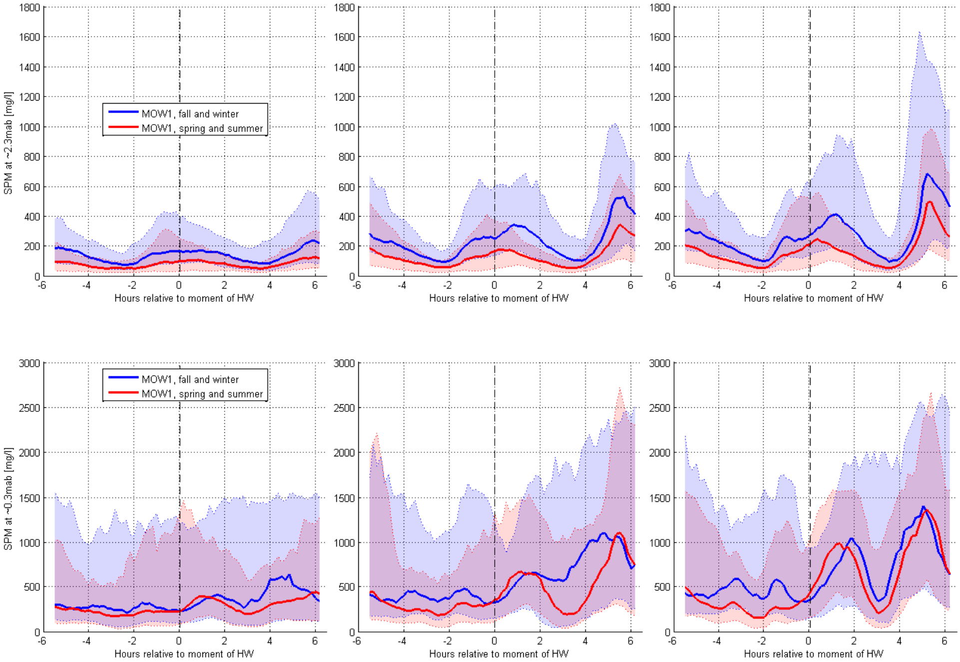

Figure 2.23: Median SSC over a tidal cycle at 2.3 mab (top panel) and at 0.3 mab (bottom panel) at MOW1 during fall-winter (in blue) and spring-summer (in red). Colored bands indicate P10 and P90 percentiles. Left panel: neap tides, middle: normal tides, right: spring tides (De Maerschalck et al., 2020).

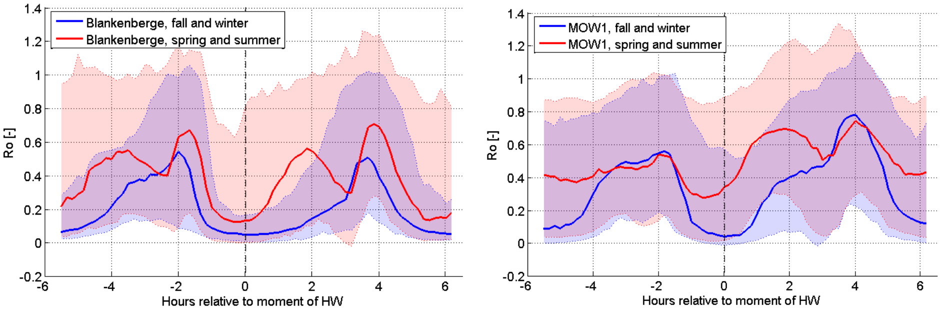

Figure 2.24: Median $\widetilde{\mathrm{Ro}}$ over a tidal cycle at Blankenberge (left panel) and MOW1 (right) during spring-summer (in red) and fall-winter (in blue). Colored bands indicate P10 and P90 percentiles (De Maerschalck et al., 2020).

References

Adriaens, R., Zeelmaekers, E., Fettweis, M., Vanlierde, E., Vanlede, J., Stassen, P., Elsen, J., Środoń, J., and Vandenberghe, N. (2018). Quantitative clay mineralogy as provenance indicator for recent muds in the southern North Sea. *Marine Geology*, 398:48–58.

Baeteman, C. (1999). The Holocene depositional history of the IJzer palaeovalley (Western Belgian coastal plain) with reference to the factors controlling the formation of intercalated peat beds. *Geologica Belgica*.

Baeye, M. (2012). *Hydro-meteorological Influences on the Behaviour and Nature of Sediment Suspensions in the Belgian-Dutch Coastal Zone*. PhD thesis, Ghent University.

Baeye, M., Fettweis, M., Voulgaris, G., and Van Lancker, V. (2011). Sediment mobility in response to tidal and wind-driven flows along the Belgian inner shelf, southern North Sea. *Ocean Dynamics*.

Bastin, A. (1974). *Regionale sedimentologie en morfologie van de Zuidelijke Noordzee en van het Schelde estuarium*. PhD thesis, Katholieke Universiteit Leuven.

BMM and AWZ (1993). Ecologische impact van baggerspecielossingen voor de Belgische kust, eindrapport. Technical report, BMM and AWZ, Brussel.

Bosboom, J. and Stive, M. (2021). *Coastal Dynamics Open Textbook*. Delft University of Technology, Delft, The Netherlands.

Burchard, H., Schuttelaars, H. M., and Ralston, D. K. (2018). Sediment Trapping in Estuaries. *Annual Review of Marine Science*, 10(1):annurev–marine–010816–060535.

CERC (1984). Shore Protection Manual. Technical report, Waterways Experiment Station, Corps of Engineers, Coastal Engineering Research Center, Vicksburg, Mississippi.

De Maerschalck, B., Nguyen, D., Vanlede, J., and Mostaert, F. (2020). Sediment Transport Model for the Port of Zeebrugge: Analysis of the OD Nature Tripod measurements. WL Rapporten, 00_067. Technical report, Vlaamse Overheid; Afdeling Waterbouwkundig Laboratorium, Antwerpen.

De Maerschalck, B., van der Werf, J., Kolokythas, G., Quataert, E., Van Oyen, T., Vroom, J., Dijkstra, J., Wang, Z., Vanlede, J., Verwaest, T., and Mostaert, F. (2017). Modellering Belgische Kustzone en Scheldemonding: Deelrapport 2 – Morfologische analyse scenario's Vlaamse Baaien. Technical report, Flanders Hydraulics Research, Antwerp.

Dronkers, J. (1986). Tide-induced residual transport of fine sediment. In Van de Kreeke, J., editor, *Physics of Shallow Estuaries and Bays*, pages 228–244. Springer-Verlag, Berlin.

Du Four, I. and Van Lancker, V. (2008). Changes of sedimentological patterns and morphological features due to the disposal of dredge spoil and the regeneration after cessation of the disposal activities. *Marine Geology*, 255(1-2):15–29.

Eisma, D. (1981). Supply and Deposition of Suspended Matter in the North Sea. In Nio, S., Shüttenhelm, R. T. E., and Van Weering, T. C. E., editors, *Holocene Marine Sedimentation in the North Sea Basin*, pages 415–428. Blackwell Publishing Ltd., Oxford, UK.

Eisma, D. and Kalf, J. (1979). Distribution and particle size of suspended matter in the Southern Bight of the North sea and the Eastern channel. *Netherlands Journal of Sea Research*, 13(2):298–324.

Eleveld, M. A., Pasterkamp, R., van der Woerd, H. J., and Pietrzak, J. D. (2008). Remotely sensed seasonality in the spatial distribution of sea-surface suspended particulate matter in the southern North Sea. *Estuarine, Coastal and Shelf Science*, 80(1):103–113.

Fettweis, M. and Baeye, M. (2015). Seasonal variation in concentration, size, and settling velocity of muddy marine flocs in the benthic boundary layer. *Journal of Geophysical Research: Oceans*, 120(8):5648–5667.

Fettweis, M., Baeye, M., and Francken, F. (2014). MOnitoring en MOdellering van het cohesieve sedimenttransport en evaluatie van de effecten op het mariene ecosysteem ten gevolge van bagger en stortoperatie (MOMO). Activiteitsrapport (1 juli 2013 - 31 december 2013). Technical report, KBIN OD Natuur, Brussels, Belgium.

Fettweis, M., Francken, F., Pison, V., and Van den Eynde, D. (2006). Suspended particulate matter dynamics and aggregate sizes in a high turbidity area. *Marine Geology*, 235:63–74.

Fettweis, M., Francken, F., Van den Eynde, D., Verwaest, T., Janssens, J., and Van Lancker, V. (2010). Storm influence on SPM concentrations in a coastal turbidity maximum area with high anthropogenic impact (southern North Sea). *Continental Shelf Research*, 30(13):1417–1427.

Fettweis, M., Houziaux, J.-S., Du Four, I., Van Lancker, V., Baeteman, C., Mathys, M., Van den Eynde, D., Francken, F., and Wartel, S. (2009). Long-term influence of maritime access works on the distribution of cohesive sediments: analysis of historical and recent data from the Belgian nearshore area (Southern North Sea). *Geo-Marine Letters*, 29(5):321–330.

Fettweis, M., Nechad, B., and Van den Eynde, D. (2007). An estimate of the suspended particulate matter (SPM) transport in the southern North Sea using SeaWiFS images, in situ measurements and numerical model results. *Continental Shelf Research*, 27(10-11):1568–1583.

Fettweis, M. and Van den Eynde, D. (1999). Bepaling van de Sedimentbalans voor de Belgische Kustwateren (SEBAB) - Activiteitsrapport 1: Literatuurstudie. Technical report, BMM, Brussel.

Fettweis, M. and Van den Eynde, D. (2003). The mud deposits and the high turbidity in the Belgian–Dutch coastal zone, southern bight of the North Sea. *Continental Shelf Research*, 23(7):669–691.

Fettweis, M. P. and Nechad, B. (2011). Evaluation of in situ and remote sensing sampling methods for SPM concentrations, Belgian continental shelf (southern North Sea). *Ocean Dynamics*, 61(2-3):157–171.

Friedrichs, C. T. (2011). Tidal flat morphodynamics: a synthesis. In Wolanski, E. and McLusky, D., editors, *Treatise on estuarine and coastal science*, chapter 3.06, pages 137–170. Academic Press.

Friedrichs, C. T. and Aubrey, D. G. (1988). Non-linear tidal distortion in shallow well-mixed estuaries: a synthesis. *Estuarine, Coastal and Shelf Science*, 27(5):521–545.

Gilson, G. (1900). Exploration de la mer sur les côtes de la Belgique en 1899. Technical report, Mem Musée R Hist Nat Belg, Springer, Berlin.

Gossé, J. G. (1977). A preliminary investigation into the possibility of erosion in the area of the Flemish banks. Technical report, Rijkswaterstaat, RIKZ.

Groen, P. (1967). On the residual transport of suspended matter by an alternating tidal current. *Netherlands Journal of Sea Research*, 3:564–574.

Gullentops, F., Moens, M., Ringelé, A., and Sengier, R. (1977). Geologische kenmerken van de suspensie en de sedimenten. In Nihoul, J. and Gullentops, F., editors, *Projekt Zee, Eindverslag, Boekdeel 4: Sedimentologie*, pages 1–121.

Holthuijsen, L. H. (2007). *Waves in oceanic and coastal waters*. Cambridge University Press.

Houziaux, J.-S., Fettweis, M., Francken, F., and Van Lancker, V. (2011). Historic (1900) seafloor composition in the Belgian–Dutch part of the North Sea: A reconstruction based on calibrated visual sediment descriptions. *Continental Shelf Research*, 31(10):1043–1056.

IMDC (2007). Langdurige monitoring van zout/zoet-verdeling in de haven van Zeebrugge en monitoring van zoutconcentratie, slibconcentratie en hooggeconcentreerde slibsuspensies in de Belgische kustzone. Deelrapport 4 : Valsnelheid slib – INSSEV – herfst 2006 kustzone. Technical report, Waterbouwkundig Laboratorium, Antwerpen.

Lacroix, G., Ruddick, K., Ozer, J., and Lancelot, C. (2004). Modelling the impact of the Scheldt and Rhine/Meuse plumes on the salinity distribution in Belgian waters (southern North Sea). *Journal of Sea Research*, 52(3):149–163.

Lauwaert, B., De Witte, B., Devriese, L., Fettweis, M., Martens, C., Timmermans, S., Van Hoey, G., and Vanlede, J. (2016). Synthesis report on the effects of dredged material dumping on the marine environment (licensing period 2012-2016). Technical report, RBINS-OD Nature/ILVO/aMT/aKust/WL, Brussels.

Li, Y. and Mehta, A. J. (2000). Fluid mud in the wave-dominated environment revisited. *Proceedings in Marine Science*, 3(C):79–93.

Manning, A. J. and Dyer, K. R. (2007). Mass settling flux of fine sediments in Northern European estuaries: Measurements and predictions. *Marine Geology*, 245(1-4):107–122.

McAnally, W. H., Mehta, A. J., and Manning, A. J. (2021). Observations on Floc Settling Velocities in the Tamar Estuary, United Kingdom. *Journal of Waterway, Port, Coastal, and Ocean Engineering*, 147(5):04021015.

McCave, I. N. (1973). Mud in the North Sea. In Goldberg, E., editor, *North Sea Science: NATO North Sea Science Conference Aviemore, Scotland, 15-20 November 1971.*, Cambridge. MIT Press.

McManus, J. P. and Prandle, D. (1997). Development of a model to reproduce observed suspended sediment distributions in the southern North Sea using Principal Component Analysis and Multiple Linear Regression. *Continental Shelf Research*, 17(7):761–778.

Nechad, B., Ruddick, K., and Park, Y. (2010). Calibration and validation of a generic multisensor algorithm for mapping of total suspended matter in turbid waters. *Remote Sensing of Environment*, 114(4):854–866.

Nihoul, J. C. J. (1975). Effect of the tidal stress on residual circulation and mud deposition in the Southern Bight of the North Sea. *Pure and Applied Geophysics*, 113:577–581.

Nihoul, J. C. J. and Ronday, F. C. (1975). The influence of the ”tidal stress” on the residual circulation. Application to the southern bight of the North Sea. *Tellus*, 27:484–490.

Otto, L., Zimmerman, J. T., Furnes, G. K., Mork, M., Saetre, R., and Becker, G. (1990). Review of the physical oceanography of the North Sea. *Netherlands Journal of Sea Research*, 26(2-4):161.

Pieters, A., Dumon, G., and Speleers, L. (2001). Onderzoek naar de ecologische impact van de baggerwerkzaamheden aan de Belgische kust in het kader van MOBAG 2000: chemisch-biologische aspecten. In *Studiedag 'Milieuaspecten van baggerwerken op de Belgische kust': conferentiemap*, page 13.

Pietrzak, J. D., de Boer, G. J., and Eleveld, M. A. (2011). Mechanisms controlling the intra-annual mesoscale variability of SST and SPM in the southern North Sea. *Continental Shelf Research*, 31(6):594–610.

Prandle, D., Ballard, G., Flatt, D., Harrison, A. J., Jones, S. E., Knight, P. J., Loch, S., McManus, J., PLayer, R., and Tappin, A. (1996). Combining modelling and monitoring to determine fluxes of water, dissolved and particulate metals through the Dover Strait. *Continental Shelf Research*, 16:237–257.

Proudman, J. and Doodson, A. (1924). The principal constituent of the tides of the North Sea. *Philosophical Transactions of the Royal Society*, 224:185–219.

Pugh, D. T. (1987). *Tides, surges and mean sea-level*. John Wiley & Sons, Chichester.

Rouse, H. (1951). *Engineering Hydraulics*. Wiley.

Suijlen, J. M. and Duin, R. N. M. (2002). Atlas of near-surface total suspended matter concentrations in the Dutch coastal zone of the North Sea. Technical report, National Institute for Coastal and Marine Management/RIKZ, The Hague.

Taylor, G. I. (1922). Tidal oscillations in gulfs and rectangular basins. *Proceedings of the London Mathematical Society*, s2-20(1):148–181.

van Alphen, J. S. (1990). A mud balance for Belgian-Dutch coastal waters between 1969 and 1986. *Netherlands Journal of Sea Research*, 25(1-2):19–30.

Van den Eynde, D. (1999). Toepassing van het sedimenttransportmodel mu-STM voor het beheer van baggerspeciestortingen. Technical report, MUMM, Brussels, Belgium.

Van den Eynde, D. (2004). Interpretation of tracer experiments with fine-grained dredging material at the Belgian Continental Shelf by the use of numerical models. *Journal of Marine Systems*, 48(1-4):171–189.

Van den Eynde, D., Nechad, B., Fettweis, M., and Francken, F. (2007). Seasonal variability of suspended particulate matter observed from SeaWiFS images near the Belgian coast. In Maa, J. P., Sanford, L. P., and Schoellhamer, D. H., editors, *Estuarine and coastal fine sediment dynamics*. Elsevier.

Van Der Giessen, A. and De Ruijter WPM, B. J. C. (1990). Three-Dimensional current structure in the Dutch Coastal Zone. *Netherlands Journal of Sea Research*, 25:45–55.

Van Lancker, V., De Batist, M., Fettweis, M., Pichot, G., and Monbaliu, J. (2007). Management, research and budgetting of aggregates in shelf seas related to end-users (Marebasse). Technical report, Belgian Science Policy, Brussel, Belgium.

van Maren, D., Vroom, J., Fettweis, M., and Vanlede, J. (2020). Formation of the Zeebrugge coastal turbidity maximum : The role of uncertainty in near-bed exchange processes. *Marine Geology*, 425:106186.

Van Mierlo, C.-J. (1899). La carte lithologique de la partie meridionale de la mer du Nord. *Bulletin de la Societe Belge de Geologie, Paleontologie et Hydrologie*.

Verduin, F. (2009). *Sediment Transport in the Westerschelde Delta (Msc thesis)*. Delft.

Verfaillie, E., Van Lancker, V., and Van Meirvenne, M. (2006). Multivariate geostatistics for the predictive modelling of the surficial sand distribution in shelf seas. *Continental shelf research*, 26:2454–2468.

Visser, M., De Ruijter, W. P. M., and Postma, L. (1991). The distribution of suspended matter in the Dutch coastal zone. *Netherlands Journal of Sea Research*, 27:127–143.

Vroom, J. and Schrijvershof, R. (2015). Overzicht van menselijke ingrepen in de Westerschelde en haar mondingsgebied in de periode 1985-2014. Technical report, Deltares, Delft.

Vroom, J., van Maren, D., van der Werf, J., and van Rooijen, A. (2016). Zand-slib modellering voor het mondingsgebied van het Schelde-estuarium. Technical report, Deltares, Delft.

Wang, Z. B., Jeuken, C., and Vriend, H. J. D. (1999). Tidal asymmetry and residual sediment transport in estuaries. Technical report, WL|Delft Hydraulics.

Winterwerp, J. C. (2001). Stratification effects by cohesive and noncohesive sediment. *Journal of Geophysical Research: Oceans*, 106(C10):22559–22574.

Winterwerp, J. C. (2003). The transport of fine sediment in shallow basins: Humber case study. Technical report, WL | Delft Hydraulics, Delft, The Netherlands.

Winterwerp, J. C., de Boer, G. J., Greeuw, G., and van Maren, D. S. (2012). Mud-induced wave damping and wave-induced liquefaction. *Coastal Engineering*, 64:102–112.

Winterwerp, J. C. and Van Kessel, T. (2003). Siltation by sediment-induced density currents. *Ocean Dynamics*, 53(3):186–196.

Witt, O. and Westrich, B. (2003). Quantification of erosion rates for undisturbed contaminated cohesive sediment cores by image analysis. In Kronvang B., editor, *The Interactions between Sediments and Water. Developments in Hydrobiology, vol 169*, pages 271–276. Springer, Dordrecht.

3

A geometric method to study water and sediment exchange in tidal harbors

3.1. Introduction

Three main flow mechanisms induce an exchange of water across the interface between a harbor and the surrounding waters under tidal influence (Eysink, 1989; Langendoen, 1992; Winterwerp, 2005; PIANC, 2008):

1. Exchange flow across the interface between flow outside the harbor and shear-induced circulation inside the harbor.

2. Exchange flow by tidal filling.

3. Exchange flow driven by a density difference inside and outside the harbor. This density difference can be driven by a horizontal gradient in salinity, temperature or sediment concentration.

In addition to the different components of the water exchange, the siltation of a harbor will also depend on the relationship between water exchange and suspended sediment concentration (de Nijs et al., 2009; van Maren et al., 2009). The relation between exchange mechanisms and harbor siltation is still poorly understood however. This chapter describes a geometric decomposition of the exchange flow, and applies it on available measurements at two important harbor basins in Belgium. The presented method can provide some insight into the complex relationship (phasing and spatial correlation) between hydrodynamics and sediment concentration that determines harbor siltation.

This chapter has been published by Vanlede and Dujardin in Ocean Dynamics **64**, 11 (2014).

Even with continuously improving computer models, detailed numerical model studies on exchange flows and siltation in harbor basins are limited (Langendoen, 1992; Stoschek and Zimmermann, 2006; van Maren et al., 2009). When studying harbor siltation with a numerical model, the model output will give total sediment fluxes due to the interaction of all processes that the modeler has included in the schematization. The geometric analysis can also be applied to the results of a numerical model, provided it has sufficient horizontal, vertical and temporal resolution to capture the dynamics at the harbor mouth. As such, it can be used as a tool in model calibration, as is illustrated in section 5.11.3 of this thesis.

3.2. Method

The method presented in this chapter is as a flux decomposition of water and sediment exchange across a fixed interface at the entrance of a harbor basin during a tidal cycle. The flow normal to the interface is decomposed geometrically into three main components (tidal, horizontal and vertical) and a residual component. The decomposed sediment flux is obtained by multiplying the decomposed flow with the concentrations at the interface. Total fluxes are obtained by integrating over a tidal cycle.

A large body of work already exists on the decomposition of mass transport. In the 60's, 70's and 80's geometric decomposition of velocity, concentration and cross sectional area was used to investigate the relative importance of tidally averaged longitudinal mass transport phenomena in estuaries, first of salt and then extended to suspended sediments. Costa (1989) gives an overview in a unified notation of the different decomposition techniques that have been used over time. Murray and Siripong (1978) use a combination of vertical, horizontal and cross-sectional averaging to decompose the flow and -separately- also the salinity in a study on salt fluxes in a shallow estuary. After averaging out over a tidal cycle, their decomposition of the mass flux has ten terms. The method presented in this chapter is kept simpler in comparison. By choosing not to decompose the sediment concentration, the mass flux is decomposed in only four terms. Also the tidal averaging is only done at the end, to enable the study of the intratidal variation of the mass flux.

3.2.1. Decomposition of flow

The exchange of water between a harbor of arbitrary shape and a tidal water body (e.g. the sea or a tidal river) is determined by the velocity field $\vec{v}(x,z,t)$ at the interface between the harbor and the connecting water body. This interface is indicated in gray in figure 3.1. The x-axis runs along the harbor entrance. The z-axis runs over depth (positive upward).

The (scalar) velocity component perpendicular to the harbor entrance $v_n(x,z,t)$ is calculated with a dot product. v_n is the only component that contributes to the exchange of water (and sediment) between the harbor and the connecting water body. $\overrightarrow{e_n}$ is the unit vector perpendicular to the harbor entrance, directed outwards.

$$v_n = \vec{v} \cdot \overrightarrow{e_n} \tag{3.1}$$

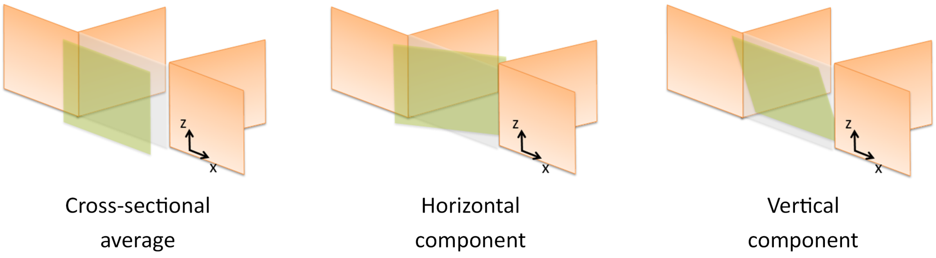

Figure 3.1: Three major components of the exchange flow at a harbor mouth.

The scalar velocity v_n is decomposed into three plus one components. Firstly, the cross-sectional average $v_{tidal}(t)$ is determined, which is the net water exchange between the harbor and the connecting water body, and is related to the water level in the harbor through a volume balance. It is depicted in the left panel of figure 3.1.

$$v_{tidal} = \frac{\iint_A v_n \, \mathrm{d}A}{A} \tag{3.2}$$

The surface of the interface between the harbor and the connecting water body is denoted as A. The remainder $\widetilde{v}(x,z,t)$ corresponds to the gross exchange of water without any net exchange:

$$\widetilde{v} = v_n - v_{tidal} \tag{3.3}$$

$\widetilde{v}$ can be geometrically split up in a horizontal component $v_{hor}(x,t)$ that has no variation over the vertical, and a vertical component $v_{ver}(z,t)$ without any variation over the horizontal. Both components are calculated separately from $\widetilde{v}$:

$$v_{hor}(x,t) = \frac{\int_{H(x,t)} \widetilde{v}(x,z,t) \, \mathrm{d}z}{H(x,t)} \tag{3.4}$$

$$v_{ver}(z,t) = \frac{\int_{B(z,t)} \widetilde{v}(x,z,t) \, \mathrm{d}x}{B(z,t)} \tag{3.5}$$

$H(x,t)$ is the available water depth at every point along the entrance transect and $B(z,t)$ is the available width of the entrance transect at every depth. v_{hor} (v_{ver}) as calculated in equation 3.4 (3.5) is a one-dimensional horizontal (vertical) scalar, and is expanded to the entire interface between the harbor and the connecting water body by repeating the 1D-scalar over the available depth (width). In the following paragraphs, v_{hor} and v_{ver} indicate the *expanded* 2D scalar fields.

Finally, the residual component $v_{res}(x,z,t)$ is determined by equation 3.6:

$$v_n = v_{tidal} + v_{hor} + v_{ver} + v_{res} \tag{3.6}$$

By definition, the following relation holds:

$$\iint_A \tilde{v}\,\mathrm{d}A = 0 \tag{3.7}$$

Note that although $\tilde{v}$ is the summation of v_{hor}, v_{ver} and v_{res} , it is only in rectangular cross-sections that the cross-sectional integrals $\iint_A v_{hor}\,\mathrm{d}A$, $\iint_A v_{ver}\,\mathrm{d}A$ and $\iint_A v_{res}\,\mathrm{d}A$ equal zero.

Note that v_{hor} and v_{ver} are determined separately from $\tilde{v}$ (a parallel approach). One could also use a sequential approach, and determine v_{ver} from horizontal averaging of $\tilde{v} - v_{hor}$, or the other way around. An unpublished sensitivity analysis on synthetic flow fields showed that for non-rectangular cross sections (which is usually the case in field conditions), this has only a limited effect in the order of 1% on the cross-sectional integrals $\iint_A v_{hor}\,\mathrm{d}A$ and $\iint_A v_{ver}\,\mathrm{d}A$.

3.2.2. Integration over time: additional operators

The instantaneous water flux $F^{wat}(t)$ is defined as:

$$F^{wat} = \iint_A v_n\,\mathrm{d}A \tag{3.8}$$

If only the positive or negative part of a scalar field is integrated, this is indicated with a superscript plus or minus sign. For instance:

$$F^{wat+} = \iint_A \max(0, v_n)\,\mathrm{d}A \tag{3.9}$$

The total flux over a tidal period is obtained by integrating over a tidal period T, and is denoted with a hat-operator. For instance:

$$\widehat{F^{wat}} = \int_0^T F^{wat}\,\mathrm{d}t \tag{3.10}$$

3.2.3. Decomposition of the sediment flux

The instantaneous sediment mass flux $F^{sed}(t)$ is defined as:

$$F^{sed} = \iint_A v_n c\,\mathrm{d}A \tag{3.11}$$

with $c(x, z, t)$ the mass concentration of sediment at the interface between the harbor and the connecting water body.

Equation 3.6 gives the decomposition of the scalar velocity field perpendicular to the harbor entrance (v_n) into three plus one scalar velocity fields that are defined at the interface between the harbor and the connecting water body. Combining equations 3.6 and 3.11, one obtains the decomposition of the total instantaneous sediment mass flux $F^{sed}(t)$ into three plus one components.As an example, the sediment flux $F^{sed}_{tidal}(t)$, related to the tidal filling and emptying, is written as:

$$F_{tidal}^{sed} = \iint_A v_{tidal} c \,\mathrm{d}A \tag{3.12}$$

In a similar way as with the calculation of the water fluxes, one might only take into account the positive (outflowing) part of the scalar velocity in the calculation of the sediment flux:

$$F_{tidal}^{sed+} = \iint_A \max(0, v_{tidal}) c \,\mathrm{d}A \tag{3.13}$$

In a cyclical tide, $\widehat{F_{tidal}^{wat}}$ is zero. There is no net exchange of water if the water level at the beginning and end of the tidal cycle is the same (provided the water exchange only happens over the entrance and there is no inflow elsewhere). Note that even in this case $\widehat{F_{tidal}^{sed}}$ will generally not be zero.

The components F_{hor}^{sed}, F_{ver}^{sed} and F_{res}^{sed} are calculated in the same way as F_{tidal}^{sed} in equation 3.12. This way, the decomposition of the instantaneous sediment flux F^{sed} is obtained:

$$F^{sed} = F_{tidal}^{sed} + F_{hor}^{sed} + F_{ver}^{sed} + F_{res}^{sed} \tag{3.14}$$

A similar relation also holds for the total fluxes $\widehat{F^{sed}}$, $\widehat{F^{sed+}}$ and $\widehat{F^{sed-}}$.

Note that the decomposition of the instantaneous sediment flux as derived in equation 3.14 combines synoptic observations of hydrodynamics and sediment concentration. That way, the spatial and temporal cross-correlation between the water exchange and the sediment concentration are implicitly taken into account.

3.2.4. Possible applications

The geometric decomposition of flow and sediment flux is diagnostic, and is meant to be applied to synoptic scalar fields of both perpendicular flow velocity and sediment concentration at the interface between a harbor and the surrounding waters. These scalar fields can be derived from measurements and/or model results.

A measurement technique particularly suited for this type of analysis is a vessel-mounted ADCP campaign (Acoustic Doppler Current Profiler) with a calibrated interpretation of the acoustic backscatter to determine the sediment concentration. This measurement technique can describe both hydrodynamics and sediment concentration with a high spatial and temporal resolution, typically along a transect and over a tidal cycle. The ADCP is typically mounted amidships on a measurement vessel, looking vertically down to the bed. Because the measurement vessel always must always be kept at a safe distance from structures, there is always an unmeasured area near-shore. Furthermore, there is always a small unmeasured area close to the surface and close to the bottom due to limitations of the measurement technique. In the processing of the datasets, the missing values have been filled in using a nearest-neighbor extrapolation.

3.3. Application to the harbor of Zeebrugge

3.3.1. Situation

The harbor of Zeebrugge is situated in the Belgian coastal zone (southern North Sea), close to the mouth of the Western Scheldt estuary, see figure 3.2. Its outer harbor is reclaimed from the sea and is protected from it by two breakwaters, each about 4 km in length. The harbor mouth is in open connection to the sea. The average tidal amplitude at Zeebrugge is 4 m. The open water surface inside the harbor is 6 x 10^6 m², which gives a tidal volume of 24 x 10^6 m³. The cross-sectional surface between harbor and sea is about 12 000 m².

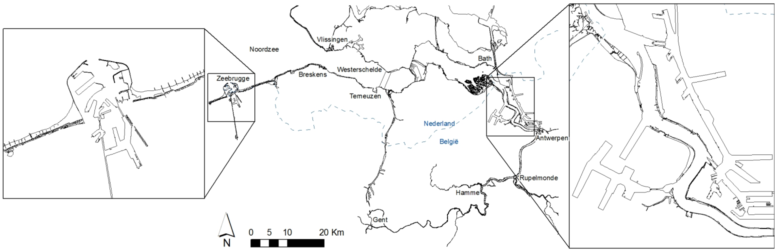

Figure 3.2: Situation plan of Zeebrugge (left) and of Deurganckdok (right) in the Scheldt estuary and the Belgian coastal zone. The measurement transects in both harbors are indicated in red.

Averaged over nine years, 4.3 MTDM/yr (Million Tonnes Dry Matter per year) of mud were dredged from Zeebrugge harbor, which corresponds to an average sediment import of about 6100 TDM/tide (see the discussion in section 2.11). This number includes maintenance dredging, but excludes capital dredging.

In 2007 a measurement campaign of flow, salinity and sediment concentration at Zeebrugge was carried out. The measurement of the 31st of July 2007 consisted of 22 sailed transects at the entrance of the harbor of Zeebrugge, performed over a tidal cycle (a spring tide in the summer of 2007). During this campaign, water velocity and sediment concentration were measured using a 600 kHz Workhorse Acoustic Doppler Current Profiler (ADCP) with a calibrated interpretation of the acoustic backscatter to determine the sediment concentration. This calibration was performed by taking water samples during the campaign (IMDC et al., 2008). A sailed transect was typically 700 m in length, and consisted of 200 to 300 ensembles (vertical profiles). Each ensemble had a vertical resolution of 50 cm.

Figure 3.3 shows a transect that was measured at 1.5h before HW during a spring tide. Flow velocity (left) and suspended sediment concentration (right) were measured at the same time. For the analysis, the data are resampled on a regular grid of 1 m x 1 m. 74% of the data points in the analysis are derived from measurements, 26% are filled-in through nearest-neighbor extrapolation.

3.3.2. Results and discussion

The instantaneous flow field of figure 3.3 is geometrically decomposed following the method outlined above. The decomposed flow field is presented in figure 3.4.

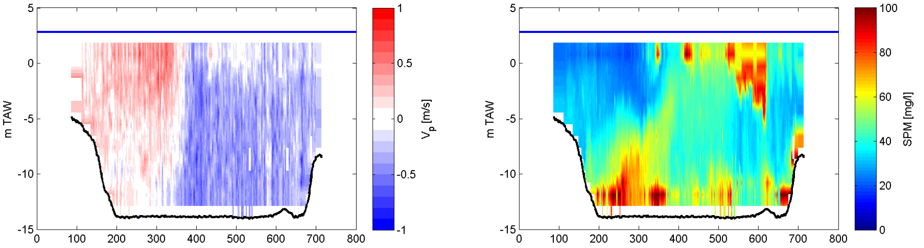

Figure 3.3: Measured perpendicular flow (left panel) and suspended sediment concentration (right panel). The measurement was performed at the entrance of the harbor of Zeebrugge, at 1.5h before HW during a spring tide.

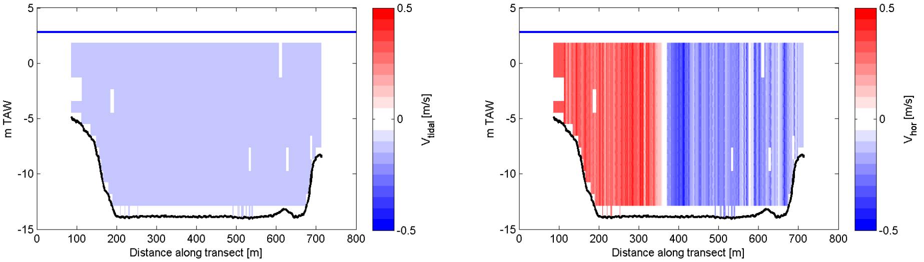

(a) v_{tidal} (b) v_{hor}

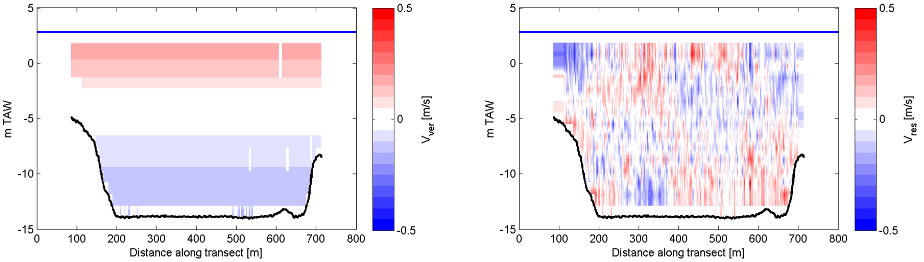

(c) v_{ver} (d) v_{res}

Figure 3.4: Result of the geometric decomposition of a measured flow transect at the entrance of the harbor of Zeebrugge (see figure 3.3) into the tidal component (or cross-sectional average) in (a), the horizontal component (b), the vertical component (c), and the residual component (d).

The geometric decomposition shown in figure 3.4 is done for all 22 measured transects. For each component and for every transect, the instantaneous water and sediment fluxes are calculated. Figure 3.5 presents those calculated fluxes for all measured transects during the entirety of the measurement campaign, which spans a tidal cycle. The left panel of figure 3.5 shows the fluxes associated with the horizontal component of the flow. The tidal variation of F_{hor}^{wat} and F_{hor}^{sed} can be seen in the top panel. F_{hor}^{wat} is decomposed into $F_{hor}^{wat^+}$ and $F_{hor}^{wat^-}$ in the second panel. The third panel shows the decomposition of F_{hor}^{sed} into ${F_{hor}^{sed}}^+$ and ${F_{hor}^{sed}}^-$. The water level is added for reference in the bottom panel. The right panel of figure 3.5 shows the fluxes associated with the vertical flow component.

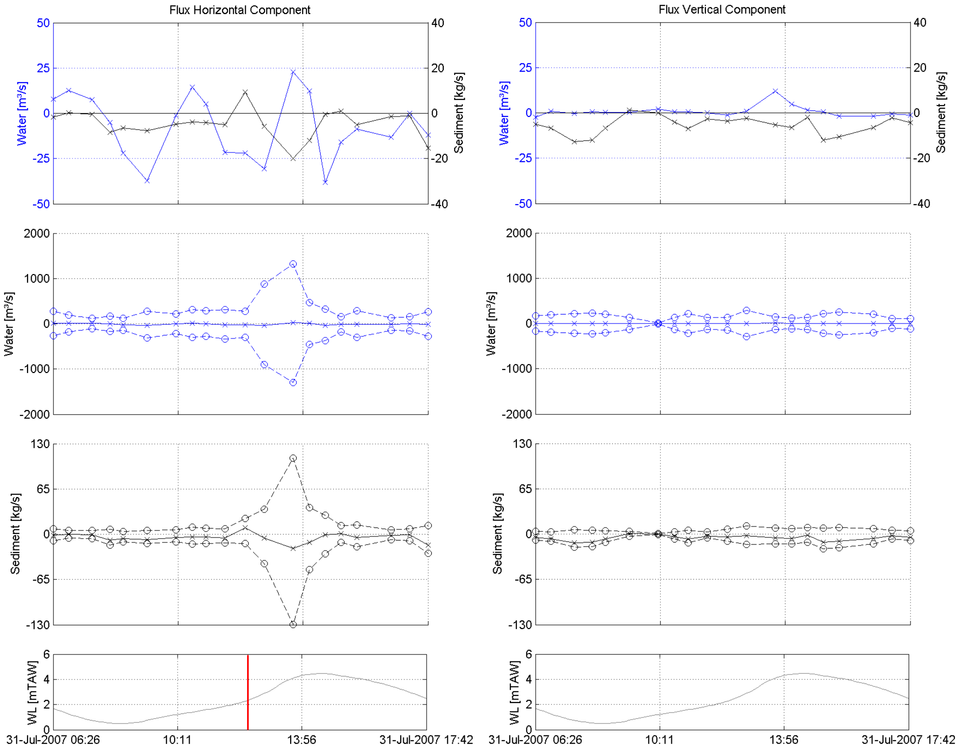

Figure 3.5: Results for the Zeebrugge harbor entrance. Horizontal exchange is shown on the left and vertical exchange on the right. Net flux of water (blue) and sediment (black) in the top panel. Gross flux (dotted line) and net flux (full line) of water (blue) and sediment (black) in the two middle panels. Water level is added for reference in the bottom panel. Inflow is negative. The time of measurement of the measured transect discussed above is indicated with a red line.

In general, the net sediment flux is directed inward. Table 3.1 gives the decomposition of the total sediment fluxes (integrated over a tidal period): $\widehat{F^{sed}}$, $\widehat{F^{sed}}^+$ and $\widehat{F^{sed}}^-$.

Table 3.1 shows that the horizontal exchange is the most important component of gross sediment exchange at the harbor mouth of Zeebrugge. The left panel in figure 3.5 shows that most horizontal sediment exchange happens from two hours before high water to high water. Around that time, the flood flow in the North Sea (directed northeastward along the Belgian coast) drives a primary gyre in the

Results in TDM/tide	Positive (outflow)	Negative (inflow)	Net	Gross
Tidal	893	-912	-18	1 805
Vertical	399	-728	-329	1 127
Horizontal	1 030	-1 330	-301	2 360
Residual	918	-978	-59	1 896
Total	3 240	-3 950	-708	7 190

Table 3.1: Decomposition of total sediment exchange (in TDM/tide) at the Zeebrugge harbor entrance during a tidal cycle (31 July 2007) into four components and into positive (outflow) and negative (inflow) contributions.

harbor. The gyre is transported into the basin with the net tidal inflow. This results in water inflow concentrated towards the eastern breakwater and outflow towards the western breakwater. The combination of a gyre with tidal inflow is evident from the measured velocity field in figure 3.3, and its decomposition in figure 3.4. Because of sediment settling in the harbor, the sediment concentration in the outflowing water is lower than that in the inflowing water.

The gross vertical water exchange is only half as important as the gross horizontal water exchange (figure 3.5, second panel from the top). The density difference inside and outside the harbor is too small to trigger a significant density driven exchange flow. The difference between horizontally and vertically driven sediment exchange is less apparent for the net sediment import into the Zeebrugge harbor (see table 3.1). This could be related to limits in accuracy when calculating a relatively small net value by subtracting two relatively large contributions.

A net import of 708 TDM during a tidal cycle in July 2007 is lower than what would be expected from the dredging statistics (~6100 TDM/tide, on average). One tidal cycle is not representative however for the average conditions over a longer period. Furthermore, the analyzed tidal cycle was measured in summer conditions, when the suspended sediment concentration (SSC) in the North Sea is generally lower (see the discussion in section 2.12.2). Note that estimates of net sediment import based on ADCP measurements are very sensitive to the extrapolation of near-bed concentrations (see the discussion in section 4.4.4). It is hypothesized that the lack of measurement data in the bottom meter causes the ADCP measurement to significantly underpredict the sediment exchange.

3.4. Application to Deurganckdok

3.4.1. Situation

Deurganckdok is a tidal dock in the Port of Antwerp, on the left bank of the Lower Sea Scheldt, which is the stretch of the Scheldt estuary between the Belgium-Dutch border and Rupelmonde (see figure 3.2). The connection between the dock and the estuary was opened in 2005. In contrast to pre-existing docks in the Port of

Antwerp, in which ships enter through locks, the entrance of Deurganckdok has an open connection to the Lower Sea Scheldt. This part of the Scheldt is characterized by a large horizontal salinity gradient and an estuarine turbidity maximum with depth-averaged concentrations ranging from 50 to 500 mg/l. During measurement campaigns in the vicinity of Deurganckdok, concentrations larger than 1 g/l were seldom found (IMDC, 2011). Additional measurements in the Scheldt estuary revealed that a thin fluid mud layer is formed during slack water, which is re-entrained during the following tidal cycle. However, no evidence of thick fluid mud formation near the Deurganckdok was found during the extensive measurement campaigns. This therefore suggests that all sediment supplied to the Deurganckdok is transported in suspension in the water column (van Maren et al., 2009).

The typical tidal amplitude at Deurganckdok is 5 m. The open water surface is 106 m^2, which gives a tidal volume of 5 x 10^6 m^3. The cross section between the dock and the Scheldt is about 6 800 m^2. Over the period 2006-2010, on average 0.8 MTDM/year was dredged in the Deurganckdok every year and disposed of on authorized disposal sites in the Lower Sea Scheldt. This number includes maintenance dredging, but excludes capital dredging.

In 2005 a measurement campaign of flow, salinity and sediment concentration was carried out in order to gain insight into the factors contributing to the siltation of Deurganckdok. One of the measurements consisted of 50 sailed transects across the entrance of Deurganckdok, performed over a tidal cycle (an average tide in march 2006). During this campaign, water velocity and sediment concentration were estimated using a 600 kHz Workhorse Acoustic Doppler Current Profiler (ADCP) with a calibrated interpretation of the acoustic backscatter to determine the sediment concentration. This calibration was performed by taking water samples during the campaign (IMDC et al., 2007).

A transect was typically 400 m in length, and consisted of 70 to 90 ensembles (vertical profiles). Each ensemble had a vertical resolution of 50 cm. Figure 3.6 shows an example transect, measured during flood tide, around the time of high water. Flow velocity (left panel) and suspended sediment concentration (right panel) were measured at the same time. For the analysis, the data are resampled over a regular grid of 1 m x 1 m. 67% of the data points in the analysis are derived from measurements, 33% are filled-in through nearest-neighbor extrapolation.

3.4.2. Results and discussion

The flow field of figure 3.6 is geometrically decomposed following the method outlined above. The decomposed flow field is presented in figure 3.7. The tidal component around high water is very small. The inflow at the right hand side of the dock (figure 3.7, panel b) indicates that there is still flood flow in the Scheldt, which drives a primary gyre across the entrance. Note the important vertical exchange (figure 3.7, panel c).

Following the same method as for the Zeebrugge case, figure 3.8 shows the intratidal variation of the horizontal and the vertical component of the flow and sediment flux. In general, the net sediment flux is directed inward. The most notable driver of this flux is the vertical component around the time of high water

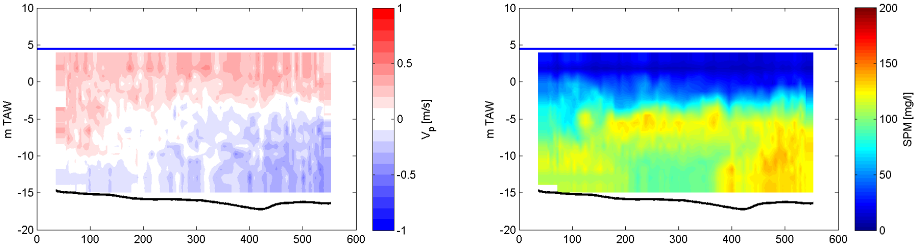

Figure 3.6: Measured perpendicular flow (left panel) and suspended sediment concentration (right panel). The measurement was performed at the entrance of Deurganckdok around HW during an average tide.

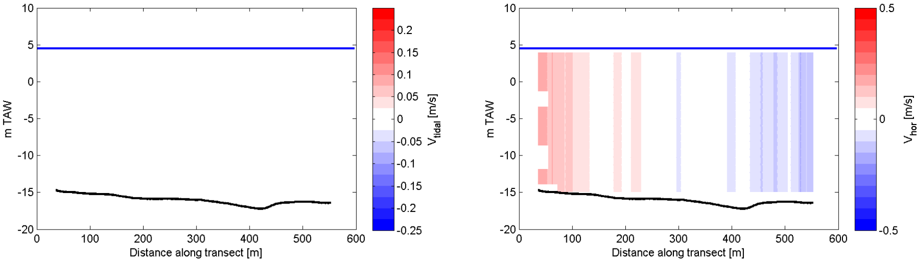

(a) v_{tidal} (b) v_{hor}

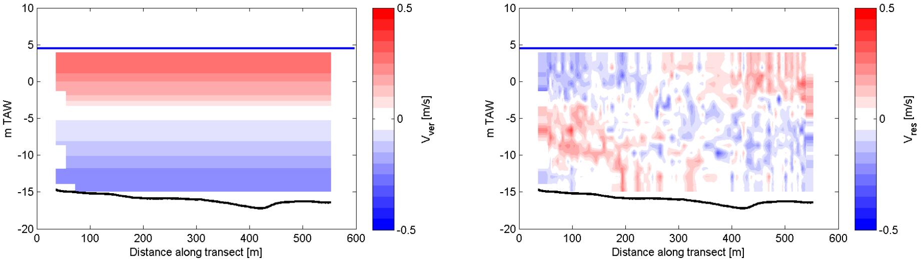

(c) v_{ver} (d) v_{res}

Figure 3.7: Result of the geometric decomposition of a measured flow transect at the entrance of Deurganckdok (see figure 3.6) into the tidal component (or cross-sectional average) in panel (a), the horizontal component (b), the vertical component (c), and the residual component (d).

(see right panel in figure 3.8 and the gross figures in table 3.2). Whereas the horizontal component is significant from four hours before high water to one hour after, it is the vertical component from half an hour before high water to two hours after that has the larger net effect, as seen in figure 3.8.

During the measurements in 2006, there was a total net import of 868 tonnes of dry matter (see table 2). This is well within the range of 1 100 +/- 420 TDM/tide obtained from 3 years of available data (IMDC, 2011). For Deurganckdok, the relative

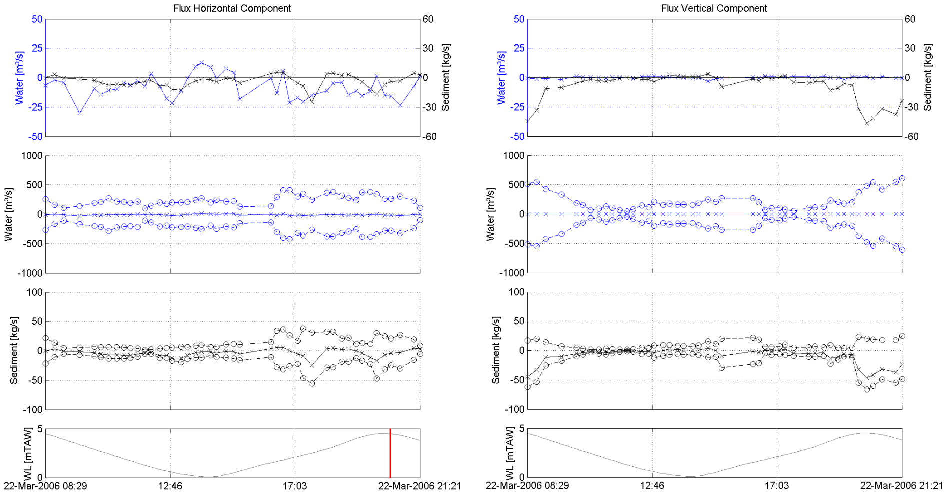

Figure 3.8: Results for the Deurganckdok harbor entrance. Horizontal exchange is shown on the left and vertical exchange on the right. Net flux of water (blue) and sediment (black) in the top panel. Gross flux (dotted line) and net flux (full line) of water (blue) and sediment (black) in the two middle panels. Water level is added for reference in the bottom panel. Inflow is negative. The time of measurement of the measured transect discussed above is indicated with a red line.

Results in TDM/tide	Positive (outflow)	Negative (inflow)	Net	Gross
Tidal	278	-174	104	452
Vertical	758	-1 540	-779	2 298
Horizontal	843	-1 040	-192	1 883
Residual	888	-889	-2	1 777
Total	2 770	-3 640	-868	6 410

Table 3.2: Decomposition of total sediment exchange (in TDM/tide) at the Deurganckdok harbor entrance during a tidal cycle (22 March 2006) into four components and into positive (outflow) and negative (inflow) contributions.

importance of vertical exchange is in accordance with the current understanding of the factors contributing to siltation there. Although the salinity in the Scheldt estuary is vertically uniform, the dock itself is strongly stratified. The horizontal gradient of salinity in the Lower Sea Scheldt in front of Deurganckdok, combined with a tidal excursion of the salinity front, yields a small tidal salinity variation. Fettweis et al. (1998) found an average tidal salinity amplitude of 4.5 ppt at Prosperpolder, a measurement station downstream of Deurganckdok. The salinity in the dock also has a tidal salinity variation which lags behind to the salinity in the Scheldt. Thus a tidally varying density current exists between the Scheldt estuary and the dock, that is driven by horizontal gradients (between river and dock) in the vertical density distribution. When the salinity in the Scheldt estuary is higher than in the dock, this results in an inflow of saline water into the dock in the lower half of the water column, which is compensated by outflow of less dense surface water. This occurs typically around high water. This flow pattern is reversed when the salinity in the dock is higher than in the Scheldt estuary (van Maren et al., 2009). Previous measurement campaigns had already established that the sediment concentration during flood reaches its maximum 0-1 hour before high water. Furthermore the sediment concentrations during flood are highest on the left bank of the Scheldt estuary, i.e. close to the Deurganckdok (IMDC et al., 2005). Thus the maximum sediment concentrations are present at the time and the location when and where the salinity-driven density exchange flow is directed into the dock close to the bottom. These established mechanisms are also apparent in the analyzed measurement data, as the right panel in figure 3.8 shows an important net amount of sediment entering the dock through the vertical component around the time of high water.

3.5. Summary and conclusions

This chapter describes a method to decompose the exchange flow of water and sediment between a harbor and the surrounding waters into three main components: cross-sectional average, horizontal and vertical exchange flows. The method is applied to measurements at two harbor basins in Belgium: Zeebrugge (a coastal harbor) and Deurganckdok (a tidal basin in the Scheldt estuary). Both basins are located close to separate turbidity maxima (respectively a coastal and an estuarine turbidity maximum), and both require maintenance dredging in order to guarantee their nautical accessibility.

When the decomposition is applied to synoptic measurements of flow and sediment flux, differences can be identified in the mechanisms that drive siltation in both harbor basins. In Deurganckdok, the method clearly identifies the density-driven vertical exchange flow around high water, also described by van Maren et al. (2009). In Zeebrugge, no clear signature is seen in the measurements of a density-driven vertical exchange flow. Most of the sediment is exchanged through a clockwise gyre that is advected into the harbor, just prior to high water. These differences are not directly apparent from the 'raw' data of velocity and sediment concentration, but become visible through the decomposition. It can be applied just as well to the results of a 3D numerical model of hydrodynamics and sediment transport, provided it has sufficient horizontal, vertical and temporal resolution to capture the dynamics at the harbor mouth. It can therefore be used as a tool in model calibration, as is illustrated in section 5.11.3 of this thesis.

References

Costa, R. (1989). Flow-fine sediment hysteresis in sediment-stratified coastal waters. Technical report, Oceanographic Engineering Department, University of Florida, Gainesville, FL, U.S.A.

de Nijs, M. A. J., Winterwerp, J. C., and Pietrzak, J. D. (2009). On harbour siltation in the fresh-salt water mixing region. *Continental Shelf Research*, 29(1):175–193.

Eysink, W. D. (1989). Sedimentation in harbour basins. Small density differences may cause serious effects. In *9th International Harbour Congress*.

Fettweis, M., Sas, M., and Monbaliu, J. (1998). Seasonal, Neap-spring and Tidal Variation of Cohesive Sediment Concentration in the Scheldt Estuary, Belgium. *Estuarine, Coastal and Shelf Science*, 47(1):21–36.

IMDC (2011). Externe effecten Deurganckdok: deelrapport 1. Syntheserapport van het Current Deflecting Wall onderzoek. Technical report, Vlaamse Overheid. Afdeling Maritieme Toegang, Antwerpen.

IMDC, WL|Delft Hydraulics, and GEMS International (2005). Uitbreiding studie densiteitsstromingen in de Beneden Zeeschelde in het kader van LTV meetcampagne naar hooggeconcentreerde slibsuspensies: deelrapport 2.5. Deurganckdok 16 februari 2005. Technical report, Waterbouwkundig Laboratorium en Hydrologisch Onderzoek, Antwerpen.

IMDC, WL|Delft Hydraulics, and GEMS International (2007). Langdurige metingen Deurganckdok: opvolging en analyse aanslibbing: deelrapport 2.3: 13u meting springtij - ingang Deurganck - 22/03/2006 - Veremans. Technical report, Waterbouwkundig Laboratorium, Antwerpen.

IMDC, WL|Delft Hydraulics, and GEMS International (2008). Langdurige monitoring van zout/zoet-verdeling in de haven van Zeebrugge en monitoring van zoutconcentratie, slibconcentratie: deelrapport 7.1. 13-uursmeetcampagne SiltProfiler en Sediview 31/07/2007 Haveningang tijdens springtij. Technical report, Waterbouwkundig Laboratorium, Antwerpen.

Langendoen, E. J. (1992). *Flow patterns and transport of dissolved matter in tidal harbours*. PhD thesis.

Murray, S. P. and Siripong, A. (1978). Role of lateral gradients and longitudinal dispersion in the salt balance of a shallow well mixed estuary. *Estuarine Transport Processes: Symposium (The Belle W. Baruch Library In Marine Science)*, pages 113–124.

PIANC (2008). Minimising harbour siltation. Report no 102. Technical report, PIANC Working Group 43.

Stoschek, O. and Zimmermann, C. (2006). Water exchange and sedimentation in an estuarine tidal harbor using three-dimensional simulation. *Journal of Waterway, Port, Coastal and Ocean Engineering*, 132(5):410–414.

van Maren, D. S., Winterwerp, J. C., Sas, M., and Vanlede, J. (2009). The effect of dock length on harbour siltation. *Continental Shelf Research*, 29(11-12):1410–1425.

Vanlede, J. and Dujardin, A. (2014). A geometric method to study water and sediment exchange in tidal harbors. *Ocean Dynamics*, 64(11):1631–1641.

Winterwerp, J. C. (2005). Reducing harbor siltation. I: Methodology. *Journal of Waterway, Port, Coastal and Ocean Engineering*, 131(6):258.

4

Mud dynamics in the Zeebrugge harbor

4.1. Introduction

The aim of this chapter is to describe the different influencing factors and time scales that are relevant to mud dynamics in the harbor basin. The harbor of Zeebrugge is subject to high siltation rates of mainly mud and, as a result, maintenance dredging works are mandatory (Fettweis and Nechad, 2011; Fettweis et al., 2016). The amount to be dredged depends on the inflow of mud into the harbor basin. The maintenance depth and the dredging strategy are guided by the principle of nautical depth. PIANC (1997) defines the nautical depth as the level at which the physical characteristics of the bottom reach a critical limit beyond which contact with a ship's keel causes either damage or unacceptable effects on controllability and maneuverability. In Zeebrugge, the nautical bottom is defined as the density level of 1200 kg/m³.

Present regulations at Zeebrugge stipulate that for safe maritime access to the harbor, the ship should have a positive Under Keel Clearance (UKC) of at least 10% (relative to its draft) above the nautical bottom and no more than 7% negative UKC below the mud-water interface, which is measured as the reflector of a 210 kHz echo sounder. This means that for the accessibility of the harbor, both the vertical position of the 210 kHz reflector and the 1200 kg/m³ density level are important. Both levels (together with the 33 kHz reflector) are monitored regularly to steer maintenance dredging. This practice is the result of extensive investigations (Delefortrie et al., 2007) and is related to the local mud and maneuvering conditions in the harbor of Zeebrugge.

The sediments between the 210 and 33 kHz reflectors consist mainly of soft or even fluid mud. Fluid mud is a high-concentration suspension that typically behaves as a non-Newtonian fluid (McAnally et al., 2016). It is formed if the rate

---

This chapter has been published by Vanlede et al. in Ocean Dynamics **69**, 9 (2019).

of sediment deposition exceeds the dewatering/consolidation rate. If not resuspended by entrainment processes, fluid mud slowly consolidates to form bed material (McAnally et al., 2007). Fluid mud typically has a volume fraction between 0.02 and 0.13 (Mehta, 1991), which corresponds to limiting bulk densities of 1060 and 1240 kg/m³. See also Mehta et al. (2014) for a description of the properties and behavior of fluid mud in relation to nautical depth estimation. Mud is generally transported in suspension or, in some cases, as near-bed fluid mud (Winterwerp, 2005; Kirby, 2011). Flow exchange mechanisms at a harbor entrance are well known and include tides, horizontal entrainment, and density currents (Vanlede and Dujardin, 2014).

4.2. Study site

Zeebrugge is a tidal harbor, situated in the dynamic and turbid Belgian coastal zone. The harbor was extended seaward to its present form in the period from 1979 to 1986, with the construction of two 4-km-long breakwaters extending about 3 km out to sea, see figure 4.1.

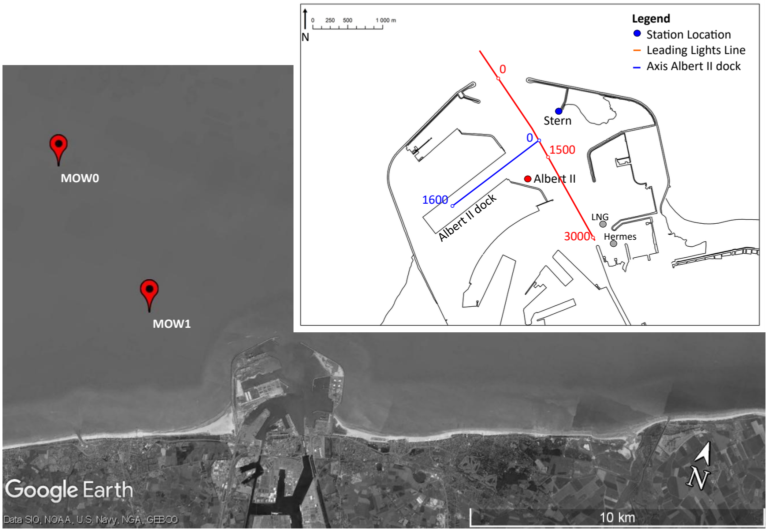

Figure 4.1: Map of the Belgian Coastal area (Southern North Sea) showing the measurement stations outside (MOW0, MOW1) and inside the harbor of Zeebrugge (Stern, Albert II, LNG, Hermes). The red line is the leading lights line. The blue line is the axis of the Albert II dock. The background is a satellite image from Google Earth. The harbor entrance is located at 51°21′N 3°11′E.

The outer harbor is maintained at a depth of up to 15.5 m below LAT (Lowest Astronomical Tide) and the connection towards the open sea at 15.8 m below LAT. The harbor and the channels are thus substantially deeper than the nearshore area, where water depths are generally less than 10 m below LAT (Fettweis et al., 2009). The analysis in this chapter is limited to the outer harbor; the inner harbor (which lies behind locks) is not considered. Averaged over nine years, 4.3 (2.6 to 5.0)

MTDM/yr of mud was dredged from Zeebrugge harbor, with the range over the period 2005 to 2013 indicated in brackets. The material is disposed at authorized disposal sites in the North Sea, at 5-15 km from the harbor (Dujardin et al., 2016; Antea Belgium, 2016). The sediments dredged in CDNB (the central part of the outer harbor) have an average mud content of 94% (Pieters et al., 2001).

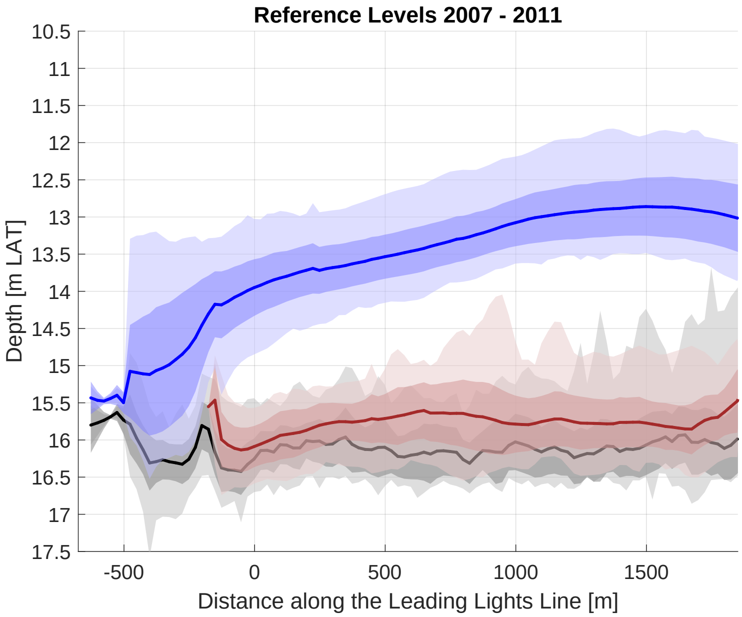

Figure 4.2: The level of the mud-water interface (210 kHz) in blue, of the 1200 kg/m³ density level in brown and of the 33 kHz reflector in black. Data of 2007-2011. Colored bands are plus and minus one standard deviation, and min and max values. Values on X-axis correspond to the distance along the leading lights line (indicated on figure 4.1).

The fluid mud layer inside the harbor basin (i.e. the layer between the 210 and 33 kHz reflectors) has a thickness of up to 3 m in front of the entrance of the Albert II dock, decreasing to 2 m at the harbor entrance (see figure 4.2). The mud-water interface has a concave-down shape.

Typical vertical density profiles inside the harbor basin are shown in figure 4.3. Note that since these profiles and the measurements along the leading lights line are not performed on exactly the same time and location, the position of the 210 (or 33) kHz reflector may differ slightly between both datasets. The vertical density profiles were measured with the Navitracker instrument, which is a continuous vertical profiling gamma-ray transmission gauge. The data in figure 4.3 show that the material found in between the 210 and 33 kHz reflectors has a density between the limiting bulk densities of fluid mud (1060 and 1240 kg/m³).

The tides are semidiurnal with a mean amplitude of 3.6 m. Peak ebb and flood

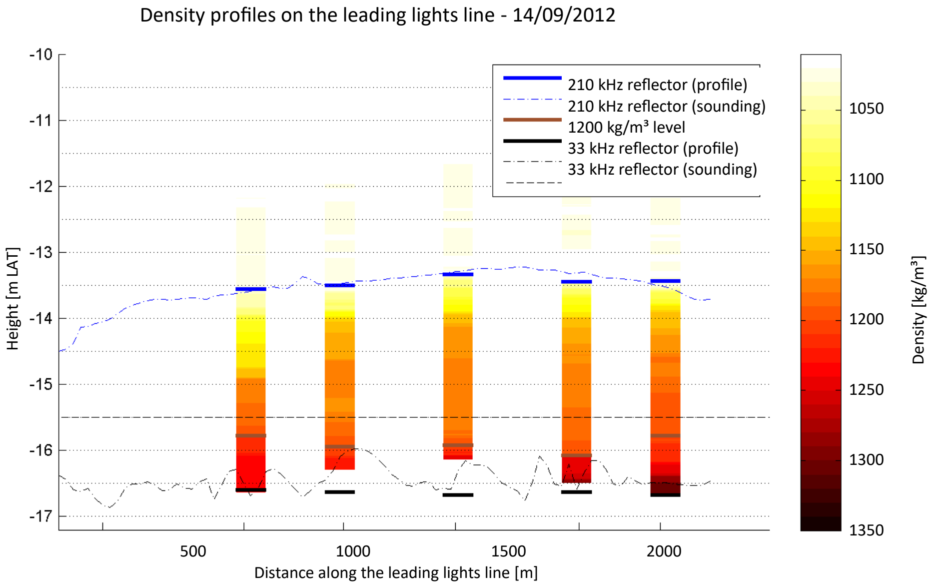

Figure 4.3: Vertical density profiles measured on the leading lights line. The 210 kHz reflector is indicated in blue, the 33 kHz reflector in black and the density level of 1200 kg/m³ in brown. The target maintenance depth of 15.5 m below LAT is indicated with a horizontal dashed line.

velocities are high in front of the harbor entrance, due to the breakwaters protruding from the coastline, which deflects ebb and flood flow close to the coast. Flood flow (directed NE) occurs from 3h before HW to 2h40 after HW during spring tide. Peak velocity in front of the harbor entrance reaches 2.1 m/s and occurs 40 minutes before HW during spring tide (Afdeling Kust - Hydrografie, 2001). The flow field inside the harbor basin is characterized by a primary gyre (figure 4.4 shows the flow field at 1.5h before HW), driven by the shear at the interface between water in the harbor and the flood flow in the North Sea. It is advected into the basin during rising tide. The primary gyre drives a smaller, secondary gyre deeper in the harbor (1h before HW to HW), which is advected out of the basin during falling tide (HW to 2h after HW).

4.3. Methodology

4.3.1. Depth soundings

Different datasets with depth soundings during the period 1999-2011 were combined for the analysis in this study. The 210 and 33 kHz reflectors were sometimes measured as map data over larger areas in the harbor, and sometimes only as line data along the leading lights line (indicated on figure 4.1). The map data were interpolated on the leading lights line resulting in a combined dataset of depth along the leading lights line over time. Sounding data are used to compute changes in

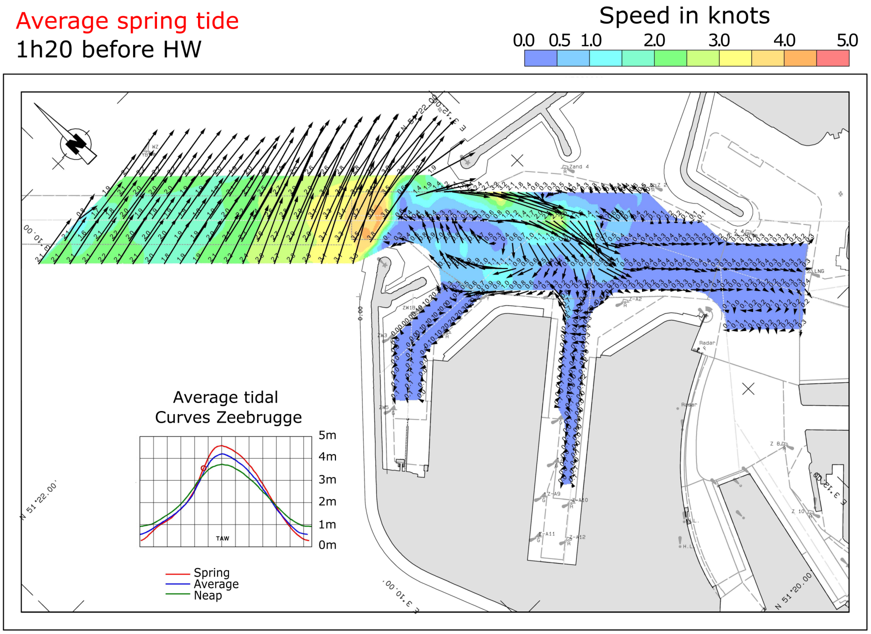

Figure 4.4: Flow field (knots) in the harbor during spring tide and maximum flood flow (1.5h before HW). Excerpt from the flow atlas of Zeebrugge (Afdeling Kust - Hydrografie, 2001).

the volume of deposited sediments in the basin. Only those depth soundings that cover more than 50% of the leading lights line are retained. Since the aim is to link observed sediment volume changes (from the soundings) with data on dredging activity and meteo conditions between two consecutive soundings, it is important that the time interval between pairs of depth soundings in the dataset remains more or less constant. Therefore only those pairs of depth soundings are retained that are less than 30 days apart. Following these selection criteria, 80% of the dataset is retained. The volume change is then derived from the depth data on the leading lights line by multiplying the average depth difference with the total surface area of the map data. The uncertainty in volume change when only line data are used has been estimated from the map data, and is about 2% (Dujardin et al., 2016).

4.3.2. Calculation of the natural depth change of the mud-water interface

The 210 kHz reflector is considered to be the mud-water interface. A depth change of this reflector corresponds to a change of the mud volume in the harbor by natural processes and dredging. A volume balance is set up to decompose the measured depth change into the natural depth change and the effect of dredging.

$$\Delta h^m = \Delta h^d + \Delta h^n \tag{4.1}$$

$$\Delta h^d = \frac{-m^d(\rho_g - \rho_w)}{A\rho_g(\rho_b - \rho_w)} \tag{4.2}$$

The natural depth change of the mud-water interface Δh^n corresponds to the cumulative effect of deposition (positive sign), and resuspension and consolidation (negative sign). It is calculated from Δh^m and Δh^d. Δh^m is the measured depth change of the mud-water interface, derived from depth soundings. A negative sign corresponds to a depth increase. Δh^d is the effect of dredging on the depth of the mud-water interface. It is calculated from the dry mass of the dredged material m^d using equation 4.2, with A the area that was dredged, ρ_g the grain density (2650 kg/m³), ρ_b the in situ bulk density and ρ_w the density of seawater (taken here as 1025 kg/m³). Note that m^d is calculated and logged directly by the dredging information system on board of the vessel.

Because the in situ bulk density ρ_b (see example in figure 4.3) is monitored at a lower sampling frequency than the daily dredging operations, it has to be estimated for each dredging campaign in order to calculate Δh^d. In this analysis, ρ_b of the dredged material is estimated from the bulk density of the sediment in the hopper dredger, which is measured and logged during each dredging campaign. The conversion is done based on an analysis of the relation between in situ volume concentration (IVC) and hopper volume concentration (HVC). We call this relation between volume concentrations the *bulking curve*. Note that theoretically, this curve has to go through (0,0) because pure water in situ will be pure water in the hopper dredger. For a similar reason, the curve also has to go through (1,1). Physically, dredging related processes such as water entrainment and de-gassing of sediment will influence this relationship.

Figure 4.5 shows the observed part of the bulking curve as a scatterplot. It is based on available density and dredging data in the harbor basin of Zeebrugge for the period 2012-2014. Each data point corresponds to one dredging campaign. The HVC is calculated from the bulk density inside the hopper dredger, as logged in the dredging information system. The corresponding IVC is calculated from the density profile closest to the dredging location and measured prior to the dredging campaign, by vertically averaging it over 1 m, centered on the dredging depth. The substantial scatter in the plot is partly due to the fact that the dredging campaign and the corresponding density profile are not carried out at the same time and place. Therefore, the reported bulk density in the hopper dredger is taken as the estimate for the in situ bulk density ρ_b (shown as the dotted 1:1 line in figure 4.5).

4.3.3. Measurements at fixed stations

Current velocity, salinity, temperature and suspended sediment concentration (SSC) were measured at four stations inside the harbor (Stern, Albert II, LNG and Hermes, see figure 4.1) at about 2 m below LAT and about 2 meters above the bed (mab). Each measuring station was equipped with a point velocimeter (Aquadopp),

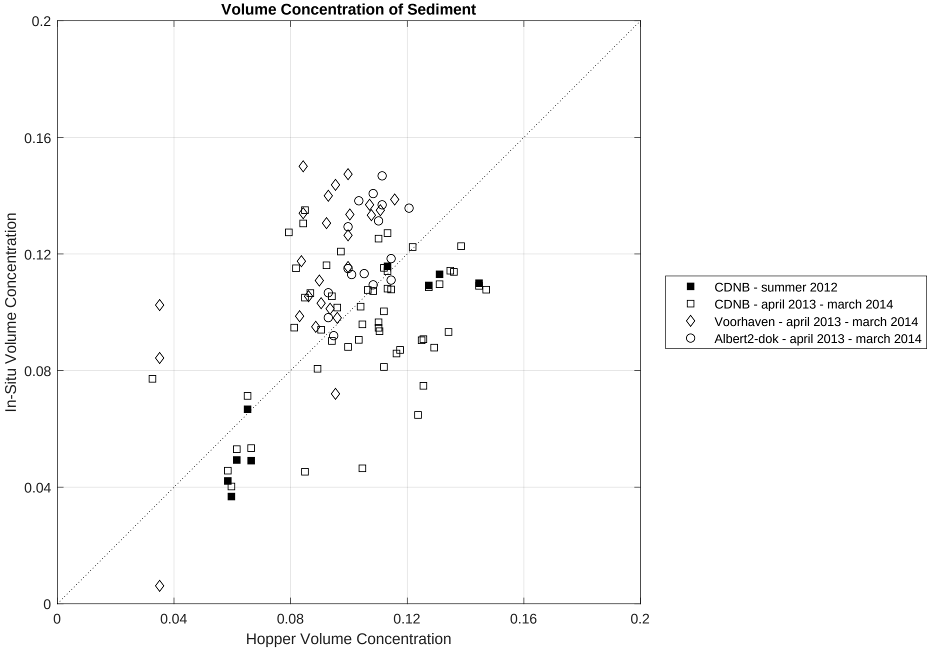

Figure 4.5: Bulking curve of in situ volume concentration [-] vs hopper volume concentration [-], based on measurement data from the Zeebrugge harbor basin from 2012-2014.

an OBS3+ and a CT-probe (Valeport 620). At station Hermes the instrumentation was mounted on a fixed cable, attached to the gangway of the pier and a concrete anchor at the bottom. In the other three measuring stations the instrumentation was fixed on a steel cable between an anchor and an underwater buoy. The data were collected every 10 minutes (averaged over 60 second bursts). The measurement campaign lasted for 400 days from 14/03/2013 to 18/04/2014. More details on the instrumentation can be found in (Antea Belgium, 2015a). Near-bed SSC in the North Sea is measured with a benthic lander located about 5 km northwest of the harbor at location MOW1 (see figure 4.1). For salinity, on average 76% of all data points are considered usable, for SSC 69%. The most important reasons for missing data were battery problems, bio-fouling with algae and barnacles and technical problems with the sensors.

The absolute heights of the sensors at locations Stern, Albert II and LNG varies over time. Since these stations are located at the edge of an area that is maintained at depth for navigation, they had to be installed on a sloping bed. This means that each time the instruments were taken out of the water and re-deployed (which occurs every 2 to 4 weeks), a variation in the horizontal position has an impact on the absolute height of the installed sensor.

4.3.4. SSC measurements from ADCP transects in- and outside the harbor

From March 2013 to April 2014, 113 longitudinal transects were sailed in the harbor with the research vessel RV Belgica (see figure 4.1 for the location of the transect). The acoustic backscatter recorded from a hull-mounted 300 kHz ADCP was converted to SSC (Thorne et al., 1994; Holdaway et al., 1999). Example SSC data are shown in figure 4.6.

The conversion from acoustic backscatter to SSC was done as follows. During an 8 hour period, water samples and vertical profiles were collected inside and outside the harbor using a CTD, an OBS and a LISST 100X. The water samples were analyzed for SPM, Particulate Organic Matter (POC) and Chlorophyll concentration. The OBS signal was converted into SSC through a linear relationship obtained after filtering and weighing of water samples. The relationship between the acoustic backscatter (in dB) and the SSC was established using the OBS data. One relationship was applied to the whole dataset. The acoustic backscatter signal depends strongly on particle size and density however, and the samples collected for calibration may not represent SPM properties in all 113 transects. Also, the SPM inside the harbor has larger floc sizes and lower densities with higher organic content, while outside the harbor the SPM occurs as bio-mineral aggregates as described by Fettweis and Lee (2017). The echo intensity of the backscattered acoustic signal should therefore only be seen as an estimate of the SSC.

It should be noted that there is a low correlation (R^2=0.35) between the SSC from the lower OBS-sensor at station Albert II and the corresponding SSC from the ADCP transects (Antea Belgium, 2015b). The SSC derived from the ADCP data are typically 2 times higher than from the OBS sensor at the fixed measurement station, with significant scatter between the two datasets. The scatter could be related to different calibrations to convert the acoustic and the optical backscatter to SSC, and to spatial variation of the concentration. Note that the concentrations that are derived from the ADCP data are only used to establish the intratidal timing; the values of sediment concentration are not used.

4.3.5. Fresh water inflow into the harbor

Fresh water discharge can contribute significantly to the siltation rate of a harbor. The relative contribution is site-specific however (Winterwerp and de Boer, 2016). Fresh water is discharged into the harbor through the Leopoldkanaal and the Schipdonkkanaal. Both canals discharge gravitationally during low water. The daily averaged total fresh water discharge of both canals has a positively skewed distribution with a low median of 1.1 m^3/s and a maximum of 80 m^3/s (Dujardin et al., 2016). Dry periods with no fresh water inflow occur typically during summer and autumn. Because fresh water can only be discharged around low water, the fresh water distribution is tidally modulated. Vertical salinity profiles are available at 27 locations inside the harbor (IMDC et al., 2011). The profiles were measured during 44 campaigns in the period 2007 to 2008.

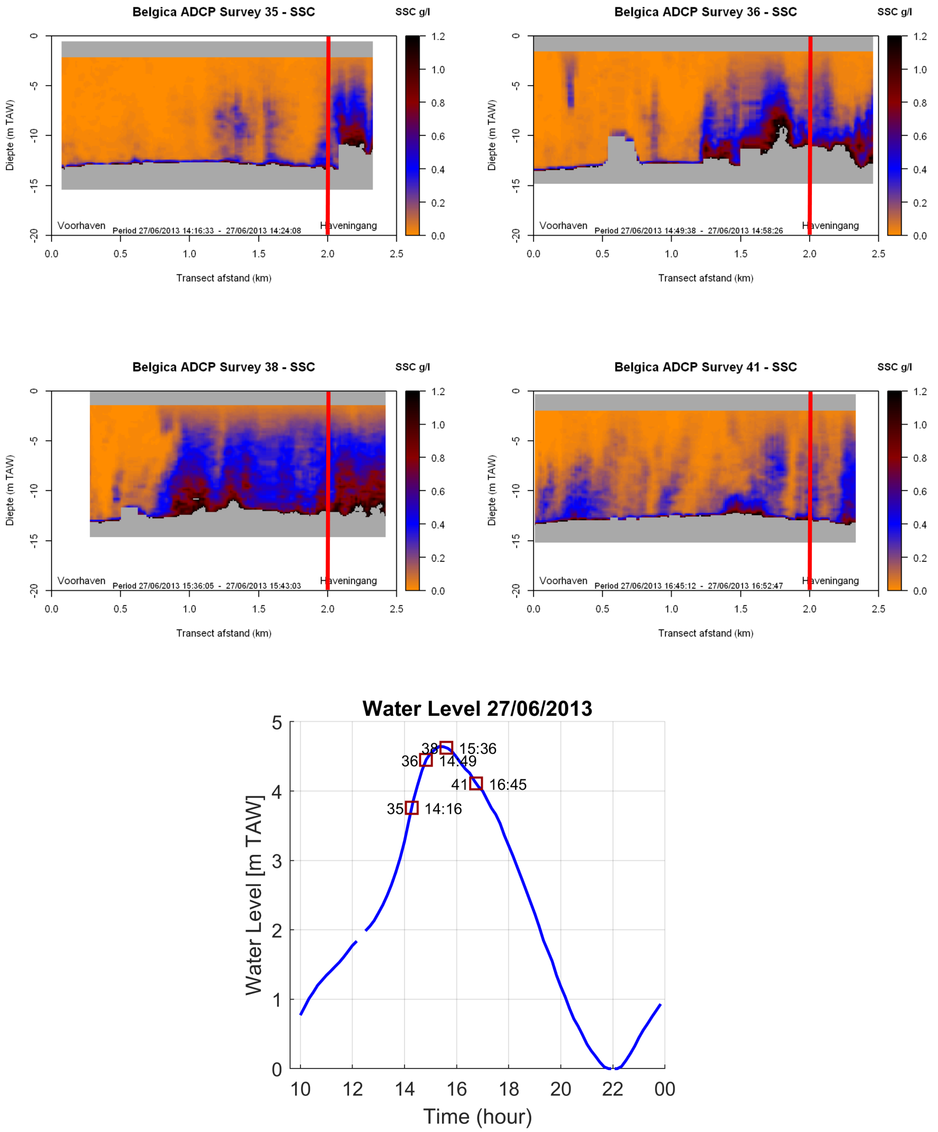

Figure 4.6: SSC from ADCP backscatter, measured on 27/06/2013 on a longitudinal transect in the harbor. The harbor entrance (indicated with a red line) is to the right of each panel. Phase during the tidal cycle clockwise from top left: 1h before HW (survey 35), 30 minutes before HW (survey 36), 30 minutes after HW (survey 38), 2h after HW (survey 41).

4.3.6. Wave data

Wave data from the directional wave buoy at Bol van Heist were analyzed for the period 1999-2011. The wave direction typically varies from north to west-southwest. The significant wave height has a median value of 0.6 m in summer and 0.75 m in winter.

4.3.7. Data classification and ensemble analysis

The time series of SSC and current velocity measured inside the harbor are split into individual tidal cycles, and interpolated with a 10 minute interval on a local time axis relative to the moment of HW. The tidal cycles are grouped in 3 classes, according to the tidal amplitude at Zeebrugge and labeled as spring, mean or neap tide, respectively. All tidal cycles in a certain tidal class are combined in an ensemble, and the average and standard deviation are calculated on the local time axis, see figure 4.7. This ensemble analysis (or phase averaging) is used to gain insight into the intratidal (section 4.4.3) and spring-neap variations (section 4.4.4) of the SSC signal.

4.4. Results and discussion

4.4.1. Influence of fresh water inflow on sediment import

The salinity in the lower half of the water column inside the harbor basin shows no observable vertical gradient. During periods of high fresh water discharge (>10 m³/s), the water column inside the harbor becomes stratified near the surface, with a thin layer (~1 m) of fresh water. This stratification typically dissipates through mixing in 6 to 8 hours. Fresh water import into the harbor may induce a density current into the harbor basin in the lower half of the water column. The velocity of the fresh water front on top of the saline water in the harbor can be estimated following Kranenburg (1998) as

$$c = \sqrt{\varepsilon g \frac{h_1}{h} \frac{(h - h_1)\,(2h - h_1)}{(1 - \beta_1)\,h_1 + (1 + \beta_1)\,h}} \tag{4.3}$$

With ε the relative density difference $\Delta\rho/\rho$, h_1 the height of the fresh water front, h the water depth and β_1 a loss term (between 0 and 1). Note that in case $h_1 = h/2$ and $\beta_1 = 0$, this formulation simplifies to the relation $c = 0.5\sqrt{\varepsilon g h}$, which is often used to describe lock-exchange flow. A fresh water front of 1 m height in a water column of 15 m has a propagation speed of 0.6 m/s ($\beta_1 = 0$), which would (assuming no net water exchange) induce a return flow of only 0.05 m/s into the harbor. This is consistent with an analysis of the velocity field around the harbor entrance of Zeebrugge which shows that water exchange due to density currents is small compared to the total exchange flow (Vanlede and Dujardin, 2014).

The direct import of sediment in suspension via the Leopoldkanaal and the Schipdonkkanaal is negligible. Assuming an average SSC of 50 mg/l in the canals, and a median fresh water discharge of 1.1 m³/s, the import of sediments by the canals only represents 0.05% of the total sediment import.

Fresh water inflow into the harbor therefore does not influence sediment import, neither through a density current, nor through sediment load in suspension. This is confirmed by the fact that no correlation is found between the natural depth change of the mud-water interface (see section 4.3.2) and the fresh water discharge

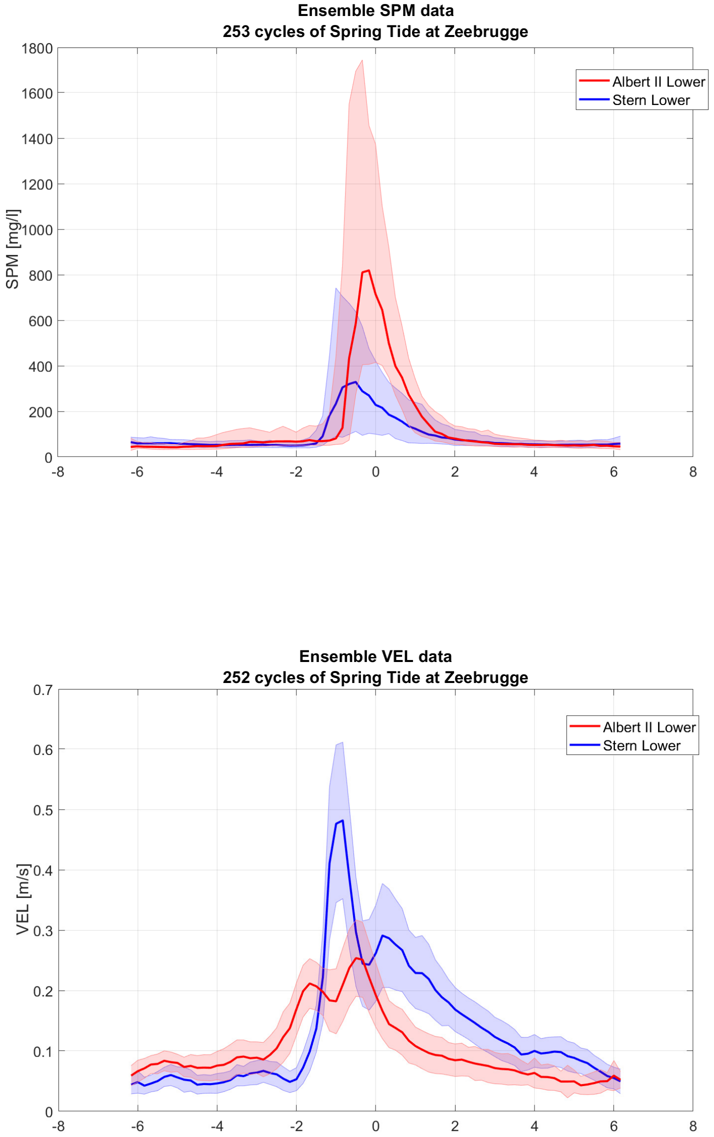

Figure 4.7: Ensemble analysis for SSC (top panel) and velocity (bottom panel), measured during spring tide at 2 mab in stations Albert II (in red) and Stern (in blue). The full line is the median, the shaded area lies between the 20th and 80th percentile.

(Dujardin et al., 2016).

4.4.2. Influence of wind and wave climate on sedimentation

The natural depth change of the mud-water interface (see section 4.3.2) is binned according to the mean wave direction and the peak wave height at station Bol van Heist. The P95 significant wave height is used as a proxy for the peak wave height, and is calculated over the period between two successive depth soundings.

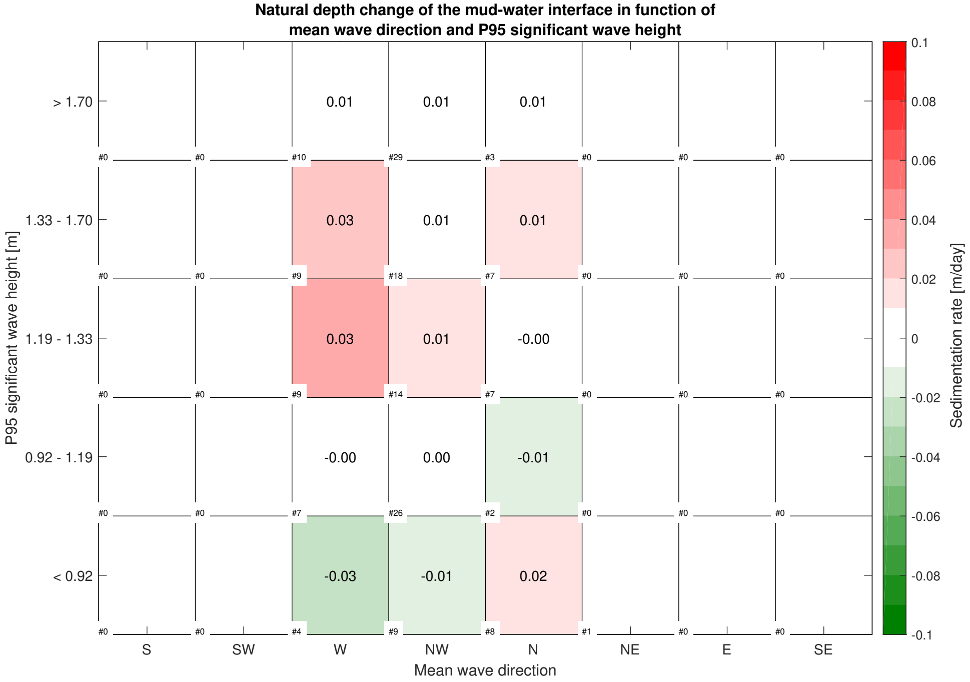

Figure 4.8: Natural depth change of the mud-water interface [m/day] classified according to mean wave direction and P95 significant wave height. The number of data points is shown in the lower left corner of each cell. Bins of less than 3 data points are represented by empty cells.

Figure 4.8 shows only a weak positive correlation (R^2=0.35) between the peak wave height and the natural depth change of the mud-water interface. The mud-water interface rises between 1 and 3 cm/day if the P95 significant wave height is larger than 1.19 m. Note that this result is in contrast to Lanckneus and Van Lancker (2001), who found higher siltation during periods of lower wave heights. The difference between both findings can be related to the low correlation between depth change and wave conditions, which can make the sign of the (weak) correlation dependent on the period that is analyzed.

Following a similar methodology, the influence of wind climate on sedimentation is investigated, but no meaningful correlation is found.

4.4.3. Intratidal variation

Intratidal variation of SSC at fixed stations

Figure 4.7 shows the ensemble analysis of both SSC and current velocity, measured at 2 m above the bed (mab) at stations Stern and Albert II during spring tide (see figure 4.1 for the location). The SSC peaks 1 hour before HW at station Stern, and 50 minutes later at Albert II. This delay is explained in terms of the time of advection of SPM from station Stern to station Albert II by the primary gyre in the harbor basin.

A 50 minute travel time over a 1000 m trajectory corresponds to an average advection velocity of 0.33 m/s. The peak SSC near the bed is higher at station Albert II (900 mg/l), which is located deeper inside the harbor basin than station Stern (600 mg/l), even though the corresponding velocity is lower at station Albert II. This result can be understood in terms of vertical settling during advection between stations Stern and Albert II. This also suggests that local resuspension is not the dominant process that determines sediment concentration in the Albert II dock. The peak SSC at the upper sensor however, is similar at both stations (350 mg/l). This suggests that a slower settling fraction determines the sediment concentrations in the upper part of the water column.

These results are consistent with the analysis of the flow exchange mechanisms between a harbor basin and the open sea, applied to Zeebrugge by Vanlede and Dujardin (2014). They concluded that horizontal exchange is the most important component of the sediment import at the harbor mouth of Zeebrugge, and that most of the sediment import occurs from 2h before high water to high water. In that time frame, flood currents in the North Sea (directed northeastward along the Belgian coast) drive the primary gyre in the harbor mouth, which is advected into the basin during rising tide. This results in water inflow near the eastern breakwater (close to the measurement station Stern, see figure 4.4), and outflow near the western breakwater. Because of sediment settling in the harbor, the sediment concentration in the outflowing water is lower than that in the inflowing water, which results in net import of SPM.

Intratidal variation of SSC from ADCP transects

Figure 4.6 shows four vertical profiles of SSC, measured during a tidal cycle in June 2013 (see section 4.3.4 for a description of the dataset, and figure 4.1 for the location of the transect). The four panels in the figure are arranged clockwise from the top left, and show SPM being transported in suspension from the harbor entrance to deeper inside the harbor. At 1h before HW (top left panel) the sediment in suspension is concentrated outside the harbor. At 30 minutes before HW (top right panel) the suspended sediment has been transported into the harbor. 30 minutes after HW (bottom right panel) the front is advected a further 500 m. 2h after HW (bottom left panel) the SSC in the water column is lower, because of settling and deposition.

The intratidal phasing of the vertical SSC profile is consistent with the evolution of SSC over a tidal cycle at stations Albert II and Stern (see section 4.4.3). The sequence of vertical profiles of SSC in figure 4.6 confirms that the bulk of the SPM is transported into the harbor through advection around HW, and that most transport occurs in the lower half of the water column.

4.4.4. Spring/Neap cycle

Spring/Neap variation in sediment import

The mass of sediment that enters the harbor in suspension has been estimated from ADCP measurements carried out on a transect across the harbor entrance, e.g. by Claeys et al. (2001). In IMDC et al. (2010) two measurement campaigns are described that were carried out during spring and neap tides. In the bottom blanking zone of the ADCP, IMDC et al. (2010) extrapolated the vertical SSC profiles towards the bed. Dujardin et al. (2009) used the same ADCP dataset, but used concurrent turbidity measurements close to the bed to derive the SSC close to the bed. The resulting estimates for the total sediment import are 5 to 10 times higher than in (IMDC et al., 2010). This result underlines the importance of near-bed data for estimating total sediment fluxes.

Table 4.1 summarizes the different estimates of the spring-neap variation in the net sediment influx into the harbor. On average, sediment import into the harbor during spring tide is two to four times higher than during neap tide. This is consistent with the spring-neap variation of SSC outside the harbor, measured with a benthic lander at MOW1 (Fettweis and Baeye, 2015). De Maerschalck et al. (2020) have shown that the peak SSC at 2.3 mab is up to be three times higher during spring than during neap tide.

Source	Net Sediment Influx - Spring Tide (TDM/day)	Net Sediment Influx - Neap Tide (TDM/day)	Ratio Spring/Neap
Claeys (2001)	6400	1590	4.0
Dujardin (2009)	13880	3454	4.0
IMDC (2010)	1468	834	1.8
Average	7357	1986	3.0

Table 4.1: Spring-Neap variation in net sediment influx to the harbor of Zeebrugge.

This is also consistent with the spring-neap variation of peak SSC observed near the entrance of the harbor. An ensemble analysis of the spring-neap variation of SSC at station Stern (figure 4.9) shows a peak in concentration prior to high water, i.e. at the moment of highest sediment import, that is four times higher during spring tide than during neap tide. No significant spring-neap variation was found however at stations deeper inside the harbor (LNG and Hermes).

The flow atlas (Afdeling Kust - Hydrografie, 2001) shows that the maximum velocity near the eastern breakwater during inflow is about 2 times higher during spring than during neap tide. The spring/neap variation in sediment import is therefore a combination of higher SSC and higher velocities during spring tide.

Sediment import, SSC in the Belgian nearshore, and SSC inside the harbor (close

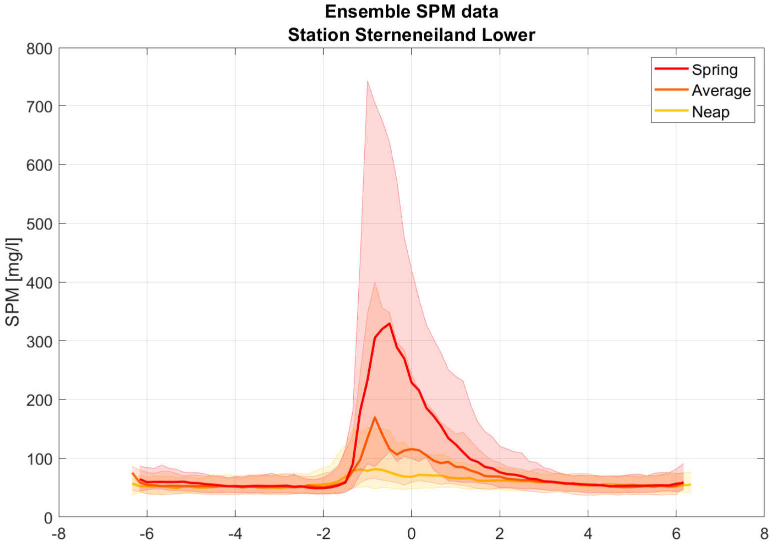

Figure 4.9: Spring (red) to neap (in yellow) variation of SSC over a tidal cycle at station Stern at 2 mab. The full line is the median, the shaded area lies between the 20th and 80th percentile.

to the entrance) are all three to four times higher during spring tide then during neap tide, which is consistent with sediment import through advection. The SSC at the landward end of the harbor does not show this spring/neap variation however, which suggests that it is influenced by different processes, such as resuspension (due to ship movements or dredging activity), or gravitational flow of mud layers inside the harbor.

Influence on the mud-water interface

The previous paragraph established that sediment import during spring tide is three to four times higher than during neap tide. However there is no spring-neap variation in the daily dredging amounts (Dujardin et al., 2016). Because the sediment extraction from the harbor does not follow the variation in sediment import, the level of the mud-water interface in Albert II dock rises up to 15 cm/day during spring tide and falls 5 to 10 cm/day during neap and mean tide.

4.4.5. Seasonal variation

SSC inside the harbor has a significant seasonal variation in all fixed measurement stations, with lower SSC in spring and summer, and higher in autumn and winter (Dujardin et al., 2016). Figure 4.10 shows the relative frequency distribution of SSC in station Albert II in summer and winter. This figure illustrates how the median

SSC is higher in winter than in summer, both for the top and the bottom sensor. There is also a higher probability of higher SSC (>100 mg/l) in winter in the lower sensor.

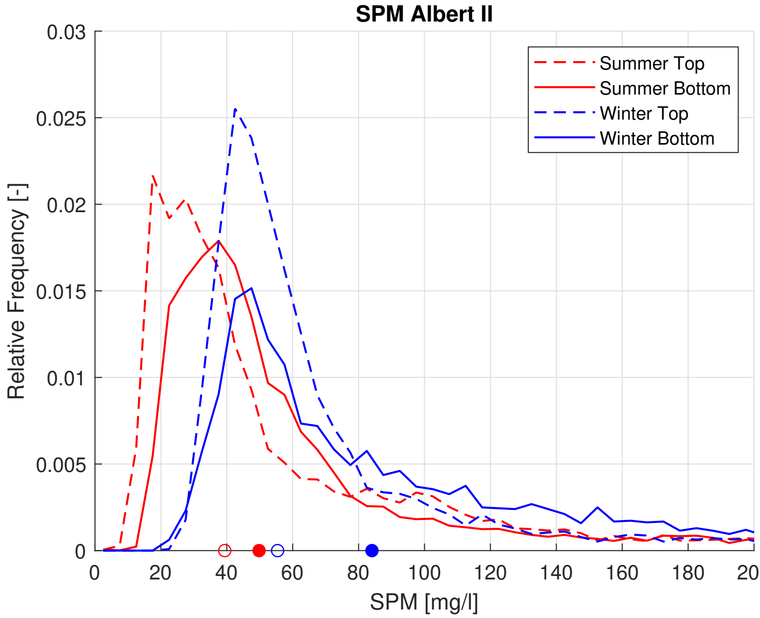

Figure 4.10: Relative frequency distribution of SSC at station Albert II in winter (in blue) and summer (in red). Top sensor in dashed line, bottom sensor in solid line. Median values are indicated with a circle on the x-axis (a filled-in circle for the bottom sensor and an outlined circle for the top sensor).

The seasonality inside the harbor is consistent with the seasonality in surface and depth-averaged SSC that is observed in the Belgian nearshore area (Van den Eynde et al., 2007; Fettweis et al., 2007; Pietrzak et al., 2011; Fettweis and Baeye, 2015). Seasonality of surface SSC in the North Sea at stations MOW0 (Wandelaar) and Vlakte van de Raan was quantified from satellite imagery. Surface SSC at these stations is about half the yearly average for spring and summer, and 70% higher in winter. The near-bed SSC from the benthic lander located at MOW1 shows a comparable seasonal variation (see section 2.12.2), with peak SSC at 2.3 mab about twice as high in autumn-winter than in spring-summer (De Maerschalck et al., 2020).

Figure 4.11 shows the seasonal variation of the most shallow point of the 210 kHz reflector along the leading lights line (location in figure 4.1). As described in the introduction, the depth of the 210 kHz reflector is part of the local definition of the nautical bottom. The minimum depth (or most shallow point) along the leading lights line is thus important to monitor. If the 210 kHz reflector rises too high anywhere in the basin, nautical accessibility is hindered. Figure 4.11 clearly shows a seasonal variation, with the top of the 210 kHz reflector being more shallow in winter.

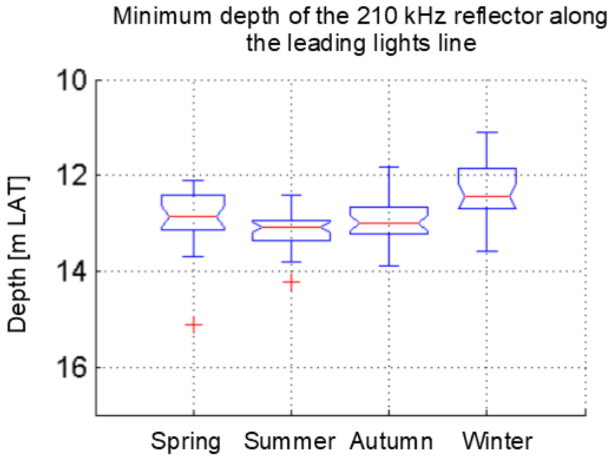

Figure 4.11: Seasonal variation of the minimum depth along the leading lights line of the 210 kHz reflector in CDNB. Data from 2007-2011.

Also, the density profiles show a lower density of the sediment layers in winter than in summer. In summer, 65% of sediment in between the 210 kHz and 33 kHz reflectors has a density below 1.18 g/l whereas in winter, that number increases to 80% (Antea Belgium, 2015b). The temperature of the pore water might play a role here. It affects the viscosity of the pore water, and the permeability is inversely proportional to viscosity (Merckelbach and Kranenburg, 2004). For winter conditions, this means a higher viscosity, a lower permeability and thus a slower consolidation in winter.

Figure 4.12 shows the seasonal pattern in the shape of the mud layer in the Albert II dock. Where the mud-water interface is flat in winter, it shows a height variation of 1 m (max. slope 1/400) in summer. Seasonal variation of the strength properties is a possible explanation for this pattern.

Fettweis and Baeye (2015) argue that microbial activity is the main driver of the seasonality in floc size yielding larger flocs in summer than in winter, rather than the seasonality in wind strength and thus wave climate. Further research is needed, however, to investigate the seasonal variations in floc properties inside the harbor (e.g. size and fractal dimension) and to link the floc properties with seasonal variations in settling velocity, sediment input rate, consolidation rate and strength properties of the bed.

4.5. Conclusions

This chapter presents the mud dynamics in the harbor basin of Zeebrugge in the Southern North Sea, based on an analysis of field data. Data on the vertical position of the mud-water interface were combined with dredging data to calculate the natural depth change of the mud-water interface. This natural depth change was

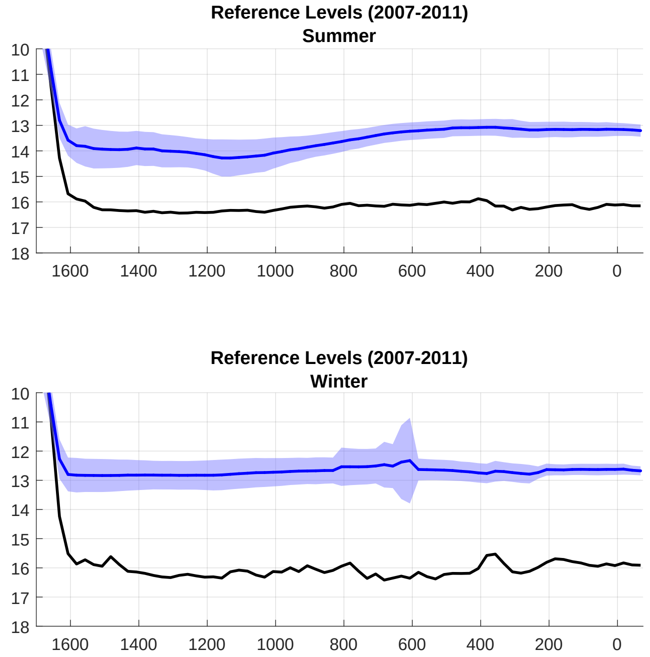

Figure 4.12: Seasonal variation of levels in Albert II dock. Mean 210 kHz level (plus-minus 1 standard deviation) in blue for summer (top panel) and winter (bottom panel). 33 kHz in black. Values on X-axis correspond to the distance along the leading lights line (indicated on figure 4.1).

cross-referenced with data on meteo-conditions (waves and fresh water inflow) to study influencing factors. The effect of fresh water inflow on sediment import into the harbor is negligible, and only a slight positive correlation was found between the peak significant wave height and the natural depth change of the mud-water interface.

Mud is typically transported into and within the harbor basin through advection of suspended particulate matter (SPM). Sediment import through advection is apparent both in the ADCP backscatter dataset (described in section 4.4.3) as in the ensembles based on the OBS dataset (see section 4.4.3). Three important timescales were identified: intratidal, spring/neap and seasonal. On the intratidal timescale, most of the sediment import occurs from two hours before high water to high water. This is consistent with the analysis of the sediment exchange mechanisms between the harbor of Zeebrugge and the North Sea presented in chapter 3, and is also apparent in the model results, as shown in section 5.11.3.

The suspended sediment concentration in the North Sea and in the harbor close to the entrance is three times higher during spring tide than during neap tide. A similar spring-to-neap ratio is also found in the sediment influx per tide. Because there is no apparent spring-neap modulation in dredging works, the level of the mud-water interface in Albert II dock typically rises 15 cm/day during spring tide conditions and falls 5 to 10 cm/day during neap and average tide conditions.

The seasonality of SSC in the harbor is consistent with the seasonality of SSC observed in the North Sea, with higher SSC during autumn-winter and lower SSC during spring-summer. The mud volume within the harbor basin is larger in winter, and reaches a minimum at the beginning of autumn. Moreover, the measured densities within the deposited mud layers are lower in winter than in summer. The most shallow point of the 210 kHz reflector is also more shallow in winter. Finally, the profile of the interface of the mud layer in the sheltered Albert II dock is more horizontal in winter than in summer, suggesting seasonal variations in the strength of the mud layer. The question to what degree the thickness and density variation of the fluid mud layer are related to differences in the suspended sediment input, to differences in the settling rates of suspended flocs, or to the mud consolidation rate remains open however.

Another siltation mechanism where large quantities of mud are entrained and flow into the harbor as high concentration benthic suspensions (HCBS) has been previously reported for the Port of Rotterdam during storms (Kirby, 1988; Winterwerp, 1999). However, in the data no evidence is found of this siltation mechanism transporting mud from the North Sea into the harbor basin, which is consistent with the conclusions of the HCBS measurement program that was carried out in the harbor in 2006-2007 (IMDC et al., 2010). It is possible however that gravitational flow of mud layers plays a role in redistributing sediment inside the harbor basin, e.g. sediment flowing gravitationally from CDNB into Albert II dock.

References

Afdeling Kust - Hydrografie (2001). Stroomatlas Haven van Zeebrugge - stroommetingen in het centrale deel van de Nieuwe Buitenhaven bij springtij. Technical report, Afdeling Kust - Hydrografie, Oostende.

Antea Belgium (2015a). Onderzoek en monitoring alternatieve stortstrategie onderhoudsbaggerwerk voorhaven Zeebrugge 2012-2015 (16EF/2011/35). Metingen in de haven: factual data rapportage: 14/09/2013-18/04/2014. Technical report, Vlaamse Overheid; Afdeling Maritieme Toegang, Antwerpen.

Antea Belgium (2015b). Onderzoek en monitoring alternatieve stortstrategie onderhoudsbaggerwerk voorhaven Zeebrugge 2012-2015 (16EF/2011/35). Studie invloed externe factoren op interne slibdynamiek in de haven. Technical report, Vlaamse Overheid; Afdeling Maritieme Toegang, Antwerpen.

Antea Belgium (2016). Onderzoek en monitoring alternatieve stortstrategie onderhoudsbaggerwerk voorhaven Zeebrugge 2012-2015 (16EF/2011/35): oriënterende studie potentiële nieuwe stortlocaties deelopdracht 6. Technical report, Vlaamse Overheid; Afdeling Maritieme Toegang, Antwerpen.

Claeys, S., Dumon, G., Lanckneus, J., and Trouw, K. (2001). Mobile turbidity measurements as a tool for determining future volumes of dredged material in access channels to estuarine ports. *Terra et Aqua*, 84.

De Maerschalck, B., Nguyen, D., Vanlede, J., and Mostaert, F. (2020). Sediment Transport Model for the Port of Zeebrugge: Analysis of the OD Nature Tripod measurements. WL Rapporten, 00_067. Technical report, Vlaamse Overheid; Afdeling Waterbouwkundig Laboratorium, Antwerpen.

Delefortrie, G., Vantorre, M., Verzhbitskaya, E., and Seynaeve, K. (2007). Evaluation of safety of navigation in muddy areas through real-time maneuvering simulation. *Journal of Waterway, Port, Coastal, and Ocean Engineering*, 133(2):125–135.

Dujardin, A., Ides, S., Schramkowski, G., Mulder, T. D., and Mostaert, F. (2009). Haven van Zeebrugge. Optimalisatie maritieme toegankelijkheid: onderzoek naar de water- en sedimentuitwisseling ter hoogte van de havenmond. Versie 2.0. WL Rapporten, 843_01. Technical report, Vlaamse Overheid; Afdeling Waterbouwkundig Laboratorium, Antwerpen.

Dujardin, A., Vanlede, J., Van Hoestenberghe, T., Verwaest, T., and Mostaert, F. (2016). Invloedsfactoren op de ligging van de top van de sliblaag in het CDNB: deelrapport 2. Analyse periode 1999-2011. versie 5.0. WL Rapporten, 00_078. Technical report, Waterbouwkundig Laboratorium en Antea Group, Antwerpen.

Fettweis, M. and Baeye, M. (2015). Seasonal variation in concentration, size, and settling velocity of muddy marine flocs in the benthic boundary layer. *Journal of Geophysical Research: Oceans*, 120(8):5648–5667.

Fettweis, M., Baeye, M., Cardoso, C., Dujardin, A., Lauwaert, B., Van den Eynde, D., Van Hoestenberghe, T., Vanlede, J., Van Poucke, L., Velez, C., and Martens, C. (2016). The impact of disposal of fine-grained sediments from maintenance dredging works on SPM concentration and fluid mud in and outside the harbor of Zeebrugge. *Ocean Dynamics*, 66(11).

Fettweis, M., Houziaux, J.-S., Du Four, I., Van Lancker, V., Baeteman, C., Mathys, M., Van den Eynde, D., Francken, F., and Wartel, S. (2009). Long-term influence of maritime access works on the distribution of cohesive sediments: analysis of historical and recent data from the Belgian nearshore area (Southern North Sea). *Geo-Marine Letters*, 29(5):321–330.

Fettweis, M. and Lee, B. J. (2017). Spatial and Seasonal Variation of Biomineral Suspended Particulate Matter Properties in High-Turbid Nearshore and Low-Turbid Offshore Zones. *Water (Switzerland)*, 9(9).

Fettweis, M., Nechad, B., and Van den Eynde, D. (2007). An estimate of the suspended particulate matter (SPM) transport in the southern North Sea using SeaWiFS images, in situ measurements and numerical model results. *Continental Shelf Research*, 27(10-11):1568–1583.

Fettweis, M. P. and Nechad, B. (2011). Evaluation of in situ and remote sensing sampling methods for SPM concentrations, Belgian continental shelf (southern North Sea). *Ocean Dynamics*, 61(2-3):157–171.

Holdaway, G. P., Thorne, P. D., Flatt, D., Jones, S. E., and Prandle, D. (1999). Comparison between ADCP and transmissometer measurements of suspended sediment concentration. *Continental Shelf Research*, 19(3):421–441.

IMDC, Deltares, and GEMS (2011). Langdurige monitoring van zout/zoet-verdeling in de haven van Zeebrugge en monitoring van zoutconcentratie, slibconcentratie en hooggeconcentreerde slibsuspensies in de Belgische kustzone: salinity profiling during 2007-2008 in the harbour of Zeebrugge. Technical report, Waterbouwkundig Laboratorium, Antwerpen.

IMDC, WL|Delft Hydraulics, and GEMS International (2010). Langdurige monitoring van zout/zoet-verdeling in de haven van Zeebrugge en monitoring van zoutconcentratie, slibconcentratie en hooggeconcentreerde slibsuspensies in de Belgische kustzone: deelrapport 8. Rapport over de aanwezigheid van HCBS lagen in de B. Technical report, Waterbouwkundig Laboratorium en Hydrologisch Onderzoek, Antwerpen.

Kirby, R. (1988). High Concentration Suspension (Fluid Mud) Layers in Estuaries. In *Physical Processes in Estuaries*, pages 463–487.

Kirby, R. (2011). Minimising harbour siltation - findings of PIANC Working Group 43. *Ocean Dynamics*, 61(2-3):233–244.

Kranenburg, C. (1998). Dichtheidsstromen. Handleiding college CT5302. Technical report, TU Delft, Delft.

Lanckneus, J. and Van Lancker, V. (2001). Relatie tussen de hydro-meteo en de sedimentatie in de haven van Zeebrugge.

McAnally, W. H., Friedrichs, C., Hamilton, D., Hayter, E., Shrestha, P., Rodriguez, H., Sheremet, A., and Teeter, A. (2007). Management of Fluid Mud in Estuaries, Bays, and Lakes. I: Present State of Understanding on Character and Behavior. *Journal of Hydraulic Engineering*, 133(1):9–22.

McAnally, W. H., Kirby, R., Hodge, S. H., Welp, T. L., Greiser, N., Shrestha, P., McGowan, D., and Turnipseed, P. (2016). Nautical Depth for U.S. Navigable Waterways: A Review. *Journal of Waterway, Port, Coastal, and Ocean Engineering*, 142(2):04015014.

Mehta, A. (1991). Understanding fluid mud in a dynamic environment. *Geo-Marine Letters*, pages 113–118.

Mehta, A. J., Samsami, F., Khare, Y. P., and Sahin, C. (2014). Fluid Mud Properties in Nautical Depth Estimation. *Journal of Waterway, Port, Coastal, and Ocean Engineering*, 140(2):210–222.

Merckelbach, L. M. and Kranenburg, C. (2004). Equations for effective stress and permeability of soft mud–sand mixtures. *Géotechnique*, 54(4):235–243.

PIANC (1997). Approach channels – A guide for design, Final report of the joint Working Group PIANC and IAPH, in cooperation with IMPA and IALA. Supplement to PIANC Bulletin, No. 95, 108 pp, 1997. Technical report.

Pieters, A., Dumon, G., and Speleers, L. (2001). Onderzoek naar de ecologische impact van de baggerwerkzaamheden aan de Belgische kust in het kader van MOBAG 2000: chemisch-biologische aspecten. In *Studiedag 'Milieuaspecten van baggerwerken op de Belgische kust': conferentiemap*, page 13.

Pietrzak, J. D., de Boer, G. J., and Eleveld, M. A. (2011). Mechanisms controlling the intra-annual mesoscale variability of SST and SPM in the southern North Sea. *Continental Shelf Research*, 31(6):594–610.

Thorne, P., Hardcastle, P., Holdaway, G., and Born, A. (1994). Analysis of results obtained from a triple frequency acoustic backscatter system for measuring suspended sediments. In *6th International Conference on Electronic Engineering in Oceanography*, volume 1994, pages 83–89. IEE.

Van den Eynde, D., Nechad, B., Fettweis, M., and Francken, F. (2007). Seasonal variability of suspended particulate matter observed from SeaWiFS images near the Belgian coast. In Maa, J. P., Sanford, L. P., and Schoellhamer, D. H., editors, *Estuarine and coastal fine sediment dynamics*. Elsevier.

Vanlede, J. and Dujardin, A. (2014). A geometric method to study water and sediment exchange in tidal harbors. *Ocean Dynamics*, 64(11):1631–1641.

Vanlede, J., Dujardin, A., Fettweis, M., Van Hoestenberghe, T., and Martens, C. (2019). Mud dynamics in the Port of Zeebrugge. *Ocean Dynamics*, 69(9):1085–1099.

Winterwerp, J. C. (1999). On the dynamics of high-concentrated mud suspensions. Technical Report 3, Delfi University of Technology, Faculty of Civil Engineering and Geosciences, Delft, The Netherlands.

Winterwerp, J. C. (2005). Reducing harbor siltation. I: Methodology. *Journal of Waterway, Port, Coastal and Ocean Engineering*, 131(6):258.

Winterwerp, J. C. and de Boer, W. P. (2016). The role of fresh water discharge on siltation rates in harbor basins. In *Pianc Copedec IX*, pages 228–229.

5

Cohesive sediment transport model for the harbor of Zeebrugge

5.1. Introduction

A model is a partial, simplified and mostly inadequate representation of the real world. It can never describe the whole complexity of the system modeled, and therefore has to make basic assumptions of the system it wants to describe and has to neglect most of the complicated, little understood relationships of the system.

A distinction is made in figure 5.1 between the conceptual model, the model code and the site-specific model schematization. A conceptual model is like a scientific theory or hypothesis, and the model code is the algorithmic implementation of it. The code may be verified within a range of applications and accuracy. A model schematization is a site-specific application that is set up and parameterized using the model code, and which may be validated, but only within the context of a specific application. Therefore, the validity of a model schematization is always limited in terms of space, time and the type of application (Refsgaard and Henriksen, 2004). This definition moves the focus away from binary categorization of individual models (e.g. valid vs. invalid), toward a continuous process of evaluation and refinement of modeling systems (Dee, 1995). Since a model schematization can only be validated in a narrow sense, it is important to clearly state the modeling objective.

5.2. Modeling objective

The model development is part of a research project on siltation in the harbor of Zeebrugge and its access channels, and is complementary to the data analysis presented in section 2.12.2 and in chapter 4. In this project framework, the model objective is to perform scenario analysis, e.g. to estimate the effects of bathymetric

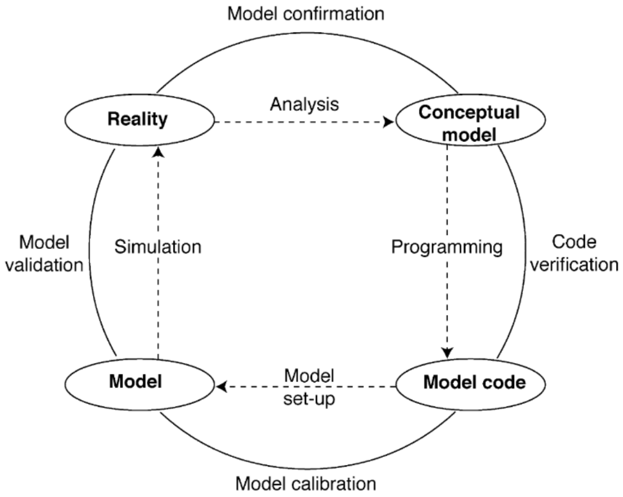

Figure 5.1: Elements of a modeling terminology (Refsgaard and Henriksen, 2004).

changes in the mouth of the Scheldt estuary, a harbor extension or a change in disposal locations on the sediment dynamics. This last example is worked out in a numerical experiment in chapter 6, and is complementary to the data analysis on a field experiment that is reported in Fettweis et al. (2016).

In the framework of this thesis, the model is used to gain insight in the mud dynamics in the Belgian Coastal Zone and the contributing factors to the formation of the coastal turbidity maximum. A sediment balance derived from the model results is used to better understand the recent results of Adriaens et al. (2018), in particular why the weakly- to medium consolidated mud in the BCZ has a different clay mineralogical composition than the English Channel mud sources, even though the residual sediment transport through the Dover Strait is an important sediment supply to the BCZ (see the discussion in section 2.7.1).

In order to fulfill the stated modeling objective, the model should be able to reproduce the following aspects:

- An accurate, process-based description of flow and wave, with a particular attention to flow and wave- induced bottom shear stress;
- The spatial distribution of suspended particulate matter (SPM), notably the coastal turbidity maximum (CTM) near Zeebrugge;
- The vertical distribution of suspended sediment concentration (SSC);
- The intratidal variation of SSC, and the variation over a spring-neap cycle;
- The spatial distribution of the bed composition in terms of sand and mud content;
- The siltation in the harbor of Zeebrugge and its access channels;
- The return flow from a disposal location back to the dredging location.

5.3. Model structure

The model structure - presented in figure 5.2 - has three separate modules: the flow model (discussed in more detail in section 5.5), the wave model (see section 5.7) and the sediment transport model (see section 5.9).

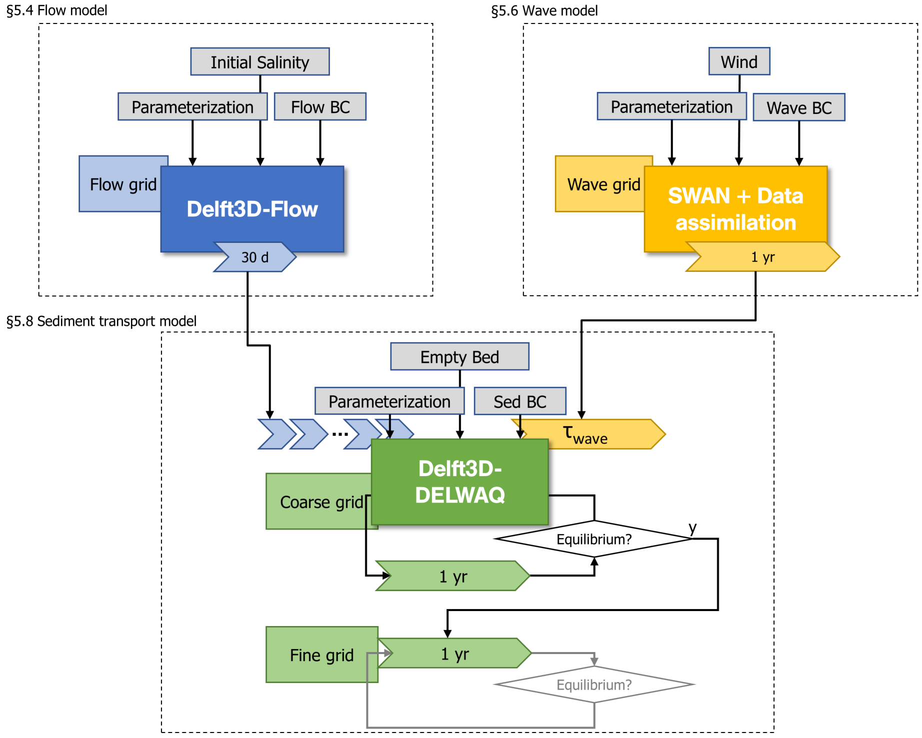

Figure 5.2: Model structure

5.4. Model domain

In order to establish a suitable model domain, two length scales are determined: the tidal excursion length and the zone of influence of the protruding breakwaters on the surrounding flow. Furthermore, it should be possible to compute the impact of major infrastructural works close to the coast and/or in the mouth of the Scheldt. Finally, the model domain has to include the deposition zones for the maintenance dredging.

5.4.1. Tidal excursion length

Tidal excursion is the distance that a particle travels from low water slack to high water slack (or vice versa). In order to avoid boundary effects, the model boundaries should be more than one tidal excursion length away from the zone of interest.

The tidal excursion is approximated by integrating the M$_2$ component of the current velocity over half a tidal cycle:

$$L_{TE}^{maj} = \int_0^{T/2} u_{M_2}^{maj} \sin(\frac{2\pi}{T}t)dt = \frac{T}{\pi} u_{M_2}^{maj} \qquad (5.1)$$

with $u_{M_2}^{maj}$ the M$_2$ amplitude of the current velocity along the major axis of the tidal ellipse, which is 0.75 m/s during spring tide at location MOW1 (see also section 2.12.1). This corresponds to L_{TE}^{maj} = 10.7 km. Similarly, for $u_{M_2}^{min}$ = 0.15 m/s, the length scale along the minor axis of the tidal ellipse is L_{TE}^{min} = 2.1 km. The tidal excursion length is plotted in relation to the model domain in figure 5.4.

5.4.2. Zone of influence of the protruding breakwaters

The breakwaters of the harbor of Zeebrugge protrude 3.4 km out of the coastline, and deflect the flow. Under the simplifying assumptions of an inviscid, incompressible fluid and irrotational flow, the effect of the Zeebrugge harbor on the flow pattern in the North Sea can be approximated by the potential flow around a cylinder (figure 5.3). The velocity potential φ for the irrotational flow past a cylinder with radius R in a two dimensional, incompressible, inviscid flow is given in polar coordinates (r, θ) in equation 5.2 (Acheson, 1991):

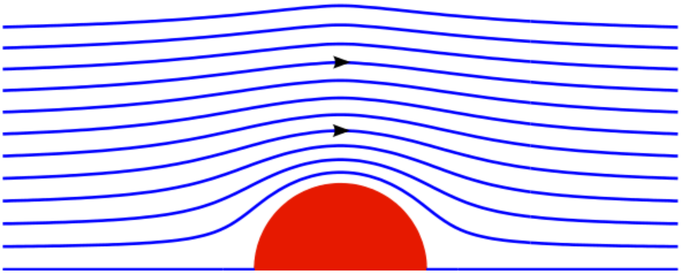

Figure 5.3: Potential flow around a cylinder (source: Wikimedia Commons).

$$\begin{aligned} \varphi &= Ur\left(1+\frac{R^2}{r^2}\right)\cos\theta \\ V_r &= \frac{\partial\varphi}{\partial r} = U\left(1-\frac{R^2}{r^2}\right)\cos\theta \\ V_\theta &= \frac{1}{r}\frac{\partial\varphi}{\partial\theta} = -U\left(1+\frac{R^2}{r^2}\right)\sin\theta \end{aligned} \qquad (5.2)$$

with U the undisturbed flow [m/s]. It is clear from equation 5.2 that the relative effect on velocity scales with R^2/r^2. For a protrusion with dimension R = 3.4 km in a flow field with U_{max} = 1.5 m/s, the effect drops below 0.1 m/s at a distance r = 13.2 km.

5.4.3. Conclusion on model domain

For the stated model aim, no available model schematization was deemed appropriate, so a new model was developed. The model domain is indicated in figure 5.4. It measures 75 km alongshore, and 30 km cross-shore. The model boundaries in the North Sea are at a distance that is deemed sufficiently large (multiple tidal excursion lengths) from both the harbor and the disposal areas. Furthermore, the zone of influence of the harbor on the flow (indicated in yellow in figure 5.4) lies well within the model domain, which is important because the harbor is not included in the model that generates the boundary conditions. The Scheldt estuary is included in the model domain up to ”Gat van Ossenisse”.

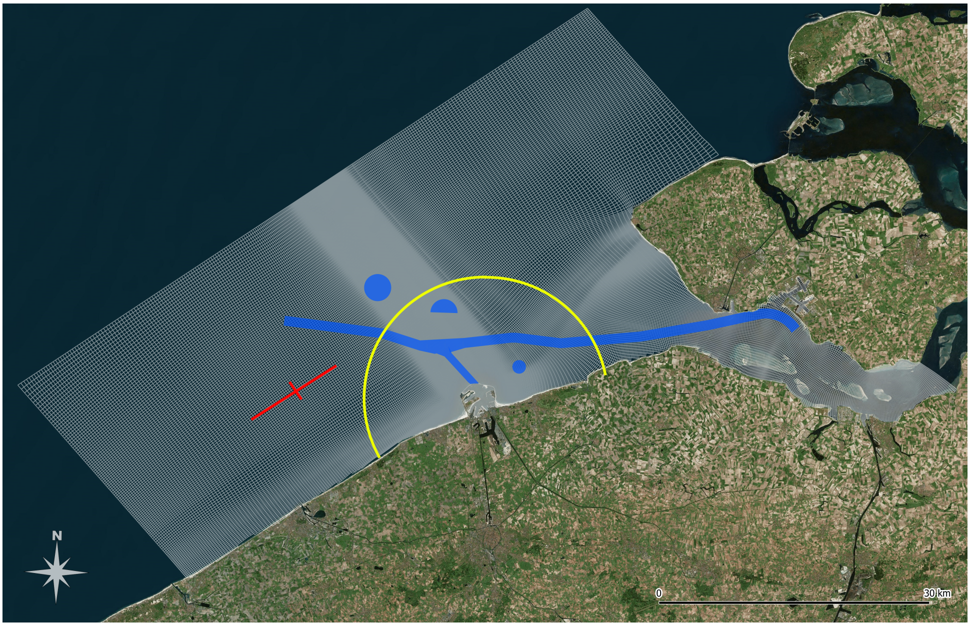

Figure 5.4: Domain of the Zeebrugge model. Dredging and disposal locations are indicated in blue, the tidal excursion lengths along the major and minor axis in red and the zone of influence of the protruding breakwaters on the surrounding flow in yellow. The background satellite image is from Bing Virtual Earth.

5.5. Flow model description

5.5.1. Vertical discretization

Flow and sediment transport are solved on the same vertical discretization: a σ-coordinate grid with 12 layers with varying thickness (top to bottom: 5, 5, 10, 10, 15, 15, 10, 10, 10, 5, 3 and 2 %). This layer distribution has the highest resolution close to the bottom, where the strongest vertical gradients of velocity and sediment concentration are expected. It also has a relatively thin top layer, in order to better resolve the surface sediment concentration, which is compared to surface SSC derived from satellite images during calibration of the sediment transport model (see section 5.11).

5.5.2. Horizontal discretization

The model grid is curvilinear, with a resolution varying from 35 m in the inner harbor to 600 m near the seaward boundary. The resolution at the harbor entrance is 70 m, with 11 cells across the entrance. Note that because of the curvilinear nature of the grid, the alignment of the grid cells in the harbor (see figure 5.5) is to a large extent dictated by the model domain shown in figure 5.4. The harbor walls of Zeebrugge are schematized by dry points. The wall roughness on the dry points is set to a partial slip condition with a roughness length of 0.15 m. The flow grid has a grid size of 417 x 380 cells, with ~67 000 active cells. In order to speed-up the initialization of the sediment transport model, it is first computed on a coarse, and then on a finer aggregation of the flow grid (see section 5.9.5).

Figure 5.5: Detail of the flow grid in the harbor of Zeebrugge. The background satellite image is from Google Earth.

5.5.3. Turbulence modelling

Since the grid is too coarse to solve the turbulent scales of motion, the turbulent processes are sub-grid and closure assumptions are necessary. The Horizontal Large Eddy Simulation (HLES) formulation is used for the horizontal component of the sub-grid eddy viscosity and the sub-grid eddy diffusivity, which are added to the background values (Deltares, 2018b). The background horizontal eddy viscosity ν_h^{back} is set to 1 m^2/s and the background horizontal eddy diffusivity D_h^{back} to

10 m²/s. In the vertical direction, the eddy viscosity ν_v and the eddy diffusivity D_v are determined with the k-ϵ turbulence closure model.

5.5.4. Selection of a cyclical simulation period

As indicated in the model structure (see figure 5.2), the hydrodynamic results are repeated in a loop during the computation of the sediment transport. The length of the hydrodynamic simulation is set at one lunar month (i.e. two spring-neap cycles). Note that the availability of storage space plays a role in choosing the length of the hydrodynamic simulation. The model output is stored in a single file which takes up 240 GB of disk space for 1 month of model output with a 10 minute interval.

As the hydrodynamic results are repeated in a loop, the simulation period should be selected in such a way that the difference in water level and current velocity between the start and the end of the period (the closure error) is as small as possible, in order to avoid discontinuities in the forcing of the sediment transport computation.

First, a search window of three months is selected with relatively calm conditions (01/04/2009 to 01/07/2009). Subsequently a sub-period of one lunar month is searched that minimizes the closure error, which is evaluated as a cost function which penalizes the difference in water level and current velocity between the start and the end. The dimensionless cost function is given in equation 5.3.

$$C = \frac{1}{N}\sum_{i=1}^{N}\left(\frac{\left|\eta_i^{\text{start}} - \eta_i^{\text{end}}\right|}{\eta_i^{\text{max}} - \eta_i^{\text{min}}} + \frac{\left|u_i^{\text{start}} - u_i^{\text{end}}\right|}{u_i^{\text{max}} - u_i^{\text{min}}} + \frac{\left|v_i^{\text{start}} - v_i^{\text{end}}\right|}{v_i^{\text{max}} - v_i^{\text{min}}}\right) \tag{5.3}$$

with C the cost function that quantifies the total closure error (in water level η and velocity u, v) over a total of N stations i. Superscripts "start" and "end" stand for the values at the first and last timestep of the sub-period, and superscripts "max" and "min" for the highest and lowest value during the sub-period Water levels and velocities for 11 stations within the study area are determined with the North Sea model that supplies the boundary conditions (see section 5.5.5).

The period from 26/04/2009 16:00 to 26/05/2009 04:10 (29.51 days) minimizes this cost function, and is selected as the hydrodynamic cycle for this study. It is illustrated in figure 5.6 for station MOW1.

5.5.5. Flow boundary conditions

The Zeebrugge flow model is nested in the ZUNO model for its boundary in the North Sea, and in the NEVLA model for the boundary condition in the Western Scheldt. Both models are briefly introduced below.

Southern North Sea model (ZUNO)

The Zeebrugge flow model has velocity boundary conditions on its east and west boundaries, and a Riemann boundary condition on the northern sea boundary. All three are derived from DCSMv6–ZUNOv4, which is a 2D curvilinear model of tidal propagation in the North Sea. The details of model setup, calibration and validation

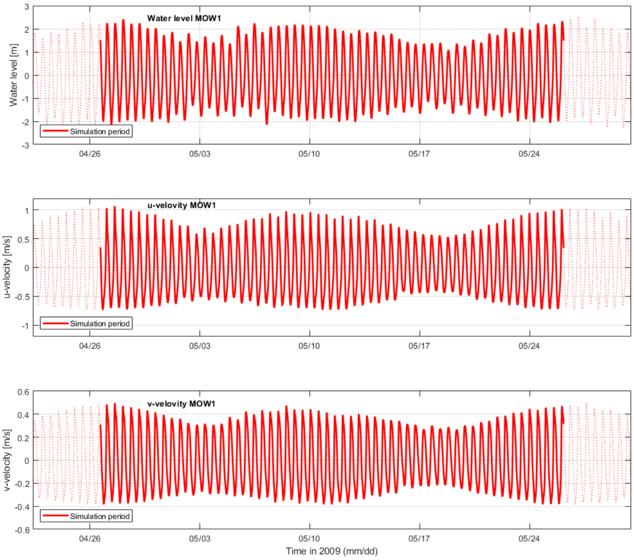

Figure 5.6: Water level and velocity at MOW1 during the selected cyclical simulation period (in full line), repeated for illustrative purposes (dashed line).

can be found in Zijl (2013). A validation run was carried out for the year 2009 to evaluate the model skill in reproducing the water levels at the Belgian coast. The meteorological forcing of wind and air pressure was ERA5, which is the fifth generation atmospheric reanalysis of ECMWF (European Centre for Medium-Range Weather Forecasts). The mean RMSE was ∼10 cm, which is a good accuracy for water level modeling in the Belgian coastal zone when compared to other North Sea models (Chu et al., 2020).

Scheldt model (NEVLA)

The Zeebrugge flow model has a discharge boundary in the Western Scheldt at ”Gat van Ossenisse”, with two separate time series for the northern and southern half of the transect. These boundary conditions are derived from the NEVLA model, which is a 3D curvilinear model of the Scheldt estuary and coastal zone. The model was extensively calibrated for water levels, velocities and salinity by Vanlede et al. (2015).

5.5.6. Model bathymetry

Figure 5.7 shows the bathymetry of the flow model, together with the locations of the measurement stations that are used for model calibration. The same bathymetric data are used for the flow model and the sediment transport model. The bathymetry is composed of available measurements from the period 1999-2009.

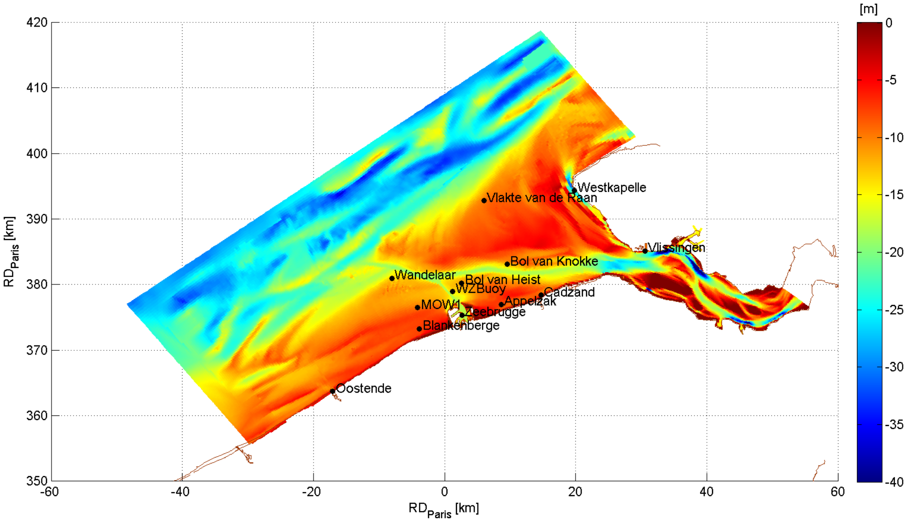

Figure 5.7: Model bathymetry in m NAP and location of the measurement stations.

Inside the harbor the target depths for maintenance dredging are used. Because a sensitivity analysis of the flow model showed the importance of the bathymetry near the eastern breakwater for the flow patterns inside the harbor, an additional depth sounding of this area was performed on 15/04/2010. These data were also included in the model bathymetry. The bathymetry near the open sea boundaries of the model is interpolated from the ZUNO bathymetry, in order to avoid instabilities at the seaward boundary introduced by the nesting procedure (see section 5.5.5). The bathymetry in the Western Scheldt is derived from the NEVLA model, and is based on bathymetric soundings of 2006, with the intertidal areas based on laser-altimetry surveys of 2003 (data provided by Rijkswaterstaat directie Zeeland).

5.5.7. Simulation time for the hydrodynamics

The hydrodynamic information is stored in a single com-file that is read in by the sediment transport model. Because of a bug in the generation of com-files in case the flow model is run in parallel, the flow model had to be run on a single core (Intel Xeon X5550 quad core (Nehalem) CPU at 2.67 GHz), which resulted in a speed-up of x3, or 10 days to generate the hydrodynamic forcing for one month.

5.6. Flow model validation

The flow model is calibrated by changing the (uniform) bottom roughness. Values for the Manning coefficient n were changed in the range 0.018 to 0.024 $\mathrm{s\,m^{-1/3}}$. The optimal model setting of 0.022 $\mathrm{s\,m^{-1/3}}$ was chosen by minimizing the RMSE of water levels in 9 stations and of velocity magnitude in 5 stations over a period of 1 month. The model skill of the calibrated model is discussed below.

5.6.1. Water level

Because of the small dimensions of the Zeebrugge flow model relative to the tidal wave length, the computed water levels are determined to a large extent by the boundary conditions from the ZUNO model (see section 5.5.5). The water level is compared with measurements in 9 stations: Oostende, Wandelaar, Zeebrugge, Bol van Heist, Vlakte van de Raan, Bol van Knokke, Cadzand, Vlissingen and Westkapelle. The location of the measurement stations is indicated in figure 5.7. The modeled and measured water levels at Zeebrugge are shown in figure 5.8. Averaged over all 9 observation stations, water levels are computed with a bias of 8 cm and a RMSE of 10 cm. Figure 5.9 shows the M2 amplitude and phase of model and measurement. The M2 amplitude in the model is overestimated by about 3 cm (2%), which is deemed acceptable. The phasing of the tidal cycle is also well represented, with an error in the timing of high and low water of 10 minutes (which corresponds to the timestep of model and measurements). The average M2 phase error is 0.5°. A detailed quantitative skill assessment for all stations can be found in section B.1.1. The results for the vertical tide show that tidal wave propagation is well represented in the model. Because this is a sediment transport model, it is also important to validate the horizontal tide. The model skill in reproducing velocities is assessed in section 5.6.2 for measurements at fixed locations, and in section 5.6.3 for measurements on sailed transects.

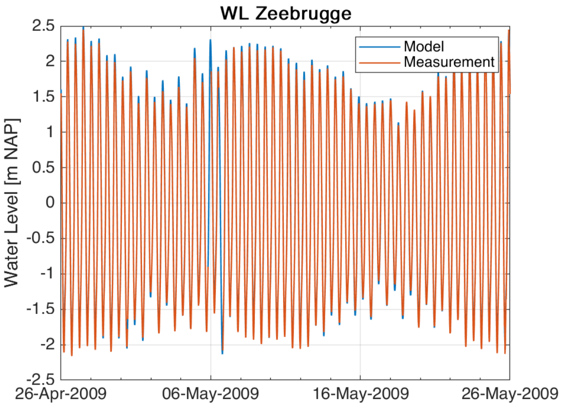

Figure 5.8: Measured and modeled water level at Zeebrugge.

5.6.2. Velocity at fixed locations

The model skill in reproducing velocities at fixed locations is evaluated in two separate ways. For two stations, a direct comparison is made of modeled and measured time series. For three other stations, modeled and measured ensembles are compared.

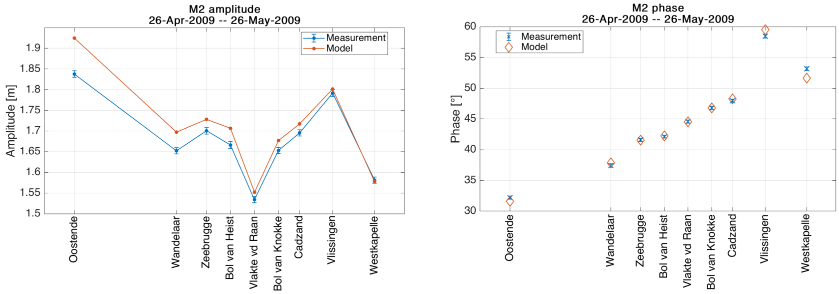

Figure 5.9: M2 amplitude (left panel) and phase (right panel) of water level for measurements (blue line + error bars) and simulation (red line).

Time series comparison

Continuous velocity measurements are available in stations Bol van Heist and Bol van Knokke. The measurements are performed with a bottom-up ADCP (DCM12 of Aanderaa instruments). A direct comparison can be made between modeled and measured velocities over the same time interval. Figure 5.10 shows the modeled and measured velocity at Bol van Knokke, at 8.75 m below the surface. Overall, velocity magnitude and direction are well represented by the model. The mean absolute error of velocity in the model is 13 cm/s at Bol van Knokke, and 23 cm/s at Bol van Heist. A detailed quantitative skill assessment can be found in appendix

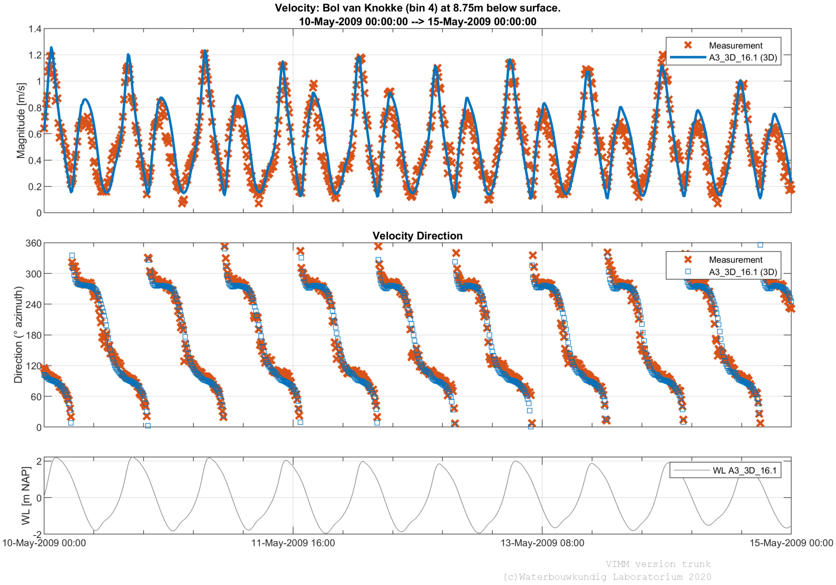

Figure 5.10: Measured and modeled velocities at Bol van Knokke at 8.75 m below the surface.

in section B.1.2.

Ensemble analysis

Measured current velocities close to the bed were available from frame measurements at stations MOW1 and Blankenberge (see section 2.12.1). Data of 51 tripod deployments were gathered over nearly 9 years (2005-2013). Since it would not be practical to perform a 9-year simulation to compare the model directly to the measured time series, a comparison of velocity ensembles was carried out. By phase averaging modeled and measured velocities, the model skill can be assessed, even with measurements outside of the modeled time frame. Figure 5.11 shows modeled and measured flow velocities at 1.9 mab for both stations. The velocity close to the bed is well represented at Blankenberge, but the model overpredicts peak flood velocity at MOW1 by about 10 cm/s.

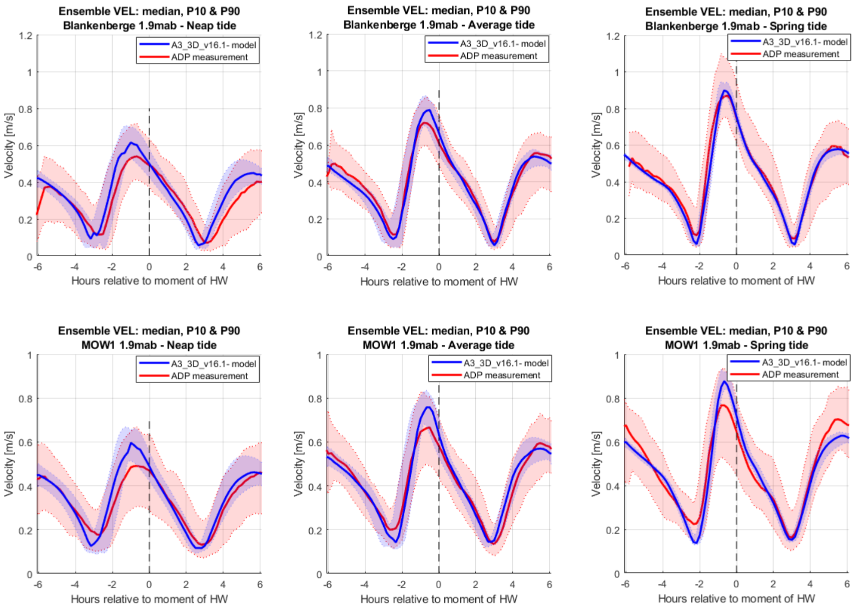

Figure 5.11: Ensembles of measured and modeled current velocities at Blankenberge (top) and MOW1 (bottom) at 1.9 mab (meters above the bed) for neap, average and spring tide.

5.6.3. Sailed ADCP measurements

In 2007, a through-tide ADCP campaign was performed that describes the flow field across the harbor entrance (see also the analysis in chapter 3). Using this campaign to assess the model skill in reproducing the flow field at the harbor entrance is not straightforward however, since modeled and measured periods do not overlap. In appendix C a method is proposed to search for a comparable tide in the modeled period that closely matches the tidal conditions during the measurement. This makes it possible to assess model skill, even if the measurements were carried out outside of the modeled time frame. The result of the comparable tide selection is presented in table 5.1.

Transect	Time frame of ADCP Campaign	Comparable Tide in model time frame
Zeebrugge harbor entrance	31/07/2007 05:18 - 31/07/2007 17:44 (3.96 m)	24/05/2009 16:18 - 25/05/2009 04:44 (4.13 m)

Table 5.1: Comparable tide selection for ADCP measurement. Tidal ranges are indicated in parentheses.

Since horizontal exchange is the most important at the harbor mouth (see chapter 3), the depth-averaged flow patterns are compared. It was shown in chapter 4 that the most important sediment exchange occurs from 2h before high water to high water. Figure 5.12 shows the modeled and measured depth-averaged velocity vector fields at 2h before HW, using the comparable tide method to select corresponding timesteps. The ADCP velocities are shown in green arrows between two rectangles indicating the start of the transect (A) and the end of the transect (B), together with the start and end time. The computed velocity field (in red) is thinned out for readability.

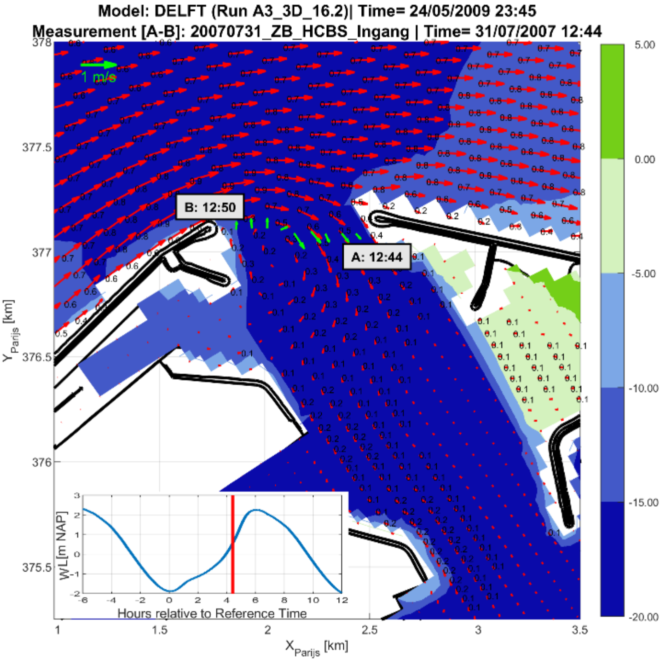

Figure 5.12: Modeled and measured flow pattern in the Zeebrugge harbor in a comparable tide at 2h before HW. Measured velocity in green, computed velocity in red.

At 2h before HW, flood flow in the North Sea drives a clockwise primary gyre in the harbor (see figure 5.12), which is transported into the basin with the net tidal inflow. This results in water inflow being concentrated towards the eastern breakwater (Vanlede and Dujardin, 2014). A secondary eddy is formed around HW, and is located deeper inside the harbor. The two eddies gradually weaken with decreasing flood flow in front of the entrance, and disappear once the ebb phase starts at about HW+3h. The ebb flow in the North Sea is not strong enough for an eddy to develop in the harbor.

5.6.4. Discussion and conclusions

The hydrodynamic model is extensively validated against measurements, both for water levels and velocities. The validation of a one-month simulation shows that the model is capable of reproducing the hydrodynamics in the model domain. The model skill for reproducing water levels (both in time and frequency domains) is presented in appendix B. The skill is comparable to that of the DCSM-ZUNO model that is used to model the tidal propagation in the North Sea and to generate the boundary conditions. The model skill in reproducing velocities at fixed locations is evaluated at five locations, using a combination of direct time series comparison, and ensembles analysis. The model is able to accurately reproduce the velocities. Using the comparable tide method of appendix C, the measured flow field across the harbor is compared with the computed flow field. A good agreement is found between model and measurement, both in intratidal phasing and magnitude of the flow.

5.7. Wave model description

As was noted earlier in section 2.4, wind-induced waves contribute to the bed shear stress in the relatively shallow zone of interest, and hence to the resuspension of sediments. Therefore it is important to include the wave-induced bed shear stress in the sediment transport model. The effect of waves could be taken into account by coupling flow and waves in the hydrodynamic simulation (online method). However, this method is rather costly, and requires a transient wave model to be set up, calibrated and validated.

For this study, the effect of waves is taken into account via the wave-induced bed shear stress τ_{wave}, which is added to τ_{flow} to obtain the total bed shear stress τ_{bed} (see equation 5.13). τ_{wave} in turn is computed from the wave height and wave period using linear wave theory (see section 5.7.3).

Two methods are described to estimate H_s and T_p without the need for a transient wave model: the fetch length approach in section 5.7.1, and an inverse distance-weighted interpolation of an annually averaged wave field in section 5.7.2. Both methods assume a fully developed wave field, ignoring transient effects. The model skill of both methods is quantified against measurements of H_s and T_p in section 5.8.1. The best performing method is then used to calculate wave component of the total bed shear stress, which is validated in section 5.8.2.

5.7.1. Fetch length approach

This method only takes geometry (bathymetry and a boundary for the fetch) and a time series of wind speed and direction in one station as input. The equilibrium wave conditions are estimated with the formulae by Groen and Dorrestein (1976) for wind-generated waves of unlimited wind duration:

$$\begin{aligned} H_s &= \frac{H_* U_{10}^2}{g} \\ H_* &= 0.24 \ \tanh\left(0.71 \ h_*^{0.763}\right) \tanh\left(\frac{0.015 \ F_*^{0.45}}{\tanh\left(0.71 \ h_*^{0.763}\right)}\right) \end{aligned} \tag{5.4}$$

$$\begin{aligned} T_p &= \frac{T_* U_{10}}{g} \\ T_* &= 2\pi \tanh\left(0.855 \ h_*^{0.365}\right) \tanh\left(\frac{0.0345 \ F_*^{0.37}}{\tanh\left(0.855 \ h_*^{0.365}\right)}\right) \end{aligned} \tag{5.5}$$

h_* and F_* are the non-dimensional water depth and fetch:

$$h_* = \frac{gh}{U_{10}^2} \quad \text{and} \quad F_* = \frac{gF}{U_{10}^2} \tag{5.6}$$

with U_{10} the wind speed at 10 m height [m/s], F the wind fetch [m] and h the water depth [m]. When the wave height, computed with equation 5.4 exceeds $0.55h$, it is kept constant at this value. The wave period also stops growing, and is kept at the value attained when the wave height is equal to $0.55h$.

5.7.2. SWAN + data assimilation approach

Static maps of annually averaged H_s^{SWAN} and T_p^{SWAN} (obtained from a SWAN wave model run of 2009) are used to generate time-dependent maps of H_s and T_p in the zone of interest, by combining the modeled spatial distribution of the annually averaged maps with the measured time series of wave height and period at seven wave stations in the southern North Sea. Figure 5.13 shows the annually averaged wave height for the North Sea area, and the location of the seven measurement stations that were used in this data assimilation approach.

A time series of H_s at any location is computed using an inverse distance-weighted interpolation scheme (eq. 5.7)

$$H_s\left(x,y,t\right) = \frac{1}{\sum_{i=1}^{7}\left(d_i\right)^p} \sum_{i=1}^{7} \left(d_i\right)^p \frac{H_{s,i}^{\mathrm{meas}}\left(t\right)}{H_{s,i}^{\mathrm{SWAN}}} H_s^{\mathrm{SWAN}}\left(x,y\right) \tag{5.7}$$

where $H_s(x,y,t)$ is the significant wave height at any (x,y) coordinate and time t. $H_{s,i}^{\mathrm{meas}}(t)$ is the measured significant wave height at station i and time t. $H_{s,i}^{\mathrm{SWAN}}$ is the computed annually averaged significant wave height at station i. p is a dimensionless spatial smoothing factor (set at 0.6). d_i is the distance from wave station i to the target coordinate. The same procedure is applied to determine $T_p(x,y,t)$.

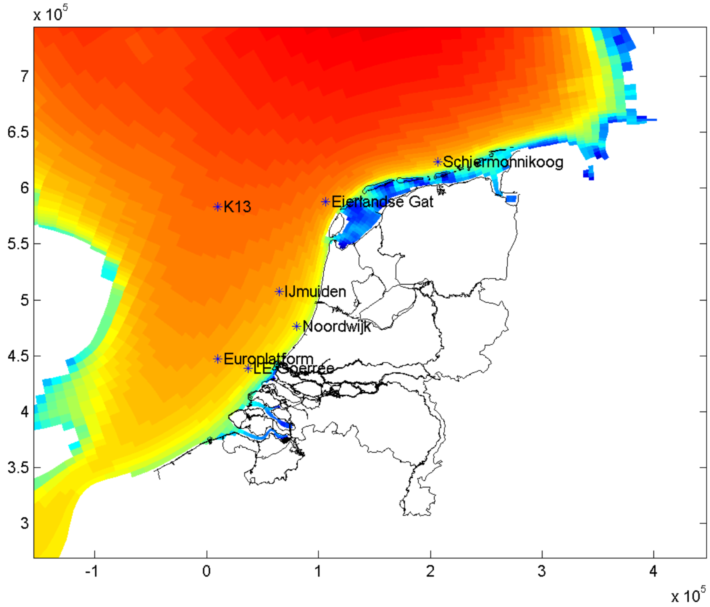

Figure 5.13: Pattern of the annually average wave height H_S^{SWAN} and the location of the measurement stations (Deltares, personal communication, 2017).

5.7.3. Wave-induced bed shear stress

The wave-induced bed shear stress is computed from wave parameters H_s and T_p using linear wave theory. First, the amplitude of the near-bed wave orbital velocity U_{orb} [m/s] is computed as:

$$U_{orb} = \frac{\pi H_s}{T_p \sinh\left(\frac{2\pi}{L}h\right)} \tag{5.8}$$

The wave length L [m] is determined from the dispersion relationship (eq. 2.1). The wave-induced bed shear stress, averaged over a wave period [N/m²] can then be computed as (van Rijn, 1993):

$$\tau_{wave} = \frac{1}{4}\,\rho_w\, f_w\, U_{orb}^2 \tag{5.9}$$

with ρ_w the density of water [kg/m³]. The dimensionless wave friction factor f_w is computed using de Swart (1974):

$$f_w = \begin{cases} 0.00251\;\exp\left(5.21\; r_*^{-0.19}\right) & \text{for } r_* > \pi/2 \\ 0.3 & \text{for } r_* \le \pi/2 \end{cases} \tag{5.10}$$

with the (dimensionless) relative roughness height r_* given by

$$r_* = \frac{A}{k_s} \tag{5.11}$$

with A [m] the semi-orbital excursion length ($A = U_{orb}T/2\pi$) and k_s the Nikuradse roughness [m]. In literature, k_s is normally related to a measure of grain size like d_{50} or d_{90}. Common relations are $k_s = 2.5d_{50}$ (Soulsby, 1997); $k_s = 3d_{50}$ (Rinaldi et al., 2008); $k_s = 2d_{90}$ (Kamphuis, 1974) or $k_s = 3d_{90}$ (van Rijn, 1993). Here the relation $k_s = 2.5d_{50}$ of Soulsby (1997) is used. The median grain size in the study area varies from a value smaller than 0.1 mm in front of the harbor to about 0.3 mm near the sea boundary of the model domain. The average value d_{50} = 0.2 mm corresponds to k_s = 0.5 mm.

5.8. Wave model validation

Wave height and period at station MOW1 are computed with both the fetch length approach (5.7.1) and the SWAN + data assimilation approach (5.7.2). The computed H_s and T_p are validated in section 5.8.1. The best performing method is then used to compute the total bed shear stress, which is subsequently validated in section 5.8.2.

5.8.1. Validation of wave parameters H_s and T_p

Figure 5.14 compares the computed H_s and T_p at station MOW1 with the measurements over a period of two weeks (1 - 14 May 2009). The measured significant wave height ranges from 0.5 m to 2 m and the wave period varies between 2 s and 8 s. The model skill in reproducing the wave height is quantified using the qualitative ranking based on the Relative Mean Absolute Error (RMAE) in table 5.2, as proposed by van Rijn et al. (2003). A formulation for the RMAE is used that takes into account an estimate of the measurement error Δo (taken as 0.1 m for wave height):

$$\text{RMAE} = \frac{\sum_1^N |m_i - o_i| - \Delta o}{\sum_1^N o_i} \tag{5.12}$$

Qualification	Wave height RMAE
Excellent	< 0.05
Good	0.05 – 0.1
Reasonable/fair	0.1 – 0.2
Poor	0.2 – 0.3
Bad	> 0.3

Table 5.2: Qualification of model performance for wave height H_s (van Rijn et al., 2003).

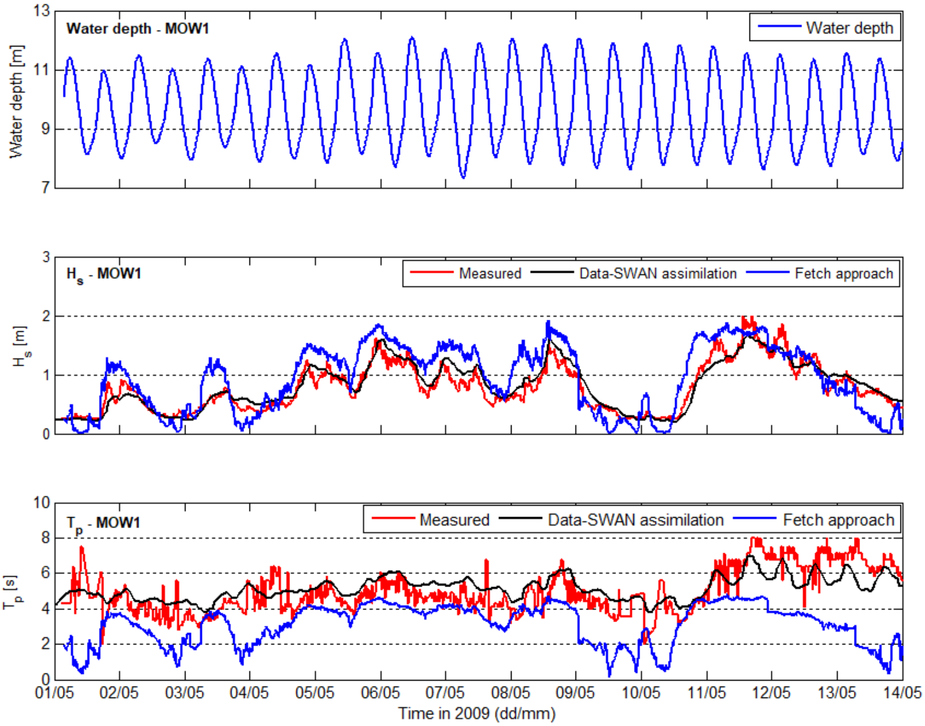

Figure 5.14: Time series of measured and computed wave heights (middle) and wave periods (bottom) at station MOW1.

SWAN + data assimilation approach

Time series of H_s and T_p obtained with the SWAN + data assimilation approach show a good agreement with the measurements, with a correlation coefficient r of 0.95 and 0.76 respectively. RMSE and RMAE of H_s are quite small (0.13 m and 0.046), which is rated as ”excellent” according to the qualification in table 5.2.

Fetch length approach

With the fetch length approach, both wave height and period are strongly correlated with the wind speed, as they are both derived from U_{10} (see eq. 5.4 and 5.5). Note the sudden jumps in computed wave height and period on 09/05 in figure 5.14, which correspond to a change in fetch length due to a shift in the wind direction.

The wave height is poorly represented with the fetch length approach. The correlation coefficient r is 0.85 and RMAE is 0.25, which is rated as ”poor” in table 5.2. The timing of higher or lower wave conditions is well captured. However, the model tends to over-predict the wave height for the higher waves and under-predict it for the lower waves. The fetch length approach also consistently underestimates the wave period over the simulated period. The computed T_p correlates poorly with the measurements (r = 0.13).

Given the better model skill in reproducing H_s and T_p with the SWAN + data assimilation approach, only this method will be used further on in the text.

5.8.2. Validation of the total bed shear stress

The total bed shear stress in the model is computed as the scalar sum of the shear stress caused by waves and flow.

$$\tau_{bed} = \tau_{flow} + \tau_{wave} \tag{5.13}$$

τ_{flow} is computed with the hydrodynamic model; τ_{wave} is the average wave-induced bed shear stress, computed using equation 5.9.

Bed shear stress measurements

Van den Eynde (2017) presents four methods to calculate bed shear stress from measurements using (1) the logarithmic profile, (2) Reynolds stresses, (3) the inertial dissipation method, and (4) turbulent kinetic energy (TKE). The bed shear stress is derived from a deployment at station MOW1 in a water depth of about 10 m. The deployment lasted from 21/08/2013 to 27/09/2013 during fair weather, with one peak wave event around day 21 (see top panel in figure 5.15). The turbulent kinetic energy method uses data from a SonTek ADV Ocean point velocity meter measuring at 18 cm above the bottom.

The results in the bottom panel of figure 5.15 show that the bed shear stress, calculated using the four methods do not correlate well with each other, and that it is therefore not straightforward to obtain a reliable estimate of τ_{bed}. Van den Eynde (2017) reports that the turbulent kinetic energy (TKE) method gives a more reliable estimate of the bed shear stress than the logarithmic profile, the inertial dissipation method and the Reynolds stresses method. The measured bed shear stress derived with the TKE method clearly shows the spring-neap tidal cycle, with higher bed shear stress during spring tide. There is also a clear increase of measured bed shear stress during a high wave event (day 21) up to nearly 2.5 Pa.

Validation of total bed shear stress

Since the SWAN wave dataset is only available for the year 2009, a period of 28 days (18/09/2009-16/10/2009) is selected that had similar wave heights as observed during the measurement campaign of 2013. The computed H_s and τ_{bed} are shown in figure 5.16. The weather was relatively calm during the first half of the period while the second half had higher wave heights, with a peak of 2.7 m on day 24.

The bottom panel of figure 5.16 shows the computed total bed shear stress for the period 18/09/2009 – 16/10/2009. τ_{flow} is computed in Delft3D-FLOW and τ_{wave} is computed with the SWAN + data assimilation approach, using k_s = 0.5 mm. Similarly to the measured τ_{bed} in figure 5.15, the computed τ_{bed} also shows the spring-neap tidal signal, superimposed with higher values during periods of higher waves (days 15-16, 24). The computed τ_{bed} has the correct order of magnitude in comparable wave conditions, with a total bed shear stress of about 2.5 Pa under a significant wave height of 2.5 m.

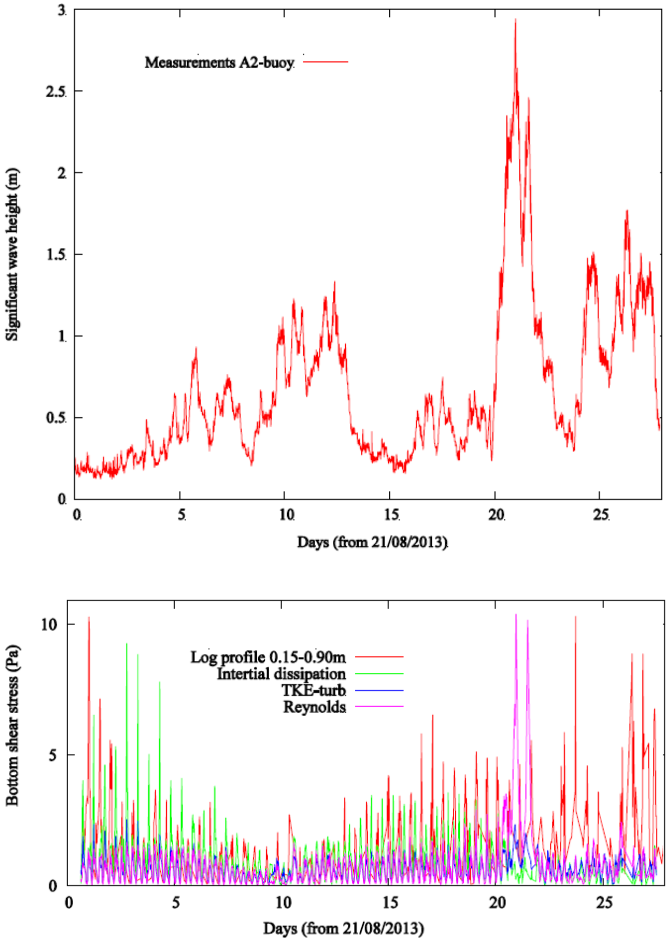

Figure 5.15: Measured Hs (top panel) and total bed shear stress (bottom panel) at MOW1 from 21/08/2013 - 18/09/2013 (Van den Eynde, 2017).

It can be concluded that the SWAN + data assimilation approach gives a good approximation of the wave-induced bed shear stress.

5.8.3. The effect of waves on the modeled bed shear stress

Figure 5.17 shows the spatial distribution of the flow and wave components of the total bed shear stress, by representing the value that is exceeded 50% of the time.

Both waves and currents contribute to the bed shear stress, but in different ways. Overall, the flow component of bed shear stress is dominant over the wave component. It influences most of the model domain, with its maximum in the channels of the Scheldt estuary. The wave-induced bed shear stress mainly influences the more shallow regions close to coast to the west of the harbor and the ”Vlakte

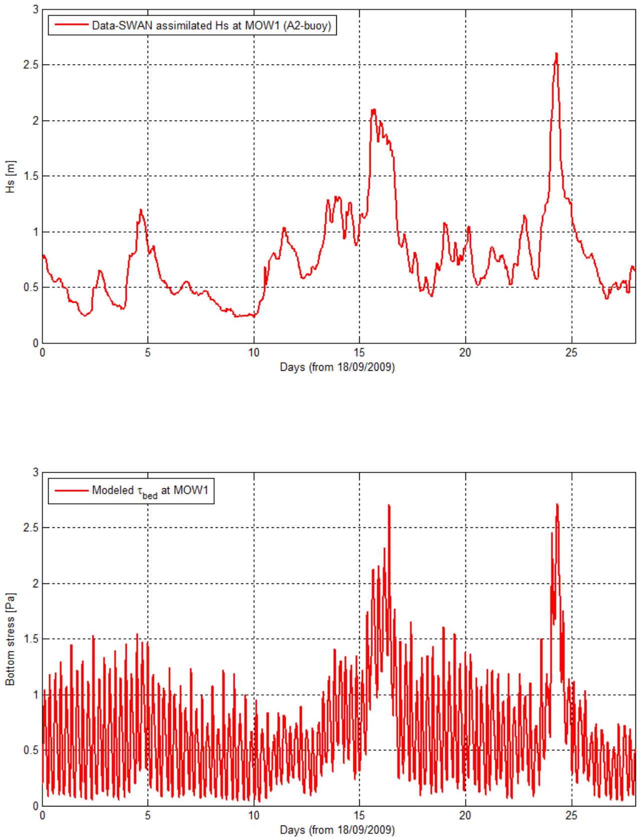

Figure 5.16: Computed Hs (top panel) and total bed shear stress (bottom panel) at MOW1 from 18/09/2009 – 16/10/2009.

van de Raan" region to the northeast of the harbor. It is negligible in the channels and the deeper areas.

The total bed shear stress which is exceeded 10% of the time (P90) is a measure for the peak bed shear stress. The spatial distribution of P90 of τ_{bed} is presented as a probability density function (PDF) in figure 5.18, both with and without the inclusion of waves in the model. As expected, the inclusion of waves shifts the shear stress distribution towards higher peak shear stress. The distribution also becomes wider, which indicates that by including waves in the model, the higher peak shear stresses (>1.5 Pa) now influence a larger part of the computational domain. Note the positive skewness in the probability density function, which causes more erosion relative to a normally distributed PDF (Winterwerp and Van Kesteren, 2004).

Figure 5.19 combines both the exceedance probability in space (on the Y-axis) and in time (in different line colors) of the computed bed shear stress with and without waves. This figure shows that, for the median shear stress, half of the area

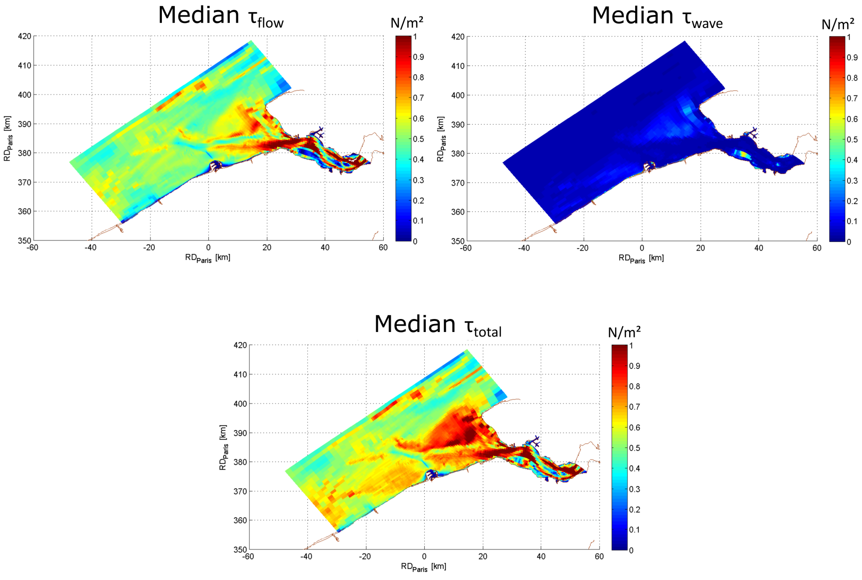

Figure 5.17: Maps of median bed shear stress: τ_{flow} (top left), τ_{wave} (top right) and τ_{total} (bottom).

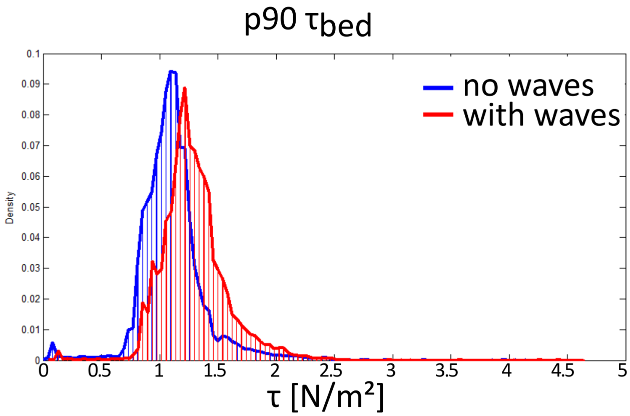

Figure 5.18: Spatial distribution (in % of the area) of the total bed shear stress that is exceeded 10% of the time.

has a shear stress that is exceeded 50% of the time of 0.5 N/m² without waves and 0.6 N/m² with waves.

With regards to the peak bed shear stress (taken here as the value that is exceeded 5% of the time): in the case without waves only 20% of the area has a peak shear stress of 1.5 N/m². In the case with waves, that proportion doubles to 40% of the area.

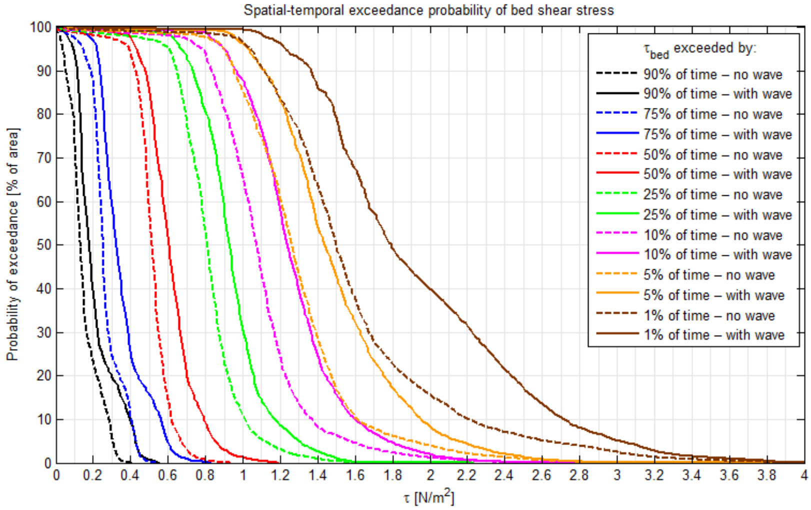

Figure 5.19: Spatio-temporal exceedance probability of bed shear stress in the model domain, with waves (full lines) and without (dashed lines).

5.9. Sediment transport model description

The third part of the model structure (see figure 5.2) is the cohesive sediment transport model. The conceptual model is discussed first (this section), section 5.10 presents the sensitivity analysis and section 5.11 describes the model calibration. The results are discussed in section 5.12.

5.9.1. Two-layer bed model

The two-layer buffer model of van Kessel et al. (2011b) is adopted as the conceptual model to describe deposition and erosion. The sandy seabed is introduced as a second layer in which fines may be buffered during calm weather and from which they may be resuspended during storms.

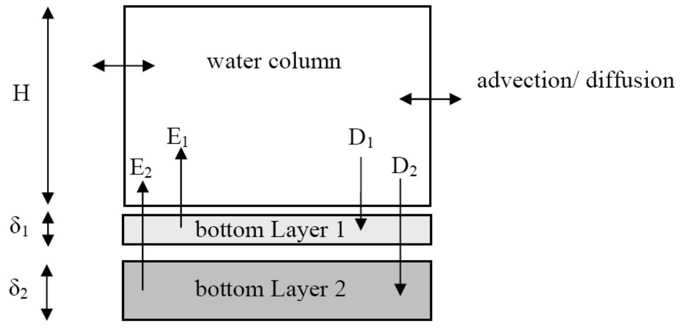

Figure 5.20: Two-layer bottom model, after van Kessel et al. (2011b).

Conceptually, the first bed layer S_1 is the thin fine sediment layer that rapidly accumulates and erodes. The second bed layer S_2 represents the sandy seabed into which fines may entrain and temporarily be stored. This layer only shows significant erosion during highly dynamic conditions, such as spring tide or storms. It therefore establishes a buffer capacity for fine sediment. Note that all interaction between the layers occurs via the water column; there is no direct transfer of sediment between the layers, or horizontal transport within the layers.

5.9.2. Deposition

The deposition flux D [kg/m²s] is computed based on the settling flux $w_s c_b$. It is expressed as $D = D_1 + D_2$, with D_1 and D_2 the deposition fluxes to layer 1 and 2 respectively:

$$\begin{aligned} D_1 &= (1-\alpha)\, w_s c_b\, P_{sed} \\ D_2 &= \alpha w_s c_b\, P_{sed} \end{aligned} \tag{5.14}$$

α is the fraction of the deposition flux contributing to layer 2 ($\alpha \ll 1$) and c_b is the concentration close to the bed [kg/m³]. P_{sed} is the sedimentation probability that varies in the range 0-1. For values smaller than one, the deposition flux becomes smaller than the settling flux, which results in higher near-bed concentrations. This is discussed in the next section.

Consolidation of mud is not explicitly modeled, but is taken into account implicitly by the gradual transfer (via the water column) of sediment from bed layer 1 towards layer 2 through erosion and re-deposition.

Deposition in the second layer is set to zero when the mud fraction p_2 of layer S_2 reaches a (user defined) maximum mud fraction p_{max}. The mud fraction p_2 is calculated as:

$$p_2 = \frac{m_2}{(1-n)\rho_s d_2} \tag{5.15}$$

with m_2 the mud mass in bed layer 2 [kg/m²], n the porosity of the layer [-], ρ_s the solids density of sand [kg/m³] and d_2 the thickness of layer S_2. In this study, d_2 is set to 30 cm, which is the best estimate for the North Sea of van Kessel et al. (2011b).

Sedimentation probability P_{sed}

The parameter P_{sed} was introduced by van Kessel and Vanlede (2010) and represents a reduction in deposition because of effects that are not modeled explicitly.

The vertical discretization near the bed may be insufficient to properly reproduce high near-bed SSC. In the decelerating phase, a relatively high-concentration layer is formed right above the sediment bed, which can cause a reduction and possibly eventual collapse of turbulence (Winterwerp, 2001; Toorman et al., 2002; Winterwerp, 2006). An underestimation of the concentration gradient (due to limited vertical resolution) can therefore lead to an overestimation of vertical mixing near the bed.

Because hindered settling is not taken into account in the model, the settling velocity w_s is not reduced when c_b approaches the gelling concentration (around

100 g/l). This would also lead to an overestimation of the deposition flux in the model.

In the model, freshly deposited sediment immediately has a critical shear stress for erosion $\tau_{cr,e}$. In reality however, $\tau_{cr,e}$ is not attained instantaneously, but only gradually through consolidation. This means that the model will tend to underestimate resuspension of recently deposited sediments. This can be compensated for by reducing the deposition flux through P_{sed}, which keeps a higher fraction of the sediment in suspension, instead of becoming part of the bed.

Finally, flocculation could limit the deposition flux. Only aggregates that are strong enough to resist the bottom shear stresses will settle on the bed and be retained to the bed by cohesive bonds. Flocs in which the strength is too low will be broken up into smaller units, and will be re-entrained into the suspension. The broken aggregates will again participate in the aggregation process in the water column (van Leussen, 1994). This continuous process of aggregation and break-up is schematically presented in figure 5.21.

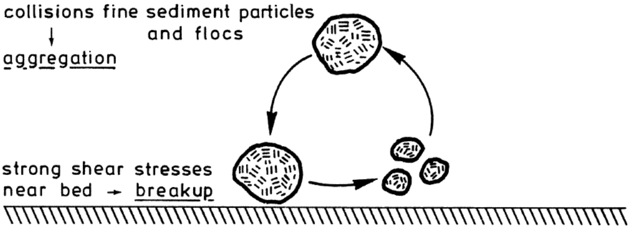

Figure 5.21: Schematic picture of floc aggregation and break-up near the bed (van Leussen, 1994).

The combined effect of the limited vertical resolution, hindered settling, consolidation and flocculation are parameterized by limiting the deposition flux, which increases the computed concentration near the bed c_b (van Maren et al., 2020). Note that P_{sed} in equation 5.14 is conceptually different from the probability of deposition $p_d = H(1 - \tau_{bed}/\tau_{cr,d})$ in the deposition formula of Krone (1962), which includes the Heaviside step function H that sets the deposition flux D to zero if the bed shear stress exceeds $\tau_{cr,d}$. In contrast, the factor P_{sed} in equation 5.14 is independent of bed shear stress and does not have a critical shear stress value. This implies a conceptual framework in which erosion and deposition can occur simultaneously (Winterwerp, 2007; Sanford and Halka, 1993).

5.9.3. Erosion

Erosion from the first and second layer are computed separately.

Erosion of the first layer S_1

The erosion flux of the first layer E_1 is computed as:

$$E_1 = \begin{cases} M_0\left(\frac{\tau}{\tau_{cr,e1}} - 1\right) & \text{for } \tau_{bed} > \tau_{cr,e1} \text{ and } m_1 > \frac{M_0}{M_1} \\ m_1 M_1\left(\frac{\tau}{\tau_{cr,e1}} - 1\right) & \text{for } \tau_{bed} > \tau_{cr,e1} \text{ and } m_1 < \frac{M_0}{M_1} \\ 0 & \text{else} \end{cases} \tag{5.16}$$

with m_1 the dry mass per unit area in layer S_1 [kg/m²], τ the total bed shear stress and $\tau_{cr,e1}$ the critical shear stress for resuspension, both in [N/m²], M_0 the zero order resuspension constant [kg/m²s] and M_1 the first order resuspension constant [1/s].

If the amount of mud in the bed m_1 is sufficiently high, the erosion flux follows the well-known empirical relation of Ariathurai-Partheniades (Ariathurai, 1974). Because in this formulation the erosion flux is independent of the amount of mud, it is a zero order process. For lower amounts of mud in the bed m_1, erosion is modeled as a first order process, in which the erosion flux scales linearly with the available sediment mass per unit area in layer 1. This modification was introduced by van Ledden et al. (2006). A thin layer of mud will probably not be uniformly distributed on the sandy seabed, but will tend to accumulate in the troughs of sand ripples and sand waves. This makes a first order resuspension rate more realistic in this case (van Kessel et al., 2011b).

Note that the first order erosion formulation introduces a stabilizing feedback in the model. A decreased deposition decreases the mud content, until an amount of mud m_1 is reached for which erosion equals deposition. The reverse is true for increasing m_1. With the classical Ariathurai-Partheniades erosion rate, there is no equilibrium mass: it is goes to zero or to infinity (van Kessel et al., 2011b).

The transition from first to zero order erosion was introduced by van Kessel et al. (2006) and occurs at $m_1 = M_0/M_1$. Using the combination of a first and zeroth order erosion has the advantage that a gradual, instead of a stepwise, transition is obtained between zones abundant in mud and zones depleted of mud, and that a dynamic equilibrium bed composition is established for any combination of sediment supply and bed shear stress climate, apart from low-dynamic zones where permanent and ongoing deposition can occur (van der Wal et al., 2010).

Erosion of the second layer S_2

Erosion of mud from the sandy seabed is only possible for conditions in which the sandy seabed itself is eroded. Rather than modeling sand transport, the erosion flux of mud E_2 is computed as the erosion flux of sand, multiplied by the mud fraction p_2 of layer S_2 (see equation 5.15). The underlying hypothesis is that the erosion of the sand particles is the dominant erosion mechanism and that the clay–silt particles are washed out together with the sand particles (Van Rijn, 2007).

For the erosion flux of sand, the empirical pick-up function of van Rijn (1984) is used. This formulation for the erosion of the buffer layer was developed in the framework of the sand mining study for Maasvlakte 2 (van Ledden et al., 2006).

$$E_2 = \begin{cases} p_2\ \phi_p\ \rho_s\sqrt{(s-1)gd_{50}} & \text{for } \tau > \tau_{cr,e2} \\ 0 & \text{else} \end{cases} \tag{5.17}$$

with p_2 the mud fraction in layer S_2 (see equation 5.15). Note that the factor p_2 in equation 5.17 makes this effectively a first order description of erosion, in that the erosion flux varies linearly with the amount of mud stored in the second layer m_2.

ϕ_p is the dimensionless pick-up rate:

$$\begin{aligned} \phi_p &= M_2\ D_*^{0.3}\ T^{1.5} \\ D_* &= d_{50}\left((s-1)\,\frac{g}{\nu^2}\right)^{1/3} \\ T &= \frac{\tau - \tau_{cr,e2}}{\tau_{cr,e2}} \end{aligned} \tag{5.18}$$

with D_* the dimensionless particle diameter and T the dimensionless excess bed shear stress. ν is the kinematic viscosity of water [m²/s] and d_{50} is the median grain diameter [m]. $s = \frac{\rho_s}{\rho_w}$ is the relative density of the sediment [-].

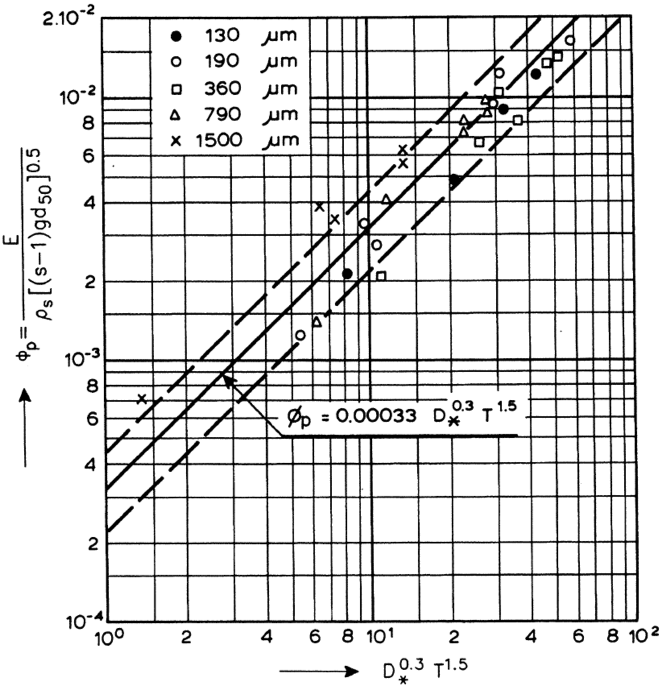

Figure 5.22: Empirical pick-up function for the erosion of sand beds (van Rijn, 1984).

M_2 is a dimensionless constant that van Rijn (1984) has calibrated based on flume experiments with pure sand as 3.3 e-4 for particles in the range of 130 to

1500 µm. The range of M_2 is estimated as (2 - 4) e-4 from the dashed lines in figure 5.22.

In the first application of this conceptual framework, van Ledden et al. (2006) reduce the value of 3.3 e-4 drastically (3 orders of magnitude) during calibration, in order to obtain a good correlation with the measured data. The overview of recently used parameterizations in table 5.3 shows that this has been the case for all listed applications since. This could be related to laboratory and field observations that show that the pickup process of the sand particles can be slowed down by the presence of clay–silt particles (van Ledden, 2003; Mitchener and Torfs, 1996).

Note that in literature, equations 5.17 and 5.18 are often abbreviated as:

$$E_2 = \begin{cases} p_2 {M_2}' \left(\frac{\tau - \tau_{cr,e2}}{\tau_{cr,e2}}\right)^{1.5} & \text{for } \tau > \tau_{cr,e2} \\ 0 & \text{else} \end{cases} \tag{5.19}$$

in which ${M_2}'$ has the unit [kg/m²s]. ${M_2}'$ and the dimensionless M_2 are related as follows:

$$ {M_2}' = M_2 \rho_s D_*^{0.3} \sqrt{(s-1) g d_{50}} \tag{5.20}$$

For ρ_s and ρ_w 2600 and 1024 kg/m³ respectively, d_{50} 300 µm and ν 1e-6 m²/s, the conversion factor on the right hand side of 5.20 is 319 kg/m²s.

Unfortunately, this short-hand notation has also led to some confusion in literature, in which dimensionless M_2 values were sometimes reported with the unit kg/m²s, without using the appropriate conversion factor. In the overview of model parameters in table 5.3, these errors were corrected.

5.9.4. Decoupling of the flow and sediment transport model

The application of the model in a scenario analysis context is one of the modeling objectives (see section 5.2). Some potential scenarios that were considered at the time of model inception (e.g. creating a string of islands in front of the coast), are expected to have an important impact on the sediment distribution in the bed. Therefore, the sediment transport computation needs to start from an empty bed, so that if the model is run sufficiently long, the results become independent of the initial sediment distribution. Reaching a sediment distribution that is in dynamic equilibrium, while starting from an empty bed typically takes a simulation of multiple years (see also the discussion in section 5.9.6). Computational efficiency is therefore important. Since the sediment transport model has a lower computational cost than the flow model, decoupling both models achieves this goal.

The choice of a model structure is often a trade-off, and decoupling the flow and sediment transport model comes at the conceptual cost of ignoring sediment-induced baroclinic pressure gradients (Winterwerp and Van Kessel, 2003) and stratification effects on turbulence (Winterwerp, 2001; Toorman et al., 2002; Winterwerp, 2006). Since sediment-induced density flows can enhance residual sediment transport into the harbor (Winterwerp and Van Kessel, 2003), this effect is parameterized by increasing the settling velocity inside the harbor in order to increase the trapping efficiency. This is further discussed in section 5.11.2.

A recent model application has shown that the sediment-induced baroclinic pressure gradient only has a limited impact on the residual current and the sediment distribution in the Belgian coastal zone, and that this effect is secondary to the salinity-induced baroclinic pressure gradient (van Maren et al., 2020). The effect of salinity on the model results is discussed in section 5.10.3. The impact of omitting the stratification effects on turbulence is discussed more in detail in section 5.12.2.

5.9.5. Grid aggregation

Hydrodynamic modeling usually requires a more detailed grid than water quality modeling. Therefore, generally it is allowed to reduce the number of computational cells in the water quality modeling in a process that is called grid aggregation (Deltares, 2018a). The numerical solvers that are available within the Delwaq suite are finite volume schemes, and therefore allow for irregular grids and the aggregation of control volumes.

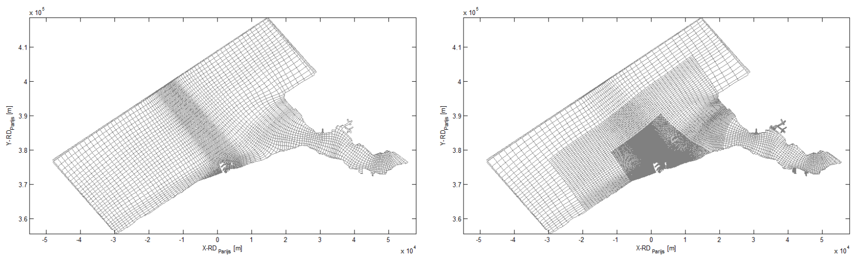

Figure 5.23: Two different aggregated grids for the sediment transport simulation: a coarse 4x4 aggregation (left panel) and a fine non-uniform aggregation (right panel).

Figure 5.23 shows the two grid aggregations that are used in the sediment transport calculation: a coarse 4x4 aggregation, and a locally aggregated grid (which corresponds to the fine grid in the model structure in figure 5.2). The non-uniformly aggregated grid is the same as the hydrodynamic grid in the area close to the harbor; it is coarsened by 3x2 in the long-shore and cross-shore direction in the intermediate region and 6x4 near the open sea boundaries. The coarse grid is used during initialization to speed up the simulation (see section 5.9.6).

5.9.6. Model spin-up

Each sediment transport simulation is started from an empty bed, with prescribed suspended sediment concentration at the four open boundaries. To accelerate the model spin-up, each simulation is first carried out using the coarse grid (see figure 5.23, left panel) until the model approaches dynamic equilibrium. This is defined as a state where the long-term variation (timescale of years) in the amount of sediment in the bed and in suspension is small compared to short-term variations (intratidal and spring-neap variation), and sediment fluxes into the model are equal to sediment fluxes out of the model. The simulation is then continued using the fine grid (see figure 5.23, right panel). During the spin-up, the thickness d_2 of the second bed layer S2 is set to 5 cm in order to speed up the adaptation process (see equation 5.15). After the model spin-up, a final run is carried out on the fine grid with the thickness of S2 and the its mud amount being scaled up by a factor of 6 (i.e. thickness of 30cm). The model results shown in this chapter are results of this final run.

5.9.7. Overview of recent model applications

The conceptual framework for erosion and deposition described above is often used in engineering applications. Table 5.3 lists the parameterizations from recent model schematizations of the North Sea and the Scheldt.

North Sea

Gerritsen et al. (2000) focus on modeling SSC patterns and their seasonal distribution on the scale of the Southern North Sea. Their model is calibrated against satellite images. van Ledden et al. (2006) use a North Sea model to assess the effects of sand extraction in the framework of Maasvlakte 2 (seaward extension of the Port of Rotterdam). They introduce both the concept of first order erosion and the two-layer bed model with an algorithm for the buffering of fines in the sandy seabed (see section 5.9.3). The model is calibrated against hourly surface SSC over 1 year at station Noordwijk, 10 km of the Dutch coast, and qualitatively compared against the silt atlas of Suijlen and Duin (2002). van Kessel et al. (2011b) further develop this model by introducing a second, finer fraction. van Kessel and van Maren (2013) parameterize the erosion of the first layer using a combination of first and zero order erosion (see section 5.9.3).

Vroom et al. (2016) developed a new model schematization for the Belgian Continental Zone. It is a morphodynamic model with 1 sand fraction and 3 mud fractions and a two-layer description of the bed. The sediment calculation is coupled with the hydrodynamic calculation through a sediment-induced buoyancy term. This model has been calibrated against a combination of frame measurements, satellite images and dredging statistics. The authors have two alternative conceptual models and corresponding parameterizations of the water-bed exchange. In one alternative, near-bed SSC is increased by introducing a sedimentation probability P_{sed} (see section 5.9.2). In another alternative, an additional erodible mud stock is introduced in the bed, which corresponds to an outcropping Holocene mud layer in the Belgian coastal zone. In a sensitivity analysis, van Maren et al. (2020) show that the sediment-density coupling increases the computed near-bed concentrations in the order of 10%, in combination with a reduced deposition ($P_{sed} = 0.1$). The near-bed concentration needs to be high enough for a positive feedback to occur, where an increased vertical gradient near the bed reduces the vertical mixing, which further increases the vertical gradient. Possibly the vertical resolution of 10 layers is not enough to accurately compute the near-bed concentration gradient, and the corresponding turbulence damping.

Scheldt estuary

van Kessel et al. (2006) and van Kessel et al. (2011a) describe the setup of a mud transport model for the Scheldt estuary. They use the two-layer bed model

		Deposition				Erosion				
		w_s	P_{sed}	$\tau_{cr,d}$	α	M_0	M_1	M_2	$\tau_{cr,e1}$	$\tau_{cr,e2}$
Reference	Study Area	mm/s	-	N/m²	-	kg/m²s	1/s	-	N/m²	N/m²
Gerritsen et al. (2000)	North Sea	0.06	-	0.1	-	2e-4	-	-	0.75	-
van Ledden et al. (2006)	North Sea	0.25	-	-	0.05	-	1.3e-6	3.5e-7	0.1	1.5
van Kessel et al. (2011b)	North Sea	1/0.125	-	-	0.0125/0.05	-	2.3e-5/5.8e-6	3.5e-7	0.1	1.5
van Kessel et al. (2013)	North Sea	0.4	-	-	0.05	1e-3	5.8e-6	3.5e-7	0.1	1.5
Vroom et al. (2016)	BCZ	0.5/2/4	1/0.1	-	?	1e-3	1e-4	3.1/6.3/12.5e-6	0.2	1
van Kessel et al. (2006)	Scheldt	1	-	-	0.1/0.05	1e-4	2.3e-5	3.5e-7	0.2	0.5
van Kessel et al. (2010)	Scheldt	1	0.1	-	0.1	1e-3	1.15e-5	1.8e-7	0.1	0.5
Cronin et al. (2018)	Scheldt	2/0.5	0.1	-	0.1	1e-3	2.3e-5	3.5e-6	0.2	1

Table 5.3: Recent parameterizations for deposition and erosion in engineering-type applications.

proposed by van Ledden et al. (2006), but adapt the first order erosion model into a combination of zero and first order erosion (see section 5.9.3).

van Kessel and Vanlede (2010) introduce the deposition probability P_{sed} into the conceptual model (see section 5.9.2) in order to increase near-bed sediment concentrations. The result was a four-fold increase in equilibrium concentrations in the estuarine turbidity maximum, because salinity-driven estuarine circulation transports more sediment upstream if the near-bed SSC is higher. Note that all the Scheldt models in table 5.3 use an off-line approach; therefore horizontal gradients in SSC do not trigger residual currents. Cronin et al. (2018) recalibrated the Scheldt model after introducing a second, finer fraction in the conceptual model.

5.9.8. Boundary and initial conditions

For the concentration boundary condition in the North Sea, the annual mean SSC is used, based on the depth-averaged concentrations derived from SeaWiFS satellite data (Van den Eynde et al., 2007). The boundary condition at the Western Scheldt was set at 50 mg/l, based on observations of SSC (Vandenbruwaene et al., 2016). Each run of the sediment transport model starts with an empty bed.

5.9.9. Dredging and disposal

Dredging and disposal are implemented following actual dredging strategies. Dredging is implemented as a daily process that is executed if the deposition thickness of layer S1 exceeds the dredging threshold. Five dredging zones are included in the model: Voorhaven, CDNB, Pas van het Zand, Scheur West and Scheur Oost (see figure 2.16 for their locations). Three disposal sites are implemented: S1, S2 and ZBO. A high disposal speed of 10^5 ton/day is chosen to ensure that the material dredged in the previous dredging event has been disposed completely, before the next dredging event the following day. The dredged sediment is distributed over the different disposal locations in a scheme that corresponds to the distribution ratios listed in table 2.1.

5.9.10. 1DV point model

In order to study model behavior and calibrate the model parameters against in situ data, a simplified 1DV point model is set up. This model computes the transient vertical distribution of a single fraction of SSC, and of the mud content in the bed. The vertical profiles of velocity and eddy viscosity, the water level and bottom shear stress are the result of a 3D hydrodynamic model. In this study, the 3D flow model described in section 5.5 is used. More details on the implementation and validation of the 1DV model can be found in appendix D.

5.10. Sensitivity analysis of the sediment transport model

5.10.1. On the formulation of excess shear stress in erosion formulas

In the conceptual model of erosion (see section 5.9.3), the excess shear stress is expressed as a dimensionless factor T:

$$T = \frac{\tau - \tau_{cr,e}}{\tau_{cr,e}} \tag{5.21}$$

Equation 5.21 is used both for erosion of the first layer (eq. 5.16) and raised to the power 1.5 for erosion of the second layer (eq. 5.17).

Alternatively, also the *dimensional* form $\tau - \tau_{cr,e}$ is sometimes used in the description of erosion of a muddy bed (Van Prooijen and Winterwerp, 2010; Winterwerp et al., 2012), which implies a different unit for the resuspension constant M. Mathematically, both formulations of the erosion formula describe a linear relation between the erosion flux and the excess shear stress. This linear relation was originally proposed by Kandiah (1974) and (Ariathurai, 1974), based on flume experiments by Partheniades. The relation was often confirmed, e.g. for high-concentration in situ conditions in the mouth of the Amazon river by Vinzon and Mehta (2003) (see figure 5.24).

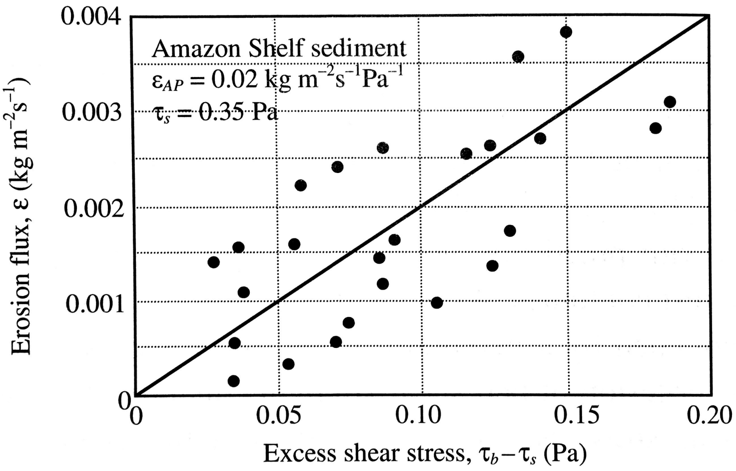

Figure 5.24: Erosion flux versus excess bed shear stress for Amazon shelf data (Vinzon and Mehta, 2003).

The inclusion of $\tau_{cr,e}$ in the denominator of equation 5.21 is attractive from a dimensional point of view, but it can introduce inaccuracies in establishing the erosion rate M from erosion parameters (Van Prooijen and Winterwerp, 2010). Furthermore, it also complicates the estimation of M and $\tau_{cr,e}$ during model calibration.

Apart from triggering the Heaviside step function (as the word ”critical” in its name suggests), $\tau_{cr,e}$ also influences the erosion flux E through its inclusion in the denominator of T (see equations 5.16 and 5.18). This introduces a co-dependency between M and $\tau_{cr,e}$ during calibration.

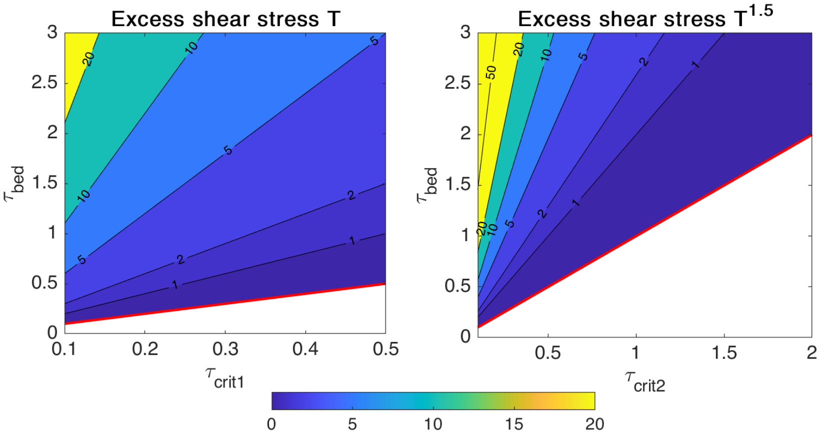

Figure 5.25: Dimensionless shear stress factor T in function of $\tau_{cr,e}$ and τ_{bed}.

This is further explored in figure 5.25, which shows the value of the dimensionless shear stress factor T as used in the erosion formulas for the first layer (left panel), and the factor $T^{1.5}$ for the second layer (right panel), for varying values of $\tau_{cr,e}$ and τ_{bed}. The step function is defined by the thick red line. T is only defined if $\tau_{bed} > \tau_{cr,e}$. The range for τ_{bed} is based on the range of bed shear stress that is expected in the model domain (see figure 5.18). $\tau_{cr,e}$ varies in the range that is typically reported in engineering type models of the Scheldt and the North Sea (listed in table 5.3). While lines of constant excess bed shear $\tau - \tau_{cr,e}$ stress would be parallel to the red (identity) line, the isolines of T (eq. 5.21) fan out in figure 5.25. This means that the erosion flux E_1 still varies linearly with the excess shear stress, but that the slope of that curve varies both with M and $\tau_{cr,e}$. The lower $\tau_{cr,e}$ is, the steeper the slope.

In a typical calibration of a sediment transport model, M and $\tau_{cr,e}$ need to be estimated to obtain a suitable erosion flux E under a given variation of τ_{bed}. M and $\tau_{cr,e}$ cannot be treated independently however, because $\tau_{cr,e}$ appears in the denominator of the non-dimensional excess shear stress (equation 5.21). This effect is stronger for the erosion formula of the second layer, because of the power 1.5. Figure 5.26 shows the annual erosion fluxes E_1 and E_2 [kg/m²] under variable $\tau_{cr,e}$, with erosion coefficients M_0 = 1e-3 [kg/m²s] and M_2 = 3.5e-7 [-]. The simulation is performed with a year of τ_{bed} (flow + wave) at station MOW1 and under the assumption of an unlimited sediment supply. The figure quantifies the total effect of $\tau_{cr,e}$ on the computed erosion fluxes and can be helpful during model calibration.

A sediment transport model that uses the non-dimensional excess shear stress T (equation 5.21) will be more sensitive to changes in $\tau_{cr,e}$ than a model that uses

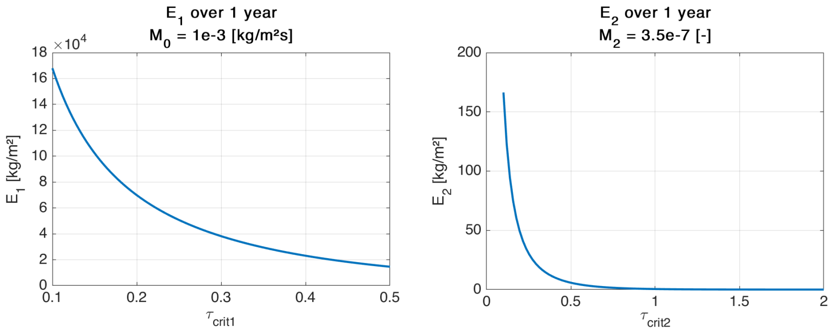

Figure 5.26: Computed annual erosion fluxes E_1 and E_2 [kg/m²] at station MOW1, with constant erosion coefficients and for varying $\tau_{cr,e}$.

the dimensional form $\tau - \tau_{cr,e}$ in the description of erosion.

5.10.2. First order resuspension rate M_1

The sensitivity of the model to the first order resuspension rate M_1 is assessed by varying the parameter over 2 orders of magnitude, while keeping all other parameters constant. Parameter settings for the sensitivity runs are listed in table 5.4.

RunID	M_1 [1/s]	M_1 [1/day]
2.40	1.2e-6	0.1
2.77	5.8e-6	0.5
2.71	1.2e-5	1
2.45	2.3e-5	2
2.78	1.2e-4	10

Table 5.4: Parameterizations for the sensitivity runs for parameter M_1.

One can observe in figure 5.27 that the computed concentrations (left panel) are to a large extent insensitive to variations in M_1. A notable exception is run 2.78: when M_1 is increased to 10/day, the result is a bed that is depleted ($m_1 = 0$ in right panel) during some parts of the tidal cycle, which has an effect on the computed concentrations.

In contrast to the SSC, the model *is* sensitive in the computed equilibrium mud mass in the first layer m_1 (right panel in figure 5.27), with lower m_1 for higher M_1. This can be understood in terms of the long-term equilibrium conditions, that can be calculated by equating deposition (equation 5.14) to first order erosion (equation 5.16) in the first layer:

$$D_1 = E_1 \tag{5.22}$$

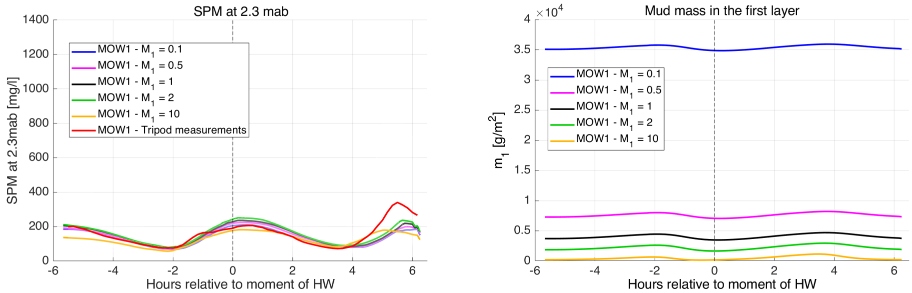

Figure 5.27: Results for the sensitivity runs for parameter M_1 at station MOW1: SSC at 2.3 mab (left panel) and mud mass m_1 in first layer (right panel).

Solving for m_1 gives:

$$m_1^{eq} = \frac{(1-\alpha)w_s c_b^{eq} P_{sed}}{M_1 T_1} \tag{5.23}$$

with T_1 shorthand for the dimensionless excess shear stress. Equation 5.23 is consistent with the model results presented in figure 5.27, in that m_1^{eq} is inversely proportional to M_1.

Interestingly, the increase in the erosion flux E_1 that would be expected by an increase in the resuspension constant M_1, is compensated by the decrease in sediment mass m_1, which causes a decrease of the first order erosion flux. These two effects appear to cancel each other out. These results illustrate how the first order erosion formulation acts as a stabilizing feedback on the erosion flux in a dynamic equilibrium. Since erosion from the second layer is also formulated as a first order process (see section 5.9.3), m_2^{eq} and M_2 are also inversely proportional, which makes E_2 also largely insensitive to changes in M_2.

5.10.3. The influence of salinity

The effect of salinity on the formation of the coastal turbidity maximum is investigated by comparing the depth-averaged sediment distribution in baroclinic and barotropic model runs which have the same sediment parameterization (see figure 5.28).

This result can be understood in terms of the density-induced residual circulation (see figure 5.29), which has an impact on the residual velocity profiles. The current velocity profiles, averaged over a spring-neap tidal cycle show that the density driven current induces a seaward residual flow in the upper part of the water column while enhancing the landward flow in the lower part. This results in more sediment being trapped in the coastal turbidity maximum in baroclinic mode.

Apart from the one run in barotropic mode that is discussed in this section on the sensitivity analysis, all other sediment transport calculations in this chapter are based on the hydrodynamic run in baroclinic mode.

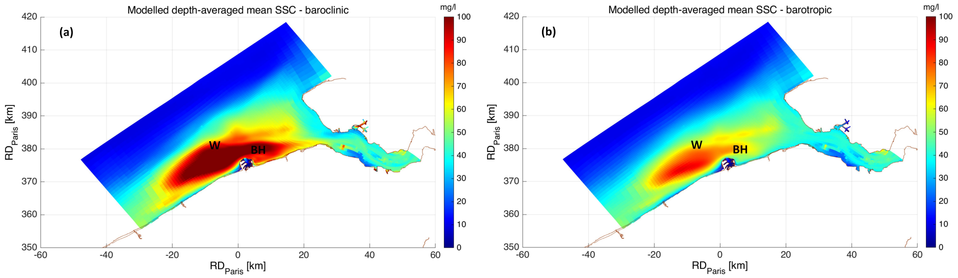

Figure 5.28: Depth-averaged SSC, averaged over one spring-neap cycle, showing the coastal turbidity maximum as modeled in baroclinic (a) and barotropic mode (b).

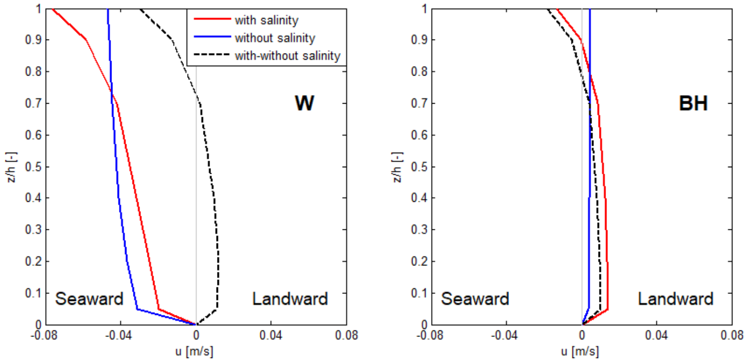

Figure 5.29: Spring-neap averaged residual current profiles computed at: (a) Wandelaar (W) and (b) Bol van Heist (BH) (see figure 5.28 for the locations). Positive values indicate landward currents.

5.10.4. The importance of interaction with the bed on the CTM

During the sensitivity analysis, the model was run with different values for the sedimentation probability P_{sed} (0; 0.25; 0.5 and 1). All runs are performed with a single fraction, with a settling velocity of 1 mm/s. For $P_{sed} < 1$, the deposition flux becomes smaller than the settling flux $w_s c_b$ (see equation 5.14). For $P_{sed} = 0$, there is no deposition, and all sediment remains in the water column. Since all runs start from an empty bed, the bed remains empty during this simulation.

Figure 5.30 shows the influence of P_{sed} on the depth-averaged SSC. It is noteworthy that the run without any interaction with the bed (P_{sed} = 0) still produces a (weak) CTM. This shows how the local hydrodynamic conditions trap sediment in the CTM (see also the discussion on the transporting agents of sediment in section 2.8). The interaction between the bed and the water column is therefore not a necessary condition for the CTM to develop. It does however have an impact on the strength of the CTM: for increasing values of P_{sed}, more sediment is present in the CTM (see figure 5.30).

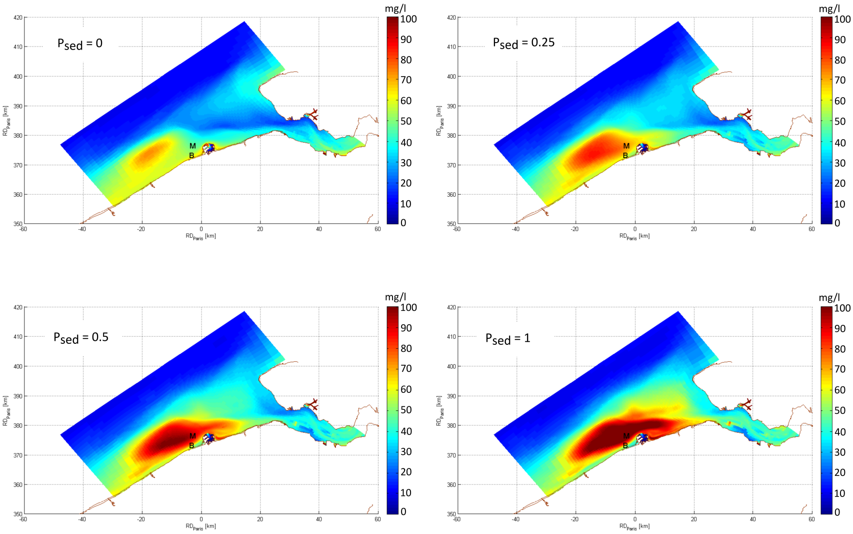

Figure 5.30: Depth-averaged SSC for different values of P_{sed}: 0 (top left); 0.25 (top right); 0.5 (bottom left) and 1 (bottom right).

5.11. Calibration of the sediment transport model

The calibration of the sediment transport model is performed in two steps. First, the dataset of observed velocity and SSC at Blankenberge (see section 2.12.2) is used to calibrate the model settings of the 1DV model in section 5.11.1. Since the governing equations of the 1DV model are taken from the 3D model, and since both models use the same simulation as hydrodynamic forcing, the calibrated parameterization of the 1DV model can be used as a starting point in the calibration of the 3D model, which is performed against a much broader dataset (see section 5.11.2).

5.11.1. Initial calibration with the 1DV point model

For a description of the 1DV model, the reader is referred to section 5.9.10 and appendix D. Table 5.5 shows the calibrated parameterization of the 1DV model. The results are discussed below, both for a coarse and a fine fraction.

Parameter	Description	Value	Unit
w_s	Settling velocity	0.5/3	mm/s
P_{sed}	Sedimentation probability	1	-
M_0	Zero order resuspension constant	1E-04	kg/m²/s
$\tau_{cr,e}$	Critical shear stress for erosion	0.1	N/m²

Table 5.5: Result of the calibration of the 1DV model.

The ensemble in the left panel of figure 5.31 is the result of a simulation of one month, with a settling velocity of 3 mm/s. For this coarse fraction, the intratidal dynamics is dominated by vertical mixing and by the interaction with the bed. During slack tide, the sediment in suspension settles below the ”sensor height” at 2.3 mab, and deposits on the bed. During maximum flood (and to a lesser extent during ebb), the bed is eroded and sediment is resuspended in the water column. The run is initialized with enough sediment in the bed as to avoid bed depletion during spring tide conditions (m_0 is 4 kg/m²).

The result in figure 5.31 can be compared for validation against the measured ensemble for normal tides in figure 2.19. The median SSC during maximum flood is 300 mg/l in the 1DV model, which is a good match with the measurements. The ebb peak in SSC is underestimated by 100 mg/l, however.

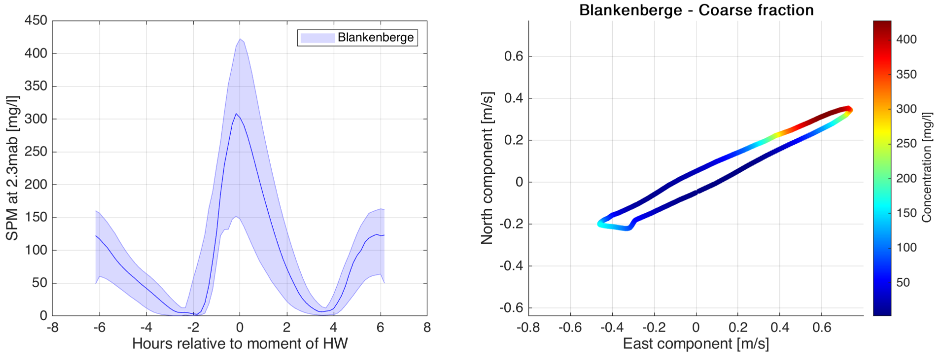

Figure 5.31: Tidal ensemble of the modeled SSC at 2.3 mab at Blankenberge from the 1DV model for a settling velocity of 3 mm/s. Ensemble average showing the median, and P10 and P90 percentiles of SSC (left panel) and a tidal ellipse extended with SSC for a spring tide (right panel).

A finer fraction with a settling velocity of 0.5 mm/s has a different intratidal signature (see figure 5.32). This run is initialized with a uniform sediment concentration of 100 mg/l. The finer fraction has less interaction with the bed. During slack, only a limited amount of mud is deposited, and this mass is easily eroded once the flow picks up again. This explains the small peak in SSC at 1.5h before HW. Because the finer fraction hardly settles, the intratidal variation in concentration is dominated by the variation in water depth (from 6 m to 10 m during a spring tide at station Blankenberge). This results in the peak in SSC around low water.

The 1DV results therefore suggest that in order to reproduce both the ebb and the flood peak in SSC, a model with two fractions is required.

5.11.2. Model parameterization(s) of the 3D model

A 3D cohesive sediment transport model with two fractions is set up. The settling velocity of the coarse and fine fraction are taken over from the 1DV model, as is the zero order resuspension constant M_0. The baseline parameterization of the sediment transport model is given in table 5.6. It is obtained through calibration, and falls within the range that is typically reported for large-scale sediment transport models of the North Sea and the Scheldt estuary (see table 5.3).

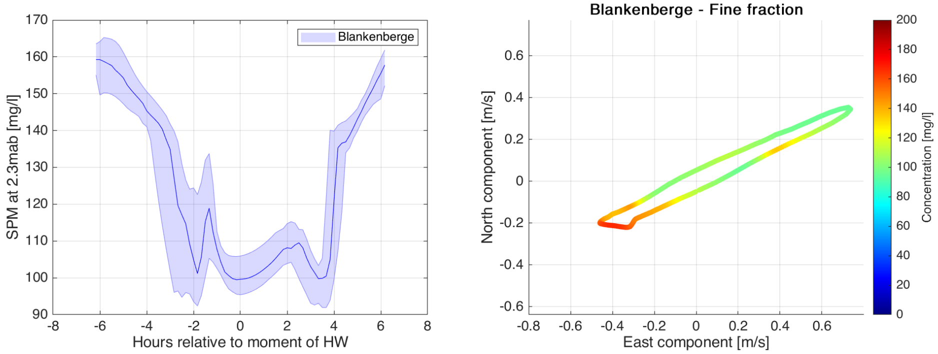

Figure 5.32: Tidal ensemble of the result from the 1DV model for a settling velocity of 0.5 mm/s: SSC at 2.3 mab at Blankenberge. Ensemble average showing the median, and P10 and P90 percentile of SSC (left panel) and a tidal ellipse extended with SSC for a spring tide (right panel).

The settling velocity inside the harbor is doubled for both fractions, in order to increase the trapping efficiency in the harbor. This is done as a parameterization of the sediment-induced density flows, which can enhance residual sediment transport into the harbor (Winterwerp and Van Kessel, 2003). Alternatively, van Kessel et al. (2011b) increased $\tau_{cr,e}$ inside the Rotterdam harbor to achieve a similar effect in their North Sea SPM model.

The erosion flux (see equation 5.16) transitions between first and zero order erosion at $m_1 = M_0/M_1$. In the parameterization of table 5.6, this corresponds to 8.6 kg m^{-2} of sediment in layer S1, or a layer of 2 cm thickness, assuming a dry density of 500 kg m^{-3}.

Parameter	Description	Value	Unit
w_s	Settling velocity	0.5/3	mm/s
	Settling velocity inside the harbor	1 /6	mm/s
P_{sed}	Sedimentation probability	1	-
α	Fraction of the deposition flux contributing to layer 2	0.1	-
d_2	Thickness of layer 2	0.3	m
M_0	Zero order resuspension	1.0E-04	kg/m²/s
M_1	First order resuspension	1.2E-05	1/s
M_2	Erosion coefficient for the second layer	1.8E-07	-
$\tau_{cr,e1}$	Critical shear stress for erosion first layer	0.1	N/m²
$\tau_{cr,e2}$	Critical shear stress for erosion second layer	0.5	N/m²

Table 5.6: Baseline parameterization of the 3D sediment transport model.

Equifinal parameterizations

Beven (2002) outlines a philosophy for the modeling of environmental systems that takes into account uncertainty and rejects the idea of being able to identify only one optimal model as being the most reliable for a given case. Environmental models may be non-unique due to e.g. errors in model structure, the period of data used for validation or the calibration of parameters. Because of this, there is the possibility of *equifinality* in that different model structures and parameterizations may give simulations that cannot be falsified from the available observational data (Refsgaard and Henriksen, 2004). Even models with moderate levels of complexity can show equifinality, see for example Beven and Freer (2001) for examples of different systems. More recently, van Maren and Cronin (2016) and van Maren et al. (2020) have applied equifinality in the parameterization of sediment transport models.

Based on the baseline parameterization, table 5.7 shows two alternative parameterizations CAL2 and CAL3, that are obtained through further calibration and sensitivity analysis.

CAL2 stems from the limited local sensitivity of the model to the sedimentation parameter P_{sed}. As argued in section 5.9.2, P_{sed} is a substitute for missing benthic boundary layer processes such as hindered settling, flocculation, sediment-induced buoyancy effects and consolidation. As shown in section 5.9.7, a lower value of P_{sed} is sometimes applied in recent model applications for the Scheldt and the North Sea. Even though a sensitivity analysis showed that the model *is* sensitive to changes in P_{sed} for a settling velocity of $1\,\mathrm{mm\,s^{-1}}$, this sensitivity decreases for higher settling velocities. Compared to the baseline run, CAL2 has less sediment in the system in the equilibrium condition, both in the water column (-5%) and in the bottom layers (-12%).

CAL3 can be understood from equation 2.5 describing the Rouse profile (see section 2.12.2). The Rouse number is the ratio between settling and turbulence strength. In parameterization CAL3, both the settling velocity and the vertical turbulent diffusion are scaled down, resulting in similar vertical profiles of SSC. The scale factor β can be seen as a damping term (<1) on the vertical mass diffusion, e.g. arising from stratification (Mehta et al., 2014). Compared to the baseline run, the equilibrium condition for CAL3 contains slightly more sediment in the water column (+1%), and 7% more sediment in the bed.

Parameter	Unit	Description	Baseline	CAL2	CAL3
w_s	mm/s	Settling velocity	0.5/3	0.5/3	0.5/2.5
P_{sed}	-	Sedimentation probability	1	0.5	1
β	-	Scale factor for vertical diffusion	1	1	0.75

Table 5.7: Equifinal parameterizations of the sediment transport model.

5.11.3. Quantification of model skill

During calibration, the parameterization of the sediment transport model is varied in order to minimize a dimensionless cost function that quantifies the model skill. The intratidal and spring-neap variation of SSC is compared to (1) measured ensembles at 2.3 and 0.3 mab. The spatial distribution of sediment is compared to (2) satellite-based maps of surface SSC and (3) maps of the observed mud fraction in the bed. Finally also the (4) dredged mass of mud is analyzed.

Since the model is calibrated against a set of measurements of varying types and from non-overlapping periods, it is important that this skill assessment is done in a coherent and consistent way. Appendix A presents a set of dimensionless cost functions to quantify model skill against three types of observational data: time series, maps and tidal ensembles. This general cost framework enables the quantification of the error between the model and a number of different observational datasets (even of different data types) into a single parameter that expresses the goodness-of-fit. A cost $C = 0$ corresponds to the perfect model. $C = 1$ means that the average of the measurements is as good a predictor as the model (with $C > 1$ meaning that the model is a worse predictor). A detailed quantification of the model skill is summarized in appendix B.2.

Ensembles of SSC

The model is validated against phase-averaged SSC at two heights (0.3 mab and 2.3 mab) in two locations (MOW1 and Blankenberge). Figure 5.33 shows the results for station MOW1. The corresponding figure for station Blankenberge is included in appendix B (figure B.1). The quantitative skill assessment (RMSE and cost) is given in table 5.8 for the baseline run. Tables B.5 and B.6 in appendix quantify the model skill of the equifinal parameterizations.

Baseline	RMSE			Cost		
Station	neap [mg/l]	average [mg/l]	spring [mg/l]	neap [-]	average [-]	spring [-]
MOW1 0.3 mab	346	474	485	0.53	0.57	0.60
MOW1 2.3 mab	68	105	128	0.35	0.22	0.12
Blankenberge 0.3 mab	344	393	504	0.52	0.53	0.66
Blankenberge 2.3 mab	101	119	179	1.04	0.85	0.84

Table 5.8: Quantitative skill assessment for SSC ensembles in the baseline run, expressed as RMSE and dimensionless cost.

The model underestimates the sediment concentration closest to the bed at 0.3 mab, but is within the the observed range at 2.3 mab. The model misses the ebb peak in SSC however.

Surface SSC

Figure 5.34 compares the modeled surface SSC in the baseline run with observations derived from satellite images (see section 2.10.2).

To quantify model skill against maps of observations, the RMSE is calculated as the square root of eq. A.5, and the cost is calculated with eq. A.7.

Even though the satellite based maps do not extend to the coast, the computed surface SSC agrees well with the measurements, both in terms of location and

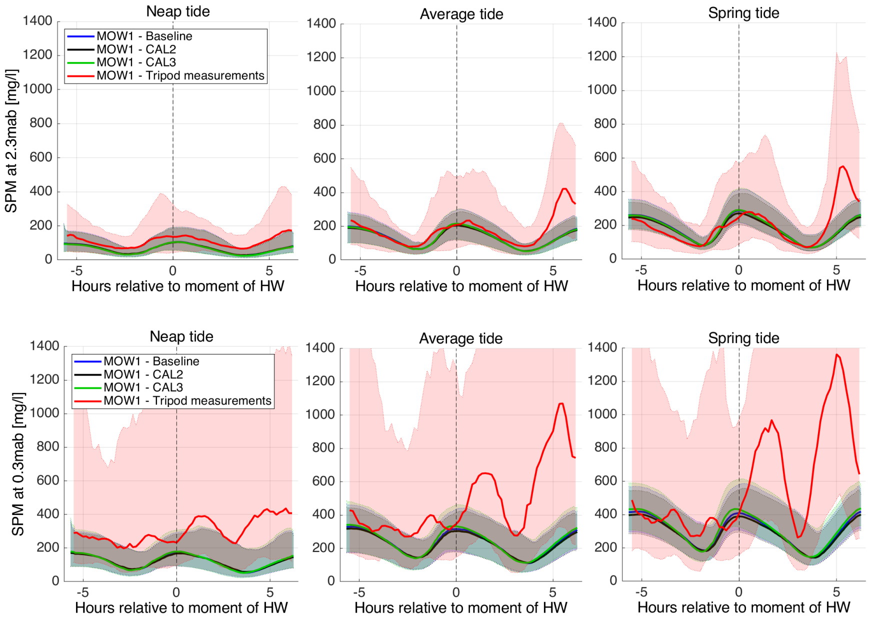

Figure 5.33: Observed (red) and modeled (blue) SSC ensembles for neap (left panel), average (middle) and spring tide (right) at station MOW1 at 2.3 mab (top) and 0.3 mab (bottom). The thick line represents the median in the ensemble; error bands indicate the P10 and P90 intervals.

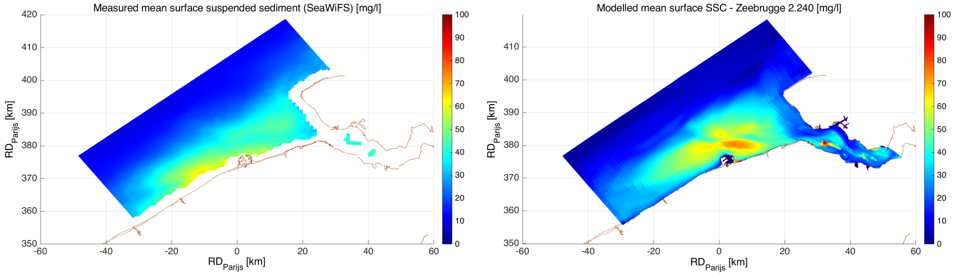

Figure 5.34: Observed (left) and modeled (right) surface SSC. Observations from Van den Eynde et al. (2007).

values. The model slightly overpredicts the observations in all three simulations. CAL2 has slightly lower surface SSC than the baseline, and CAL3 slightly higher, which agrees with the different equilibrium sediment mass in the water column noted above. All three equifinal parameterizations result in the same cost for the reproduction of surface SSC.

Mud content in the bed

Because every run starts from an empty bed, the computed sediment distribution on the bed represents the dynamic equilibrium that corresponds to the chosen

	Surface concentration		
Simulation	Bias mg/l	RMSE mg/l	Cost -
Baseline	2.8	8.5	0.4
CAL2	1.2	7.7	0.4
CAL3	0.4	8.2	0.4

Table 5.9: Quantitative skill assessment for surface SSC, expressed as RMSE and dimensionless cost against surface SSC derived from satellite images.

parameter settings. It is compared to the measured distribution to assess model skill. The modeled mud content in the bed p_2 is computed from the yearly averaged mud content in the second layer in the model (see eq. 5.15).

Figure 5.35 compares the computed mud content in the bed (from the baseline simulation) with the observed values (see section 2.10.1 and Van Lancker et al. (2007b)). The model skill is quantified in table 5.10.

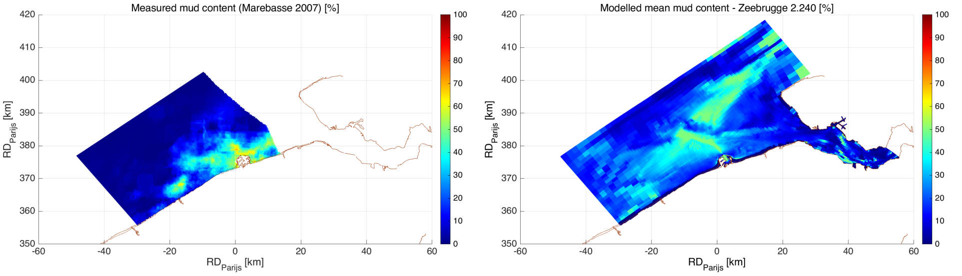

Figure 5.35: Observed (left) and modeled (right) mud content in the bed. Observations from Van Lancker et al. (2007b).

	Mud content in the bed		
Simulation	Bias %	RMSE %	Cost -
Baseline	12.9	17.5	1.5
CAL2	10.9	16.4	1.3
CAL3	14.2	18.3	1.6

Table 5.10: Quantitative skill assessment for mud content in the bed, expressed as RMSE and dimensionless cost against the bed composition map of Van Lancker et al. (2007b).

The observations of Van Lancker et al. (2007b) only cover the Belgian part of the continental shelf, and therefore also only a part of the model domain. But even with this partial coverage, it is clear that the model does not accurately reproduce the mud content in the bed. The cost >1 indicates that the model is actually a worse predictor than the average of the observations. Within the complete set of calibration runs, the cost never drops below 0.98. This suggests that the conceptual model that is described in section 5.9 fails to predict the observed distribution of mud mass in the bed. As an alternative modeling strategy, one might therefore consider using the observed mud content in the bed as an initial condition, and running the model for a shorter period.

Dredging and disposal

The modeled and observed dredged mass is compared in table 5.11, separately for the harbor and the access channels (Scheur and Pas van het Zand).

	Observed MTDM	Modeled MTDM		
		Baseline	CAL2	CAL3
Harbor	4.3 (2.6 - 5.0)	1.4	1.3	1.4
Channels	2.3 (1.5 - 3.0)	1.7	1.3	2.0

Table 5.11: Observed and modeled yearly dredged sediment mass in million tonnes dry matter of mud/year. The numbers in brackets are the range over the period 2005 to 2013.

The model gives a fair reproduction of the siltation in the access channels, but systematically underpredicts the siltation in the harbor by a factor of three. The model does not include sediment-induced density flows, which can enhance residual sediment transport into the harbor (Winterwerp and Van Kessel, 2003). This effect is parameterized by doubling the settling velocity inside the harbor in order to increase the trapping efficiency (see section 5.9.4). Even with this parameterization, the model underpredicts the siltation in the harbor. Note that this underprediction of harbor siltation has also been reported in a separate modeling study that *did* include sediment-induced density flows (Vroom et al., 2016; van Maren et al., 2020).

The inflow of SSC in the harbor is studied more in detail using the geometric decomposition method (presented in chapter 3). Figure 5.36 shows the horizontal component of sediment exchange, both from the baseline model and from the measurement campaign that was used to validate the flow pattern in section 5.6.3. The horizontal component of the exchange flow captures the advection of SSC from 2h before HW to HW. The timing of the inflow is correct, but the model shows a *higher* inflow of sediment than the measurement. This is somewhat unexpected, given that the results in table 5.11 suggest that the model underestimates the sediment import in the harbor. The analysis in chapter 3 shows that the total net import of sediment calculated from this measurement is 708 TDM (over a spring tide in summer). However, the observed dredging amount is 4.3 MTDM/yr, which corresponds to an average sediment import of about 6100 TDM/tide. Due to the blanking distance, the ADCP measurement has no data in the bottom 1 meter. It is hypothesized that the lack of measurement data in the bottom meter causes the ADCP measurement to underpredict the sediment exchange. Note that estimates

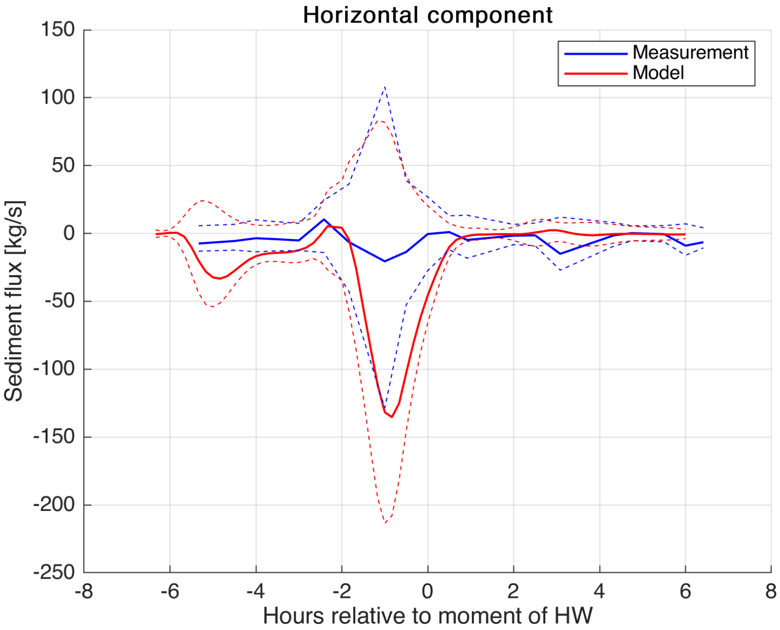

Figure 5.36: Horizontal component of sediment exchange at the harbor mouth. Model in red, measurements in blue. Net flux in full line, gross flux in dashed lines (inflow is negative).

of net sediment import based on ADCP measurements are very sensitive to the extrapolation of near-bed concentrations (see table 4.1 and its discussion in section 4.4.4).

Because the hydrodynamic validation of the model (see section 5.6.3) established that the model is able to reproduce the flow patterns at the entrance of the harbor, and because the data analysis in chapter 4 found no evidence of siltation through moving HCBS layers (a phenomenon that cannot be represented by the model), it is proposed that the underprediction of the harbor siltation by the model is related to the underprediction of the sediment concentrations close to the bed (established in section 5.11.3).

5.12. Discussion

5.12.1. Sediment balance

Figure 5.37 shows a schematized mass balance from the baseline run. Fluxes are expressed in million tonnes dry matter (MTDM) per year. The northeastward residual flux of 19.4 MTDM/yr corresponds well with the 19.2 MTDM/yr that was calculated by Fettweis et al. (2007) using a combination of satellite images, in situ measurements and a 2D hydrodynamic numerical model (see also section 2.7.1 for a discussion on the uncertainty around this number). The annual siltation in the harbor of 1.4 MTDM/yr is discussed more in detail in section 5.11.3.

Since the model is in dynamic equilibrium, the net erosion/deposition flux in figure 5.37 is close to zero. The yearly erosion (or deposition) flux in the North Sea part of the model domain is ~6000 MTDM/yr, which is about 300 times larger than the net flux through the western boundary. This high ratio underlines the importance of the deposition/resuspension cycle in the mud dynamics of the zone of interest. It also helps to understand the insight from clay mineralogical analysis that even though the influx of sediment from the Dover strait is an important input in the Southern North Sea, it has a different clay mineralogical composition (see section 2.7.2). The SPM from the English Channel is mixed with the larger mass of sediment that is ”trapped” in the sedimentation/erosion cycle. This helps to explain the difference in clay composition between SPM in the English Channel and SPM from the Belgian Coastal Zone (BCZ). The high ratio also indicates that, even though sediment dynamics in the BCZ is understood as an open system in connection with the North Sea (Fettweis and Van den Eynde, 2003), the tidal erosion and deposition cycle gives it some characteristics of a closed system, like a distinct clay mineralogical fingerprint.

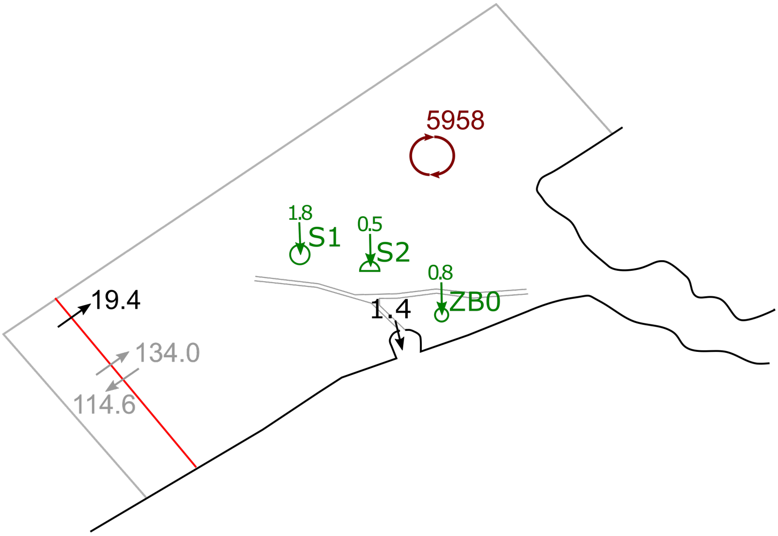

Figure 5.37: Sediment balance in the baseline run, in MTDM/yr. Net fluxes in black; disposal fluxes in green; erosion/deposition over the North Sea domain (excluding the Scheldt estuary) in red.

5.12.2. Vertical gradient of SSC

The computed SSC at 0.3 and 2.3 mab are used to determine the vertical gradient strength $\widetilde{\mathrm{Ro}}$ (introduced in section 2.12.2). Figure 5.38 compares the modeled and measured $\widetilde{\mathrm{Ro}}$ at station MOW1.

Except during the short time span between max flood (HW-1h) and HW, the model systematically underestimates both the absolute value and the intratidal variation of $\widetilde{\mathrm{Ro}}$.

One possible explanation is the fact that the model does not include aggregation

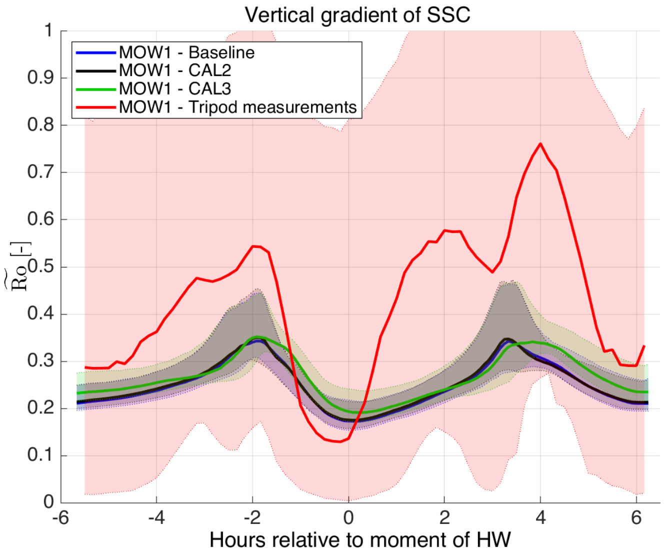

Figure 5.38: Tidal ensemble of measured (red) and modeled vertical gradient strength $\widetilde{\mathrm{Ro}}$ at station MOW1. The thick line represents the median in the ensemble; error bands indicate the P10 and P90 intervals.

dynamics. Fettweis and Baeye (2015) have shown from in situ measurements at MOW1 that the floc size and settling velocity are higher during slack tide than during peak flow conditions. Indeed, at higher levels of turbulence, floc break-up is enhanced, resulting in the decrease in size and settling velocity of the flocs during peak flow conditions. Conversely, a higher settling velocity during slack results in a higher value of $\widetilde{\mathrm{Ro}}$.

Stratification-induced turbulence damping could also be a contributing factor (Le Hir et al., 2000; Winterwerp, 2001; Toorman et al., 2002; Winterwerp, 2006). The large flocs that occur during slack water settle quickly, and form a lutocline. Stratification-induced turbulence damping contributes to the formation and stability of this lutocline. The resulting reduction of vertical mass diffusion would also contribute to a higher value of $\widetilde{\mathrm{Ro}}$. Bed boundary level changes up to 25 cm around the slack tide preceding ebb (HW+3h) and up to 7 cm at the slack tide preceding flood (HW-3h) were observed with an acoustic detection method at station MOW1 (Baeye et al., 2012). This suggests the occurrence of lutoclines below the bottom sensor at 0.3 mab.

5.12.3. Flocculation

The model does not include aggregation dynamics, and a constant value of settling velocity is implemented (see table 5.6). However, directly observed values of settling velocity inside the harbor (see figure 2.7 and its discussion in section 2.6.2) show that there is an intratidal variation of one order of magnitude of settling velocity. The observed settling velocities can be understood in terms of the conceptual relationship proposed by Dyer (1989). The settling velocity increases at low shear stresses due to flocculation enhanced by shear, and decreases due to floc disruption at higher stresses for the same concentration (Manning and Dyer, 2007).

Higher values of w_s have been observed than those implemented in the model. However, increasing the settling velocity in the model significantly decreased the model skill.

Fettweis et al. (2014) argue that the seasonality in SSC in the Belgian nearshore area (southern North Sea) is mainly caused by the higher biological activity in spring and summer, which causes the formation of larger and stronger flocs, which in turn leads to higher settling rates. They argue that this effect is more important than the relatively smaller seasonality in wind strength and thus wave climate. Since this model only includes the seasonality in wave forcing, and not in settling velocity, it would be ill-suited to study the seasonal variation of SSC in the North Sea.

Recently, Shen et al. (2018) were able to reproduce the intratidal variation of the floc size distribution at station WZ Buoy, which is located at about 2 km from the entrance of the Zeebrugge harbor. They used a tri-modal flocculation model (microflocs, macroflocs and megaflocs) in a 1DV model. It is a promising approach that in principle could be extended to a 3D application in an engineering type model.

5.12.4. Erosion of consolidated mud layers

By comparing the value in the model for $\tau_{cr,e}$ (see table 5.6) to measured vertical profiles of $\tau_{cr,e}$ (see figure 2.5), it is clear that the model only describes the erodibility of the top of the mud layer. This relates to the fact that the model does not take into account consolidation.

The largest potential reservoir of fine-grained sediments in the nearshore area consists of medium-consolidated Holocene mud (Fettweis et al., 2009). These bed layers are difficult to erode however, with measurements showing $\tau_{cr,e}$ of over 10 Pa (see section 2.6.1). The computed bed shear stress remains well under 10 Pa (see section 5.8.3).

Erosion of consolidated mud in stormy conditions could occur by mass failure (Li and Mehta, 2000). Mud pebbles would be an indication of this type of erosion and they have been observed in BCZ (Fettweis et al., 2009). This would indicate that erosion of Holocene mud can indeed occur, but only under storm conditions (Van Lancker et al., 2007a). Since mass failure is not included in this model, the Holocene mud source is not included in the model. This is in contrast to one of the equifinal models proposed by van Maren et al. (2020), in which the holocene mud source is included in the model, but with a $\tau_{cr,e}$ of 1 Pa in order to allow for erosion.

5.13. Conclusions

The modeling objective (see section 5.2) inspired the choice of the conceptual model and the corresponding model structure.

The modeling of the hydrodynamic forcing (flow, wave and total bed shear stress) was successful, as shown in the quantified skill assessment in sections 5.6 and 5.8. For the wave model, a combination of a SWAN model of the southern part of the North Sea with data assimilation shows a good agreement with the measurements, both for the wave height and wave period. In comparison, a fetch length approach gives a poor representation of the wave height, and a systematic underestimation of the wave period. Note that the remaining uncertainty in the measurement method of total bed shear stress (discussed in section 5.8.2) complicates the validation of the hydrodynamic forcing.

The calibration of the sediment transport model is performed in two steps. First, a 1DV model is calibrated against observations. The results highlight the different intratidal signatures for a coarse and a fine fraction. The calibration suggests that, in order to reproduce both the ebb and the flood peak in SSC, a model with two fractions is necessary. Since the governing equations of the 1DV model are taken from the 3D model, and since both models use the same simulation as hydrodynamic forcing, the calibration result of the 1DV model is the starting point for the calibration of the 3D model.

The 3D sediment transport model is based on a conceptual model that is often used in engineering applications (see overview in section 5.9.7). During calibration, no parameterization was found however that satisfied all modeling objectives. While giving a reasonable reproduction of the SSC at 2.3 mab, the model systematically underpredicts the concentration at 0.3 mab and hence also the vertical gradient. Sections 5.9.2 and 5.12.2 discuss some important conceptual uncertainties that remain in the description of the near-bed sediment dynamics.

The ability to start the sediment transport calculation from an empty bed played a role in the choice of model structure, particularly in the choice to decouple the flow and the sediment transport model (see section 5.9.4). However, no model parameterization was found that showed adequate skill in reproducing the observed sediment distribution in the bed (see section 5.11.3). Therefore, for future applications of a large scale sediment transport model (e.g. an estuary or a coastal zone), the modeler could consider to initialize the model with the observed sediment distribution in the bed, if such a dataset is available and if the model aim permits it.

The lessons learned on the siltation of the harbor are synthesized in the general conclusions in section 7.3.

5.14. Acknowledgments

Data on bathymetry, wave and currents were gathered and made available by Flemish Hydrography from the Agency for Maritime and Coastal Services - Coastal Division. Additional data of bathymetry and dredging works were provided by the Maritime Access Division of the Ministry of Public Works. In situ data of velocity, SSC and turbulence were kindly provided by RBINS – OD Nature.

References

Acheson, D. J. (1991). *Elementary Fluid Dynamics*. Clarendon press, Oxford, UK.

Adriaens, R., Zeelmaekers, E., Fettweis, M., Vanlierde, E., Vanlede, J., Stassen, P., Elsen, J., Środoń, J., and Vandenberghe, N. (2018). Quantitative clay mineralogy as provenance indicator for recent muds in the southern North Sea. *Marine Geology*, 398:48–58.

Ariathurai, C. R. (1974). *A finite element model for sediment transport in estuaries*. PhD thesis, University of California, Davis.

Baeye, M., Fettweis, M., Legrand, S., Dupont, Y., and Van Lancker, V. (2012). Mine burial in the seabed of high-turbidity area—Findings of a first experiment. *Continental Shelf Research*, 43:107–119.

Beven, K. (2002). Towards a coherent philosophy for modelling the environment. *Proceedings of the Royal Society of London. Series A: Mathematical, Physical and Engineering Sciences*, 458(2026):2465–2484.

Beven, K. and Freer, J. (2001). Equifinality, data assimilation and uncertainty estimation in mechanistic modelling of complex environmental systems using the GLUE methodology. *Journal of hydrology*, 249:11–29.

Chu, K., Vanlede, J., Decrop, B., and Mostaert, F. (2020). Validation of North Sea models: Sub report 1 – Validation and sensitivity analysis. Technical report, Flanders Hydraulics Research and IMDC, Antwerp, Belgium.

Cronin, K., van Kessel, T., Smits, B., and van Maren, B. (2018). Update of the LTV mud model. Technical report, Deltares, Delft.

de Swart, H. E. (1974). *Offshore sediment transport and equilibrium beach profiles.* PhD thesis, TU Delft.

Dee, D. P. (1995). A pragmatic approach to model validation. *Coastal and Estuarine Studies*, 47:1–12.

Deltares (2018a). D-Water Quality. Versatile water quality modelling in 1D, 2D or 3D systems including physical, (bio)chemical and biological processes. User Manual Version: 5.06. Technical report, Deltares, Delft, The Netherlands.

Deltares (2018b). Delft3D-FLOW: Simulation of multi-dimensional hydrodynamic flows and transport phenomena, including sediments. User Manual. Technical report, Deltares, Delft, The Netherlands.

Dyer, K. R. (1989). Sediment processes in estuaries: future research requirements. *Journal of Geophysical Research*, 94(C10).

Fettweis, M. and Baeye, M. (2015). Seasonal variation in concentration, size, and settling velocity of muddy marine flocs in the benthic boundary layer. *Journal of Geophysical Research: Oceans*, 120(8):5648–5667.

Fettweis, M., Baeye, M., Cardoso, C., Dujardin, A., Lauwaert, B., Van den Eynde, D., Van Hoestenberghe, T., Vanlede, J., Van Poucke, L., Velez, C., and Martens, C. (2016). The impact of disposal of fine-grained sediments from maintenance dredging works on SPM concentration and fluid mud in and outside the harbor of Zeebrugge. *Ocean Dynamics*, 66(11).

Fettweis, M., Baeye, M., Van der Zande, D., Van den Eynde, D., and Joon Lee, B. (2014). Seasonality of floc strength in the southern North Sea. *Journal of Geophysical Research: Oceans*, 119(3):1911–1926.

Fettweis, M., Houziaux, J.-S., Du Four, I., Van Lancker, V., Baeteman, C., Mathys, M., Van den Eynde, D., Francken, F., and Wartel, S. (2009). Long-term influence of maritime access works on the distribution of cohesive sediments: analysis of historical and recent data from the Belgian nearshore area (Southern North Sea). *Geo-Marine Letters*, 29(5):321–330.

Fettweis, M., Nechad, B., and Van den Eynde, D. (2007). An estimate of the suspended particulate matter (SPM) transport in the southern North Sea using SeaWiFS images, in situ measurements and numerical model results. *Continental Shelf Research*, 27(10-11):1568–1583.

Fettweis, M. and Van den Eynde, D. (2003). The mud deposits and the high turbidity in the Belgian–Dutch coastal zone, southern bight of the North Sea. *Continental Shelf Research*, 23(7):669–691.

Gerritsen, H., Vos, R. J., van der Kaaij, T., Lane, A., and Boon, J. G. (2000). Suspended sediment modelling in a shelf sea. *Coastal Engineering*, 41:317–352.

Groen, P. and Dorrestein, R. (1976). Zeegolven. Technical report, KNMI, 's Gravenhage.

Kamphuis, J. W. (1974). Determination of sand roughness for fixed beds. *Journal of Hydraulic Research*, 12(2 (1974)):193–203.

Kandiah, A. (1974). *Fundamental aspects of surface erosion of cohesive soils*. PhD thesis, University of California, Davis.

Krone, R. B. (1962). Flume Studies of the transport of sediment in estuarial shoaling processes. Technical report, University of California.

Le Hir, P., Bassoullet, P., and Jestin, H. (2000). Application of the continuous modeling concept to simulate high-concentration suspended sediment in a macrotidal estuary. *Proceedings in Marine Science*, 3(C):229–247.

Li, Y. and Mehta, A. J. (2000). Fluid mud in the wave-dominated environment revisited. *Proceedings in Marine Science*, 3(C):79–93.

Manning, A. J. and Dyer, K. R. (2007). Mass settling flux of fine sediments in Northern European estuaries: Measurements and predictions. *Marine Geology*, 245(1-4):107–122.

Mehta, A. J., Samsami, F., Khare, Y. P., and Sahin, C. (2014). Fluid Mud Properties in Nautical Depth Estimation. *Journal of Waterway, Port, Coastal, and Ocean Engineering*, 140(2):210–222.

Mitchener, H. and Torfs, H. (1996). Erosion of mud/sand mixtures. *Coastal Engineering*, 29:1–25.

Refsgaard, J. C. and Henriksen, H. J. (2004). Modelling guidelines - terminology and guiding principles. *Advances in Water Resources*, 27:71–82.

Rinaldi, M., Mengoni, B., Luppi, L., Darby, S. E., and Mosselman, E. (2008). Numerical simulation of hydrodynamics and bank erosion in a river bend. *Water Resources Research*, 44(9).

Sanford, L. P. and Halka, J. P. (1993). Assessing the paradigm of mutually exclusive erosion and deposition of mud, with examples from upper Chesapeake Bay. *Marine Geology*, 114(1-2):37–57.

Shen, X., Lee, B. J., Fettweis, M., and Toorman, E. A. (2018). A tri-modal flocculation model coupled with TELEMAC for estuarine muds both in the laboratory and in the field. *Water Research*, 145(September):473–486.

Soulsby, R. (1997). *Dynamics of Marine Sands : A Manual for Practical Applications*. Thomas Telford, London.

Suijlen, J. M. and Duin, R. N. M. (2002). Atlas of near-surface total suspended matter concentrations in the Dutch coastal zone of the North Sea. Technical report, National Institute for Coastal and Marine Management/RIKZ, The Hague.

Toorman, E., Bruens, A., Kranenburg, C., and Winterwerp, J. (2002). Interaction of suspended cohesive sediment and turbulence. In *Proceedings in Marine Science*, volume 5, pages 7–23.

Van den Eynde, D. (2017). Measuring, using ADV and ADP sensors, and modelling bottom shear stresses at the MOW1 site (Belgian continental shelf). In MOMO activity report (1 januari 2017 – 30 juni 2017). Technical report, Royal Belgian Institute of Natural Sciences, Brussels.

Van den Eynde, D., Nechad, B., Fettweis, M., and Francken, F. (2007). Seasonal variability of suspended particulate matter observed from SeaWiFS images near the Belgian coast. In Maa, J. P., Sanford, L. P., and Schoellhamer, D. H., editors, *Estuarine and coastal fine sediment dynamics*. Elsevier.

van der Wal, D., van Kessel, T., Eleveld, M., and Vanlede, J. (2010). Spatial heterogeneity in estuarine mud dynamics. *Ocean Dynamics*, 60(3):519–533.

van Kessel, T. and van Maren, D. (2013). Far-field and long-term dispersion of released dredged material. In *Proceedings of the XXth WODCON conference*.

van Kessel, T. and Vanlede, J. (2010). Impact of harbour basins on mud dynamics Scheldt estuary. Technical report, Deltares and Flanders Hydraulics Research, Delft.

van Kessel, T., Vanlede, J., and Bruens, A. (2006). Development of a mud transport model for the Scheldt estuary in the framework of LTV. Technical report, WL|Delft Hydraulics, Delft.

van Kessel, T., Vanlede, J., and de Kok, J. (2011a). Development of a mud transport model for the Scheldt estuary. *Continental Shelf Research*, 31(10 SUPPL.).

van Kessel, T., Winterwerp, H., Van Prooijen, B., Van Ledden, M., and Borst, W. (2011b). Modelling the seasonal dynamics of SPM with a simple algorithm for the buffering of fines in a sandy seabed. *Continental Shelf Research*, 31(10):S124–S134.

Van Lancker, V., Baeye, M., Du Four, I., Janssens, R., Degraer, S., Fettweis, M., Francken, F., Houziaux, J., Luyten, P., Van den Eynde, D., Devolder, M., De Cauwer, K., Monbaliu, J., Toorman, E., Portilla, J., Ullman, A., Liste Munoz, M., Fernandez, L., Komijani, H., Verwaest, T., Delgado, R., De Schutter, J., Janssens, J., Levy, Y., Vanlede, J., Vinckx, M., Rabaut, M., Vandenberghe, N., Zeelmaekers, E., and Goffin, A. (2007a). Quantification of Erosion/Sedimentation patterns to Trace the natural versus anthropogenic sediment dynamics (QUEST4D). Technical report, Belgian Science Policy Office (Belspo), Brussels.

Van Lancker, V., De Batist, M., Fettweis, M., Pichot, G., and Monbaliu, J. (2007b). Management, research and budgetting of aggregates in shelf seas related to end-users (Marebasse). Technical report, Belgian Science Policy, Brussel, Belgium.

van Ledden, M. (2003). *Sand-Mud segregation in estuaries and tidal basins*. PhD thesis, TU Delft.

van Ledden, M., van Prooijen, B., van Kessel, T., Nolte, A., Los, H., Boon, J., and de Jong, W. (2006). Impact sand extraction Maasvlakte 2 - Mud transport, nutrients and primary production. Technical report.

van Leussen, W. (1994). *Estuarine Macroflocs and their role in fine-grained sediment transport*. PhD thesis, Universiteit Utrecht.

van Maren, D. and Cronin, K. (2016). Uncertainty in complex three-dimensional sediment transport models: equifinality in a model application of the Ems Estuary, the Netherlands. *Ocean Dynamics*, pages 1665–1679.

van Maren, D., Vroom, J., Fettweis, M., and Vanlede, J. (2020). Formation of the Zeebrugge coastal turbidity maximum : The role of uncertainty in near-bed exchange processes. *Marine Geology*, 425:106186.

Van Prooijen, B. C. and Winterwerp, J. C. (2010). A stochastic formulation for erosion of cohesive sediments. *Journal of Geophysical Research: Oceans*, 115(1):1–15.

van Rijn, L. C. (1984). Sediment Pick-Up Functions. *Journal of Hydraulic Engineering*, 110(10):1494–1502.

van Rijn, L. C. (1993). *Principles of sediment transport in rivers, estuaries and coastal seas.* Aqua Publications, Amsterdam.

Van Rijn, L. C. (2007). Unified view of sediment transport by currents and waves. I: initiation of motion, Bed roughness and bed-load transport. *Journal of hydraulic engineering*, pages 649–667.

van Rijn, L. C., Walstra, D., Grasmeijer, B., Sutherland, J., Pan, S., and Sierra, J. (2003). The predictability of cross-shore bed evolution of sandy beaches at the time scale of storms and seasons using process-based profile models. *Coastal Engineering*, 47(3):295–327.

Vandenbruwaene, W., Vanlede, J., Plancke, Y., Verwaest, T., and Mostaert, F. (2016). Slibbalans Zeeschelde: Deelrapport 4 – Historische evolutie SPM. Technical report, Flanders Hydraulics Research, Antwerp, Belgium.

Vanlede, J., Delecluyse, K., Primo, B., Verheyen, B., Leyssen, G., Plancke, Y., Verwaest, T., and Mostaert, F. (2015). Verbetering randvoorwaardenmodel: Subreport 7 - Calibration of NEVLA 3D. Technical report, Flanders Hydraulics Research, Antwerp.

Vanlede, J. and Dujardin, A. (2014). A geometric method to study water and sediment exchange in tidal harbors. *Ocean Dynamics*, 64(11):1631–1641.

Vinzon, S. B. and Mehta, A. J. (2003). Lutoclines in high concentration estuaries: Some observations at the mouth of the Amazon. *Journal of Coastal Research*, 19(2):243–253.

Vroom, J., van Maren, D., van der Werf, J., and van Rooijen, A. (2016). Zand-slib modellering voor het mondingsgebied van het Schelde-estuarium. Technical report, Deltares, Delft.

Winterwerp, J. (2007). On the sedimentation rate of cohesive sediment. In *Proceedings in Marine Science*, volume 8, pages 209–226.

Winterwerp, J. C. (2001). Stratification effects by cohesive and noncohesive sediment. *Journal of Geophysical Research: Oceans*, 106(C10):22559–22574.

Winterwerp, J. C. (2006). Stratification effects by fine suspended sediment at low, medium, and very high concentrations. *Journal of Geophysical Research: Oceans*, 111(5).

Winterwerp, J. C. and Van Kessel, T. (2003). Siltation by sediment-induced density currents. *Ocean Dynamics*, 53(3):186–196.

Winterwerp, J. C. and Van Kesteren, W. (2004). *Introduction to the physics of cohesive sediment transport in the marine environment*. Elsevier, Amsterdam.

Winterwerp, J. C., van Kesteren, W. G. M., van Prooijen, B., and Jacobs, W. (2012). A conceptual framework for shear flow-induced erosion of soft cohesive sediment beds. *Journal of Geophysical Research: Oceans*, 117(C10).

Zijl, F. (2013). Development of the next generation Dutch Continental Shelf Flood Forecasting models. Set-up, calibration and validation. Technical report, Deltares, Delft, The Netherlands.

6

Case study: the impact of the relocation of a disposal site

6.1. Introduction

On average, 4.3 MTDM/year (Million Tonnes Dry Matter per year) of mud is dredged from the Zeebrugge harbor, and an additional 2.3 MTDM/year from the access channels (see section 2.11 for more details). The material is disposed in the North Sea at three designated disposal sites: Zeebrugge Oost (ZBO), S1 and S2 (see figure 2.16 for the locations). Table 2.1 lists the distribution of the dredged material over the different disposal sites.

Earlier numerical work on return flow indicated that the dredging amount could potentially be decreased by relocating one or more disposal sites (Van den Eynde, 2004; Van den Eynde and Fettweis, 2006, 2014). Based on these results a proposal for an in situ test was drafted (Fettweis et al., 2010).

Between March 2013 and April 2014, a field study was carried out to investigate the efficiency of the disposal site ZBO. During one month (21 Oct 2013 - 20 Nov 2013), the dredged material that would have been disposed at ZBO, was disposed at an alternative disposal site Zeebrugge West (ZBW) instead (see figure 6.1 for the locations). The hypothesis was that the temporary substitution of the disposal site ZBO would lead to a measurable decrease of the return flow to the harbor. This field study is described in detail in Fettweis et al. (2016).

The field campaign could not show unambiguously that the relocation resulted in either a decrease in the suspended sediment concentration (SSC), or a reduction of the siltation inside the harbor. In their conclusions, Fettweis et al. (2016) point to the large natural variability of SSC in the North Sea, and that the 1-month period with disposal on ZBW was probably too short to get statistically significant results.

In this chapter, the relocation of the disposal site ZBO to ZBW is studied further using the numerical model that is described in chapter 5.

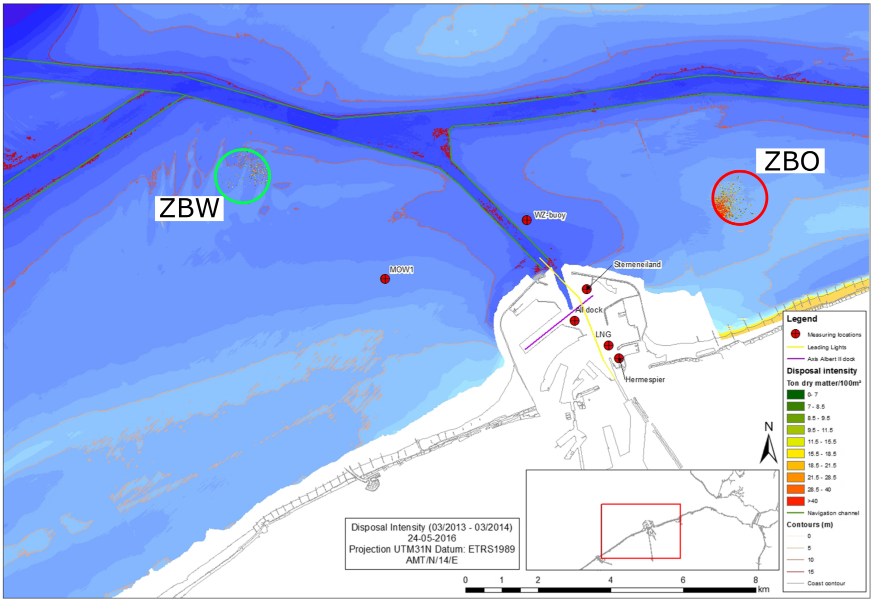

Figure 6.1: Map showing the regular disposal site ZBO (red) and the alternative disposal site ZBW (green) that was used during the field experiment (Fettweis et al., 2016).

6.2. Model setup

A scenario analysis is set up to compare the return flow from locations ZBO and ZBW to the harbor. The hydrodynamics and the sediment parameterization is taken from the calibrated sediment transport model. A simulation of 1 year is set up, in which all sediment that is dredged in the harbor is disposed at the ZBO site. The siltation in the channels is distributed over disposal sites S1 and S2 (see figure 2.16 for the locations). Sediment that is dredged in the harbor (and disposed at ZBO) is tagged in the simulation, so that it can be distinguished from the background SSC. For the scenario analysis, a similar simulation is set up in which the disposal site ZBO is replaced by the ZBW site.

In order to take into account the uncertainty due to model structure, the scenario analysis is performed with all three equifinal parameterizations of the sediment transport model (see section 5.11.2).

6.3. Model results

The recirculation is quantified as the ratio of the dredged mass from the harbor that has been disposed earlier at ZBO (or ZBW), to the total dredged mass from the harbor. Figure 6.2 shows the return flow to the harbor from both sites ZBO and ZBW. The height of the bars indicates the average return flow over the three equifinal parameterizations. The error bars indicate the minimum and maximum over the three equifinal parameterizations. The length of the error bar (max-min) gives an indication of the uncertainty. IM1 is the fraction with a settling velocity of 3 mm/s, while IM2 has a settling velocity of 0.5 mm/s. TIM stands for Total Inorganic Matter, and is the sum of both fractions.

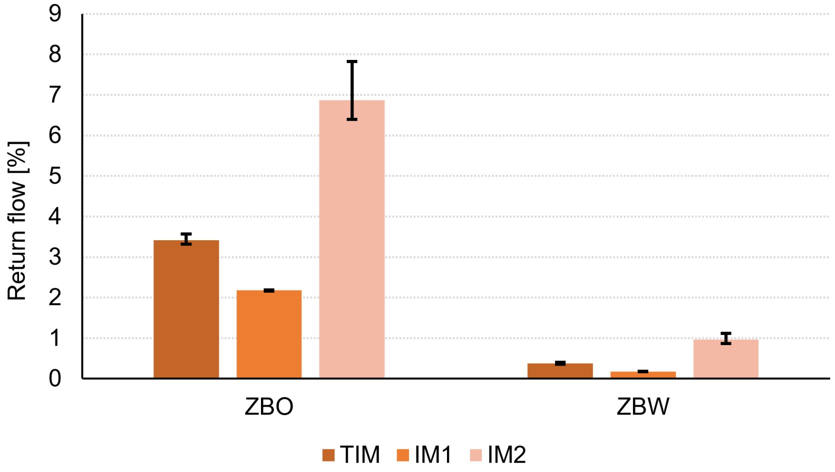

Figure 6.2: Return flow to the harbor from disposal sites ZBO and ZBW.

It is clear from the results in figure 6.2 that the expected return flow from disposal site ZBO (3.4%) is higher than from ZBW (0.4%). Furthermore, the finer fraction (IM2) has a higher return flow. This is related to the fact that the finer fraction disperses over a wider area than the coarser fraction. Note that the uncertainty of the return flow is also larger for the finer fraction.

Even though there is a clear effect on the return flow, there is only a very limited effect on the SSC. This is illustrated in figure 6.3 for the effect on SSC at location MOW1. This explains why Fettweis et al. (2016) did not find a significant effect on the SSC in six measurement points (including MOW1) during the field experiment. The model results show that the expected effects on near-bed SSC are so small, that even with a longer field experiment it would be near-impossible to distinguish the effect on SSC from the natural variation during the field experiment.

6.4. Discussion and conclusion

When the disposal site is relocated from ZBO to ZBW, a clear reduction of the (limited) sediment recirculation to the harbor is expected, but only a very limited effect on SSC.

The return flow from location ZBO, which is located less than 6 km eastward of the harbor entrance, might seem counter-intuitive at first in a system that is characterized by a northeastward residual sediment flux (see the discussion in section 2.7.1). It can be understood in terms of salinity and the tidal excursion length. The salinity-driven baroclinic effects result in a near-bed residual flow that is directed towards the coast (see the discussion in section 2.8.2). This residual current can

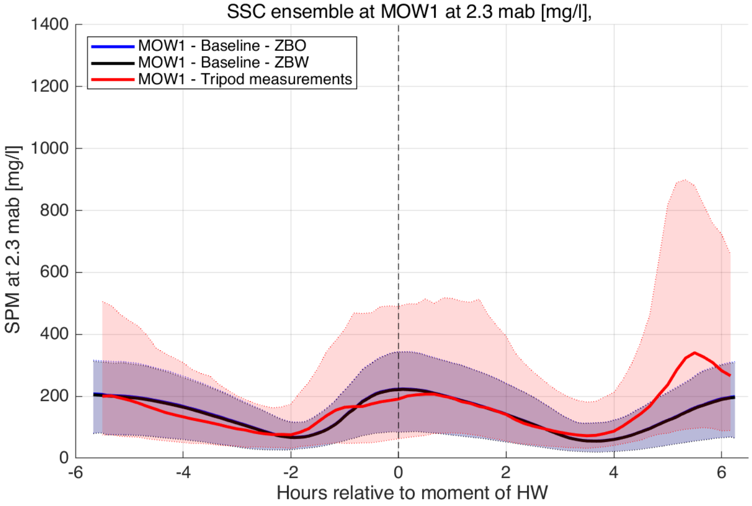

Figure 6.3: SSC at MOW1 at 2.3 mab, in the baseline scenarios of disposal sites ZBO and ZBW.

transport material from offshore to onshore. Tidal advection and dispersion will also play a role, as ZBO is located less than one tidal excursion length eastward of the harbor entrance. The alongshore tidal excursion length is estimated to be around 10km during spring tide (see section 5.4.1).

In this application of the sediment transport model, a model schematization with known limitations in its conceptual model is used in a scenario analysis context. The underlying assumption is, that if the same conceptual errors are made both in the scenario as in the reference case, the error cancels out in the effects (in first order). It is very hard to assess however, whether the changes introduced in the scenario do not enlarge the conceptual errors (Refsgaard et al., 2006).

A tracer experiment would be the most direct way to quantify the return flow from different disposal sites. In the 90's, a series of tracer experiments was set up, using long-life radio-isotopes to study the dispersion of disposed sediment. The results showed that if sediment is disposed less than 25 km from the coast, a fraction of it will recirculate towards the coast within a few days. This can be understood in terms of the salinity-driven baroclinic effects. It is important to note however, that the amount of recirculation could not be quantified from the tracer experiments, due to uncertainties in the interpretation (Van den Eynde, 2004). Due to the regulatory complications of working with radio-isotopes, and due to the uncertainties in the quantification of the return flow from this type of experiment, it was decided not to use tracers in the field experiment of 2013-2014.

This case study therefore highlights the limitation of using only observations to quantify the return flow from disposal sites. It is an example of how a calibrated model can be a useful tool for predictions of a variable (such as return flow) that is difficult to measure directly.

References

Fettweis, M., Baeye, M., Cardoso, C., Dujardin, A., Lauwaert, B., Van den Eynde, D., Van Hoestenberghe, T., Vanlede, J., Van Poucke, L., Velez, C., and Martens, C. (2016). The impact of disposal of fine-grained sediments from maintenance dredging works on SPM concentration and fluid mud in and outside the harbor of Zeebrugge. *Ocean Dynamics*, 66(11).

Fettweis, M., Van den Eynde, D., and Martens, C. (2010). Optimalisatie stortbeleid: Voorstel voor een terreinproef. Technical report, BMM, Brussels.

Refsgaard, J. C., van der Sluijs, J. P., Brown, J., and van der Keur, P. (2006). A framework for dealing with uncertainty due to model structure error. *Advances in Water Resources*, 29(11):1586–1597.

Van den Eynde, D. (2004). Interpretation of tracer experiments with fine-grained dredging material at the Belgian Continental Shelf by the use of numerical models. *Journal of Marine Systems*, 48(1-4):171–189.

Van den Eynde, D. and Fettweis, M. (2006). Modelling of fine-grained sediment transport and dredged material on the Belgian Continental Shelf. In *Journal of Coastal Research - Proceedings of ICS 2004*, pages 1564–1569.

Van den Eynde, D. and Fettweis, M. (2014). Towards the application of an operational sediment transport model fort the optimisation of dredging works in the Belgian coastal zone (southern North Sea). In Dahlin, H., Flemming, N. C., and Petersson, S. E., editors, *Proc 6th Int Conf EuroGOOS*, pages 250–257, Sopot – Poland.

7

Conclusions and recommendations

The first three sections of this chapter cover the lessons learned on the mud dynamics of the Belgian Coastal Zone (BCZ). The area of interest is characterized by a residual transport directed towards the northeast. Section 7.1 shows how salinity-driven baroclinic effects, tidal asymmetry and local gradients in the residual current all play a role in trapping sediment in a coastal turbidity maximum (CTM). The resulting mud deposits are a persistent feature in the BCZ, at least since the beginning of the 20th century. Even though the sediment dynamics in the BCZ is understood as an open system in connection with the North Sea, the relative importance of local erosion and deposition with regards to the residual transport gives it some characteristics of a closed system (see section 7.2). Section 7.3 summarizes the lessons learned on the siltation mechanisms of the harbor of Zeebrugge, and the effect on the nautical accessibility.

The last three sections cover methodologies for data analysis that are used in this thesis. They are synthesized here, in the hope that they can also be useful in other applications. Section 7.4 highlights three different use cases of the geometric decomposition of water and sediment exchange. It can be seen as an extension to Vanlede and Dujardin (2014), in that it also shows applications that were published after the original paper. Section 7.5 shows how the application of ensemble analysis on time series of SSC can separate the influence of advection from local erosion and settling. Finally section 7.6 shows how the smart use of both tidal ensembles and the comparable tide method maximizes the set of measurements that is available for model calibration and validation.

7.1. On the persistence of mud deposits in the Belgian coastal zone

The presence of large patches of high mud content (>50%) in the BCZ is well-documented. They are already indicated on the maps of Van Mierlo (1899), in a similar location as today. The mud deposits are also present in the reconstruction of the nearshore sedimentary environment from the period 1900-1910, based on the historical Gilson collection (Houziaux et al., 2011). The historic data therefore indicate a trend to deposit muddy sediment in the coastal area, which was already present prior to the construction of the port of Zeebrugge (1899-1903) and the initial dredging of the Pas van het Zand access channel.

There is a strong connection between the location of the mud deposits and that of the CTM, because of the sediment exchange between the bed and the water column. Local hydrodynamic conditions trap suspended particulate matter (SPM) in the BCZ. Relevant transporting agents include tidal asymmetry, a decreasing residual current between Oostende and Zeebrugge, and salinity-driven baroclinic effects (see the discussion in section 2.8). A higher local suspended sediment concentration (SSC) leads to a higher mud content in the bed through deposition. The erosion and resuspension of the recently deposited, poorly consolidated material subsequently increases the local SSC.

The effect of salinity on the formation of the CTM is further investigated with a numerical model in section 5.10.3. The horizontal salinity gradient has a clear influence on the residual current profiles. It induces a seaward residual flow in the upper part of the water column while enhancing the landward flow in the lower part. This results in more sediment being trapped in the CTM. The salinity gradient is not a sufficient condition for the formation of the CTM however, as it is also present in a barotropic run (albeit less pronounced).

In the sediment transport model, all simulations start from an empty bed. This means that the CTM in the model is a dynamic equilibrium that is independent from the initial conditions. The modeled CTM is remarkably robust: it is observed over a broad range of parameterizations. During an extensive sensitivity analysis (35 runs), the CTM was present in all runs, except for two: one run with a single fraction that hardly settles ($w_s = 0.1\,\mathrm{mm\,s^{-1}}$) and one run with a high horizontal dispersion coefficient ($D_h = 100\,\mathrm{m^2\,s^{-1}}$).

Interestingly, a relatively weak CTM was also present in a run where the interaction with the bed was disabled (see section 5.10.4). This confirms that the local hydrodynamic conditions trap sediment in the CTM. The interaction between the bed and the water column is therefore not a necessary condition for the CTM to develop. It does have an impact on the strength of the CTM however: the higher the interaction with the bed, the more sediment is trapped in the CTM.

7.2. On the importance of the English Channel mud source

The residual sediment transport through the Dover Strait is an important sediment supply to the Southern North Sea (see the discussion in section 2.7.1). The north-eastward residual sediment flux is estimated as 19.2 MTDM/yr (million tons of dry matter/year) in the BCZ (Fettweis et al., 2007).

A clay mineralogical analysis has shown however that the English Channel mud sources have a different clay mineralogical composition than the weakly- to medium consolidated mud in the BCZ (Adriaens et al., 2018). This means that the English Channel is not the dominant sediment supply for SPM in the BCZ.

A sediment balance derived from the model helps to resolve this apparent contradiction. The mass of sediment that is involved in the erosion/deposition cycle is about 300 times larger than the net influx of sediment from the Dover strait (see the discussion in section 5.12.1). This high ratio shows the importance of the deposition/resuspension cycle in the mud dynamics in the BCZ. The SPM from the English Channel is mixed with the larger mass of sediment that is trapped in the sedimentation/erosion cycle.

Even though the sediment dynamics in the BCZ is understood as an open system in connection with the North Sea (Fettweis and Van den Eynde, 2003), the cycle of erosion and deposition gives it some characteristics of a closed system, like a distinct clay mineralogical fingerprint.

7.3. On the siltation of the harbor of Zeebrugge

Averaged over the period 2005 to 2013, 4.3 MTDM/yr of sediment was dredged from the harbor. This corresponds to an average sediment import of 6100 TDM/tide. A sensitivity analysis has shown the importance of the near-bed SSC on the total sediment import into the harbor (see section 4.4.4). This can explain why the sediment transport model, which underestimates the near-bed SSC, also systematically underpredicts the siltation of the harbor (see section 5.11.3).

An important sediment import mechanism is advection, from two hours before high water to high water. Flood currents in the North Sea (directed northeastward along the Belgian coast) drive the primary gyre in the harbor, which is advected into the basin during rising tide. This results in water inflow near the eastern breakwater and outflow near the western breakwater. Because of sediment settling in the harbor, this results in a net import of sediment. This siltation mechanism is supported by the geometric decomposition of the exchange flow (see also the next section 7.4), by the phase lag that is observed between two stations at the edge of the primary gyre (see section 7.5), and by the fact that the spring-to-neap ratio for near-bed SSC is the same for stations in the North Sea and for stations near the harbor entrance.

Fresh water inflow into the harbor (via the ”Leopold” and the ”Schipdonk” channels) does not have a significant impact on the sediment import. The median inflow of 1.1 m^3/s is not enough to induce stratification. The water column inside the harbor only becomes stratified during periods of high fresh water discharge

(>10 m^3/s), with a thin layer of 1 m of fresh water near the surface that dissipates through mixing after 6 to 8 hours. This fresh water only induces a return flow of 0.05 m/s into the harbor. This is too low to cause any significant sediment import into the harbor (see the discussion in section 4.4.1). Consequently, no correlation is found between the siltation in the harbor and the fresh water discharge. Also, no evidence is found of sediment import via a density-driven vertical exchange flow in the application of the geometric decomposition method in chapter 3.

7.3.1. Mud inside the harbor

Once the suspended sediment has entered the harbor, the sediment settles. The vertical mass diffusion is damped by the effect of density stratification. Furthermore, the rate of sediment deposition exceeds the dewatering/consolidation rate. This enables the formation of a high concentration benthic suspension (HCBS) and/or fluid mud inside the harbor, with a thickness of 2 to 3 m.

The shape of the mud-water interface inside the harbor shows an interesting seasonality. While the interface in the Albert II dock is flat in winter, it has a vertical variation of 1 m in summer (with a maximum slope of 1/400, see section 4.4.5). This could indicate a seasonality in the strength and structure inside the fluid mud layer. The seasonality of the fluid mud properties is still not well understood. Further research is recommended on the seasonal variation of floc properties inside the harbor (e.g. their size and fractal dimension), since the seasonality in floc properties is a contributing factor in the seasonal variation of settling velocity, sediment input rate, consolidation rate and strength properties of the bed.

7.3.2. The effect on the nautical accessibility

The harbor of Zeebrugge has a dual accessibility criterion, which means that both the vertical position of the mud-water interface (the lutocline which is measured as the 210 kHz reflector) and the 1200 kg/m^3 density level are important for the safe nautical access.

On average, the sediment import into the harbor during a spring tide is two to four times higher than during a neap tide. There is, however, no spring-neap variation in the daily dredging amounts. As a result, the level of the mud-water interface rises up to 15 cm/day during spring tide, and falls 5 to 10 cm/day during neap and mean tide.

Despite year-round dredging, there is an additional seasonal variation of about 1 m in the height of the mud-water interface inside the harbor. The top of the mud layer is more shallow in winter. This is related to seasonal variation of the density of the fluid mud, which is lower in winter (see section 4.4.5). The shallower mud-water interface in winter has a negative impact on the nautical accessibility, particularly during spring tide.

7.3.3. Return flow from the disposal site to the harbor

The material that is dredged in the harbor is disposed in the North Sea on three designated disposal sites: Zeebrugge Oost (ZBO), S1 and S2 (see figure 2.16 for the locations).

In situ tracer experiments in the 90's showed that if the sediment is disposed less than 25 km from the coastline, a fraction of it will recirculate towards the coast within a few days. The amount of recirculation could not be quantified however, due to uncertainties in the interpretation of the experiments.

In 2013-2014, this was investigated further with a field trial. During one month, the dredged material that would have been disposed on location ZBO, was disposed on an alternative disposal site Zeebrugge West (ZBW) instead (see figure 6.1 for the locations). The field campaign could not show unambiguously however that the relocation resulted in either a decrease in the suspended sediment concentration (SSC), or a reduction of the siltation inside the harbor.

Therefore a numerical experiment is set up in chapter 6 to quantify the return flow from both locations ZBO and ZBW. The results show a reduction of the return flow when the sediment is disposed at location ZBW instead of ZBO. The results do not show a significant effect on SSC however, which helps to explain why the statistical analysis of SSC signals during the field experiment could not find a significant effect. This case study is an example of how a calibrated model is a useful tool to predict a variable (such as return flow) that is difficult to measure directly.

7.4. Three different applications of the geometric decomposition method

Chapter 3 introduces a general method to geometrically decompose the exchange of water and sediment between a harbor and open water. The decomposition results in three main components: tidal filling, horizontal and vertical exchange. This paragraph describes three different use cases in which the method is applied to models, measurements, or a combination of both.

Vanlede and Dujardin (2014) apply the method to ADCP measurements in two Belgian harbor basins. The results highlight the different factors driving the harbor siltation in both cases. For the Deurganckdok (in the Sea Scheldt) on the one hand, the decomposition shows the importance of the density-driven vertical exchange flow, which is related to the phase lag between salinity in the Scheldt and the Deurganckdok. For Zeebrugge on the other hand, most of the sediment is exchanged through a clockwise gyre that is advected into the harbor just prior to high water. This application on measurements shows that the geometric decomposition can provide insights that are not directly apparent from the 'raw' data of velocity and sediment concentration.

For the Deurganckdok in the Sea Scheldt, the geometric decomposition method has subsequently been used to estimate the expected siltation for different geometries that are considered for an extension of the dock (IMDC, 2018). This application combines the geometric decomposition with an empirical siltation model. The annual siltation has first been linked empirically to the three exchange components by IMDC and Deltares (2014). The exchange components for the different geometries are derived from a 3D hydrodynamic model. The empirical relation is then used to estimate the expected siltation for the different geometries. The main limitations of this approach are that the empirical siltation model does not consider interactions between the three components, and that the empirical coefficients are kept the same for the different geometries.

Finally, in section 5.11.3 the method is applied on both model and measurements during the calibration of the sediment transport model. The decomposition method enables us to focus on the most important exchange mechanism during model calibration.

7.5. On the use of ensemble analysis in the interpretation of field measurements

Dyer (1995) notes that one particular problem in the interpretation of field measurements of SSC, is the separation of the effects of advection from local erosion and settling. The method of ensemble analysis can be helpful in this regard, as is shown below with three selected applications from this thesis.

Ensemble analysis is used in section 2.12.2 to study the intratidal variation of SSC and velocity at stations MOW1 and Blankenberge in the North Sea (see figure 2.17 for the locations). For station Blankenberge, the SSC at 2.3 mab (meters above the bed) is dominated by local erosion from an ”infinite” source. There is little to no phase lag between local velocity and SSC, and the peak in SSC rises monotonically with the velocity magnitude over a spring-neap cycle. Because horizontal advection does not play an important role in the SSC variation at Blankenberge, it can be studied further with a 1DV sediment model in section 5.11.1.

Even though the two stations are not far apart, the SSC ensemble at MOW1 is clearly different from that at Blankenberge. The ebb peak of the SSC at MOW1 for example is stronger than the flood peak, even though the ebb peak of the velocity is lower than the flood peak. This suggests that the ebb peak of the SSC is *not* due to local resuspension, but that the SPM is advected with the ebb flow. This would put the sediment source eastward of the measurement location. One potential candidate is the freshly deposited sediment in the access channel ”Pas van het Zand”.

In section 4.4.3, an ensemble analysis is performed on both SSC and velocity at two stations inside the harbor. The phase lag of 50 minutes in peak SSC between both stations is related to advection. There is also evidence of vertical settling during advection: for the station deeper inside the harbor, the peak SSC at 2 mab is higher than for the station near the entrance, even though the local velocity is lower.

Section 4.4.4 uses ensemble analysis to establish that only the SSC near the entrance is influenced by advection from the North Sea, and that this influence disappears deeper inside the harbor. The analysis shows that the spring-to-neap ratio for near-bed SSC is a factor 3 to 4, both for stations in the North Sea and for stations near the entrance of the harbor. Stations deeper inside the harbor do not show any significant spring-neap variation however. The hypothesis is that SPM enters the first half of the harbor through advection, and that deeper inside the harbor, the sediment dynamics is influenced by other processes, such as gravitational redistribution of mud inside the harbor, and local resuspension due to ship movements.

Ensemble analysis is also used to bin tidal cycles into different classes. This is useful e.g. to quantify the seasonal variation, or to isolate the influence of a certain forcing factor on SSC, for example the influence of waves. Both examples are worked out in section 2.12.2.

Finally, ensemble analysis is also useful when comparing a model with measurements, as is shown in the next section.

7.6. On the importance of using a sufficiently broad set of measurements in validation

The validation of the sediment transport model in section 5.11 highlights the important conceptual uncertainties that remain in the description of the near-bed sediment dynamics. These shortcomings can only manifest themselves if the model is validated against a sufficiently broad set of measurements. If the dataset would be too narrow (e.g. only surface concentrations), it is likely that a model parameterization could still be found that gives a good agreement with the limited set of observations. In that case, the conceptual uncertainty would remains hidden, resulting in a model that would give the right answer for the wrong reasons. The availability of data, used to estimate the model parameterization is of crucial significance to the value of the model results (Beven, 2018).

Validation against a broad set of measurements implies the combination of multiple types of measurements (e.g. maps and time series) and multiple timescales into one overall assessment. This can be challenging to implement coherently and consistently. This thesis highlights three techniques (ensemble averaging, the comparable tide method and a general cost framework) that are helpful in this regard. These techniques are illustrated below in the context of the sediment transport model.

Concentration measurements close to the bed are important in the validation of the sediment transport model. Frame measurements are well suited for this purpose, because they can cover multiple timescales in one deployment (e.g. intratidal and spring-neap). Multiple deployments can be combined to assess the seasonal variation. Tidal ensembles are a useful tool to disentangle the different timescales (see also the discussion in the previous section 7.5). If they are applied to both model and measurements, they are also useful to quantify the model skill. Appendix B introduces formulas for bias and RMSE that are based on ensembles of modeled and measured time series. This method for assessing model skill has the interesting property that for the comparison of ensembles, the underlying periods do not need to overlap.

A through-tide (13h) measurement is a useful additional data source for horizontal velocities and sediment concentration over a transect. Due to their relatively high cost, such measurements are few and far between however. This means that modeled and measured periods often do not overlap. The comparable tide method (presented in appendix C) enables the use of any through-tide measurement to assess model skill, even if the campaign was carried out outside of the modeled time frame.

By relaxing the need that the modeled and measured periods overlap, the smart use of tidal ensembles and the comparable tide method extends the set of measurements that is available for model calibration and validation.

The set of dimensionless cost functions that is presented in appendix A enables model validation against measurements of varying types and from non-overlapping periods. The cost functions are used to quantify model skill against three types of observational data: time series, maps and tidal ensembles. To the best of our knowledge, the quantification of model skill based on tidal ensembles has never been shown before.

The general cost framework of appendix A enables the coherent and consistent synthesis of the model skill assessment into one single goodness-of-fit parameter. This synthesis is important if one wants to assess the adequacy of a conceptual model. The validation of the sediment transport model in section 5.11 has shown the limitations of the conceptual model that is often used in engineering applications of cohesive sediment transport. No parameterization was found however that showed a good skill (defined as a cost « 1) against all the different types of observations.

The development of an improved conceptual model for sediment transport will probably be rooted in a combination of empiricism, and reasoning from first principles. It will also be important to apply this new conceptual model to the real world, by including it in a model schematisation. After careful validation against a broad set of measurements in a unified cost framework, an improvement in the conceptual model is expected to correspond to a decrease in the overall cost of the calibrated parameterization (accuracy), and possibly also to a decrease in the range of equifinal parameterizations (precision).

References

Adriaens, R., Zeelmaekers, E., Fettweis, M., Vanlierde, E., Vanlede, J., Stassen, P., Elsen, J., Środoń, J., and Vandenberghe, N. (2018). Quantitative clay mineralogy as provenance indicator for recent muds in the southern North Sea. *Marine Geology*, 398:48–58.

Beven, K. (2018). *Environmental Modelling: An Uncertain Future?* Routledge, Taylor and Francis, London.

Dyer, K. (1995). Sediment transport processes in estuaries. *Developments in Sedimentology 53*, pages 423–449.

Fettweis, M., Nechad, B., and Van den Eynde, D. (2007). An estimate of the suspended particulate matter (SPM) transport in the southern North Sea using SeaWiFS images, in situ measurements and numerical model results. *Continental Shelf Research*, 27(10-11):1568–1583.

Fettweis, M. and Van den Eynde, D. (2003). The mud deposits and the high turbidity in the Belgian–Dutch coastal zone, southern bight of the North Sea. *Continental Shelf Research*, 23(7):669–691.

Houziaux, J.-S., Fettweis, M., Francken, F., and Van Lancker, V. (2011). Historic (1900) seafloor composition in the Belgian–Dutch part of the North Sea: A reconstruction based on calibrated visual sediment descriptions. *Continental Shelf Research*, 31(10):1043–1056.

IMDC (2018). Complex Project ECA – Analyse impact ECA bouwstenen en alternatieven op watersysteem en slibhuishouding - Technisch rapport modellering. Technical report, MOW, Afdeling Maritieme Toegang, Antwerp, Belgium.

IMDC and Deltares (2014). Evaluation of the external effects on the siltation in Deurganckdok - Report 1.8: Analysis of external effects on siltation processes and factors. Technical report, Maritime Access division, Antwerp.

Van Mierlo, C.-J. (1899). La carte lithologique de la partie meridionale de la mer du Nord. *Bulletin de la Societe Belge de Geologie, Paleontologie et Hydrologie*.

Vanlede, J. and Dujardin, A. (2014). A geometric method to study water and sediment exchange in tidal harbors. *Ocean Dynamics*, 64(11):1631–1641.

A

A set of dimensionless cost functions for model calibration, validation and sensitivity analysis

A quantitative assessment of the mismatch between model and observations (the model skill) is useful during model calibration, to evaluate a model's predictive capability (validation), or to express model sensitivity.

This appendix presents a set of dimensionless cost functions to quantify model skill against three different types of observational data: time series, maps and tidal ensembles. For each data type a separate dimensionless cost function is introduced. All cost functions are scaled with the variance of the observations. The separate costs can therefore be combined into an overall cost using a weighted sum, with the weights expressing the scale-invariant importance of each data source. This general cost framework enables the quantification of the deviation between the model and a number of different observational datasets (even of different data types) into a single goodness-of-fit parameter in a coherent and consistent way.

In the formulation of the separate cost functions the type of variable that is modeled (and observed) is not specified. It can be water level, velocity, suspended sediment concentration, ... (or a combination thereof). As an example application, consider the model skill of an hydraulic model that is expressed as a weighted sum of separate costs against time series of observed water levels and velocities in different stations. By setting the weights, the modeler can emphasize certain parts of the model domain, or certain datasets in the overall cost. The selection of a particular set of cost functions and their respective weights is specific for each model application, and should reflect the modeling objective.

A.1. General form

All cost functions have the following general form:

$$C = \frac{\text{MSE}}{\sigma^{obs}} \tag{A.1}$$

The dimensionless cost C is defined as the Mean Square Error (MSE) between the model and the observations, scaled with the variance of the observations σ^{obs}. $C = 0$ corresponds to the perfect model. $C = 1$ means the average of the measurements is as good a predictor as the model (with $C > 1$ meaning that the model is a worse predictor). C is closely related to the coefficient of efficiency E of Nash and Sutcliffe (1970): $C = 1 - E$. Note that since both C and E use the square of the error, they are more sensitive to larger differences (Legates and McCabe, 1999).

Since model simulations are discrete in time and space, the different cost functions are formulated in a discrete notation.

A.2. A dimensionless cost function for time series

For a time series of N timesteps, the cost C^{TS} can be calculated if model results m and observations o are available on the same timestep i.

$$C^{TS} = \frac{\text{MSE}}{\sigma^{obs}} = \frac{\sum_{i=1}^{N} (m_i - o_i)^2}{\sum_{i=1}^{N} (o_i - \overline{o})^2} \tag{A.2}$$

with $\overline{o}$ the mean of the observations.

A.3. A dimensionless cost function for maps

The error statistics are calculated over all grid cells j that lie within a polygon Ω. Each grid cell has its surface area A_j, and the polygon Ω has a surface area A_Ω. Measured map data are averaged over the model grid cells. Let o_j be the observed data, averaged over grid cell j.

$$A_\Omega = \sum_{j \in \Omega} A_j \tag{A.3}$$

$$\overline{o}_\Omega = \frac{1}{A_\Omega} \sum_{j \in \Omega} o_j A_j \tag{A.4}$$

$$\text{MSE} = \frac{1}{A_\Omega} \sum_{j \in \Omega} (m_j - o_j)^2 A_j \tag{A.5}$$

$$\sigma^{obs} = \frac{1}{A_\Omega} \sum_{j \in \Omega} (o_j - \overline{o}_\Omega)^2 A_j \tag{A.6}$$

The cost function for maps C^{map} then becomes:

$$C^{map} = \frac{\mathrm{MSE}}{\sigma^{obs}} = \frac{\sum_{j\in\Omega}\left(m_j - o_j\right)^2 A_j}{\sum_{j\in\Omega}\left(o_j - \overline{o}_\Omega\right)^2 A_j} \tag{A.7}$$

A.4. A dimensionless cost function for tidal ensembles

Tidal ensembles are constructed by converting the absolute time in a time series to a relative phase within the tidal cycle (e.g. hours before/after high water). By binning the data points according to their phase in the tidal cycle, the phase-averaged tidal cycle can be calculated. The method was introduced by Murphy and Voulgaris (2006) and applied on North Sea measurement data by IMDC et al. (2008) and Baeye et al. (2011). The method is applied in section 4.3.7 to study the relation between suspended sediment concentration (SSC) and velocity inside the harbor of Zeebrugge, and in section 2.12.1 to study the spring-neap variation of velocity in the North Sea.

This paragraph extends the ensemble method, so that it can be used to quantify model performance in a dimensionless cost function. By calculating the cost function from tidal ensembles, it is no longer necessary that the modeled and the measured periods overlap. This significantly enlarges the amount of data that can be used in model calibration and validation. To the best of our knowledge, the expression of model skill based on tidal ensembles has never been shown before.

Let N be the number of timesteps in an ensemble. At each timestep i of the ensemble ($i = 1 \dots N$), N_i^{mod} is the total number of modeled data at that timestep, and m_{ij} is the j-th member of the modeled ensemble ($j = 1 \dots N_i^{mod}$). N_i^{obs} is the total number of observed data at timestep i, and o_{ik} is k-th member of the observed ensemble ($k = 1 \dots N_i^{obs}$).

The following statistical parameters are defined for each timestep i in the ensemble: the mean of modeled values $\overline{m}_i$, the mean of observed values $\overline{o}_i$, the variance σ_i^{obs} of the observations, and the cost C_i.

$$\overline{m}_i = \frac{1}{N_i^{mod}} \sum_{j=1}^{N_i^{mod}} m_{ij} \tag{A.8}$$

$$\overline{o}_i = \frac{1}{N_i^{obs}} \sum_{k=1}^{N_i^{obs}} o_{ik} \tag{A.9}$$

$$\sigma_i^{obs} = \frac{1}{N_i^{obs}} \sum_{k=1}^{N_i^{obs}} \left(o_{ik} - \overline{o}_i\right)^2 \tag{A.10}$$

$$C_i = \frac{\left(\overline{m}_i - \overline{o}_i\right)^2}{\sigma_i^{obs}} \tag{A.11}$$

The cost C^{ens} for the ensemble is then calculated as:

$$C^{ens} = \frac{1}{N}\sum_{i=1}^{N} C_i \tag{A.12}$$

Note that the general form of the cost function (equation A.1) only applies for each individual timestep i in the ensemble. The term σ_i^{obs} takes into account the non-stationarity of the variance in the observations over the tidal cycle (heteroscedasticity). This way, the same model bias implies a higher cost in a period of lower variance in the observations.

A.5. Overall dimensionless cost

Each separate cost is dimensionless, and each is scaled with the variance of the observations. Therefore they can be combined into an overall cost using a weighted sum, with the weights expressing the importance of each data source in the overall cost.

$$C = \sum_i w_i C_i^{TS} + \sum_j w_j C_j^{map} + \sum_k w_k C_k^{ens} \tag{A.13}$$

with

$$\sum_i w_i + \sum_j w_j + \sum_k w_k = 1 \tag{A.14}$$

References

Baeye, M., Fettweis, M., Voulgaris, G., and Van Lancker, V. (2011). Sediment mobility in response to tidal and wind-driven flows along the Belgian inner shelf, southern North Sea. *Ocean Dynamics*.

IMDC, WL|Delft Hydraulics, and GEMS International (2008). Long term monitoring of salinity gradients in the harbour of Zeebrugge and monitoring of salinity, suspended sediment concentration and HCBS in the Belgian coastal zone - Report 2.3 : Analysis of ambient conditions Zeebrugge. Technical report, Waterbouwkundig Laboratorium, Antwerp, Belgium.

Legates, D. R. and McCabe, G. J. (1999). Evaluating the use of ”goodness-of-fit” measures in hydrologic and hydroclimatic model validation. *Water resources research*, 35:233–241.

Murphy, S. and Voulgaris, G. (2006). Identifying the role of tides, rainfall and seasonality in marsh sedimentation using long-term suspended sediment concentration data. *Marine Geology*, 227(1-2):31–50.

Nash, J. E. and Sutcliffe, J. V. (1970). River flow forecasting through conceptual models. Part I - a discussion of principles. *Journal of hydrology*, 10:282–290.

B

Quantitative skill assessment

This appendix quantifies the model skill of the flow and the sediment transport model.

New formulas of bias and RMSE are proposed that are based on ensembles of modeled and measured time series. This methodology broadens the set of measurements that can be used in model calibration and validation, by relaxing the need that the modeled and measured periods overlap.

B.1. Flow model

B.1.1. Water levels

Table B.1 quantifies the model skill for water levels in 9 stations. First, bias and Root Mean Square Error (RMSE) are calculated on the complete time series. Subsequently, high and low water levels are determined for both modeled and measured time series, and the bias is calculated separately for the timing and the level. The bias is calculated as model - measurement, so a positive bias means the model is too high (or too late). The location of the measurement stations is indicated in figure 5.7.

For a time series of N samples, bias and RMSE are calculated from model results m_i and observations o_i on corresponding timesteps i.

$$\text{Bias} = \frac{\sum_{i=1}^{N}(m_i - o_i)}{N} \tag{B.1}$$

$$\text{RMSE} = \sqrt{\frac{\sum_{i=1}^{N}(m_i - o_i)^2}{N}} \tag{B.2}$$

	Time series		High Water		Low Water	
Station	Bias [m]	RMSE [m]	Bias Time [min]	Bias Level [m]	Bias Time [min]	Bias Level [m]
Cadzand	0.13	0.14	-1.2	0.16	-1.2	0.11
Oostende	0.06	0.10	-6.8	0.16	-2.4	-0.01
Vlissingen	0.07	0.10	3.8	0.07	0.7	0.06
Westkapelle	0.09	0.11	-2.6	0.09	-4.1	0.08
Vlakte van de Raan	0.08	0.10	-2.8	0.09	-3.9	0.07
Bol van Knokke	0.09	0.11	-0.8	0.12	-0.8	0.08
Wandelaar	0.08	0.10	-3.3	0.12	-1.8	0.04
Bol van Heist	0.07	0.09	-2.7	0.11	-0.9	0.05
Zeebrugge	0.03	0.06	-1.4	0.06	-2.4	0.01

Table B.1: Quantitative skill assessment for water levels, expressed as bias and RMSE of time series, and bias in timing and level of both HW and LW, calculated in 9 stations over the period 26/04/2009 16:00 - 26/05/2009 04:10.

Table B.2 quantifies the model error in the frequency domain for 4 important tidal constituents (M2, M4, S2 and K1), both for amplitude and phase.

	Amplitude bias				Phase bias			
Station	M2 [cm]	M4 [cm]	S2 [cm]	K1 [cm]	M2 [°]	M4 [°]	S2 [°]	K1 [°]
Cadzand	2	1	-1	1	0.3	-1.0	1.8	-2.1
Oostende	9	1	1	1	-0.6	-1.9	-1.0	-2.6
Vlissingen	1	0	-1	1	1.0	-1.7	2.4	-2.2
Westkapelle	0	1	-2	1	-1.5	-1.0	-1.4	-4.0
Vlakte van de Raan	2	0	-1	1	-0.1	1.6	1.2	-2.2
Bol van Knokke	2	1	-1	1	0.0	-0.8	0.3	-4.0
Wandelaar	4	0	0	1	0.4	4.0	0.0	-2.3
Bol van Heist	4	2	-1	1	0.1	0.9	-0.1	-3.9
Zeebrugge	3	1	-1	1	-0.1	0.4	0.5	-3.0

Table B.2: Quantitative skill assessment for water levels, expressed as amplitude and phase errors of 4 important tidal constituents, calculated in 9 stations over the period 26/04/2009 16:00 - 26/05/2009 04:10.

B.1.2. Velocities

Time series

When a direct comparison can be made between time series over the same period, the model skill for velocities can be calculated in two ways. Either from the time series of velocity magnitude as bias (eq. B.1) and RMSE (eq. B.2), or from the vector difference between model and observations as Mean Absolute Error (MAE, eq. B.3) and Relative Mean Absolute Error (RMAE, eq. B.4).

$$\text{MAE} = \frac{\sum_{i=1}^{N} \|\vec{m}_i - \vec{o}_i\|}{N} \tag{B.3}$$

$$\text{RMAE} = \frac{\sum_{i=1}^{N} \|\vec{m}_i - \vec{o}_i\|}{\sum_{i=1}^{N} \|\vec{o}_i\|} \tag{B.4}$$

with $\vec{m}_i$ and $\vec{o}_i$ the measured and observed velocity vectors on corresponding timesteps i.

Table B.3 quantifies the model skill for velocities in two stations where continuous velocity measurements are available. The location of both measurement stations is indicated in figure 5.7.

	Vector difference		Magnitude	
Station	MAE [m/s]	RMAE [-]	Bias [m/s]	RMSE [m/s]
Bol van Heist	0.23	0.37	-0.14	0.21
Bol van Knokke	0.13	0.25	0.02	0.11

Table B.3: Quantitative skill assessment for velocities, expressed as MAE and RMAE of the vector difference, and bias and RMSE of the velocity magnitude, calculated in 2 stations over the period 26/04/2009 16:00 - 26/05/2009 04:10.

Ensemble analysis

When model results and observations do not cover the same period, the model skill for velocities can still be quantified from the tidal ensembles of velocity magnitude. By relaxing the requirement of overlapping periods, more data can be used in model calibration and validation.

Let N be the number of timesteps in an ensemble. At each timestep i of the ensemble ($i = 1 \dots N$), N_i^{mod} is the total number of modeled data points at that timestep in the ensemble, and m_{ij} is the j-th member of the modeled ensemble ($j = 1 \dots N_i^{mod}$). N_i^{obs} is the total number of observed data at timestep i in the ensemble, and o_{ik} is k-th member of the observed ensemble ($k = 1 \dots N_i^{obs}$).

$$\overline{m}_i = \frac{1}{N_i^{mod}} \sum_{j=1}^{N_i^{mod}} m_{ij} \tag{B.5}$$

$$\overline{o}_i = \frac{1}{N_i^{obs}} \sum_{k=1}^{N_i^{obs}} o_{ik} \tag{B.6}$$

$$\text{Bias} = \frac{\sum_{i=1}^{N}(\overline{m}_i - \overline{o}_i)}{N} \tag{B.7}$$

$$\text{RMSE} = \sqrt{\frac{\sum_{i=1}^{N}(\overline{m}_i - \overline{o}_i)^2}{N}} \tag{B.8}$$

Table B.4 quantifies the model skill for velocities in three stations where tidal ensembles are determined both from modeled and measured time series. The location of the measurement stations is indicated in figure 5.7.

	Bias			RMSE		
Station	neap [m/s]	average [m/s]	spring [m/s]	neap [m/s]	average [m/s]	spring [m/s]
MOW1	0.00	-0.01	-0.02	0.04	0.06	0.07
Blankenberge	0.02	0.00	-0.02	0.07	0.08	0.09
WZbuoy	-0.04	-0.04	-0.07	0.07	0.09	0.12

Table B.4: Quantitative skill assessment for velocities, expressed as bias and RMSE of the phase-averaged velocity magnitude.

B.2. Sediment transport model

B.2.1. SSC ensembles

The model skill for reproducing suspended sediment concentration (SSC) is quantified from the tidal ensembles in two stations, at two heights. RMSE is calculated with eq. B.8. The cost is calculated with eq. A.12. The location of the measurement stations is indicated in figure 5.7.

The model skill is quantified for the baseline parameterizations in table 5.8, and for the two equifinal parameterizations in tables B.5 and B.6.

CAL2	RMSE			Cost		
Station	neap [mg/l]	average [mg/l]	spring [mg/l]	neap [-]	average [-]	spring [-]
MOW1 0.3 mab	348	481	495	0.53	0.59	0.63
MOW1 2.3 mab	69	109	133	0.35	0.25	0.13
Blankenberge 0.3 mab	345	397	511	0.52	0.54	0.68
Blankenberge 2.3 mab	102	122	186	1.04	0.89	0.90

Table B.5: Quantitative skill assessment for SSC in CAL2, expressed as RMSE and dimensionless cost of the phase-averaged SSC.

CAL3	RMSE			Cost		
Station	neap [mg/l]	average [mg/l]	spring [mg/l]	neap [-]	average [-]	spring [-]
MOW1 0.3 mab	342	466	474	0.52	0.56	0.57
MOW1 2.3 mab	70	106	128	0.38	0.23	0.12
Blankenberge 0.3 mab	343	391	499	0.52	0.52	0.65
Blankenberge 2.3 mab	103	121	181	1.08	0.89	0.87

Table B.6: Quantitative skill assessment for SSC in CAL3, expressed as RMSE and dimensionless cost of the phase-averaged SSC.

Figure B.1 show the modeled and observed tidal ensembles of SSC at two heights at locations Blankenberge for the baseline parameterization. It supplements figure 5.33, which shows the results for station MOW1 in the main text.

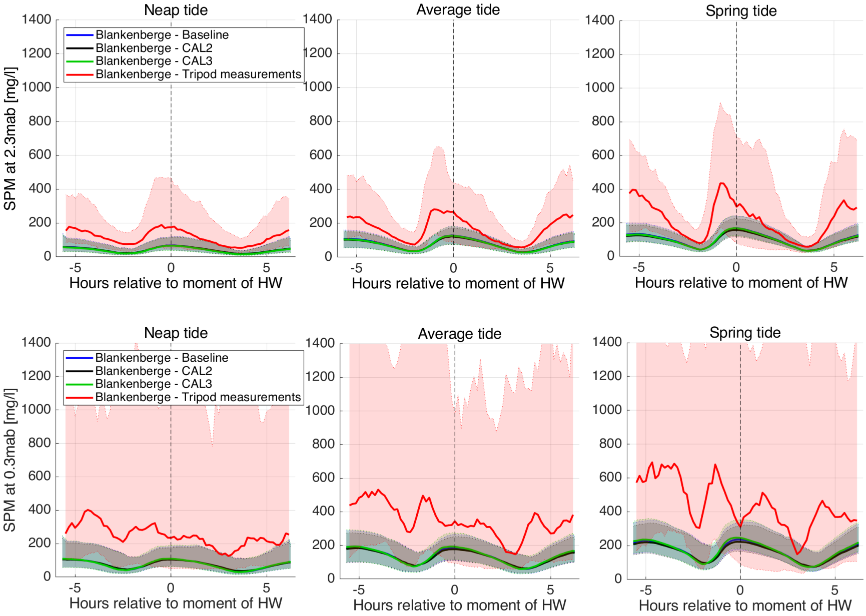

Figure B.1: Observed (red) and modeled (blue) SSC ensembles for neap (left panel), average (middle) and spring tide (right) at station Blankenberge at 2.3 mab (top) and 0.3 mab (bottom). The thick line represents the median in the ensemble; error bands indicate the P10 and P90 intervals.

C

Comparable tide method

C.1. Introduction

A through-tide (13h) measurement is a useful data source for horizontal velocities and sediment concentration over a transect. A vessel sails the same transect during one entire tidal cycle, and in the meantime measures the water velocity with a bottom-mounted ADCP (Acoustic Doppler Current Profiler) device. Sediment concentrations can be derived from the acoustic backscatter.

Due to their relatively high cost, such measurements are few and far between however. As a consequence, the modeled and the measured periods often do not overlap. One could discard all measurements that fall out of the modeled time frame, but that would shrink the dataset that is available for calibration/validation . Alternatively, one could perform additional model runs to cover each measured tide, but that quickly becomes impractical for larger sets of 13h measurements.

This appendix describes a method to search for a *comparable tide* in the modeled time frame, i.e. one that closely matches the tidal conditions during the measurement. The assumption is that under similar tidal conditions, one expects comparable velocities.

the comparable tide method enables the use of any through-tide measurement to assess model skill, even if the campaign was carried out outside of the modeled time frame. This can mean a dramatic expansion of the set of measurements that is available for calibration/validation.

C.2. Comparable tide method

Imagine a measurement (e.g. a 13h ADCP campaign) that is carried out in a time frame $[t_{start,meas}\ \ t_{stop,meas}]$. The model is run in the time frame $[t_{start,model}\ \ t_{stop,model}]$. Both periods don't necessarily overlap.

Parts of this chapter have been published by Vanlede et al. in the conference proceedings of the 2020 TELEMAC-MASCARET user conference.

Figure C.1 illustrates the comparable tide (CT) method. WL$_{meas}$ is the measured water level at a station near the measured transect, during the measurement time frame. WL$_{mod}$ is the computed water level at the same station during the (longer) modeled time frame.

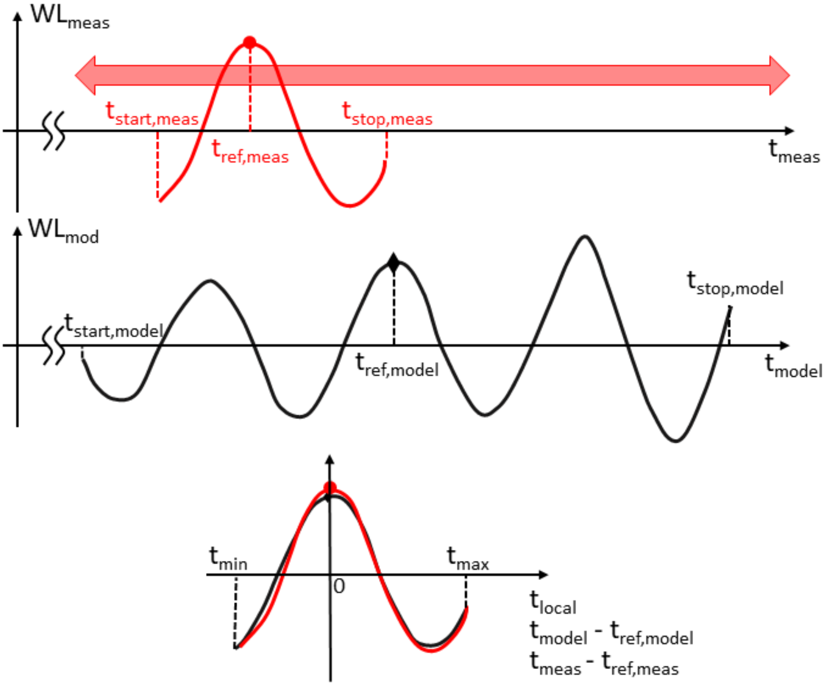

Figure C.1: The construction of the local time axis in the comparable tide method. The top panel shows the water level during the 13h campaign. The middle panel represents the longer time series of computed water level. Both time series are combined on a local time axis, centered around the reference time (bottom panel).

First, one timestep of the measurement is designated as the reference time $t_{ref,meas}$. In figure C.1, the moment of high water is chosen, but the method works for any reference time. The aim is to construct a local time axis, expressed in hours before and after this reference time.

The algorithm then searches for the $t_{ref,model}$ inside the modeled time frame $[t_{start,model}\ t_{stop,model}]$ that minimizes the error between the modeled and measured water level on the local time axis $(t_{model} - t_{ref,model})$.

The assumption is, that because the water levels match, the computed velocity on the local time axis (e.g. the velocity 1 hour before high water) will match the measured velocity on the local time axis, even if the measurement time frame $[t_{start,meas}\ t_{stop,meas}]$ lies outside the modeled time frame $[t_{start,model}\ t_{stop,model}]$.

The error between the modeled and measured water level can be defined either as a RMSE, or a bias-corrected RMSE_0:

$$\mathrm{RMSE} = \sqrt{\frac{\sum_{t_{min}}^{t_{max}} \left(\mathrm{WL}_{mod} - \mathrm{WL}_{meas}\right)^2}{N}} \tag{C.1}$$

$$\mathrm{RMSE}_0 = \sqrt{\frac{\sum_{t_{min}}^{t_{max}} \left(\mathrm{WL}_{mod} - \mathrm{WL}_{meas} - \overline{\left(\mathrm{WL}_{mod} - \mathrm{WL}_{meas}\right)}\right)^2}{N}} \tag{C.2}$$

with $[t_{min}\ t_{max}]$ the time frame on the local time axis and the term $\overline{\mathrm{WL}_{mod} - \mathrm{WL}_{meas}}$ the average error between modeled and measured water level in the time frame $[t_{min}\ t_{max}]$.

By choosing RMSE as the error quantification, the algorithm will pick the modeled sub-period where the computed water level is closest to the water level that was measured during the campaign. With RMSE_0 as the error quantification, a (small) bias between modeled and measured water levels is not counted in the cost function that is minimized to find $t_{ref,model}$. It is primarily the tidal amplitude, and the shape of the tidal curve, that determine the velocities. The mean water level has only a secondary influence on the velocities, e.g. by determining which part of the bathymetry is subject to wetting and drying, or by influencing the tidal wave celerity. A difference between the average water level could for example be related to a difference in surge between the two time frames. The choice between RMSE and RMSE0 is ultimately up to the modeler.

Since the bathymetry influences the local velocity, the assumption that matching tidal conditions also mean matching velocities only holds if the model bathymetry and the bathymetry during the measurement are not too different. In light of the morphological evolution of the system, this means that the measured time frame $[t_{start,meas}\ t_{stop,meas}]$ should not be too distant from the modeled time frame $[t_{start,model}\ t_{stop,model}]$. Another case where matching tidal conditions don't necessarily mean matching velocities would be when density currents are known to be important. It is up to the modeler to decide which measurements can still be taken into account in the model calibration.

References

Vanlede, J., Chu, K., and Fonias, E. (2020). Introducing the VIMM toolbox for the (re)calibration of the SCALDIS model. In Breughem, A., Frederickx, L., Koutrouveli, T., Kulkarni, R., Chu, K., and Decrop, B., editors, *Online proceedings of the papers submitted to the 2020 TELEMAC-MASCARET User Conference*, pages 153–158, Antwerp, Belgium. IMDC.

D

1DV point model

D.1. Introduction

A simplified model can be a useful complementary tool to a more complex model, e.g. to study model behavior, to do an initial calibration of model parameters, or to perform sensitivity analyses.

1DV point models have been used successfully in the past for sediment-related research, e.g. to calibrate the parameterization of a North Sea sediment transport model (van Kessel et al., 2011), to study stratification effects in sediment-laden flow (Winterwerp, 2001, 2006) or for the interpretation of in situ data (van der Ham and Winterwerp, 2001).

In this thesis, the 1DV model is used to perform an initial calibration of the sediment transport model in section 5.11.1.

D.2. Governing equations

The 1DV advection-diffusion equation for suspended sediment concentration in the water column is given in equation D.1.

$$\frac{\partial c}{\partial t} = -w_s \frac{\partial c}{\partial z} + \frac{\partial}{\partial z}\left(D_v \frac{\partial c}{\partial z}\right) + S \tag{D.1}$$

with c the mass concentration of sediment [kg/m³] and D_v the eddy diffusivity [m²/s].

The eddy diffusivity D_v is calculated as

$$D_v = \frac{\nu_T}{\sigma_T} \tag{D.2}$$

with σ_T the Prandtl-Schmidt number and ν_T the eddy viscosity.

Equation D.1 can be converted into flux form using Gauss' theorem:

$$\frac{dM}{dt} = -\oint_A c w_s dA + \oint_A D_v \frac{\partial c}{\partial z} dA + S_f \tag{D.3}$$

with A the top and bottom boundary of the control volume and M the mass of sediment per unit area in the control volume [kg/m²].

The source and sink terms S_f are the erosion and deposition fluxes [kg/m²s]. Deposition is modeled as a continuous process (see also section 5.9.2):

$$D = w_s c_b P_{sed} \tag{D.4}$$

with P_{sed} the sedimentation probability that can vary between 0 and 1 (see also the discussion in section 5.9.2), w_s the settling velocity and c_b the concentration close to the bed [kg/m³].

Erosion is described either as a zero order or as a first order process (see also section 5.9.3):

$$\begin{gathered} E = M_0 \left(\frac{\tau - \tau_{cr,e}}{\tau_{cr,e}} \right) \text{ for } \tau > \tau_{cr,e} \\ \text{or} \\ E = m M_1 \left(\frac{\tau - \tau_{cr,e}}{\tau_{cr,e}} \right) \text{ for } \tau > \tau_{cr,e} \end{gathered} \tag{D.5}$$

with M_0 the zero order resuspension constant [kg/m²s] and M_1 the first order resuspension constant [1/s]. m is the dry mass per unit area in the bed [kg/m²] and τ is the total bed shear stress [N/m²]. Erosion is supply-limited with the available amount in the bed m.

D.3. Discretization and numerical scheme

Equations D.3 - D.5 are solved numerically on a staggered grid (see figure D.1), using a finite volume scheme.

Concentration and velocity are defined on cell centers, the eddy diffusivity on cell interfaces. The advective and diffusive term are treated implicitly, whereas the source terms E and D are treated explicitly. A central scheme is used for the diffusive flux.

u,v, τ and D_v are read in from the result of a 3D hydrodynamic simulation.

For each timestep, the 1DV scheme solves the vertical profile of c and the mud content in the bed m.

D.4. Residual transport

The horizontal sediment flux $\vec{f}$ [kg/m²s] is calculated as:

$$\vec{f}\,(z) = \vec{u}\,(z)\, c\,(z) \tag{D.6}$$

The sediment transport $\vec{F}$ per unit width [kg/ms] is the vertical integration of the sediment flux $\vec{f}$:

$$\vec{F} = \int_0^H \vec{f} dz \tag{D.7}$$

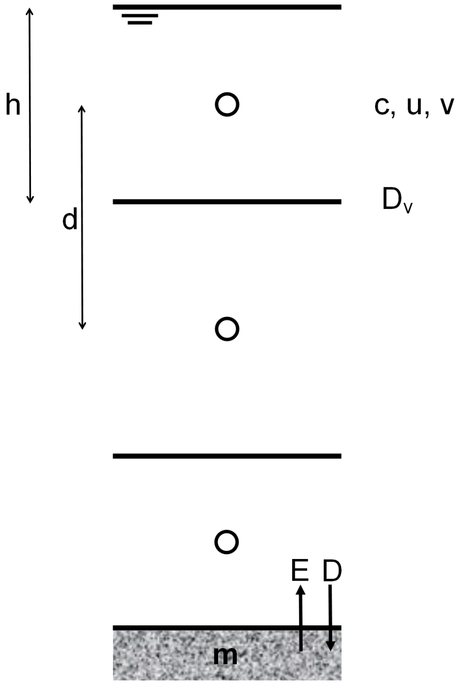

Figure D.1: Illustration of the staggered grid. Lines are cell interfaces, circles represent cell centres.

The residual transport per unit width $\overrightarrow{F_{res}}$ [kg/m] is calculated as:

$$\overrightarrow{F_{res}} = \int_0^T \vec{F} dt \tag{D.8}$$

with T a suitably long period (e.g. a spring/neap cycle).

D.5. Validation

The 1DV scheme is validated against the Rouse profile for stationary, uniform flow. The testcase is taken from Ruessink and Roelvink (2000). First, a long flume is simulated in Delft3D-FLOW. Its dimensions are M x N x K = 51 x 11 x 8, with a longitudinal and transverse grid spacing of 200 m and 20 m, respectively. Thus, the flume is 10 km long and 200 m wide. The water depth in the flume is 20 m. The bed slope matches the friction losses of the flow at the desired (depth-averaged) flow velocity u of 1 m/s, with a Chezy coefficient of 50 $m^{0.5}$ s^{-1}. The hydrodynamic simulation uses the k-ϵ turbulence model.

The 1DV model is subsequently run with a settling velocity of 1 mm/s and a Prandtl-Schmidt number of 0.7. $\tau_{cr,e}$ is 1 Pa. The zero order erosion coefficient M_0 is 0.001 kg/m²s. The initial suspended sediment concentration is 0.01 kg/m³. The result in figure D.2 shows the equilibrium profile simulated with the 1DV model, and the analytical solution.

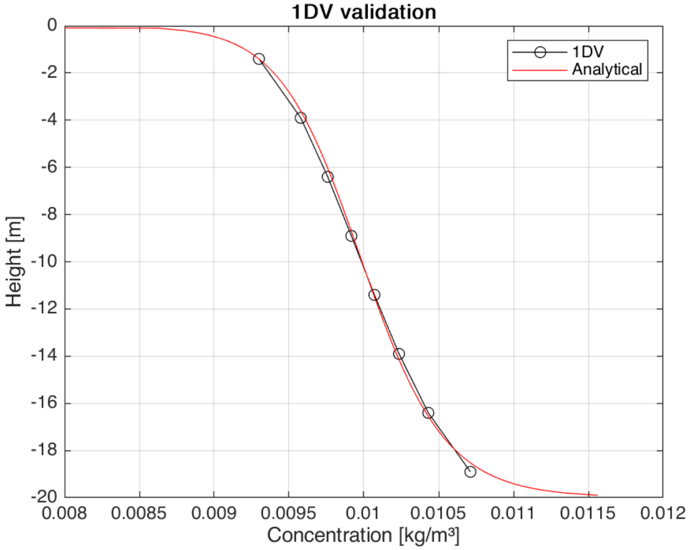

Figure D.2: Comparison between theoretical Rouse concentration profile and 1DV simulation.

References

Ruessink, G. and Roelvink, D. (2000). Validation of On-line mud transport within Delft3D Flow. Technical report.

van der Ham, R. and Winterwerp, J. (2001). Turbulent exchange of fine sediments in a tidal channel in the Ems/Dollard estuary. Part II. Analysis with a 1DV numerical model. *Continental Shelf Research*, 21(15):1629–1647.

van Kessel, T., Winterwerp, H., Van Prooijen, B., Van Ledden, M., and Borst, W. (2011). Modelling the seasonal dynamics of SPM with a simple algorithm for the buffering of fines in a sandy seabed. *Continental Shelf Research*, 31(10):S124–S134.

Winterwerp, J. C. (2001). Stratification effects by cohesive and noncohesive sediment. *Journal of Geophysical Research: Oceans*, 106(C10):22559–22574.

Winterwerp, J. C. (2006). Stratification effects by fine suspended sediment at low, medium, and very high concentrations. *Journal of Geophysical Research: Oceans*, 111(5).

List of symbols

A	Interface area between a harbor and the connecting water body	m^2
A	Semi-orbital excursion length,eq. 5.11	m
a	Reference height above the bed, eq. 2.5	m
c	Velocity of a saline front, eq. 4.3	m/s
c	Mass concentration of sediment	kg/m^3
c_a	Reference sediment concentration at height a above the bed	kg/m^3
c_b	Concentration close to the bed	kg/m^3
c_g	Gelling concentration	kg/m^3
C	Cost function	-
D_*	Dimensionless particle diameter, eq. 5.18	-
d_{50}	Median grain diameter	m
D	Deposition flux, eq. 5.14	kg/m^2s
E_1	Erosion flux of the first layer, eq. 5.16	kg/m^2s
E_2	Erosion flux of the second layer, eq. 5.17	kg/m^2s
d_{50}	Median grain size	m
f_w	Dimensionless wave friction factor, eq. 5.9	-
F	Wind fetch, eq. 5.6	m
F_*	Non-dimensional wind fetch, eq. 5.6	-
F^{sed}	Net sediment flux, eq. 3.11	kg/s
F^{sed+}	Sediment flux related to outflow	kg/s
F^{sed-}	Sediment flux related to inflow	kg/s
$\widehat{F^{sed}}$	Net sediment flux over a tidal cycle	kg
F^{sed}_{hor}	Net sediment flux related to horizontal exchange	kg/s
F^{sed}_{tidal}	Net sediment flux related to tidal filling and emptying, eq. 3.12	kg/s
F^{sed}_{ver}	Net sediment flux related to vertical exchange	kg/s
F^{wat}	Water flux, eq. 3.8	m^3/s
$\widehat{F^{wat}}$	Total water flux over a tidal cycle, eq. 3.10	m^3
g	Gravitational acceleration	m/s^2
h	Water depth	m
h_1	Height of the fresh water front, eq. 4.3	m
h_*	Non-dimensional water depth, eq 5.6	-
H_s	Significant wave height	m
k_s	Nikuradse roughness	m
L	Wave length, eq. 2.1	m

L_{TE}^{maj}	Tidal excursion length along the major axis of the tidal ellipse, eq. 5.1	m
M_0	Zero order resuspension constant	kg/m^2s
M_1	First order resuspension constant	$1/s$
M_2	Erosion coefficient for the second (sandy) layer, eq. 5.18	-
$M_2{}'$	Erosion coefficient for the second (sandy) layer, alternative formulation, eq. 5.19	kg/m^2s
m^d	Amount of dry matter dredged	kg
m_1	Mud (dry) mass in the first layer	kg/m^2
m_2	Mud (dry) mass in the second layer	kg/m^2
n	Porosity	-
p_2	Mud fraction of the second layer, eq. 5.15	-
P_{sed}	Sedimentation probability	-
r_*	Dimensionless relative roughness height, eq. 5.11	-
s	Relative density of the sediment	-
R	Cylinder Radius, eq. 5.2	m
Ro	Rouse number, eq. 2.5	-
T_p	Wave period	s
u_*	Shear velocity, eq. 2.5	m/s
$u_{M_2}^{maj}$	M_2 velocity amplitude along the major axis of the tidal ellipse, eq. 5.1	m/s
U	Undisturbed (far-field) flow around a cylinder, eq. 5.2	m/s
U_{10}	Wind speed at 10 m height, eq. 5.6	m/s
U_{orb}	Near-bed wave orbital velocity, eq. 5.8	m/s
$\widetilde{v}$	Velocity component with no net exchange, eq. 3.3	m/s
v_{hor}	Velocity component corresponding to horizontal exchange, eq. 3.4	m/s
v_n	Velocity component perpendicular to harbor entrance, eq. 3.1	m/s
v_{tidal}	Cross-sectionally averaged velocity component, eq. 3.2	m/s
v_{ver}	Velocity component corresponding to vertical exchange, eq. 3.5	m/s
w_s	Settling velocity	m/s
w_s^{macro}	Settling velocity of macroflocs $> 160\mu m$	m/s
z	Height above the bed	m

α	Fraction of the deposition flux contributing to layer 2	-
β_1	Loss term, eq. 4.3	-
β	Coefficient relating mass and momentum transfer	-
Δh^d	Depth change of the mud-water interface due to dredging, eq. 4.2	m
Δh^m	Measured depth change of the mud-water interface, eq. 4.1	m
Δh^n	Natural depth change of the mud-water interface	m

Δo	Measurement error	
η	Water level	m
θ_U	Pase-lag between M_2 and M_4 component of velocity, eq. 2.3	°
κ	von Kármán constant	-
ν	Kinematic viscosity of water	m^2/s
ε	Relative density difference $\Delta\rho/\rho$, eq. 4.3	-
ρ_g	Grain density	kg/m^3
ρ_b	In situ bulk density (mass wet sediment/total wet volume)	kg/m^3
ρ_w	Density of seawater	kg/m^3
σ^{obs}	Variance of the observations, eq. A.1	
τ_{bed}	Total bed shear stress, eq. 5.13	N/m^2
$\tau_{cr,e}$	Critical shear stress for erosion	N/m^2
$\tau_{cr,d}$	Critical shear stress for deposition	N/m^2
τ_{flow}	Flow-induced bed shear stress	N/m^2
τ_{wave}	Wave-induced bed shear stress, eq. 5.9	N/m^2
ϕ_p	Dimensionless pick-up rate, eq. 5.18	-
φ	Velocity potential for irrotational flow, eq. 5.2	m^2/s

List of abbreviations

ADCP	Acoustic Doppler Current Profiler
ADP	Acoustic Doppler Profiler
ADV	Acoustic Doppler Velocimeter
BCZ	Belgian Coastal Zone
CDNB	Centraal Deel Nieuwe Buitenhaven (Dutch) Central part of the new outer harbor (English)
CT	Comparable Tide
CTM	Coastal Turbidity Maximum
ECMWF	European Centre for Medium-range Weather Forecasts
FHR	Flanders Hydraulics Research (English) Waterbouwkundig Laboratorium (Dutch)
FTU	Formazine Turbidity Units
GLLWS	Gemiddeld Laag Laagwater Sprintij (Dutch) Mean Lower Low Water (MLLW, English)
HCBS	High Concentration Benthic Suspension
HLES	Horizontal Large Eddy Simulation
HIC	Hydrologisch Informatie Centrum (Dutch)
HVC	Hopper Volume Concentration (see section 4.3.2)
IVC	In situ Volume Concentration (see section 4.3.2)
LAT	Lowest Astronomical Tide
LNG	Liquefied Natural Gas
mab	Meter Above the Bed
MAE	Mean Absolute Error
MSE	Mean Square Error
MTDM	Million Tonnes Dry Matter
NAP	Normaal Amsterdams Peil (Dutch)
OBS	Optical Backscatter
PDF	Probability Density Function
RBINS	Royal Belgian Institute of Natural Sciences
RMAE	Relative Mean Absolute Error
RMSE	Root Mean Square Error
SPM	Suspended Particulate Matter
SSC	Suspended Sediment Concentration
SWAN	Simulating Waves Nearshore
TDM	Tonnes Dry Matter
TEU	Twenty Foot Equivalent Unit
TIM	Total Inorganic Matter
TKE	Turbulent Kinetic Energy

UKC	Under Keel Clearance
ZBO	Disposal location ”Zeebrugge Oost”
ZBW	Disposal location ”Zeebrugge West”
ZUNO	Zuidelijke Noordzee (Dutch) Southern North Sea (English)

Acknowledgements

First of all, I would like to thank my promotor Han Winterwerp. It was during the NCK summer school of 2009 on the island of Texel, that he first raised the possibility to combine my research work at Flanders Hydraulics Research (FHR) with part-time Phd research at TUDelft, and also suggested Zeebrugge as a possible topic. I am grateful for that talk on the beach of Texel that planted the seed, and made this journey possible. Thank you for believing in me, and for challenging me along the way to think deeper and express myself more clearly.

The research described in this thesis was initiated as part of the R&D program at FHR, and was done in part–time, next to my daily work as a researcher at FHR. I would like to thank the coordinator at that time of the research group Tom De Mulder, and the division heads Frank Mostaert and Karim Bellafkih for giving me this opportunity, and for their continuing support. Furthermore I would like to thank my collaborators at the lab who joined me during various stages of this research project: Gert Leyssen, Alice Scanu, George Schramkowski, Bart De Maerschalck, Arvid Dujardin and Diem Nguyen. I really enjoyed working together on this topic, and I am proud of the results that we achieved.

I am also grateful to the organizers of the PECS, INTERCOH and NCK communities, which have provided a platform to find inspiration, discuss results and receive valuable suggestions.

On a more personal note, I want to thank my parents Erwin and Veerle for the supporting environment I grew up in. You recognized my curiosity early on, and always encouraged me to explore and to learn. I also want to thank my parents-in-law Hubert and Anita for the unwavering support you give to our family.

Last but not least, I want to thank my wife Annick for her loving support during the writing phase, and for celebrating the little victories and bigger blessings along our way, together.

Curriculum Vitæ

Joris Vanlede

Joris Vanlede was born on May 31st, 1980 in Sint-Niklaas, Belgium, where he grew up with his younger brother and sister. After completing his secondary education at Sint-Jozef-Klein-Seminarie (ASO Greek and mathematics), he studied civil engineering at KU Leuven from 1998 to 2003, where he graduated as a geotechnical engineer. In his final year he was a trainee in the soil mechanics lab of the Universidad Mayor de San Simon (Cochabamba, Bolivia). His master's thesis was on the behavior of rock mass around tunnels at large depth. The work focused on the Misicuni tunnel, which was under development at the time, and which currently serves to provide drinking water to the city of Cochabamba.

He went on to obtain a master of science in water resources engineering (2003-2004), a joint degree organized by the KU Leuven and the Free University of Brussels. His thesis was on the implementation of the European water framework directive in the Nete catchment in Belgium.

He started working as a research engineer at Flanders Hydraulics Research in Antwerp (Belgium) in 2004, where he currently works on numerical modeling and field measurements of hydraulics and sediment transport. Since 2012 he is product manager of numerical modeling at the institute, and since 2013 he holds the position of senior expert.

He is fascinated by water. He is a a PADI-certified diver, and likes to go out sailing in the open sea. He is also passionate about food. He received his training as a professional chef at PIVA in Antwerp (2010-2015) and enjoys exploring the rich culinary world of taste, texture and technique.

He married Annick Claessens in 2018. Together they have two sons, Stan and Leon.

Selected publications

12. van Maren, D.S.; Vroom, J.; Fettweis, M.; **Vanlede, J.** (2020). Formation of the Zeebrugge coastal turbidity maximum : The role of uncertainty in near-bed exchange processes. Mar. Geol. 425: 106186.

11. **Vanlede, J.**; Dujardin, A.; Fettweis, M.; Van Hoestenberghe, T.; Martens, C. (2019). *Mud Dynamics in the Port of Zeebrugge.* Ocean Dynamics, 69(9): 1085-1099.

10. Adriaens, R.; Zeelmaekers, E.; Fettweis, M.; Vanlierde, E.; **Vanlede, J.**; Stassen, P.; Elsen, J.; Srodon, J.; Vandenberghe, N. (2018) *Quantitative clay mineralogy as provenance indicator for recent muds in the southern North Sea.* Marine Geology 398: 48-58.

9. Fettweis, M.; Baeye, M.; Cardoso, C.; Dujardin, A.; Lauwaert, B.; Van den Eynde, D.; Van Hoestenberghe, T.; **Vanlede, J.**; Van Poucke, L.; Velez, C.; Martens, C. (2016). *The impact of disposal of fine-grained sediments from maintenance dredging works on SPM concentration and fluid mud in and outside the harbor of Zeebrugge.* Ocean Dynamics 66(11): 1497-1516.

8. **Vanlede, J.**; Dujardin, A. (2014). *A Geometric Method to study Water and Sediment Exchange in Tidal Harbors.* Ocean Dynamics, 64(11): 1631–1641.

7. **Vanlede, J.**; Coen, L.; Deschamps, M. (2014). *Tidal prediction in the Sea Scheldt (Belgium) using a combination of harmonic tidal prediction and 1D hydraulic modeling.* Natural Resources 5: 627-633.

6. van Kessel, T.; **Vanlede, J.**; de Kok, J. (2011). *Development of a mud transport model for the Scheldt estuary.* Continental Shelf Research 31(10): S165-S181.

5. van Maren, D.S.; Winterwerp, J.C.; Decrop, B.; Wang, Z.B.; **Vanlede, J.** (2011). *Predicting the effect of a current deflecting wall on harbour siltation.* Continental Shelf Research, 31(10): S182-S198.

4. van der Wal, D.; van Kessel, T.; Eleveld, M.; **Vanlede, J.** (2010). *Spatial heterogeneity in estuarine mud dynamics.* Ocean Dynamics 60(3): 519-533.

3. van Maren, D.S.; Winterwerp, J.C.; Sas, M.; **Vanlede, J.** (2009). *The effect of dock length on harbour siltation.* Continental Shelf Research 29(11-12): 1410-1425.

2. Manning, A.J.; Martens, C.; De Mulder, T.; **Vanlede, J.**; Winterwerp, J.C.; Ganderton, P.; Graham, G.W. (2007). *Mud floc observations in the turbidity maximum zone of the Scheldt estuary during neap tides* Journal of Coastal Research SI 50: 832-836

1. Winterwerp, J.C.; Manning, A.J.; Martens, C.; De Mulder, T.; **Vanlede, J.** (2006). *A heuristic formula for turbulence-induced flocculation of cohesive sediment.* Estuarine, Coastal and Shelf Science 68(1-2): 195-207.

Epilogue

On exactitude in science

In that empire, the art of cartography attained such perfection that the map of a single province occupied the entirety of a city, and the map of the empire, the entirety of a province. In time, those unconscionable maps no longer satisfied, and the cartographers guilds struck a map of the empire whose size was that of the empire, and which coincided point for point with it. The following generations, who were not so fond of the study of cartography as their forebears had been, saw that that vast map was useless, and not without some pitilessness was it, that they delivered it up to the inclemencies of sun and winters. In the deserts of the west, still today, there are tattered ruins of that map, inhabited by animals and beggars.

Jorge Luis Borges, *Collected Fictions*, 1946
translated by Andrew Hurley